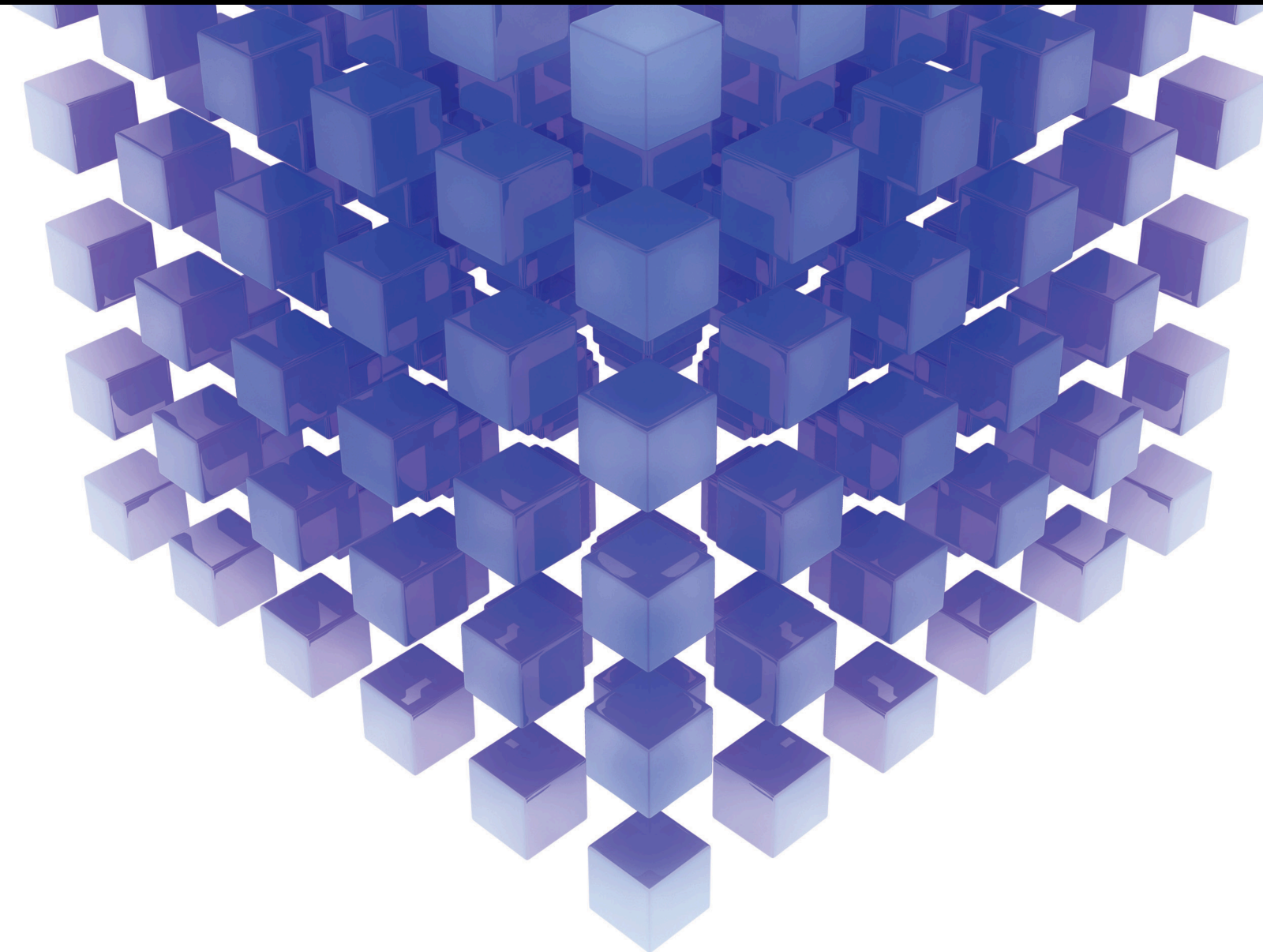


Computational Methods and Applications to Simulate Water-Related Natural Hazards

Lead Guest Editor: Raffaele Albano

Guest Editors: Sauro Manenti, José M. Domínguez, Shaowu Li, and Dong Wang





Computational Methods and Applications to Simulate Water-Related Natural Hazards

Mathematical Problems in Engineering

**Computational Methods and Applications to
Simulate Water-Related Natural Hazards**

Lead Guest Editor: Raffaele Albano

Guest Editors: Sauro Manenti, José M. Domínguez, Shaowu
Li, and Dong Wang



Copyright © 2020 Hindawi Limited. All rights reserved.

This is a special issue published in “Mathematical Problems in Engineering.” All articles are open access articles distributed under the Creative Commons Attribution License, which permits unrestricted use, distribution, and reproduction in any medium, provided the original work is properly cited.

Chief Editor

Guangming Xie, China

Editorial Board

Mohamed Abd El Aziz, Egypt
AITOUCHE Abdelouhab, France
Leonardo Acho, Spain
José Ángel Acosta, Spain
Daniela Addressi, Italy
Paolo Addresso, Italy
Claudia Adduce, Italy
Ramesh Agarwal, USA
Francesco Aggogeri, Italy
Juan C. Agüero, Australia
Ricardo Aguilar-Lopez, Mexico
Tarek Ahmed-Ali, France
Elias Aifantis, USA
Muhammad N. Akram, Norway
Guido Ala, Italy
Andrea Alaimo, Italy
Reza Alam, USA
Nicholas Alexander, United Kingdom
Salvatore Alfonzetti, Italy
Mohammad D. Aliyu, Canada
Juan A. Almendral, Spain
José Domingo Álvarez, Spain
Cláudio Alves, Portugal
Juan P. Amezcua-Sanchez, Mexico
Lionel Amodeo, France
Sebastian Anita, Romania
Renata Archetti, Italy
Felice Arena, Italy
Sabri Arik, Turkey
Francesco Aristodemo, Italy
Fausto Arpino, Italy
Alessandro Arsie, USA
Edoardo Artioli, Italy
Fumihiko Ashida, Japan
Farhad Aslani, Australia
Mohsen Asle Zaem, USA
Romain Aubry, USA
Richard I. Avery, USA
Viktor Avrutin, Germany
Francesco Aymerich, Italy
Sajad Azizi, Belgium
Michele Baccocchi, Italy
Seungik Baek, USA
Adil Bagirov, Australia

Khaled Bahlali, France
Laurent Bako, France
Pedro Balaguer, Spain
Stefan Balint, Romania
Ines Tejado Balsera, Spain
Alfonso Banos, Spain
Jerzy Baranowski, Poland
Roberto Baratti, Italy
Andrzej Bartoszewicz, Poland
David Bassir, France
Chiara Bedon, Italy
Azeddine Beghdadi, France
Denis Benasciutti, Italy
Ivano Benedetti, Italy
Rosa M. Benito, Spain
Elena Benvenuti, Italy
Giovanni Berselli, Italy
Giorgio Besagni, Italy
Michele Betti, Italy
Pietro Bia, Italy
Carlo Bianca, France
Vittorio Bianco, Italy
Vincenzo Bianco, Italy
Simone Bianco, Italy
David Bigaud, France
Antonio Bilotta, Italy
Paul Bogdan, USA
Guido Bolognesi, United Kingdom
Rodolfo Bontempo, Italy
Alberto Borboni, Italy
Paolo Boscarol, Italy
Daniela Boso, Italy
Guillermo Botella-Juan, Spain
Boulaïd Boulkroune, Belgium
Fabio Bovenga, Italy
Francesco Braghin, Italy
Ricardo Branco, Portugal
Maurizio Brocchini, Italy
Julien Bruchon, France
Matteo Bruggi, Italy
Michele Brun, Italy
Vasilis Burganos, Greece
Tito Busani, USA
Raquel Caballero-Águila, Spain

Filippo Cacace, Italy
Pierfrancesco Cacciola, United Kingdom
Salvatore Caddemi, Italy
Roberto Caldelli, Italy
Alberto Campagnolo, Italy
Eric Campos, Mexico
Marko Canadija, Croatia
Salvatore Cannella, Italy
Francesco Cannizzaro, Italy
Maosen Cao, China
Javier Cara, Spain
Ana Carpio, Spain
Caterina Casavola, Italy
Sara Casciati, Italy
Federica Caselli, Italy
Carmen Castillo, Spain
Inmaculada T. Castro, Spain
Miguel Castro, Portugal
Giuseppe Catalanotti, United Kingdom
Nicola Caterino, Italy
Alberto Cavallo, Italy
Gabriele Cazzulani, Italy
Luis Cea, Spain
Song Cen, China
Miguel Cerrolaza, Venezuela
M. Chadli, France
Gregory Chagnon, France
Ludovic Chamoin, France
Ching-Ter Chang, Taiwan
Xiaoheng Chang, China
Qing Chang, USA
Michael J. Chappell, United Kingdom
Kacem Chehdi, France
Peter N. Cheimets, USA
Xinkai Chen, Japan
Luca Chiapponi, Italy
Francisco Chicano, Spain
Nicholas Chileshe, Australia
Adrian Chmielewski, Poland
Ioannis T. Christou, Greece
Hung-Yuan Chung, Taiwan
Simone Cinquemani, Italy
Roberto G. Citarella, Italy
Joaquim Ciurana, Spain
John D. Clayton, USA
Francesco Clementi, Italy
Piero Colajanni, Italy

Giuseppina Colicchio, Italy
Vassilios Constantoudis, Greece
Francesco Conte, Italy
Enrico Conte, Italy
Alessandro Contento, USA
Mario Cools, Belgium
Jean-Pierre Corriou, France
J.-C. Cortés, Spain
Carlo Cosentino, Italy
Paolo Crippa, Italy
Andrea Crivellini, Italy
Erik Cuevas, Mexico
Maria C. Cunha, Portugal
Mehmet Cunkas, Turkey
Peter Dabnichki, Australia
Luca D'Acerno, Italy
Weizhong Dai, USA
Andrea Dall'Asta, Italy
Purushothaman Damodaran, USA
Bhabani S. Dandapat, India
Farhang Daneshmand, Canada
Giuseppe D'Aniello, Italy
Sergey Dashkovskiy, Germany
Fabio De Angelis, Italy
Samuele De Bartolo, Italy
Abílio De Jesus, Portugal
Pietro De Lellis, Italy
Alessandro De Luca, Italy
Stefano de Miranda, Italy
Filippo de Monte, Italy
José António Fonseca de Oliveira Correia, Portugal
Maria do Rosário de Pinho, Portugal
Michael Defoort, France
Alessandro Della Corte, Italy
Xavier Delorme, France
Laurent Dewasme, Belgium
Angelo Di Egidio, Italy
Roberta Di Pace, Italy
Ramón I. Diego, Spain
Yannis Dimakopoulos, Greece
Zhengtao Ding, United Kingdom
M. Djemai, France
Alexandre B. Dolgui, France
Georgios Dounias, Greece
Florent Duchaine, France
George S. Dulikravich, USA

Bogdan Dumitrescu, Romania
Horst Ecker, Austria
Saeed Eftekhar Azam, USA
Ahmed El Hajjaji, France
Antonio Elipe, Spain
Fouad Erchiqui, Canada
Anders Eriksson, Sweden
R. Emre Erkmén, Canada
Gilberto Espinosa-Paredes, Mexico
Leandro F. F. Miguel, Brazil
Andrea L. Facci, Italy
Giacomo Falcucci, Italy
Giovanni Falsone, Italy
Hua Fan, China
Nicholas Fantuzzi, Italy
Yann Favennec, France
Fiorenzo A. Fazzolari, United Kingdom
Roberto Fedele, Italy
Giuseppe Fedele, Italy
Zhongyang Fei, China
Arturo J. Fernández, Spain
Jesus M. Fernandez Oro, Spain
Massimiliano Ferraioli, Italy
Massimiliano Ferrara, Italy
Francesco Ferrise, Italy
Eric Feulvarch, France
Barak Fishbain, Israel
Simme Douwe Flapper, The Netherlands
Thierry Floquet, France
Eric Florentin, France
Alessandro Formisano, Italy
Francesco Franco, Italy
Elisa Francomano, Italy
Tomonari Furukawa, USA
Juan C. G. Prada, Spain
Mohamed Gadala, Canada
Matteo Gaeta, Italy
Mauro Gaggero, Italy
Zoran Gajic, USA
Erez Gal, Israel
Jaime Gallardo-Alvarado, Mexico
Mosè Gallo, Italy
Ugo Galvanetto, Italy
Akemi Gálvez, Spain
Rita Gamberini, Italy
Maria L. Gandarias, Spain
Zhong-Ke Gao, China

Zhiwei Gao, United Kingdom
Giovanni Garcea, Italy
Luis Rodolfo Garcia Carrillo, USA
Jose M. Garcia-Aznar, Spain
Akhil Garg, China
Harish Garg, India
Alessandro Gasparetto, Italy
Gianluca Gatti, Italy
Oleg V. Gendelman, Israel
Stylianos Georgantzinou, Greece
Fotios Georgiades, United Kingdom
Parviz Ghadimi, Iran
Mergen H. Ghayesh, Australia
Georgios I. Giannopoulos, Greece
Agathoklis Giaralis, United Kingdom
Pablo Gil, Spain
Anna M. Gil-Lafuente, Spain
Ivan Giorgio, Italy
Gaetano Giunta, Luxembourg
Alessio Gizzi, Italy
Jefferson L.M.A. Gomes, United Kingdom
Emilio Gómez-Déniz, Spain
Antonio M. Gonçalves de Lima, Brazil
David González, Spain
Chris Goodrich, USA
Rama S. R. Gorla, USA
Kannan Govindan, Denmark
Antoine Grall, France
George A. Gravvanis, Greece
Fabrizio Greco, Italy
David Greiner, Spain
Simonetta Grilli, Italy
Jason Gu, Canada
Federico Guarracino, Italy
Michele Guida, Italy
Zhaoxia Guo, China
José L. Guzmán, Spain
Quang Phuc Ha, Australia
Petr Hájek, Czech Republic
Zhen-Lai Han, China
Weimin Han, USA
Thomas Hanne, Switzerland
Mohammad A. Hariri-Ardebili, USA
Xiao-Qiao He, China
Nicolae Herisanu, Romania
Alfredo G. Hernández-Díaz, Spain
M.I. Herreros, Spain

Eckhard Hitzer, Japan
Paul Honeine, France
Jaromir Horacek, Czech Republic
Muneo Hori, Japan
András Horváth, Italy
S. Hassan Hosseinnia, The Netherlands
Gordon Huang, Canada
Sajid Hussain, Canada
Asier Ibeas, Spain
Orest V. Iftime, The Netherlands
Przemyslaw Ignaciuk, Poland
Giacomo Innocenti, Italy
Emilio Insfran Pelozo, Spain
Alessio Ishizaka, France
Nazrul Islam, USA
Benoit lung, France
Benjamin Ivorra, Spain
Payman Jalali, Finland
Mahdi Jalili, Australia
Łukasz Jankowski, Poland
Samuel N. Jator, USA
Juan C. Jauregui-Correa, Mexico
Reza Jazar, Australia
Khalide Jbilou, France
Piotr Jędrzejowicz, Poland
Isabel S. Jesus, Portugal
Linni Jian, China
Bin Jiang, China
Zhongping Jiang, USA
Emilio Jiménez Macías, Spain
Xiaoliang Jin, USA
Ningde Jin, China
Liang Jing, Canada
Dylan F. Jones, United Kingdom
Palle E. Jorgensen, USA
Viacheslav Kalashnikov, Mexico
Tamas Kalmar-Nagy, Hungary
Tomasz Kapitaniak, Poland
Julius Kaplunov, United Kingdom
Haranath Kar, India
Konstantinos Karamanos, Belgium
Krzysztof Kecik, Poland
Jean-Pierre Kenne, Canada
Chaudry M. Khalique, South Africa
Nam-Il Kim, Republic of Korea
Do Wan Kim, Republic of Korea
Jan Koci, Czech Republic

Ioannis Kostavelis, Greece
Sotiris B. Kotsiantis, Greece
Manfred Krafczyk, Germany
Frederic Kratz, France
Petr Krysl, USA
Krzysztof S. Kulpa, Poland
Shailesh I. Kundalwal, India
Jurgen Kurths, Germany
Cedrick A. K. Kwuimy, USA
Kyandoghere Kyamakya, Austria
Davide La Torre, Italy
Risto Lahdelma, Finland
Hak-Keung Lam, United Kingdom
Giovanni Lancioni, Italy
Jimmy Lauber, France
Antonino Laudani, Italy
Hervé Laurent, France
Aimé Lay-Ekuakille, Italy
Nicolas J. Leconte, France
Dimitri Lefebvre, France
Eric Lefevre, France
Marek Lefik, Poland
Yaguo Lei, China
Kauko Leiviskä, Finland
Thibault Lemaire, France
Roman Lewandowski, Poland
Chen-Feng Li, China
Yang Li, China
Jian Li, USA
Huchang Liao, China
En-Qiang Lin, USA
Zhiyun Lin, China
Wanquan Liu, Australia
Peter Liu, Taiwan
Bonifacio Llamazares, Spain
Alessandro Lo Schiavo, Italy
Jean Jacques Loiseau, France
Francesco Lolli, Italy
Paolo Lonetti, Italy
Sandro Longo, Italy
António M. Lopes, Portugal
Sebastian López, Spain
Pablo Lopez-Crespo, Spain
Luis M. López-Ochoa, Spain
Ezequiel López-Rubio, Spain
Vassilios C. Loukopoulos, Greece
Jose A. Lozano-Galant, Spain

haiyan Lu, Australia
Gabriel Luque, Spain
Valentin Lychagin, Norway
Dazhong Ma, China
Antonio Madeo, Italy
José María Maestre, Spain
Alessandro Magnani, Italy
Fazal M. Mahomed, South Africa
Noureddine Manamanni, France
Paolo Manfredi, Italy
Didier Maquin, France
Giuseppe Carlo Marano, Italy
Damijan Markovic, France
Rui Cunha Marques, Portugal
Rodrigo Martínez-Bejar, Spain
Guiomar Martín-Herrán, Spain
Denizar Cruz Martins, Brazil
Benoit Marx, France
Elio Masciari, Italy
Franck Massa, France
Paolo Massioni, France
Alessandro Mauro, Italy
Fabio Mazza, Italy
Laura Mazzola, Italy
Driss Mehdi, France
Roderick Melnik, Canada
Pasquale Memmolo, Italy
Xiangyu Meng, USA
Jose Merodio, Spain
Alessio Merola, Italy
Mahmoud Mesbah, Iran
Luciano Mescia, Italy
Laurent Mevel, France
Mariusz Michta, Poland
Aki Mikkola, Finland
Giovanni Minafò, Italy
Hiroyuki Mino, Japan
Pablo Mira, Spain
Dimitrios Mitsotakis, New Zealand
Saleh Mobayen, Iran
Vito Mocella, Italy
Sara Montagna, Italy
Roberto Montanini, Italy
Francisco J. Montáns, Spain
Gisele Mophou, France
Rafael Morales, Spain
Marco Morandini, Italy

Javier Moreno-Valenzuela, Mexico
Simone Morganti, Italy
Caroline Mota, Brazil
Aziz Moukrim, France
Shen Mouquan, China
Dimitris Mourtzis, Greece
Emiliano Mucchi, Italy
Josefa Mula, Spain
Jose J. Muñoz, Spain
Giuseppe Muscolino, Italy
Marco Mussetta, Italy
Hakim Naceur, France
Alessandro Naddeo, Italy
Hassane Naji, France
Mariko Nakano-Miyatake, Mexico
Keivan Navaie, United Kingdom
Luís C. Neves, United Kingdom
AMA Neves, Portugal
Dong Ngoduy, New Zealand
Nhon Nguyen-Thanh, Singapore
Tatsushi Nishi, Japan
Xesús Nogueira, Spain
Ben T. Nohara, Japan
Mohammed Nouari, France
Mustapha Nourelfath, Canada
Wlodzimierz Ogryczak, Poland
Roger Ohayon, France
Krzysztof Okarma, Poland
Mitsuhiro Okayasu, Japan
Alberto Olivares, Spain
Enrique Onieva, Spain
Calogero Orlando, Italy
Alejandro Ortega-Moñux, Spain
Sergio Ortobelli, Italy
Naohisa Otsuka, Japan
Erika Ottaviano, Italy
Pawel Packo, Poland
Arturo Pagano, Italy
Alkis S. Paipetis, Greece
Roberto Palma, Spain
Alessandro Palmeri, United Kingdom
Pasquale Palumbo, Italy
Weifeng Pan, China
Jürgen Pannek, Germany
Elena Panteley, France
Achille Paolone, Italy
George A. Papakostas, Greece

Xosé M. Pardo, Spain
Vicente Parra-Vega, Mexico
Manuel Pastor, Spain
Petr Páta, Czech Republic
Pubudu N. Pathirana, Australia
Surajit Kumar Paul, India
Sitek Paweł, Poland
Luis Payá, Spain
Alexander Paz, Australia
Igor Pažanin, Croatia
Libor Pekař, Czech Republic
Francesco Pellicano, Italy
Marcello Pellicciari, Italy
Zhi-ke Peng, China
Haipeng Peng, China
Mingshu Peng, China
Zhengbiao Peng, Australia
Marzio Pennisi, Italy
Maria Patrizia Pera, Italy
Matjaz Perc, Slovenia
A. M. Bastos Pereira, Portugal
Ricardo Perera, Spain
Francesco Pesavento, Italy
Ivo Petras, Slovakia
Francesco Petrini, Italy
Lukasz Pieczonka, Poland
Dario Piga, Switzerland
Paulo M. Pimenta, Brazil
Antonina Pirrotta, Italy
Marco Pizzarelli, Italy
Vicent Pla, Spain
Javier Plaza, Spain
Kemal Polat, Turkey
Dragan Poljak, Croatia
Jorge Pomares, Spain
Sébastien Poncet, Canada
Volodymyr Ponomaryov, Mexico
Jean-Christophe Ponsart, France
Mauro Pontani, Italy
Cornelio Posadas-Castillo, Mexico
Francesc Pozo, Spain
Christopher Pretty, New Zealand
Luca Pugi, Italy
Krzysztof Puszynski, Poland
Giuseppe Quaranta, Italy
Vitomir Racic, Italy
Jose Ragot, France

Carlo Rainieri, Italy
Kumbakonam Ramamani Rajagopal, USA
Ali Ramazani, USA
Higinio Ramos, Spain
Alain Rassineux, France
S.S. Ravindran, USA
Alessandro Reali, Italy
Oscar Reinoso, Spain
Jose A. Reinoso, Spain
Fabrizio Renno, Italy
Carlo Renno, Italy
Nidhal Rezg, France
Ricardo Riaza, Spain
Francesco Riganti-Fulginei, Italy
Gerasimos Rigatos, Greece
Francesco Ripamonti, Italy
Jorge Rivera, Mexico
Eugenio Roanes-Lozano, Spain
Bruno G. M. Robert, France
Ana Maria A. C. Rocha, Portugal
José Rodellar, Spain
Luigi Rodino, Italy
Rosana Rodríguez López, Spain
Ignacio Rojas, Spain
Alessandra Romolo, Italy
Debasish Roy, India
Gianluigi Rozza, Italy
Jose de Jesus Rubio, Mexico
Rubén Ruiz, Spain
Antonio Ruiz-Cortes, Spain
Ivan D. Rukhlenko, Australia
Mazen Saad, France
Kishin Sadarangani, Spain
Andrés Sáez, Spain
Mehrddad Saif, Canada
John S. Sakellariou, Greece
Salvatore Salamone, USA
Vicente Salas, Spain
Jose Vicente Salcedo, Spain
Nunzio Salerno, Italy
Miguel A. Salido, Spain
Roque J. Saltarén, Spain
Alessandro Salvini, Italy
Sylwester Samborski, Poland
Ramon Sancibrian, Spain
Giuseppe Sanfilippo, Italy
José A. Sanz-Herrera, Spain

Nickolas S. Sapidis, Greece
Evangelos J. Sapountzakis, Greece
Luis Saucedo-Mora, Spain
Marcelo A. Savi, Brazil
Andrey V. Savkin, Australia
Roberta Sburlati, Italy
Gustavo Scaglia, Argentina
Thomas Schuster, Germany
Oliver Schütze, Mexico
Lotfi Senhadji, France
Junwon Seo, USA
Joan Serra-Sagrasta, Spain
Gerardo Severino, Italy
Ruben Sevilla, United Kingdom
Stefano Sfarra, Italy
Mohamed Shaat, United Arab Emirates
Mostafa S. Shadloo, France
Leonid Shaikhet, Israel
Hassan M. Shanechi, USA
Bo Shen, Germany
Suzanne M. Shontz, USA
Babak Shotorban, USA
Zhan Shu, United Kingdom
Nuno Simões, Portugal
Christos H. Skiadas, Greece
Konstantina Skouri, Greece
Neale R. Smith, Mexico
Bogdan Smolka, Poland
Delfim Soares Jr., Brazil
Alba Sofi, Italy
Francesco Soldovieri, Italy
Raffaele Solimene, Italy
Jussi Sopanen, Finland
Marco Spadini, Italy
Bernardo Spagnolo, Italy
Paolo Spagnolo, Italy
Ruben Specogna, Italy
Vasilios Spitas, Greece
Sri Sridharan, USA
Ivanka Stamova, USA
Rafał Stanisławski, Poland
Florin Stoican, Romania
Salvatore Strano, Italy
Yakov Strelniker, Israel
Ning Sun, China
Qiuye Sun, China
Sergey A. Suslov, Australia

Thomas Svensson, Sweden
Andrzej Swierniak, Poland
Andras Szekrenyes, Hungary
Kumar K. Tamma, USA
Yang Tang, Germany
Hafez Tari, USA
Alessandro Tasora, Italy
Sergio Teggi, Italy
Ana C. Teodoro, Portugal
Alexander Timokha, Norway
Gisella Tomasini, Italy
Francesco Tornabene, Italy
Antonio Tornambe, Italy
Javier Martinez Torres, Spain
Mariano Torrisi, Italy
Sang-Bing Tsai, China
George Tsiatas, Greece
Antonios Tsourdos, United Kingdom
Federica Tubino, Italy
Nerio Tullini, Italy
Andrea Tundis, Italy
Emilio Turco, Italy
Ilhan Tuzcu, USA
Efstratios Tzirtzilakis, Greece
Francesco Ubertini, Italy
Filippo Ubertini, Italy
Mohammad Uddin, Australia
Hassan Ugail, United Kingdom
Giuseppe Vairo, Italy
Eusebio Valero, Spain
Pandian Vasant, Malaysia
Marcello Vasta, Italy
Carlos-Renato Vázquez, Mexico
Miguel E. Vázquez-Méndez, Spain
Josep Vehi, Spain
Martin Velasco Villa, Mexico
Kalyana C. Veluvolu, Republic of Korea
Fons J. Verbeek, The Netherlands
Franck J. Vernerey, USA
Georgios Veronis, USA
Vincenzo Vespri, Italy
Renato Vidoni, Italy
Venkatesh Vijayaraghavan, Australia
Anna Vila, Spain
Rafael J. Villanueva, Spain
Francisco R. Villatoro, Spain
Uchechukwu E. Vincent, United Kingdom

Francesca Vipiana, Italy
Stanislav Vitek, Czech Republic
Thuc P. Vo, United Kingdom
Jan Vorel, Czech Republic
Michael Vynnycky, Sweden
Shuming Wang, China
Yongqi Wang, Germany
Hao Wang, USA
Liliang Wang, United Kingdom
Roman Wan-Wendner, Austria
Jaroslaw Was, Poland
P.H. Wen, United Kingdom
Waldemar T. Wójcik, Poland
Desheng D. Wu, Sweden
Yuqiang Wu, China
Changzhi Wu, China
Michalis Xenos, Greece
Xue-Jun Xie, China
Gen Q. Xu, China
Hang Xu, China
Joseph J. Yame, France
Xingang Yan, United Kingdom
Yongheng Yang, Denmark
Jixiang Yang, China
Mijia Yang, USA
Luis J. Yebra, Spain
Peng-Yeng Yin, Taiwan
Yuan Yuan, United Kingdom
Qin Yuming, China
Elena Zaitseva, Slovakia
Arkadiusz Zak, Poland
Daniel Zaldivar, Mexico
Francesco Zammori, Italy
Vittorio Zampoli, Italy
Rafal Zdunek, Poland
Ibrahim Zeid, USA
Qingling Zhang, China
Huaguang Zhang, China
Zhao Zhang, China
Xuping Zhang, Denmark
Kai Zhang, China
Xianming Zhang, Australia
Hao Zhang, China
Haopeng Zhang, USA
Yifan Zhao, United Kingdom
Jian G. Zhou, United Kingdom
Quanxin Zhu, China

Mustapha Zidi, France
Gaetano Zizzo, Italy
Zhixiang Zou, China

Contents

Computational Methods and Applications to Simulate Water-Related Natural Hazards

Raffaele Albano , Sauro Manenti , José M. Domínguez, Shaowu Li , and Dong Wang
Editorial (3 pages), Article ID 4363095, Volume 2020 (2020)

Spatial Distribution and Temporal Trends of Rainfall Erosivity in Three Gorges Reservoir Area of China

Huiying Liu , Guanhua Zhang , Pingcang Zhang, and Shengnan Zhu 
Research Article (15 pages), Article ID 5302679, Volume 2020 (2020)

Are Feature Agreement Statistics Alone Sufficient to Validate Modelled Flood Extent Quality? A Study on Three Swedish Rivers Using Different Digital Elevation Model Resolutions

Nancy Joy Lim  and Sven Anders Brandt 
Research Article (16 pages), Article ID 9816098, Volume 2019 (2019)

A Meshless WCSSPH Boundary Treatment for Open-Channel Flow over Small-Scale Rough Bed

Yang Shi , Jiahua Wei , Shaowu Li , Peng Song , and Bangwen Zhang 
Research Article (17 pages), Article ID 1573049, Volume 2019 (2019)

Investigation of Interaction Solutions for Modified Korteweg-de Vries Equation by Consistent Riccati Expansion Method

Jin-Fu Liang  and Xun Wang 
Research Article (8 pages), Article ID 9535294, Volume 2019 (2019)

Remote Sensing: An Advanced Technique for Crop Condition Assessment

Karim Ennouri  and Abdelaziz Kallel
Review Article (8 pages), Article ID 9404565, Volume 2019 (2019)

Mechanism of Fracturing in Shaft Lining Caused by High-Pressure Pore Water in Stable Rock Strata

Jihuan Han , Jiuqun Zou, Weihao Yang , and Chenchen Hu 
Research Article (9 pages), Article ID 5234642, Volume 2019 (2019)

Numerical Simulation on Thermodynamics Performance in the Fireproof Sealing by Finite Element Analysis

Shuai Gao, Guoqing Zhu , Yunji Gao, Guoqiang Chai, and Jinju Zhou
Research Article (9 pages), Article ID 9593626, Volume 2019 (2019)

Fatigue Strength Assessment of Trimaran Cross-Deck Structure Based on Spectral and Simplified Fatigue Method

Chunbo Zhen , Tianlin Wang , Pengyao Yu, and Liang Feng 
Research Article (13 pages), Article ID 6121584, Volume 2019 (2019)

Editorial

Computational Methods and Applications to Simulate Water-Related Natural Hazards

Raffaele Albano ¹, **Sauro Manenti** ², **José M. Domínguez**,³ **Shaowu Li** ⁴,
and Dong Wang^{5,6}

¹*School of Engineering, University of Basilicata, 85100 Potenza, Italy*

²*Department of Civil Engineering and Architecture, University of Pavia, via Ferrata 3, 27100 Pavia, Italy*

³*EPHYSLAB Environmental Physics Laboratory, Universidade de Vigo, As Lagoas 32004, Ourense, Spain*

⁴*State Key Laboratory of Hydraulic Engineering Simulation and Safety, Tianjin University, Tianjin 300072, China*

⁵*Department of Civil & Environmental Engineering, National University of Singapore, 21 Lower Kent Ridge Road, Singapore 119077*

⁶*College of Environmental Sciences and Engineering, Dalian Maritime University, Dalian 116000, China*

Correspondence should be addressed to Raffaele Albano; raffaele.albano@unibas.it

Received 30 January 2020; Accepted 30 January 2020; Published 19 February 2020

Copyright © 2020 Raffaele Albano et al. This is an open access article distributed under the Creative Commons Attribution License, which permits unrestricted use, distribution, and reproduction in any medium, provided the original work is properly cited.

Thanks to the availability of high-performance computers, in the last few years, Computational Fluid Dynamics (CFD) has been widely applied to simulate natural hazards in the field of environmental and civil engineering [1]. In order to explore different risk scenarios and potential risk-reduction options and to address hazard related uncertainty, the development of numerical models represents an important task in supporting emergency response agencies, water resource managers, insurance companies, and other decision-makers [2]. The application purpose of CFD modeling requires contextual attention to the output variables of predictive interest and their time and space scales, the level of accuracy required considering eventually real-time data assimilation, and computational efficiency demands [3, 4].

The main aim of this special issue is to highlight the most recent advances in CFD modeling and its application related to water-related natural hazards and discusses future directions. Special focus is devoted to the modeling, handling of uncertainty, and the applications related to relevant natural hazard problems of practical and theoretical interest. A brief summary of all accepted papers is provided below.

In the paper by Y. Shi et al., they have investigated, through the numerical CFD test, the influence of bed surface

roughness on the flow structure in an open channel. In particular, they have developed a CFD meshless method, such as a weakly compressible smoothed particle hydrodynamics (WCSPH) [5], for open-channel turbulence simulation. The proposed rough bed model is based on the ghost boundary particles (GBPs) [6]; it uses wall function for a small-scale rough boundary. The results outperform the traditional mixed-length-based subparticle scale (SPS) turbulence model [7] by obtaining small numerical errors in the mainstream and near-surface region but it is found that errors varied widely for the inner region; the authors showed that the latter error is positively correlated with the channel bed slope and the equivalent roughness. On the basis of these results, the study proposes empirical formulae to calculate the ghost particle velocity under different hydraulic conditions using data mining.

C. Zhen et al. have investigated the fatigue failure for trimaran ship, which is actually considered as a good alternative to monohulls in high-speed transportation and in naval applications [8]. In particular, they have presented a simplified fatigue analysis of trimaran cross-deck structure based on three-dimensional (3D) linear potential flow theory and global finite element (FE) analysis for wave loads and stress transfer functions calculation; at the same time, a stochastic spectral fatigue analysis is carried out considering

the weighted wave heading factors. Then, the authors have demonstrated the application of the proposed method by simulating the fatigue lives of a few hot spots. The outcome of the study is to extend Lloyd's Register Rules guideline [9] for the structural design of these types of ships adding more specifications on the fatigue characteristic of trimaran cross-deck structure, which includes the most dangerous fatigue position and the fatigue damage proportion of various wave heading directions.

In the paper by J. Han et al., they have investigated, through the finite element numerical simulations, the mechanism of fracturing in shaft lining, i.e., the passageway of mine production, due to high-pressure pore water. In particular, the authors have adopted the ANSYS numerical simulation (<https://www.ansys.com>) to obtain the volume change of the cubic model under the pore water pressure. Based on the calculation results, they have derived an approximate analytical solution of the hydraulic expansion coefficient by means of the multivariate nonlinear regression method. Analyzing the interaction between the pore water pressure and the porous rock and shaft lining, the authors found that the hydraulic expansion effect on the surrounding rock increases with its porosity and decreases with its elastic modulus and Poisson's ratio.

S. Gao et al. have used ANSYS finite element numerical software to simulate thermodynamic performance in the fireproof sealing, which is widely employed to limit the scale of fire in multistory building, commercial building, industrial building, medical building, and other types of public buildings. They have estimated the main thermal parameters, including temperature field, thermal flux, and thermal gradient, for two fireproof sealing models that differ in terms of model shape and the initial fire surface. The authors, through the finite element numerical simulations, have evaluated the performances of the two models in terms of fire protection concluding that the rectangle model outperforms the "T" shape model. The conclusions of the study are meaningful to improve the thermodynamic performance of the fire-proof sealing in the converter station.

J. F. Liang and X. Wang have proposed a consistent Riccati expansion method [10] for obtaining interaction solutions, such as soliton-soliton, multiple resonant soliton, soliton-cosine wave, and soliton-cnoidal wave solutions, to the modified Korteweg-de Vries (mKdV) equation [11] that could be used in the water wave system. In particular, they have demonstrated that interaction solutions such as the soliton-tangent wave solution cannot be constructed for the mKdV equation. Moreover, they have shown that soliton and soliton-soliton wave interaction solutions can be derived from the soliton-cnoidal wave interaction solution by making the limit of the modulus approach either 0 or 1 (i.e., lower or upper bounds for the modulus in the Jacobi elliptical function).

In the paper by N. J. Lim and S. A. Brandt, they have analyzed how the change of resolution in the adopted DEM (Digital Elevation Model) in combination with the roughness parameter can affect the performances of hydraulic numerical modelling for areas with different topographies.

In particular, they have estimated the uncertainties in terms of flood extent, respectively, for one-dimensional (i.e., HEC-RAS [12]) and a two-dimensional models (i.e., CAESAR-LISFLOOD [13]) in flat and mountain river basins by comparing the simulations result with the observed flood data of historical events. The results showed that poor-resolution DEMs might produce a global high feature agreement score with historical data but may fail to provide good flood extent estimations locally, particularly in flat areas. Instead, high-resolution DEMs (1 to 5 m) remain advantageous for modelling as they represent better the topography of the study area but it is important to carefully calibrate the models by the use of the roughness parameter. The outcomes of the study confirm that the knowledge of the magnitude and source of uncertainties helps to improve assessments and leads to better inform decisions on flood risk mitigation alternatives [14]. Moreover, numerical models need to be controlled, for example, through a calibration process that adjusts model parameters, assumptions, or equations to optimize concordance between observed data and model predictions [15].

In this context, remote sensing is a low-cost technology that represents an important source of information in the water-related hazards and in water resource management fields [16]. K. Ennouri and A. Kallel have reviewed the advantages and limitations (e.g., spatiotemporal constraints) of the main remote sensing sensors, indices, and algorithms for image analysis (e.g., postprocessing techniques, classification algorithms, and evaluation techniques) in the field of crop condition assessment. They have discussed and highlighted how the remote sensing monitoring plays a central role in diagnosing climate and management impacts on agricultural systems.

H. Liu et al. focused their study on soil erosion risk assessment and soil conservation planning. In particular, the authors have analyzed the temporal trends and spatial patterns of rainfall erosivity (R factor) for a large basin in China (i.e., Three Gorges Reservoir Area) during the period of 1960–2010. They have used the Mann–Kendall test [17] and co-kriging interpolation to analyzed data of meteorological stations and hydrological rain and gauging stations aiming to examine the spatial distribution of annual and seasonal R factor and to characterize the temporal trends of R factor for different time scales in the light of the same data span. The outcomes highlighted in this study can support watershed planning of soil conservation measures in the Three Gorges Reservoir Area.

Conflicts of Interest

The editors declare that they have no conflicts of interest regarding the publication of this Special Issue.

Acknowledgments

The guest editors would like to thank all the authors for their contributions and the reviewers for their timely and constructive feedback. We hope this special issue can

contribute to advancements of the scientific community in the field of engineering and natural hazard assessment and management.

Raffaele Albano
 Sauro Manenti
 José M. Domínguez
 Shaowu Li
 Dong Wang

References

- [1] S. Manenti, D. Wang, J. M. Domínguez, S. Li, A. Amicarelli, and R. Albano, "SPH modeling of water-related natural hazards," *Water*, vol. 11, no. 9, p. 1875, 2019.
- [2] R. Albano, L. Mancusi, A. Sole, and J. Adamowski, "Flood-Risk: a collaborative free and open-source software for flood risk analysis," *Geomatics Natural Hazard and Risk*, vol. 8, no. 2, pp. 1812–1832, 2017.
- [3] R. Albano, D. Mirauda, A. Sole, and J. Adamowski, "Modeling large floating bodies in urban floods via a smoothed particle hydrodynamics model," *Journal of Hydrology*, vol. 541, pp. 344–358, 2016.
- [4] S. Manenti, A. Amicarelli, and S. Todeschini, "WCSPH with limiting viscosity for modeling landslide hazard at the slopes of artificial reservoir," *Water*, vol. 10, no. 4, p. 515, 2018.
- [5] A. Amicarelli, R. Albano, D. Mirauda, G. Agate, A. Sole, and R. Guandalini, "A smoothed particle hydrodynamics model for 3D solid body transport in free surface flows," *Computers & Fluids*, vol. 116, pp. 205–228, 2015.
- [6] L. Fu and Y.-C. Jin, "A mesh-free method boundary condition technique in open channel flow simulation," *Journal of Hydraulic Research*, vol. 51, no. 2, pp. 174–185, 2013.
- [7] H. Gotoh, T. Shibahara, and T. Sakai, "Sub-particle-scale turbulence model for the MPS method Lagrangian flow model for hydraulic engineering," *Advanced Methods for Computational Fluid Dynamics*, vol. 9, pp. 339–347, 2001.
- [8] T. Armstrong, "On the performance of a large high-speed trimaran," *Australian Journal of Mechanical Engineering*, vol. 3, no. 2, pp. 123–131, 2006.
- [9] L.'s Register, *Rules for the Classification of Trimarans*, Lloyd's Register, London, UK, 2006.
- [10] S. Y. Lou, "Consistent Riccati expansion for integrable systems," *Studies in Applied Mathematics*, vol. 134, no. 3, pp. 372–402, 2015.
- [11] R. Hirota, "Exact solution of the Korteweg–de Vries equation for multiple collisions of solitons," *Physical Review Letters*, vol. 27, no. 18, pp. 1192–1194, 1971.
- [12] T. J. Coulthard, J. C. Neal, P. D. Bates, J. Ramirez, G. A. M. de Almeida, and G. R. Hanrock, "Integrating the LISFLOOD-FP 2D hydrodynamic model with the CAESAR model: implications for modelling landscape evolution," *Earth Surface Processes and Landforms*, vol. 38, no. 15, pp. 1897–1906, 2013.
- [13] US Army Corps of Engineers Hydrologic Engineering Center, "HEC-RAS: river analysis system," *User's Manual (V. 4.0)*, US Army Corps of Engineers Hydrologic Engineering Center, Davis, CA, USA, 2008.
- [14] R. Albano, A. Sole, J. Adamowski, A. Perrone, and A. Inam, "Using floodrisk GIS freeware for uncertainty analysis of direct economic flood damages in Italy," *International Journal of Applied Earth Observation and Geoinformation*, vol. 73, pp. 220–229, 2018.
- [15] S. Scaprino, R. Albano, A. Cantisani, L. Mancusi, A. Sole, and G. Milillo, "Multitemporal SAR data and 2D hydrodynamic model flood scenario dynamics assessment," *ISPRS International Journal of Geo-Information*, vol. 7, no. 105, 2018.
- [16] R. Albano and A. Sole, "Geospatial methods and tools for natural risk management and communications," *ISPRS International Journal of Geo-Information*, vol. 7, no. 12, p. 470, 2018.
- [17] H. B. Mann, "Nonparametric tests against trend," *Econometrica*, vol. 13, no. 3, pp. 245–259, 1945.

Research Article

Spatial Distribution and Temporal Trends of Rainfall Erosivity in Three Gorges Reservoir Area of China

Huiying Liu ^{1,2}, Guanhua Zhang ³, Pingcang Zhang^{1,3} and Shengnan Zhu ²

¹College of Water Conservancy and Hydropower Engineering, Hohai University, Nanjing 210098, China

²School of Hydraulic and Ecological Engineering, Nanchang Institute of Technology, Nanchang 330099, China

³Soil and Water Conservation Department, Yangtze River Scientific Research Institute, Wuhan 430010, China

Correspondence should be addressed to Guanhua Zhang; zgh83113@126.com

Received 25 May 2019; Revised 12 November 2019; Accepted 21 December 2019; Published 30 January 2020

Guest Editor: José M. Domínguez

Copyright © 2020 Huiying Liu et al. This is an open access article distributed under the Creative Commons Attribution License, which permits unrestricted use, distribution, and reproduction in any medium, provided the original work is properly cited.

Rainfall erosivity is a key factor to predict soil erosion rate in universal soil loss equation (USLE) and revised USLE (RUSLE). Understanding rainfall erosivity characteristics, especially its spatial distribution and temporal trends, is essential for soil erosion risk assessment and soil conservation planning. In this study, the spatial-temporal variation of rainfall erosivity in the Three Gorges Reservoir Area (TGRA) of China during 1960–2010, at annual and seasonal scales, was explored based on daily rainfall data from 40 stations (26 meteorological stations and 14 hydrologic stations). The Mann–Kendall test and Co-kriging interpolation method were applied to detect the temporal trends and spatial patterns. The results showed that TGRA's annual rainfall erosivity increased from west, south, and east to the north-central, ranging from 3647.0 to 10884.8 MJ·mm·ha⁻¹·h⁻¹ with an average value of 6108.1 MJ·mm·ha⁻¹·h⁻¹. The spatial distribution of summer and autumn rainfall erosivity was similar to the pattern of annual rainfall erosivity. Summer is the most erosive season among four seasons, accounting for 53% of the total annual rainfall erosivity, and winter is the least erosive season. July is the most erosive month with an average of 1327.3 MJ·mm·ha⁻¹·h⁻¹, and January is the least erosive month. Mean rainfall erosivity was 5969.2 MJ·mm·ha⁻¹·h⁻¹ during 1960–2010, with the lowest value of 3361.0 MJ·mm·ha⁻¹·h⁻¹ in 1966 and highest value of 8896.0 MJ·mm·ha⁻¹·h⁻¹ in 1982. Mann–Kendall test showed that the annual rainfall erosivity did not change significantly across TGRA. Seasonal rainfall erosivity showed a significant decrease in autumn and insignificant decrease in summer and winter. Monthly rainfall erosivity in TGRA showed insignificant increases from Jun to Jul and then underwent decreases from Aug to Nov. and from Dec to Feb and it rose again in Feb reaching a 0.01 level significance. The daily rainfall data of supplemental stations is very useful to interpolate rainfall erosivity map, which could help to find the credible maximum and minimum value of TGRA. In total, the findings could provide useful information both for soil erosion prediction, land management practices, and sediment control project of TGRA.

1. Introduction

Soil erosion is recognized as a serious eco-environmental problem of world-wide [1]. Universal soil loss equation (USLE) and its revised version (RUSLE and RUSLE2) [2, 3] were commonly used to predict soil erosion, then to assess soil erosion risk, and evaluate the effectiveness of soil conservation measures [4, 5]. Rainfall erosivity (*R* factor) is one of the important factors influencing soil erosion [6, 7]. It represents the ability of rainfall to detach soil particles and erode the landscape and is determined by rainfall maximum 30-min intensity (I_{30}) and its kinetic energy (*E*), classically

expressed as EI_{30} in USLE and RUSLE [3, 6]. Wischmeier and Smith [6] developed the first iteration of the modern rainfall erosivity index used today [2, 6, 7] and has also proved EI_{30} 's applicability in the Loess Plateau of China during the 1980s [8, 9]. However, EI_{30} is difficult to determine and the basic data involved are not readily available in many parts of the world as it relies much more on long-term rainfall data of high temporal resolution [3, 6, 10]. Consequently, some simple algorithms were developed to calculate *R*-factor relying on daily rainfall [11–13] or monthly rainfall [14], among which, half-month [15] and month models [13, 14] were the most widely used ones

[11, 15]. Furthermore, this simplified model was adopted by the Chinese government in First National Census for Water [16]. Nowadays, this simplified model has been used worldwide [11, 17–20] to explore the spatial distribution and temporal trends of R factor, including China, both on the national [19] and regional scales [21–26].

Due to the rapid growth of population, coupling with the widespread deforestation and expansion of agricultural land during the last century [5], Three Gorges Reservoir Area (TGRA) has become one of the most severely erosive areas in the Yangtze River basin [21]. It is thus very necessary to explore both the temporal (when) and spatial (where) characteristics of rainfall erosivity in for making soil conservation and sediment control strategies. However, the spatial and temporal coverage of pluviograph data are usually very scarce because of limited data span and expensive cost. Lacking of long-term rainfall intensity data makes the USLE and RUSLE difficult to be applied rationally in this region. Although some researchers had used this simplified model in some tributaries of Yangtze River basin [27–31], evaluation of R factor has not been well documented in TGRA. There are still some different opinions on the spatial-temporal variations among them [30–33]. The analysis about spatial distribution of R factor in their studies has not been well demonstrated and was insufficient to answer the spatial and temporal distribution characteristics of rainfall erosivity in TGRA. Furthermore, different data sources and time series of rainfall records resulted in significant differences in spatial distribution and annual value of R in TGRA [27–30]. Daily rainfall data, downloaded from China Meteorological Data Sharing Service System, is the most popular choice for most scholars studying R factor in TGRA [29, 30]. Daily rainfall data from hydrological gauging station also are the primary choice of other researchers [32, 34]. The diverse spans of rainfall records impose restriction on spatial-temporal variations of R factor when the previous researches were compared and analyzed. Nevertheless, the length of rainfall records does influence the confidence level for annual R factor, as the data series should have more than 20 years of record in order to include dry and wet climate periods [2, 3, 33]. It is well known that limited or scarce stations also restrict the generalization and application of research findings [29, 30]. More importantly, the previous studies indicated an insignificant decreasing trend in annual precipitation accompanied by an increasing R factor in sub-basin of TGRA during 2001–2010 [31, 32, 34], which potentially results in a higher water erosion risk in TGRA. The features of R factor are closely related to soil erosion and sediment yield which flows into the Three Gorges Reservoir.

Although Wu et al. and Wang [29, 30] constructed the spatial distribution of R factor in TGRA, the analysis about sub-basins in their study was too weak to answer the spatial and temporal distribution of R factor. There remains a need, therefore, to provide an assessment of R factor and guide the watershed planning of soil conservation measures in sub-regions of TGRA. It is very critical to analyze systematical the spatial distribution and temporal trends of R factor in TGRA based on the same data span, data sources, and calculating method.

Therefore, the specific objectives of this study are as follows: (1) to examine the spatial distribution of annual and seasonal R factors of TGRA combined meteorological stations with hydrological rain gauging stations and (2) to characterize the temporal trends of R factor for different time-scales in the light of the same data span of 1960–2010. The results in this study offer a relatively reliable R value on the soil erosion prediction in TGRA and provide an applicable spatial distribution of R factor for the evaluation of the effectiveness of soil conservation measures.

2. Materials and Methods

2.1. Study Area. TGRA is located at the end of the upper Yangtze River (106°16′–111°28′E, 28°56′–31°44′N) (Figure 1) and consists of 22 counties (cities) or districts of Chongqing municipality and Hubei province with an area of 58000 km² [29, 30, 35]. It is characterized by a humid subtropical monsoon climate with an obvious seasonality. The annual precipitation ranges from 755.0 to 1786.0 mm with 60% of falling between June and September during 1960–2010. TGRA has an altitude ranging from -22 to 3096 m a.s.l. and the mean altitude is nearly 800 m a.s.l. with a mean temperature of 15–18°C. Mountainous terrain occupies over 90% of the total region [35]. The main soil types are purple, yellow, yellow brown, and so on. Erodible purple soil is the dominant soil type. Highly erodible bedrock, including purple sandstone and shale, crops out throughout much of the area. The total eroded area was 38800 km², accounting for 66.8% of the study region in the mid-1980's (Water Resources Ministry, 2003). Consequently, in 1989, this area was selected for the testing zone of measures designed for soil erosion control, and it has in subsequent years been the subject of a succession of conservation projects. The China Bulletin of Soil and Water Conservation (2017) showed that soil erosion area of the TGRA was about 23000 km², in which moderate erosion and strong erosion were 41.27% and 10.27%, and the extremely strong erosion and severe erosion were 4.20% and 1.14%, respectively.

In order to deeply analyze the rainfall erosivity distribution characteristics, the study region was divided into seven subregions as shown in Figure 1. Subregion A includes the Dong River and the Longxi River Basin, subregion B the Mudong River and part of Wujiang River Basin, subregion C the Xiaojiang River Basin, subregion D the Long River Basin, subregion E the Tangxi and Daning River Basin, subregion F the Modaoxi and Daxi River Basin, and subregion G the Hubei province section of TGRA. In Yangtze River Basin, the seasons were divided as follows: spring was from March to May, summer June to August, autumn September to November, and winter December to February of the following year.

2.2. Precipitation Data Collection. Rainfall data of 1960–2010 were collected from 40 stations (Figure 1). Two data sources were employed: one is daily rainfall data, downloaded from China Meteorological Data Sharing Service System (<http://cdc.cma.gov.cn>), which includes 51 years' (1960–2010) data

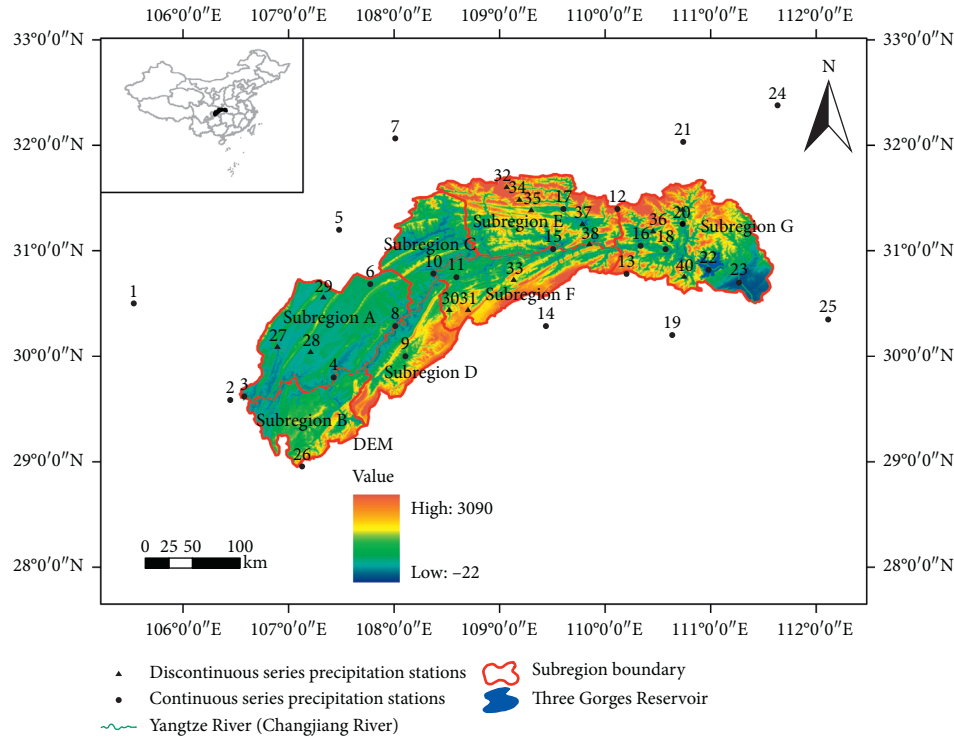


FIGURE 1: Geographical location of Three Gorges Reservoir Area and rain gauge stations.

of 26 continuous series precipitation stations; another one is excerpted from China Hydrological Almanac issued by Yangtze River Water Resources Committee of China which contains 41 years' (1960–1990, 2001–2010) data of 14 discontinuous series precipitation stations. During 1991–2000, the precipitation records from China Hydrological Almanac are not available because of the changed policy and expensive cost. The precipitation records from China Meteorological Data Sharing Service System include 17 rain gauge stations within the TGRA and 9 stations from surrounding areas (Figure 1). All 40 stations were selected to ensure reliability, continuity, and availability of long-term data series in the study region.

2.3. Methods

2.3.1. Rainfall Erosivity Calculation. As mentioned above, continuous rainfall data series with a high time resolution for classical algorithm of R factor (USLE R factor) are rarely available and daily rainfall data have been widely used worldwide to estimate R factor. Zhang and Fu [15] compared five simple models for estimating R factor based on average annual rainfall, average monthly rainfall, and daily rainfall data, respectively and then proposed a new daily rainfall model to estimate R factor which was subsequently widely used in China. The daily rainfall model was expressed as

$$R_k = \alpha \sum_{i=1}^j P_{ik}^\beta, \quad (1)$$

where R_k is the rainfall erosivity of the k th half-month, $\text{MJ}\cdot\text{mm}\cdot\text{ha}^{-1}\cdot\text{h}^{-1}$; $k = 1, 2, \dots, 24$; P_{ik} is the effective rainfall

for day i of the k th half-month, and it is the actual rainfall when the actual rainfall is higher than 12 mm, otherwise, it is considered to be 0 [36]; j is the number of days in the k th half-month, $j = 13, 14, 15, 16$; α and β are parameters determined by the following formulas:

$$\beta = 0.8363 + \frac{18.144}{P_{d12}} + \frac{24.455}{P_{y12}}, \quad (2)$$

$$\alpha = 21.586\beta^{-7.1891}, \quad (3)$$

where P_{d12} is the average daily rainfall which is greater than 12 mm and P_{y12} is the annual average of erosive rainfall. The monthly, seasonal, and annual mean R values were successively computed based on equations (1)–(3).

2.3.2. Trend Analysis of Rainfall Erosivity. The Mann–Kendall trend test [37, 38] has been widely applied to meteorological time series because it could identify monotonic trends of a time-series [21, 39, 40]. It is based on two useful indexes S and Z in the Mann–Kendall test to determine whether a time series of n data points has a significant trend. A positive Z indicates an upward trend and negative Z indicates a downward trend. The trend is statistically significant at $\alpha = 0.05$ and 0.01 significance level when $|Z| > 1.96$ and 2.58, respectively. The detailed procedure of the Mann–Kendall trend test is presented [40] and [39]. We used it to identify the trend of annual R factor at 26 sites spanning 51 years in the current study.

2.3.3. Spatial Interpolation of Rainfall Erosivity. To understand the spatial distribution and temporal changes of R factor, the mean annual, seasonal, and multiperiod R factors were interpolated through the Geostatistical Analyst module of the ArcGIS 10.2 (ESRI, America). The Co-kriging method was selected to interpolate the spatial distribution of R factor, because it can incorporate the neighboring primary data and make best prediction compared with other methods [21, 41]. Additionally, the Co-kriging method has been proved to be the most suitable interpolation method for rainfall erosivity in mainland China [24].

3. Results

3.1. Spatial Distribution of Rainfall Erosivity in TGRA. The spatial distribution of annual R factor for 1960–2010 and different decades (1960–1990, 1991–2000, and 2001–2010) in TGRA is presented in Figure 2. It is noted that the spatial distribution of 51-year annual R factor showed a strong variability (Figure 2(a)). It generally increased from west, south, and east to the north-central area, respectively, ranging from 3647.0 to 10884.8 MJ·mm·ha⁻¹·h⁻¹·yr⁻¹ with a mean value of 6108.1 MJ·mm·ha⁻¹·h⁻¹·yr⁻¹. The spatial characteristics indicated that the annual R factor of was characterized by a low on both sides and high in the middle in TGRA. The highest annual R factor was found in the subregion E and the lowest was in the subregion B. The annual R factor of the seven geographical subregions in the TGRA showed an order of subregion E > subregion C > subregion F > subregion D > subregion G > subregion A > subregion B (Table 1). The annual R factor in the subregion C, subregion E, and subregion F showed significant differences with other subregions (Table 1). For different decades (Figures 2(b)–2(d)), the spatial distribution of R factor in 1960–1990 and 2001–2010 displayed similar patterns to that of 1960–2010: the relative higher values were distributed in subregion C (Xiaojiang River basin) and subregion E (Daning River basin) while the subregion B possessed a lower level (Mudong River basin). It was noticed that the spatial distribution of annual R factor in 1991–2000 demonstrated a different pattern that increases from west and east to the central area, respectively, and high erosivity area slightly moving to the southwest (Figure 2(c)). In this decade, the annual R factor ranged from 3848.0 to 7286.0 MJ·mm·ha⁻¹·h⁻¹·yr⁻¹, with an average of 5641.9 MJ·mm·ha⁻¹·h⁻¹·yr⁻¹. However, the mean R values were 6134.5 MJ·mm·ha⁻¹·h⁻¹·yr⁻¹ during 1960–1990 and 5937.0 MJ·mm·ha⁻¹·h⁻¹·yr⁻¹ in 2001–2010, respectively (Table 1 and Table 2). The spatial mean R factor of 1991–2000 was 29% lower than that of 1960–1990 in the subregion E, 10% lower than in the subregion B, subregion C, and subregion G. The spatial mean R factor of 1991–2000 was 32% lower than that of 2001–2010 in subregion E. More differences could be found about maximum, minimum and standard deviation in subregion E (Figure 3). Rainfall erosivity exhibited a strong seasonal variability which was roughly consistent with the corresponding precipitation in this region (Figure 4). Generally, summer was the most erosive season, followed by spring and autumn, and winter was the least erosive season.

The spring R factor ranged from 895.4 to 2917.3 MJ·mm·ha⁻¹·h⁻¹ with an average of 1414.6 MJ·mm·ha⁻¹·h⁻¹ that accounts for 23.6% of the total annual R factor. The spring R factor for the seven subregions showed an order of subregion E > subregion C > subregion F > subregion D > subregion G > subregion A > subregion B (Table 1). The highest spring R factor was also found in subregion C (Xiaojiang River basin) and subregion E (Daning River basin) and the lowest was in subregion B (Mudong River basin). The highest season R factor was found in summer, accounting for 53.3% of the total annual R factor in TGRA, which ranged from 1997.5 to 5887.3 MJ·mm·ha⁻¹·h⁻¹ with the average value of 3253.3 MJ·mm·ha⁻¹·h⁻¹. The highest R factor of summer also appeared in the upstream of Daning River basin (subregion E) and the lowest was in Mudong River basin (subregion B). The summer R for the seven subregions showed an order of subregion E > subregion C > subregion F > subregion G > subregion D > subregion A > subregion B (Table 1). The summer order is different from annual order and spring order in subregion D and subregion G. The spatial distribution of summer R factor was similar to annual R factor, which was higher in subregion C, subregion E, and subregion F (Figure 4). The autumn R factor varied from 684.3 to 2782.7 MJ·mm·ha⁻¹·h⁻¹ with an average of 1366.6 MJ·mm·ha⁻¹·h⁻¹ accounting for 22.2% of the total annual R factor. The spatial distribution of autumn R factor was similar to the pattern of annual and summer R factor, which increased from west, south, and east to the north-central. The autumn R factor percentages of the seven geographical subregions showed a same order as those of summer. The lowest seasonal R factor was found in winter, only accounting for 1.0% of the total annual R factor and ranging from 23.0 to 138.4 MJ·mm·ha⁻¹·h⁻¹. In most of the 40 stations, the winter R factor was lower than 100 MJ·mm·ha⁻¹·h⁻¹, indicating a very low R factor level. The spatial distribution of winter R factor was different from that of the other three seasons; higher winter R factor appeared in most of the east-central TGRA. In conclusion, subregion E held the highest R value and subregion B possessed the lowest R value in TGRA.

The monthly R factor varied greatly within one year because rainfall including high-intensity storms was not evenly distributed (Figure 5). July is the most erosive month with an average R factor of 1327.3 MJ·mm·ha⁻¹·h⁻¹, followed by June of 1034 MJ·mm·ha⁻¹·h⁻¹. January is the least erosive month with the lowest R factor being only 11.7 MJ·mm·ha⁻¹·h⁻¹. The mean monthly R factor of May–Sep occupied 82.5%. The monthly R factor during the flood season (Apr–Oct) was almost 18 times of that in dry season (Nov–Mar).

3.2. Temporal Variation of Rainfall Erosivity. R factor of each station was calculated based on average daily precipitation from 1960 to 2010 (Table 3). It can be seen from Table 3 that the coefficient of variance was 0.20 for TGRA and 0.25–0.46 for all the stations, indicating a moderate variability of 51-year annual R factor in both TGRA and each station. For the

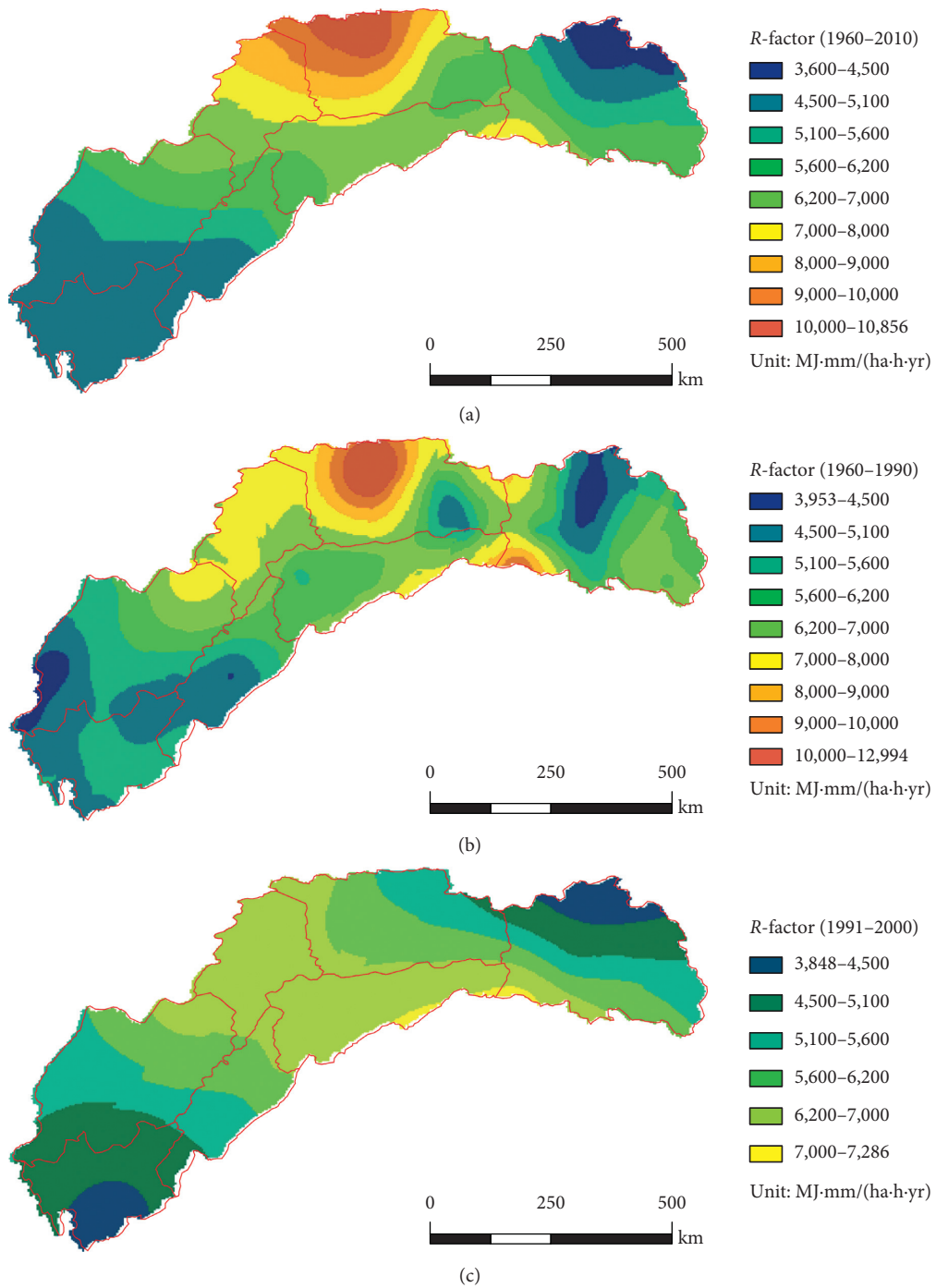


FIGURE 2: Continued.

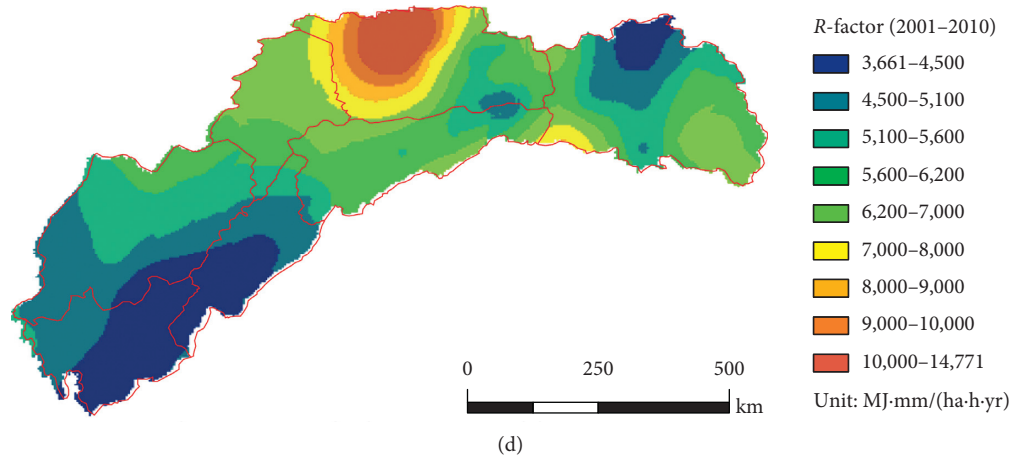


FIGURE 2: Spatial distribution of mean annual R factor for 51-year and different decades in TGRA.

TABLE 1: Statistical characteristics of average rainfall erosivity ($\text{MJ}\cdot\text{mm}\cdot\text{ha}^{-1}\cdot\text{h}^{-1}$) for each subregion in the TGRA during 1960–2010.

Subregion	Annual		Spring		Summer		Autumn		Winter	
	Mean	Stdev	Mean	Stdev	Mean	Stdev	Mean	Stdev	Mean	Stdev
Region A	5315.0	504.0	1418.3	144.5	2772.3	288.5	1103.2	185.7	38.4	3.7
Region B	4687.1	57.0	1191.4	45.2	2499.6	98.0	924.4	25.5	31.0	4.0
Region C	7132.0	769.0	1551.0	62.5	3837.2	437.9	1729.3	238.1	53.7	8.3
Region D	5406.0	455.0	1367.0	74.8	2834.5	327.1	1115.7	113.9	44.8	3.6
Region E	8146.0	1515.7	1736.9	399.7	4289.3	908.2	2016.8	416.1	94.6	15.2
Region F	6529.0	293.0	1451.0	92.0	3399.8	170.6	1495.8	125.3	74.8	17.1
Region G	5401.0	777.9	1199.1	199.6	3014.7	428.9	1143.2	252.7	86.7	15.2
TGRA	6108.1	1455.7	1414.6	287.3	3253.3	789.6	1366.6	457.0	63.7	26.7

TABLE 2: Annual average rainfall erosivity ($\text{MJ}\cdot\text{mm}\cdot\text{ha}^{-1}\cdot\text{h}^{-1}$), Z of MK test, and precipitation (mm) for different periods in each subregion.

Subregions	Elevation (a.s.l)	1960–1990			1991–2000			2001–2010			1960–2010		
		R	Z	P	R	Z	P	R	Z	P	R	Z	P
Region A	447	5484.7	0.41	1146.5	5484.4	0.21	1157.1	5115.4	0.29	1119.8	5315.0	-0.16	1140.0
Region B	726	5074.0	0.29	1166.9	4615.8	0.24	1165.0	4422.4	0.36	1091.6	4687.1	-0.14	1143.2
Region C	556	6988.5	0.61	1205.7	6367.7	0.44	1188.4	6182.4	0.21	1131.9	7132.0	-0.32	1192.1
Region D	896	5401.1	0.60	1201.2	5771.3	0.35	1186.4	4786.8	0.30	1082.7	5406.0	-0.27	1178.4
Region E	1017	7641.7	0.50	1348.0	5920.0	0.56	1152.6	7828.1	0.08	1303.5	8146.0	-0.22	1343.6
Region F	948	6288.2	0.49	1270.0	6527.3	0.53	1169.2	5958.2	0.16	1151.7	6529.0	-0.23	1233.9
Region G	971	5827.8	0.60	1119.3	5262.4	0.59	1081.9	5595.6	0.69	1092.6	5401.0	0	1102.1
TGRA	800	6134.5	0.50	1204.9	5641.9	0.43	1148.4	5937.0	0.32	1147.4	6108.1	-0.17	1190.2

whole study region, the annual mean R factor from 1960 to 2010 was $5969.17 \text{ MJ}\cdot\text{mm}\cdot\text{ha}^{-1}\cdot\text{h}^{-1}\cdot\text{yr}^{-1}$, with the lowest value of $3361.08 \text{ MJ}\cdot\text{mm}\cdot\text{ha}^{-1}\cdot\text{h}^{-1}\cdot\text{yr}^{-1}$ in 1966 and highest value of $8896.84 \text{ MJ}\cdot\text{mm}\cdot\text{ha}^{-1}\cdot\text{h}^{-1}\cdot\text{yr}^{-1}$ in 1982 (Figure 6). For the specific station, Cuntan station was located in the boundary of subregion A and subregion B held the minimum R factor of $1112 \text{ MJ}\cdot\text{mm}\cdot\text{ha}^{-1}\cdot\text{h}^{-1}\cdot\text{yr}^{-1}$ in 2001, and Jianlou station seated in the subregion E of TGRA held the maximum R factor $>23000 \text{ MJ}\cdot\text{mm}\cdot\text{ha}^{-1}\cdot\text{h}^{-1}\cdot\text{yr}^{-1}$ in 1967 (Table 3). However, different decades had different temporal mean annual R value that decreases in the order of $1960\text{--}1990 > 2001\text{--}2010 > 1991\text{--}2000$.

The trend variations were also analyzed for each station, subregions, and the entire basin using the Mann–Kendall

test at monthly, seasonal, and yearly scales, respectively (Tables 2 and 4). The critical value of Mann–Kendall test is 1.96 at significance level $\alpha=0.05$ (95% confidence level). According to Table 2, except subregion G, R values for the other six subregions showed an insignificant decreasing trend during 1960–2010; but for 1960–1990, 1991–2000, and 2001–2010, all subregions over various time scales showed an insignificant increasing trend. The trend line slope of annual R factor showed a linearly decreasing trend over entire basin of 51 years (Figure 6).

The Mann–Kendall test of each station was performed to analyze the temporal changes of R factor across TGRA. Insignificant increasing trends were reported for 51-year R factor and three periods (1961–1990, 1991–2000, and

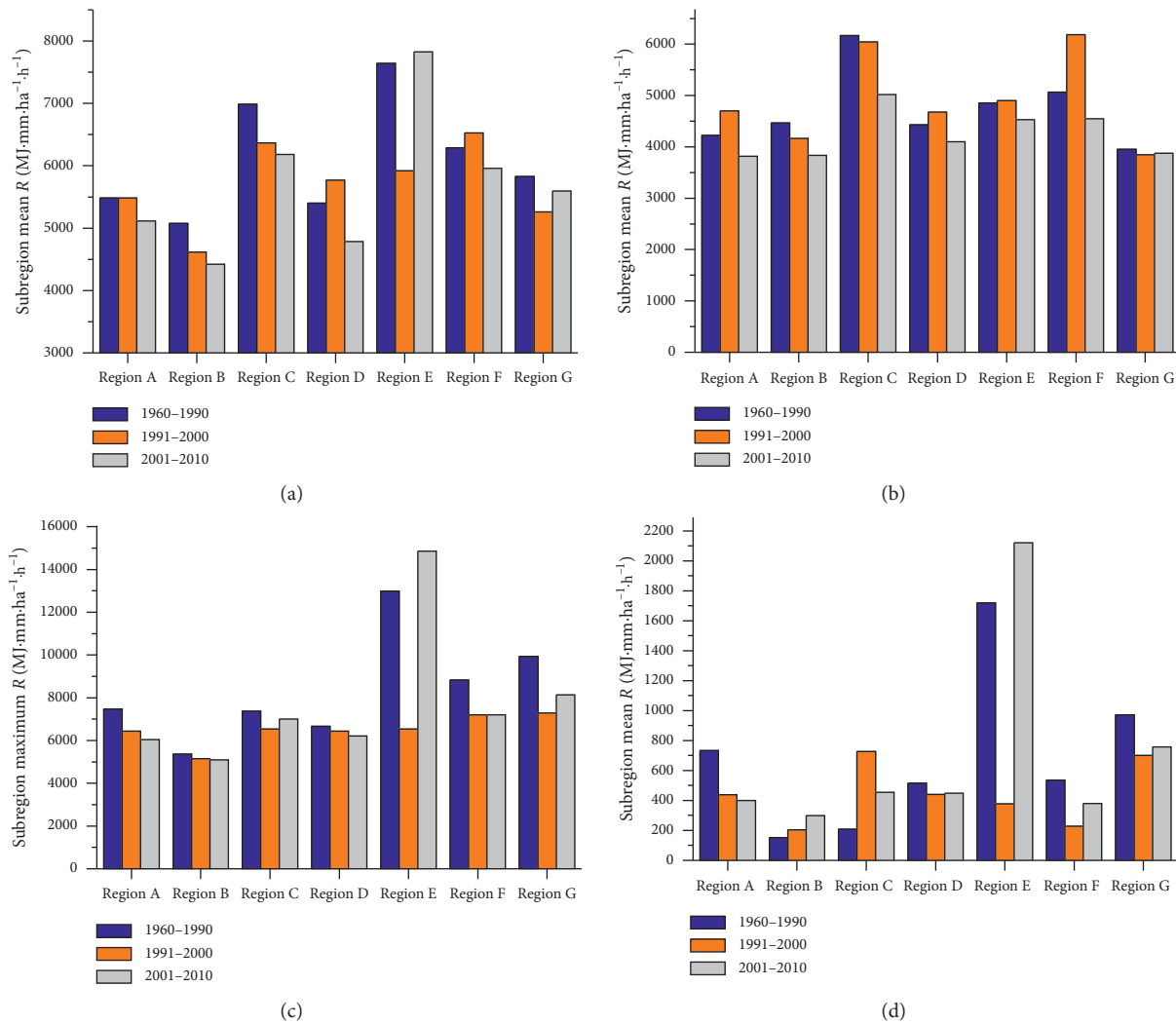


FIGURE 3: Statistics characteristics of R for different periods in each subregion.

2001–2010) (Figure 7). The spatial distribution of long-term annual Z was generally negative in subregion A and subregion B and positive in subregion G (Figure 7(d)), indicating that the annual R factor decreased in the western TGRA while it increased in the eastern TGRA in the past 51 years. It is also noted that the spatial distribution of temporal trends differed substantially for different periods due to its numbers of stations. The highest $Z=0.89$ was observed in the decade of 1991–2000, and the lowest $Z=0.18$ was during 2001–2010. Temporal changes of annual R for most of the stations were similar to the changes in TGRA; only Zigui station and Jinfoshan station had significant increasing trends (0.05 level) that probably substantially contributed to the increasing trend in 2001–2010.

Table 4 displayed the temporal trends of annual, seasonal, and monthly R factor for TGRA and each station. Mean Z of spring R factor for TGRA was -0.05, indicating a decrease in spring R factor that was probably attributed to the significant decreasing trend at the 0.01 level in Suining station. Though half of the stations showed an increase in spring R factor over the time series, none of them reached a

significant level. The summer R factor in TGRA showed an insignificant increase during 1960–2010, as might be considerably contributed by the significant increasing trends in Suining, Wanyuan, Longjiao, and Laohekou stations. Significant decreasing trend at the 0.05 level was detected for the autumn R factor in TGRA. Most of the stations indicated a decrease in autumn from 1960 to 2010 and the significant decreasing trends of Qingxichang, Banqiao, and Lvcongpo stations ($\alpha=0.01$) and Suining, Shapingba, and Laohekou stations ($\alpha=0.05$) substantially contributed to the total decreasing trend. Similar to the temporal trend of summer R factor, the winter R factor in TGRA also showed an insignificant increase during 1960–2010, as probably devoted by the significant increasing trends at 0.01 level in Lvcongpo, Wufeng, and Jingzhou stations.

The monthly R factor in TGRA showed insignificant increases from Jun to Jul and then underwent decreases from Aug to Nov (Table 4). From Dec to Feb, monthly R rose again with Feb reaching a 0.01 level significance, which might mainly contribute to the increasing trend of winter R . Furthermore, there were 7 stations in Feb indicating

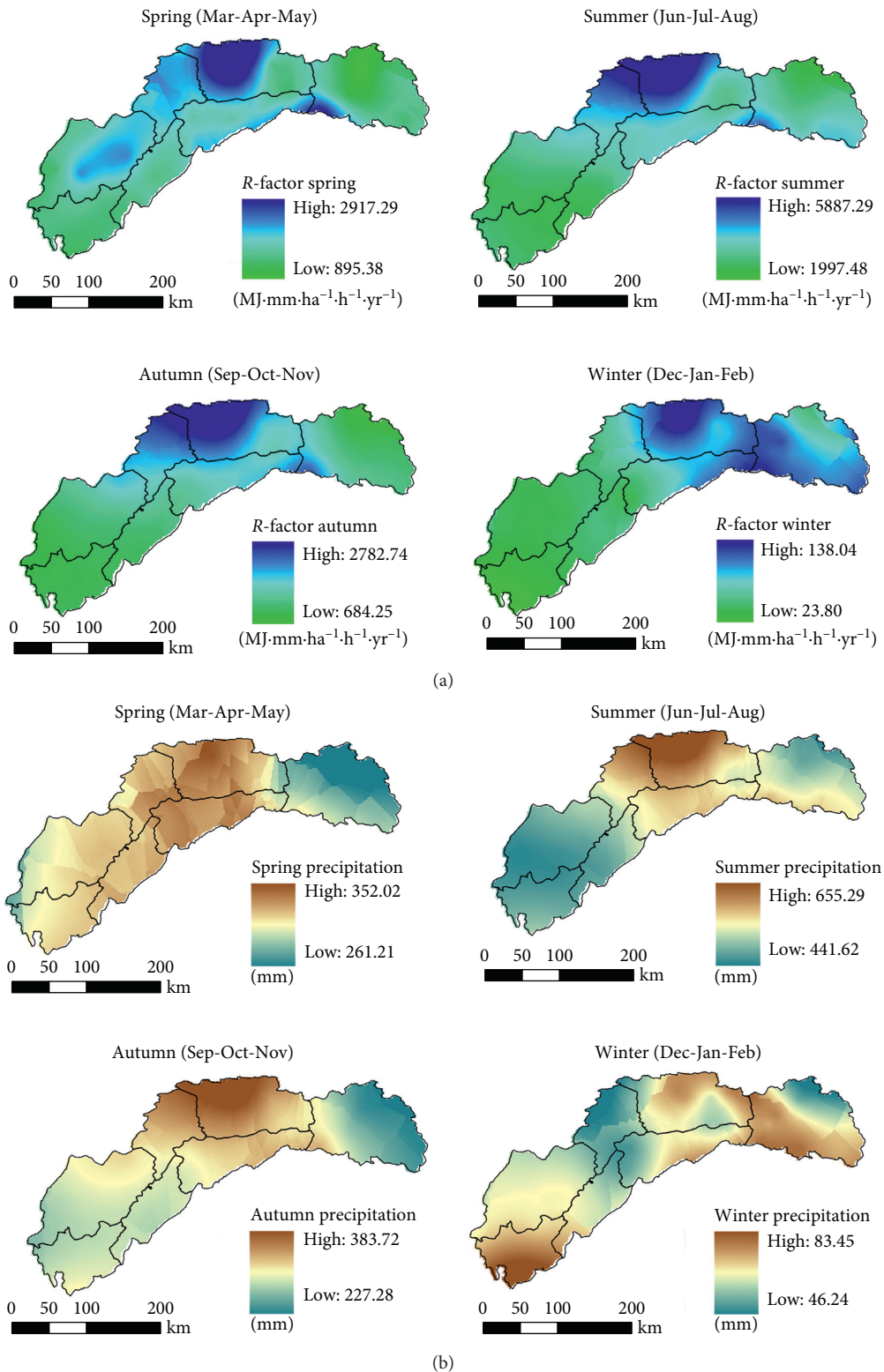


FIGURE 4: Spatial distribution of seasonal (a) *R* factor and (b) precipitation during 1960–2010.

significant increasing trends (0.01 level), greatly leading to the increasing trend in this month. It is noticeable that there were 11 and 7 stations showing significant increasing trends in Jun and Jul, respectively, which probably substantially

contributed to the increasing trends in these two months. A similar situation also occurred in Sep when 16 stations showed significant decreases, which was more likely to contribute the decreasing trend of this month.

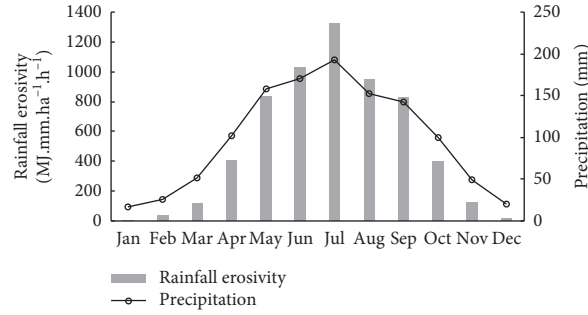


FIGURE 5: Mean monthly R factor and precipitation.

TABLE 3: Annual R factor of 51 year and different decades in TGRA and each station (MJ·mm·ha⁻¹·h⁻¹·yr⁻¹).

No.	Station	Altitude (m)	Data source	1960–1990	1991–2000	2001–2010	1960–2010				
				Mean	Max	Min	Mean	Std.	Cv		
1	Suining	355	CMAS	4919.74	4514.43	5493.68	8388.27	1844.93	4970.67	1667.07	0.34
2	Shapingba	259	CMAS	5118.33	5756.41	5691.59	10669.18	2393.02	5318.64	1809.32	0.34
3	Cuntan	210	CMAS	4391.01	4662.95	5065.85	11015.84	1111.88	4576.66	1862.26	0.41
4	Qingxichang	212	CMAS	4758.47	4501.44	3800.91	7895.39	2067.71	4520.32	1266.13	0.28
5	Daxian	345	CMAS	6693.96	5933.33	7662.95	13260.98	1943.77	6766.98	2255.83	0.33
6	Liangping	455	CMAS	7494.76	6880.68	5777.34	14915.13	2379.90	7037.75	2302.40	0.33
7	Wanyuan	674	CMAS	6908.07	6962.32	5838.47	19027.57	3280.52	9020.30	3211.40	0.36
8	Zhongxian	270	CMAS	5921.87	6039.74	4912.29	10661.88	2704.90	5747.02	1752.94	0.31
9	Shizhu	580	CMAS	4416.42	5060.38	4082.04	11186.78	1673.11	4477.12	1571.49	0.35
10	Wanxian	188	CMAS	6908.07	6962.32	5838.47	12914.70	3648.34	6707.28	2041.47	0.30
11	Longjiao	1500	CMAS	5490.48	5617.68	6261.35	13670.90	2830.15	5666.57	2001.13	0.35
12	Banqiao	1100	CMAS	8078.16	4573.13	6784.92	12362.13	2283.49	7035.06	2457.61	0.35
13	Lvcongpo	1820	CMAS	10428.42	8979.02	8424.96	16675.65	5917.31	10324.68	2792.60	0.27
14	Enshi	457	CMAS	8813.33	8554.49	7376.80	13597.67	3443.28	8434.31	2602.92	0.31
15	Fengjie	188	CMAS	5838.07	5996.24	5406.67	10089.92	3083.50	5670.66	1558.84	0.27
16	Badong	109	CMAS	5412.25	5576.08	5468.37	11123.61	2391.74	5455.38	1785.43	0.33
17	Wuxi	300	CMAS	5489.63	5203.64	5309.12	9177.43	1834.11	5398.16	1636.68	0.30
18	Zigui	151	CMAS	4711.67	4403.30	5344.48	8934.55	2545.27	4790.81	1629.04	0.34
19	Wufeng	620	CMAS	7764.11	7699.31	6454.02	13935.53	3716.33	7442.06	2374.10	0.32
20	Xingshan	210	CMAS	4224.27	4522.98	4710.55	8856.24	1849.96	4378.19	1543.16	0.35
21	Fangxian	427	CMAS	2985.06	2556.35	2979.62	5615.30	1176.67	2913.63	962.43	0.33
22	Sandouping	800	CMAS	6439.26	5611.81	6329.44	12021.94	3086.47	6333.13	1780.58	0.28
23	Yichang	133	CMAS	6126.22	5566.38	6359.33	12825.72	2320.96	6012.67	2020.79	0.34
24	Laohekou	90	CMAS	3598.05	3320.42	4160.95	8954.83	1033.34	3576.28	1577.55	0.44
25	Jingzhou	32	CMAS	5745.72	5691.50	5626.56	11362.58	2093.81	5812.22	2069.19	0.36
26	Jinfoshan	1906	CMAS	4873.23	4077.01	5344.48	11902.95	2496.49	4865.67	1674.26	0.34
27	Metan	270	CHA	4209.18		4546.32	6510.41	1604.60	4291.41	1329.78	0.31
28	Shuanghe	440	CHA	5452.64		5385.90	12334.15	2817.51	5436.36	1632.52	0.30
29	Gaotan	285	CHA	5617.08		4927.16	9449.45	1991.04	5617.08	1713.72	0.31
30	Jiannan	640	CHA	5771.95		5061.60	9915.53	2965.75	5594.36	1551.95	0.28
31	Moudao	1380	CHA	6480.31		5570.94	12355.14	3319.26	6258.51	1594.34	0.25
32	Gaolou	1100	CHA	11018.92		11904.79	18792.42	5746.04	11304.69	3002.74	0.27
33	Tuxiang	840	CHA	5824.89		5539.94	10292.67	3387.06	5755.39	1533.88	0.27
34	Jianlou	260	CHA	13158.45		14993.26	23046.65	6142.71	13605.96	4314.90	0.32
35	Tangfang	230	CHA	9124.60		8408.03	15297.45	4566.68	8949.83	2453.17	0.27
36	Xiangshuihe	600	CHA	5876.79		4749.04	10085.41	2422.05	5601.73	1870.74	0.33
37	Dachang	155	CHA	5084.65		6126.28	14291.06	2083.19	5338.71	2465.70	0.46
38	Wushan	271	CHA	5019.37		4489.53	8299.70	2154.98	4890.14	1357.59	0.28
39	Zhengjiaping	259	CHA	3932.62		4012.37	7334.61	1450.66	3952.07	1406.44	0.36
40	Yanglinqiao	500	CHA	5215.29		4976.50	8203.06	3011.73	5155.59	1305.26	0.25
	TGRA			6134.46	5641.46	5799.27	8896.84	3361.08	5969.17	1189.32	0.20

CMAS: China Meteorological Data Sharing Service System; CHA: China Hydrological Almanac; Cv: coefficient of variation.

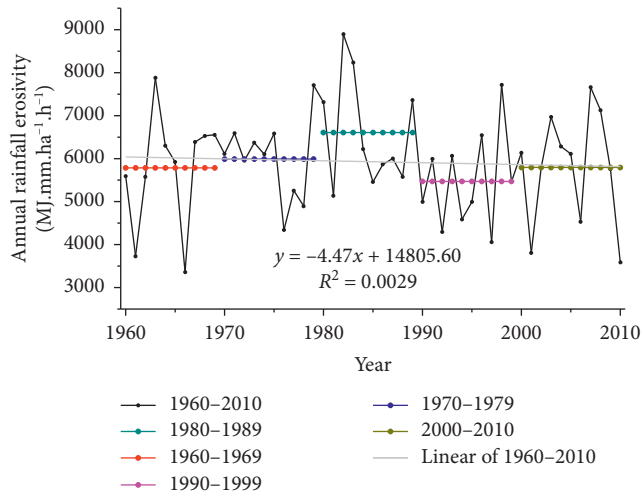


FIGURE 6: Temporal changes of annual R factor in TGRA from 1960 to 2010.

4. Discussion

4.1. Spatial Distribution of Rainfall Erosivity. Zhang's semimonth model was developed in China and is favored for its high-quality results [15, 20, 21]. Annual rainfall erosivity was calculated, and its spatial distribution was obtained using the Co-kriging interpolation technique. As mentioned above, the annual rainfall erosivity spatially ranged from 3647.0 to 10,884.8 $\text{MJ}\cdot\text{mm}\cdot\text{ha}^{-1}\cdot\text{h}^{-1}$ with an average value of 6108.1 $\text{MJ}\cdot\text{mm}\cdot\text{ha}^{-1}\cdot\text{h}^{-1}$ and standard deviation of 1455.6 $\text{MJ}\cdot\text{mm}\cdot\text{ha}^{-1}\cdot\text{h}^{-1}$. According to the criterion of Huang et al. [41], TGRA was classified as medium rainfall erosivity. Therefore, the quantitative relationship was discussed between the rainfall erosivity and the rainfall in TGRA. The distribution map of seasonal precipitation (Figure 4) was generated based on the average daily rainfall. From Figure 4, although some differences exist in parts of the region, the spatial distribution of seasonal rainfall erosivity visually agrees well with that of seasonal precipitation, which indicates that the precipitation almost determines the rainfall erosivity both in amount and spatial distribution. To analyze the influence of geographic location and elevation on R factor, the linear relationships between average annual R factor and longitude, latitude, elevation, and mean annual rainfall of each station were performed (Figure 8). The critical value of correlation coefficient test $R_{0.05, 40} = 0.312$. According to Figure 8, the correlation coefficients between R factor and longitude, latitude, and elevation were not significant. Only the relationship between annual R -factor and annual precipitation reached a significant level. Figure 8(d) indicates that the correlation between areal rainfall erosivity and areal rainfall during 1960–2010 reached a significant level ($\alpha < 0.05$). Rainfall is the main external factor contributing to rainfall erosivity. Intra-annually, the proportion of R factor was higher than that of precipitation in summer, indicating that erosive rainfall occurred mostly in summer compared with other seasons (Figure 5).

Compared with the previous studies in TGRA, the results concerning the spatial-temporal distribution of R factor

were inconsistent and some important differences could be discovered, primarily in subregion C and subregion F. Fan et al. [27] and Wang et al. [28] found the mean annual R factor in upper Yangtze River basin was 3000.0–4000.0 $\text{MJ}\cdot\text{mm}\cdot\text{ha}^{-1}\cdot\text{h}^{-1}\cdot\text{yr}^{-1}$. However, they did not detect the highest R factor area of Daning River basin and underestimated approximately 40% of the R factor in TGRA as their stations are not located in subregion E. The Daning River basin of subregion E held the highest R factor in TGRA and also has the most precipitation [32, 34]. The R value of the current study was consistent with the results of Fan et al. [27] and Wang et al. [28] in subregion G. Wu et al. [29] and Wang [30] both studied the TGRA supported by meteorological stations and showed a similar annual R factor of 3500.0–7500.0 $\text{MJ}\cdot\text{mm}\cdot\text{ha}^{-1}\cdot\text{h}^{-1}\cdot\text{yr}^{-1}$ but a higher R factor located in southwest of subregion G. However, there is over 20% difference between Wu et al. [29] and Wang [30] in subregion E. The mean annual R factor of subregion E in the present study is consistent with the results of Hua et al. [34] and Ren and Liu [32]. The small differences of R factor in the subregion E came from the impact of data series length in determining rainfall erosivity. The R value fluctuates by the short span of rainfall data series because of climatic change in the previous researches.

A long series of rainfall records from sufficient stations is the premise of studies on spatial distribution and temporal trends of R factor. This study collected the daily precipitation data from the China Meteorological Data Sharing Service System (1960–2010) and China Hydrological Almanac (1960–1990 and 2001–2010) to investigate the spatial-temporal distribution of R factor. Spatial interpolation was conducted to predict R factor distribution for the three periods of 1960–1990, 1991–2000, and 2001–2010 (Figure 2).

Figures 2(b) and 2(d) show the spatial distribution of mean annual R factor during 1960–1990 and 2001–2010 containing 40 stations (26 continuous series precipitation stations and 14 discontinuous series precipitation stations), respectively. Figure 2(c) shows the spatial distribution of mean annual R factor during 1991–2000 based on 26 continuous series precipitation stations. Figures 2(b) and 2(d) have similar spatial characteristics in TGRA except the extreme value. The reason was that the short length of rainfall data resulted in fluctuation of R factor during 2001–2010. However, Figure 2(c) is different from Figures 2(b) and 2(d). The highest R value could not be detected in Figure 2(c) due to the lack of rainfall stations during 1991–2000. Figure 2(c) demonstrates the same results as those of the previous studies [27, 28]. Therefore, only Figure 2(b) appears to have a similar spatial distribution to Figure 2(a). Furthermore, the daily rainfall data of supplemental stations in this study were very helpful to interpolate R factor, which improved the spatial interpolation accuracy and strengthened the spatial-temporal distribution reliability of R factor. The distribution map could provide a relatively reliable R factor for USLE and RUSLE of regional erosion. It also provided a scientific basis to investigate soil erosion and evaluate the effects of soil conservation measures and ecological restoration projects.

TABLE 4: Temporal trends of annual, seasonal, and monthly R factors for TGRA and each station.

Station	Jan	Feb	Mar	Apr	May	Jun	Jul	Aug	Sep	Oct	Nov	Dec	Spring	Summer	Autumn	Winter	Annual
TGRA	1.49	2.58**	-0.70	0.71	-0.15	1.61	1.35	-0.05	-1.90	-0.60	-0.70	0.12	-0.55	1.28	-2.03*	1.72	0.06
Suining	-0.68	0.03	-1.80	-2.00*	0.17	3.41**	1.01	1.85	-2.40*	-3.60**	-0.31	0.50	-2.75**	2.44*	-2.07*	-0.62	1.04
Shapingba	-0.21	1.77	0.05	1.46	0.36	2.84**	1.14	-0.60	-3.80**	-0.65	1.93	-1.53	0.65	1.38	-2.18*	0.61	0.00
Cuntan	-0.37	-0.32	-0.18	0.78	0.70	1.85	0.68	1.92	-2.50*	-0.49	-0.24	0.32	0.18	1.88	-1.30	0.36	0.31
Qingxichang	-0.80	-0.18	-2.50*	-0.31	-0.88	-1.48	2.94**	-3.00**	-4.20**	-1.58	-2.10*	0.26	-0.94	-0.07	-2.61**	-0.18	-1.61
Daxian	0.03	0.32	-0.05	-2.00*	3.57**	2.16*	2.57*	1.43	-3.50**	0.99	1.07	1.19	1.01	1.61	-1.19	0.22	0.41
Liangping	0.84	0.19	-1.69	-1.28	-0.32	2.63**	-1.12	0.44	-2.50*	-0.11	-0.50	-1.51	-0.81	0.34	-1.46	-0.74	-0.93
Wanyuan	0.00	-1.10	-1.07	-2.30*	2.83**	2.65**	4.78**	1.07	-2.30*	0.39	-2.10*	0.39	0.42	2.66**	-0.99	-0.28	-0.67
Zhongxian	0.08	-0.91	-2.60**	1.74	-0.05	0.60	-1.09	0.70	-1.93	-1.74	-1.74	-1.33	-0.54	-0.13	-0.95	-1.45	-0.62
Shizhu	1.98*	0.84	-3.80**	2.31*	0.23	-0.16	0.63	1.80	-3.70**	0.16	1.61	0.65	-0.05	0.94	-1.12	0.69	0.41
Wanxian	-0.28	0.78	-4.50**	-1.58	-1.33	2.96**	-2.50*	1.64	-1.06	1.02	-0.28	-1.43	-1.22	0.13	-0.44	-0.42	-0.67
Longjiao	-0.26	1.45	-2.00*	0.68	-0.62	4.26**	-1.43	4.19**	-1.38	3.33**	0.44	1.32	-0.16	2.10*	-0.19	0.60	1.61
Banqiao	-2.00*	0.08	-1.16	-0.06	-2.20*	0.98	0.15	-1.78	-5.30**	-3.80**	-1.70	-2.70**	-1.00	0.21	-3.65**	0.60	-1.55
Lyconggpo	3.38**	2.86**	2.27*	1.48	-5.30**	-2.50*	-0.03	-0.41	-4.80**	-3.30**	-3.20**	3.14**	-1.25	-0.47	-2.87**	4.29**	-1.56
Enshi	2.52*	0.89	-1.82	0.88	2.05*	-0.52	0.49	-1.33	-3.60**	-0.57	-0.73	-0.05	0.26	-0.54	-1.56	0.31	-1.09
Fengjie	0.21	-0.08	-2.50*	-0.80	-3.10**	2.70**	3.64**	0.00	-1.82	-1.40	-0.97	0.26	-1.85	-0.54	-1.07	-0.16	0.08
Badong	0.42	3.78**	-1.19	2.42*	-0.62	-1.07	0.10	1.43	-2.20*	-0.68	-2.30*	-0.23	-0.24	-0.54	-1.12	1.65	-0.13
Wuxi	-0.06	0.68	-1.80	1.58	-1.04	2.75**	0.16	-2.10*	-1.45	-0.68	1.01	-1.51	0.28	0.32	-0.49	-0.74	0.10
Zigui	-0.22	2.81**	0.27	0.74	1.28	-0.65	4.34**	3.98**	-1.95	-0.45	0.63	0.00	0.39	1.94	-0.42	0.62	1.40
Wufeng	0.52	4.95**	-0.11	1.54	0.68	-1.49	1.28	-0.16	-3.20**	-1.09	0.36	1.40	0.58	0.32	-2.00	2.92**	0.05
Xingshan	1.33	2.79**	0.00	3.44**	0.65	1.85	0.97	3.36**	-3.30**	-0.65	-1.80	-2.20*	1.06	1.27	-1.32	0.94	1.09
Fangxian	0.58	1.51	-1.53	0.31	2.60**	0.70	1.75	-0.75	-1.25	-1.58	-0.29	0.00	1.20	0.55	-1.22	0.97	0.23
Sandouping	0.26	0.76	-0.39	-0.85	-0.38	0.28	0.72	0.87	0.13	0.24	-1.87	-1.44	-1.75	0.03	0.73	-0.82	-0.31
Yichang	0.99	3.36**	-0.23	-0.39	0.29	0.81	0.52	1.14	1.72	-0.42	-0.29	-0.24	0.02	0.45	0.63	1.67	0.42
Laohekou	2.10*	1.17	2.05*	-1.92	1.62	4.04**	3.12**	2.49*	-3.00**	-0.67	-2.60**	1.45	0.32	2.05*	-2.18*	1.38	0.68

***Statistically significant at 0.01 and 0.05 significance levels, respectively.

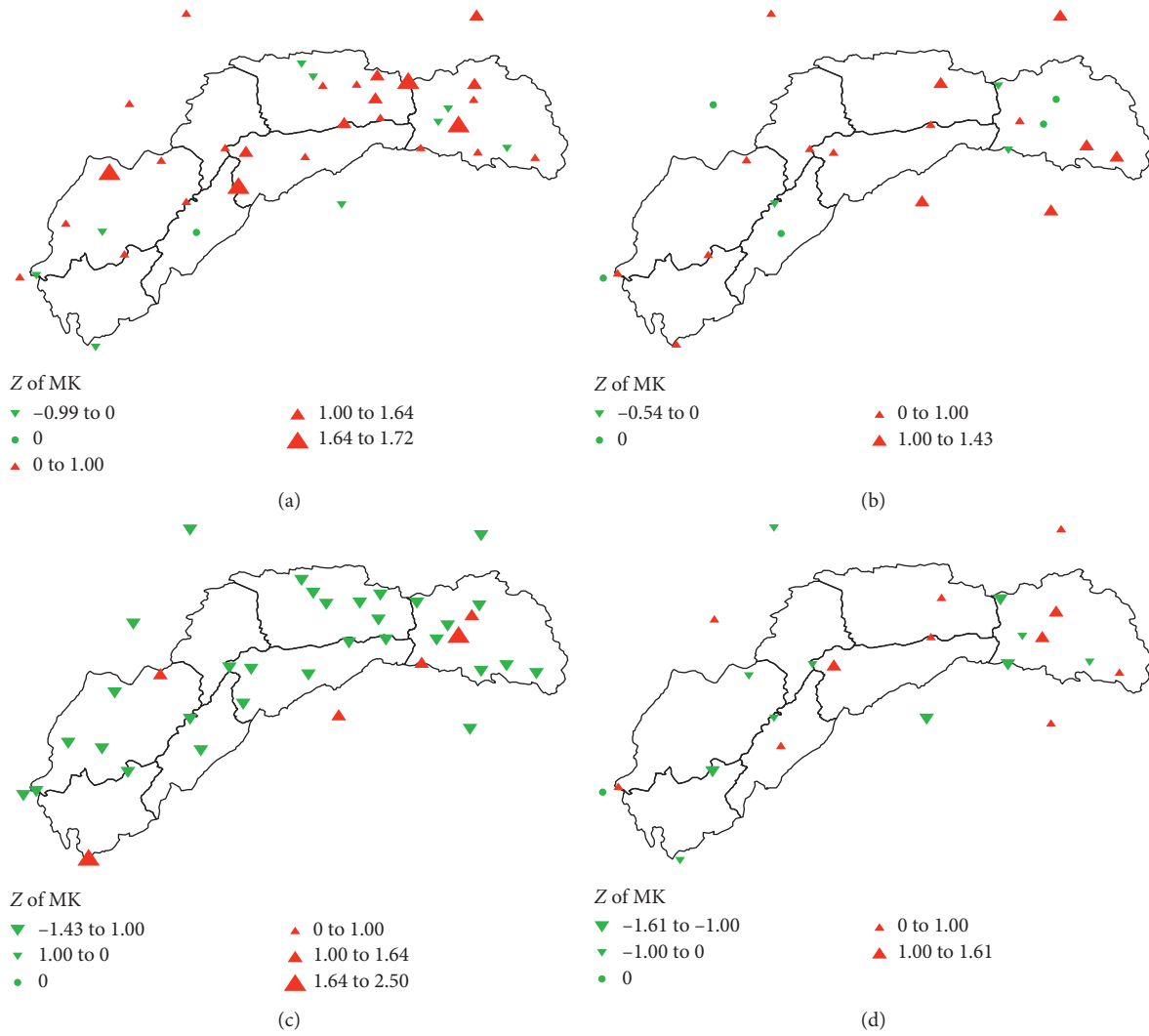


FIGURE 7: Spatial distribution of R factor variation trends in different periods. (a) 1960–1990. (b) 1991–2000. (c) 2001–2010. (d) 1960–2010.

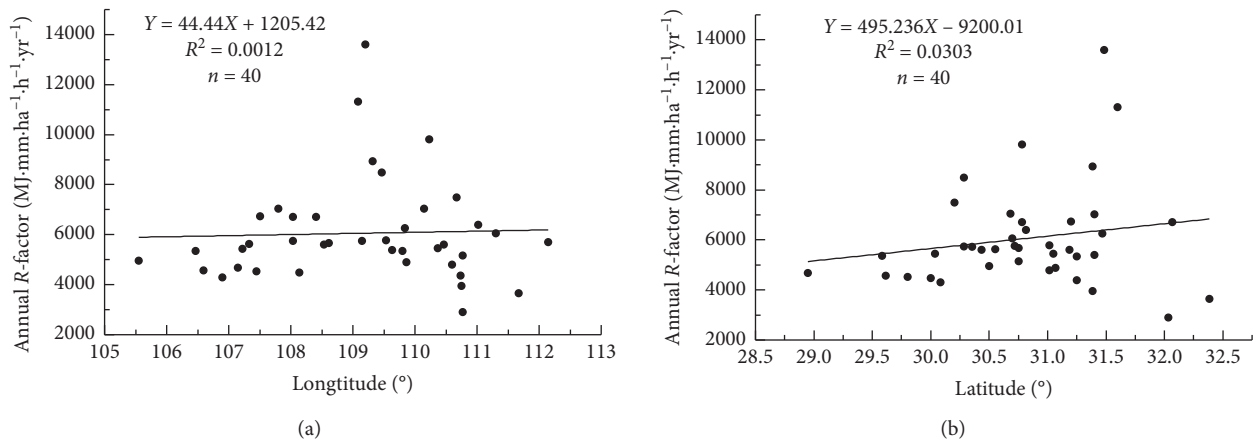


FIGURE 8: Continued.

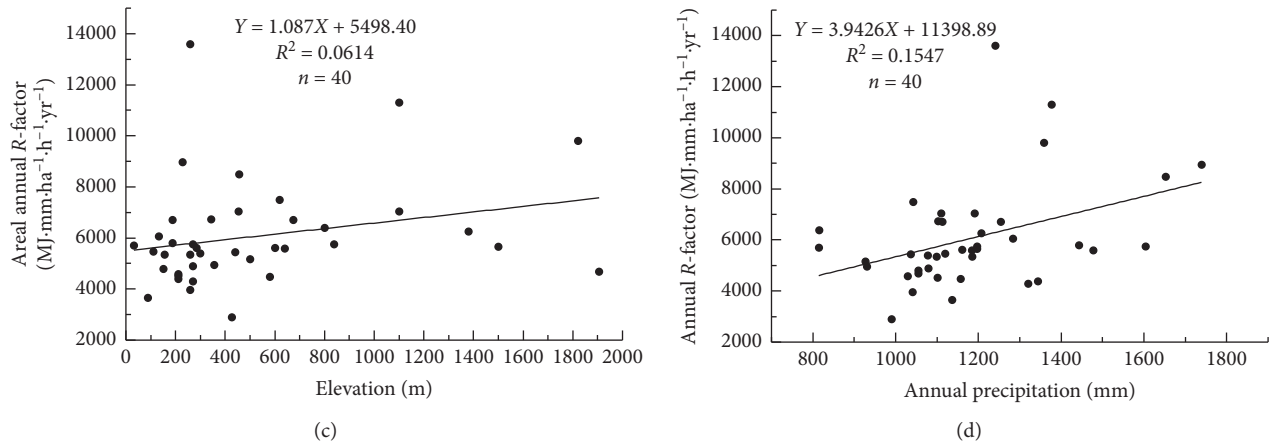


FIGURE 8: Relationship between annual rainfall erosivity, longitude, latitude, and precipitation.

4.2. Parameters of the Calculated Method. It is important to recognize that, although the method used in this study has its inherent advantages in depicting the changing characteristics of R factor, several uncertainties still exist regarding the application of the method. First, α and β are the important parameters in the calculation formula of R factor, and their values are closely related to the zonal climate characteristics and the underlying surface of the basin. The same amount of rainfall in summer can generate a totally different erosivity than that in the winter, because the summer rains tended to be more intense than winter rains. Even though values of α and β were calculated by the same way in different basins of China, the R value need more evidences to prove. According to its definition, the R factor is directly related to the rainfall's kinetic energy and intensity. In this study, the R factor is calculated from the daily erosive rainfall whether the actual daily rainfall is higher than 12 mm or not; this may also have introduced uncertainties into the estimation of the R factor. Future studies would be improved by investigating the relationship of parameters α and β and the climate and catchment characteristics to reduce or eliminate parameter value uncertainties. Moreover, it is necessary to take more factors into account when estimating the R factor in the future studies.

5. Conclusions

The spatial distribution and temporal trend of annual, seasonal, and monthly R factors in TGRA of China from 1960 to 2010 were analyzed using daily rainfall data from 40 stations. The main findings are summarized as follows.

Spatially, the annual R factor varied from 3647.0 to 10884.8 $\text{MJ}\cdot\text{mm}\cdot\text{ha}^{-1}\cdot\text{h}^{-1}$ with an average value of 6108.1 $\text{MJ}\cdot\text{mm}\cdot\text{ha}^{-1}\cdot\text{h}^{-1}$. The spatial distribution of summer and autumn R factors was similar to the pattern of annual R factor, which increased from west, south, and east to the north-central. The highest seasonal R factor was found in summer, accounting for 53% of the total annual R factor, and winter is the least erosive season. July is the most erosive month with an average of 1327.3 $\text{MJ}\cdot\text{mm}\cdot\text{ha}^{-1}\cdot\text{h}^{-1}$, and January is the least erosive month.

Temporally, the mean annual R factor was 5969.2 $\text{MJ}\cdot\text{mm}\cdot\text{ha}^{-1}\cdot\text{h}^{-1}$, with the lowest value of 3361.0 $\text{MJ}\cdot\text{mm}\cdot\text{ha}^{-1}\cdot\text{h}^{-1}$ in 1966 and highest value of 8896.0 $\text{MJ}\cdot\text{mm}\cdot\text{ha}^{-1}\cdot\text{h}^{-1}$ in 1982. The M-K test showed that the annual R factor did not change significantly across TGRA. The seasonal R factor showed a significant decrease in autumn and insignificant decrease in summer and winter. The monthly R factor in TGRA showed insignificant increases from Jun to Jul and then underwent decreases from Aug to Nov. From Dec to Feb; monthly R rose again with Feb reaching $a = 0.01$ -level significance which was probably attributed to the significant increasing trends ($\alpha = 0.01$) of 7 stations.

Future studies should relate the trends of R factor detected from this study to sediment loading in major rivers across Yangtze River Basin or China to further evaluate the usefulness of the R factor in evaluating potential soil erosion at the large basin to regional scale.

Data Availability

The data used to support the findings of this study are available from the corresponding author upon request.

Conflicts of Interest

The authors declare no conflicts of interest regarding the publication of this article.

Authors' Contributions

Huiying Liu and Guanhua Zhang conceived and designed the experiments and wrote the manuscript. Pingcang Zhang and Shengnan Zhu analyzed the data.

Acknowledgments

This work was funded by the National Natural Science Foundation of China (Nos. 41761058, 41877082, and 51569016) and supported by Scientific Research Project of Jiangxi Province Educational Bureau (No. GJJ161098).

References

- [1] Z. H. Shi, L. Ai, N. F. Fang, and H. D. Zhu, "Modeling the impacts of integrated small watershed management on soil erosion and sediment delivery: a case study in the Three Gorges Area, China," *Journal of Hydrology*, vol. 438-439, pp. 156-167, 2012.
- [2] W. H. Wischmeier and D. D. Smith, "Predicting rainfall erosion losses—a guide to conservation planning," *Agriculture Handbook No. 537*, Department of Agriculture, Washington, DC, USA, 1978.
- [3] M. A. Nearing, S.-q. Yin, P. Borrelli, and V. O. Polyakov, "Rainfall erosivity: an historical review," *Catena*, vol. 157, pp. 357-362, 2017.
- [4] P. I. A. Kinnell, "Event soil loss, runoff and the universal soil loss equation family of models: a review," *Journal of Hydrology*, vol. 385, no. 1-4, pp. 384-397, 2010.
- [5] X. X. Lu and D. L. Higgitt, "Estimating erosion rates on sloping agricultural land in the Yangtze Three Gorges, China, from caesium-137 measurements," *Catena*, vol. 39, no. 1, pp. 33-51, 2000.
- [6] W. H. Wischmeier and D. D. Smith, "Rainfall energy and its relationship to soil loss," *Transactions, American Geophysical Union*, vol. 39, no. 2, pp. 285-291, 1958.
- [7] P. Panagos, P. Borrelli, J. Spinoni et al., "Monthly rainfall erosivity: conversion factors for different time resolutions and regional assessments," *Water*, vol. 8, no. 4, p. 119, 2016.
- [8] P. H. Zhou, B. Z. Dou, Q. F. Sun et al., "Experimental study on rainfall energy," *Bulletin of Soil and Water Conservation*, vol. 1, no. 1, pp. 51-61, 1981.
- [9] W. Z. Wang, "Study on the relations between rainfall characteristics and loss of soil in loess region," *Bulletin of Soil and Water Conservation*, vol. 3, no. 4, pp. 7-13, 1983.
- [10] J. M. J. Arnoldus, "Methodology used to determine the maximum potential average annual soil loss due to sheet and rill erosion in Morocco," *FAO Soils Bull*, vol. 34, pp. 39-51, 1977.
- [11] H. Lu and B. Yu, "Spatial and seasonal distribution of rainfall erosivity in Australia," *Soil Research*, vol. 40, no. 6, pp. 887-901, 2002.
- [12] C. W. Richardson, G. R. Foster, and D. A. Wright, "Estimation of erosion index from daily rainfall amount," *Transactions of the ASAE*, vol. 26, no. 1, pp. 153-156, 1983.
- [13] B. Yu and C. J. Rosewell, "An assessment of a daily rainfall erosivity model for New South Wales," *Soil Research*, vol. 34, no. 1, p. 139, 1996.
- [14] K. G. Renard and J. R. Freimund, "Using monthly precipitation data to estimate the R-factor in the revised USLE," *Journal of Hydrology*, vol. 157, no. 1-4, pp. 287-306, 1994.
- [15] W. B. Zhang and J. S. Fu, "Rainfall erosivity estimation under different rainfall amount," *Resources Science*, vol. 25, no. 1, pp. 35-41, 2003, in Chinese.
- [16] <http://www.mwr.gov.cn/sj/tjgb/dycqgslpcgb/>.
- [17] P. Panagos, C. Ballabio, P. Borrelli, and K. Meusburger, "Spatio-temporal analysis of rainfall erosivity and erosivity density in Greece," *Catena*, vol. 137, pp. 161-172, 2016.
- [18] A. A. Fenta, H. Yasuda, K. Shimizu et al., "Spatial distribution and temporal trends of rainfall and erosivity in the Eastern Africa region," *Hydrological Processes*, vol. 31, no. 25, pp. 4555-4567, 2017.
- [19] B. Klik, K. Haas, A. Dvorackova, and I. C. Fuller, "Spatial and temporal distribution of rainfall erosivity in New Zealand," *Soil Research*, vol. 53, no. 7, pp. 815-825, 2015.
- [20] W. B. Zhang, Y. Xie, and B. Y. Liu, "Spatial distribution of rainfall erosivity in China," *Journal of Mountain Science*, vol. 21, no. 1, pp. 33-40, 2003.
- [21] X. Ma, Y. He, J. Xu, M. van Noordwijk, and X. Lu, "Spatial and temporal variation in rainfall erosivity in a himalayan watershed," *Catena*, vol. 121, no. 5, pp. 248-259, 2014.
- [22] Z. Gu, X. Duan, B. Liu, J. Hu, and J. He, "The spatial distribution and temporal variation of rainfall erosivity in the Yunnan plateau, southwest China: 1960-2012," *Catena*, vol. 145, pp. 291-300, 2016.
- [23] C. Lai, X. Chen, Z. Wang et al., "Spatio-temporal variation in rainfall erosivity during 1960-2012 in the Pearl River Basin, China," *Catena*, vol. 137, pp. 382-391, 2016.
- [24] W. Qin, Q. Guo, C. Zuo, S. Shan, L. Ma, and G. Sun, "Spatial distribution and temporal trends of rainfall erosivity in mainland China for 1951-2010," *Catena*, vol. 147, pp. 177-186, 2016.
- [25] S. Liu, S. Huang, Y. Xie et al., "Spatial-temporal changes of rainfall erosivity in the loess plateau, China: changing patterns, causes and implications," *Catena*, vol. 166, pp. 279-289, 2018.
- [26] L. Xue, X. Liu, and X.-y. Ma, "Spatiotemporal distribution of rainfall erosivity in the Yanhe river watershed of hilly and gully region, Chinese loess plateau," *Environmental Earth Sciences*, vol. 75, no. 4, p. 315, 2016.
- [27] J. R. Fan, D. Yan, and X. Guo, "Spatial and temporal distribution of rainfall erosivity based on GIS in the upper Yangtze River basin," *Research of Soil & Water Conservation*, vol. 17, no. 1, pp. 92-96, 2010, in Chinese.
- [28] A. J. Wang, Z. G. Li, and F. Liu, "Spatiotemporal distribution of rainfall erosivity for water erosion district in upper reaches of Yangtze river," *Bulletin of Soil & Water Conservation*, vol. 33, no. 1, pp. 8-11, 2013, in Chinese.
- [29] C. G. Wu, D. S. Lin, and W. F. Xiao, "Spatio-temporal distribution characteristics of rainfall erosivity in three Gorges reservoir area," *Chinese Journal of Applied Ecology*, vol. 22, no. 1, pp. 151-158, 2011, in Chinese.
- [30] X. M. Wang, *Rainfall Erosivity of Three Gorges Reservoir Area*, College of horticulture & forestry Sciences of Huazhong Agriculture University, Wuhan, China, 2011, in Chinese.
- [31] H. Y. Liu, H. Y. Ren, C. W. Zhang, and P. C. Zhang, "Temporal and spatial variations of rainfall erosivity in the Xiangxi river watershed of the Three Gorges Reservoir region," *Science of Soil & Water Conservation*, vol. 84, no. 6, pp. 362-371, 2015, in Chinese.
- [32] H. Y. Ren and H. Y. Liu, "Temporal-spatial variations of rainfall erosivity in Daning river watershed of Three Gorges Reservoir region," *Bulletin of Soil & Water Conservation*, vol. 36, no. 3, pp. 1-7, 2016, in Chinese.
- [33] Y. C. Yan, S. P. Yue, and S. W. Zhang, "The confidence coefficient of mean annual rainfall erosivity influenced by record length of rainfall datasets," *Journal of Natural Resources*, vol. 28, no. 2, pp. 21-27, 2012, in Chinese.
- [34] L. Z. Hua, X. B. He, C. Z. Yan, and H. W. Nan, "Temporal-spatial variations of rainfall erosivity in Daning river watershed of Three Gorges Reservoir region," *Bulletin of Soil & Water Conservation*, vol. 28, no. 4, pp. 22-25, 2008, in Chinese.
- [35] P. Cui, Y. G. Ge, and Y. M. Lin, "Soil erosion and sediment control effects in the Three Gorges Reservoir region, China," *Journal of Resources and Ecology*, vol. 2, no. 4, pp. 289-297, 2011.
- [36] Y. Xie, B. Liu, and M. A. Nearing, "Practical thresholds for separating erosive and non-erosive storms," *Transactions of the ASAE*, vol. 45, no. 6, pp. 1843-1847, 2002.

- [37] H. B. Mann, "Nonparametric tests against trend," *Econometrica*, vol. 13, no. 3, pp. 245–259, 1945.
- [38] M. G. Kendall, *Rank Correlation Methods*, Griffin, London, UK, 1975.
- [39] S. G. Meshram, S. K. Singh, C. Meshram, R. C. Deo, and B. Ambade, "Statistical evaluation of rainfall time series in concurrence with agriculture and water resources of Ken River Basin, Central India (1901–2010)," *Theoretical and Applied Climatology*, vol. 134, no. 3-4, pp. 1231–1243, 2017.
- [40] J. Huang, J. Zhang, Z. Zhang, and C.-Y. Xu, "Spatial and temporal variations in rainfall erosivity during 1960–2005 in the Yangtze River Basin," *Stochastic Environmental Research and Risk Assessment*, vol. 27, no. 2, pp. 337–351, 2013.
- [41] M. Men, Z. Yu, and H. Xu, "Study on the spatial pattern of rainfall erosivity based on geostatistics in Hebei Province, China," *Frontiers of Agriculture in China*, vol. 2, no. 3, pp. 281–289, 2008, in Chinese.

Research Article

Are Feature Agreement Statistics Alone Sufficient to Validate Modelled Flood Extent Quality? A Study on Three Swedish Rivers Using Different Digital Elevation Model Resolutions

Nancy Joy Lim  and Sven Anders Brandt 

Department of Computer and Geospatial Sciences, University of Gävle, SE-801 76 Gävle, Sweden

Correspondence should be addressed to Nancy Joy Lim; naylim@hig.se

Received 26 April 2019; Revised 22 August 2019; Accepted 13 September 2019; Published 13 November 2019

Guest Editor: Raffaele Albano

Copyright © 2019 Nancy Joy Lim and Sven Anders Brandt. This is an open access article distributed under the Creative Commons Attribution License, which permits unrestricted use, distribution, and reproduction in any medium, provided the original work is properly cited.

Hydraulic modelling is now, at increasing rates, used all over the world to provide flood risk maps for spatial planning, flood insurance, etc. This puts heavy pressure on the modellers and analysts to not only produce the maps but also information on the accuracy and uncertainty of these maps. A common means to deliver this is through performance measures or feature statistics. These look at the global agreement between the modelled flood area and the reference flood that is used. Previous studies have shown that the feature agreement statistics do not differ much between models that have been based on digital elevation models (DEMs) of different resolutions, which is somewhat surprising since most researchers agree that high-resolution DEMs are to be preferred over poor resolution DEMs. Hence, the aim of this study was to look into how and under which conditions the different feature agreement statistics differ, in order to see when the full potential of high-resolution DEMs can be utilised. The results show that although poor resolution DEMs might produce high feature agreement scores (around $F > 0.80$), they may fail to provide good flood extent estimations locally, particularly when the terrain is flat. Therefore, when high-resolution DEMs (1 to 5 m) are used, it is important to carefully calibrate the models by the use of the roughness parameter. Furthermore, to get better estimates on the accuracy of the models, other performance measures such as distance disparities should be considered.

1. Introduction

Flood risk maps have become standard documents in local, regional, national, and sometimes even international spatial planning. They are widely used and considered as valuable sources of information, mainly in planning and development projects. Detailed positioning of houses, buildings, and infrastructure is decided based on these maps. However, the reliability of these flood maps have been questioned for years. Deterministic flood maps, in particular, which show defined flooded areas associated with a specific flood-return year (e.g., the 100-year flood), are criticised to mislead map users to think that they show absolute boundaries of flood extent. Nonetheless, they can never be exact due to effects of different factors and modelling assumptions (e.g., input data,

model, and model parameters) in the production of these maps. Different data, models, or parameters can change the position of the flood borders.

To overcome this limitation of flood model results, they are calibrated (e.g., using different roughness values) against a historic (reference) flood event with the same discharge. Each flood extent from the calibration is then validated for its accuracy through a performance (goodness-of-fit) measure that quantifies the model quality. Numeric scores provided by the performance measures are used to justify the choice of an optimal model that can be used as a flood hazard map. In uncertainty and probabilistic mapping implemented through the Generalised Likelihood Uncertainty Estimation (GLUE) methodology [1], these performance estimators play an important role, where they are used for deriving the

likelihood weights assigned to the results of the ensemble, prior to the creation of the map [2]. Moreover, performance scores are widely used to analyse the sensitivity of the modelled flood to the effects of the input topographic data [3–6], roughness value [7–11], and hydraulic models, or their numerical solutions [3, 7, 8].

In flood extent validation studies, performance measures used include various types of feature agreement (F) statistics [9], as well as disparity measures [2]. F -statistics are the most commonly applied in assessing flood model predictions. They give a general view of the model's performance by considering the total sizes of over- and underestimation and overlap between the model and the reference data [12], but the outcome may be affected by what is prioritised in the equation. The disparity measures (mean and median disparities), on the contrary, account for the distance between the modelled and reference data at each point sample location [2, 12]. Nevertheless, the scores will be dependent on where the samples are taken or the sampling strategy employed. According to Beven [13], all these equations have their assumptions, which can have implications on the choice of optimal models. Hence, decisions of the optimal model can be relative to the performance equation used.

Lim and Brandt [12] also showed that the combination of the digital elevation model (DEM) and roughness (Manning's n) can influence the performance measures such as the F -statistics scores. However, it remains uncertain how these various statistical estimators' results differ and when they differ. Hence, the aims of this study are to evaluate the following: (1) how the different performance measures, such as the different feature agreement statistics, vary in their results, in terms of the quantified values they produce; (2) how the generated flood extents of models considered as "best" coincide with the validation data and the computed performance scores; (3) how the sizes of overlap and under- and overestimation vary with the given DEM or DEM and roughness pairs; and (4) how the proportion of areas correctly and incorrectly modelled agree with the performance measures.

The effects of model performance in the assessment of simulation results based on the influence of the DEM alone, or both the DEM and roughness values used, are investigated in relation to the aims. The topographic data remains an important hydraulic numerical model input that provides the geometry of the study area (through, e.g., cells, triangular meshes or cross sections) and is the main source of the elevation values [2]. The grid size or the resolution mainly affects the details in the modelling and the accuracy (both vertical and horizontal) of model results [4, 5]. Nonetheless, as what is shown in some studies [3, 6, 12], even lower resolution DEMs (≥ 25 m) can produce better quantified performance. Thus, basing decisions on optimal models from a given performance measure alone may discard the benefits of using fine resolution DEMs. In addition, as the Manning's n is the parameter that is adjusted during the calibration, it is important to also see how these values, especially when paired with different DEMs, can affect the performance scores.

2. Verification Measures for Spatial Predictions of Floods

One way to distinguish the goodness of predictions from simulation result or modelling is through its quality or agreement to the observed data (truth) [14]. This quality is assessed through verification methods that help describe or quantify their performance. A model is usually compared with observational data, based on binary conditions (i.e., *yes/presence* or *no/absence*), through a 2×2 contingency table [15]. In Table 1, *hits* (A) represent predicted events to happen and did take place. *False alarms* (B) are events modelled to occur but did not occur, whereas *misses* (C) are events that actually happened but were not modelled to happen. Model results that are correctly predicted not to happen fall under *correct rejection* (X). A number of performance estimators based on this table are described in Mason [15].

In flood inundation studies, the goodness of model prediction can be evaluated by assessing the overall, so called global, spatial accuracy of the simulated flood result produced from model calibrations or ensemble modelling, against a reference dataset, which is often a historical flood extent having the same magnitude as the modelled one. In such applications where the quality of spatial predictions of modelled events are verified, performance measures that can be applied will include *accuracy*, the *critical success index* (CSI), *hit rate* or the *probability of detection* (POD), *false alarm rate* or the *probability of false detection* ($POFD$), and the *false alarm ratio* (FAR) [9].

The degree of correspondence between the model and the observation data can be estimated through computing the proportion correctly predicted by the model (i.e., *accuracy*) [9, 15]:

$$\text{accuracy} = \frac{A + X}{A + B + C + X} \quad (1)$$

According to Schaefer [16], this equation can be affected by the size or number of *correct rejections*, especially if it is large, which can lead to high accuracy score. In flood modelling, where dry areas are usually larger, a high accuracy score can be achieved, despite the low number of *hits* in the model [10]. Thus, in most performance measures used, *correct rejection* (X) is disregarded. The removal of the *correct rejection* from the original accuracy equation leads to another performance measure widely known as the *critical success index* or the threat score:

$$CSI = \frac{A}{A + B + C} \quad (2)$$

In flood model verification, the application of CSI allows to focus on the correct prediction made by the model (*hits*, A), and the two main causes of flood modelling errors, i.e., *false alarm* (B) and *misses* (C). There are several equations based on the CSI , and they are known as the feature agreement (F) statistics. Generally, they are implemented by either considering (1) the binary flooding conditions (i.e., flooded = 1 or dry = 0) of each cell (in a raster data) in the observed (D) and modelled (M) result [9, 17] or (2) by comparing the areal size and location of the modelled flood

TABLE 1: 2×2 contingency table assessing the quality of model results [15].

		Observation	
		Yes (presence)	No (absence)
Model	Yes (presence)	Hits (A)	False alarm (B)
	No (absence)	Misses (C)	Correct rejection (X)

against the reference data [18] (in vector data). All F -statistics equations rely on three important factors in the contingency table that help assess how well the model forecast the flooding. These are (1) the total number of cells (P) correctly modelled to be flooded (M_1D_1) or the size of overlap (A , *hits*) between the modelled and the reference data, (2) total number of cells (M_1D_0) or size (B) overestimated (*false alarms*) by the model, and (3) total cells (M_0D_1) or size underpredicted (C , *misses*).

The most typically used F -statistics is $F1$, which is based on the original CSI equation. It is based on getting the intersection (*hits*) and union (*hits* + *false alarm* + *misses*) of the modelled and observed event [3] (equation (3)). The values generated by the equation is from 0 (no fit) to 1 (perfect model fit):

$$F1 = \frac{M \cap D}{M \cup D} \quad (3)$$

However, this feature agreement statistics is also known to give bias in the results it produces [9], especially when the prediction gives large overlap size (*hits*) [12]. If the flooded area is large, as is the case when rivers flood wide flat floodplains, the modelled flood area will overlap the reference flood area to a relatively big extent, compared with the areas that are either over- or under-estimated. This means that a rather poor model can achieve strong statistics. As stated by Lim and Brandt [12], as long as the model has *hits* greater than the combined sizes of *misses* and *false alarms*, the equation will lead to an F -value > 0.50 . Because of this limitation, several variants of the equation have been introduced (Table 2) to improve the quantified scores. These versions of the equation modify the numerator to penalise the model with the overprediction ($F2_O$), underprediction ($F2_U$), or both under- and overpredictions ($F3$) it produces [9]. Among these variants, $F2_O$ is a widely used performance estimator in flood extent validation studies and in creating probabilistic maps. According to Hunter [9] and Hunter et al. [8], it constrains the overlap produced by the model in $F1$, by penalising it with the overprediction it produces. $F2_U$ and $F3$ are the least applied among the four equations. In $F2_U$, the overlap is subtracted by the underestimation made by the model, whereas in $F3$, both under- and overestimation are subtracted from the overlap. Maximum value of these performance measures is also 1, indicating a perfect model fit with the reference data. Their minimum can be -1 .

Other spatial performance measures that can be used in flood modelling are the *hit rate* or *probability of detection*, *probability of false detection*, and *false alarm ratio*. The POD is a standard statistics that indicates the ratio of

correct prediction by the model, to the total observed data [15, 16]. In flood model verification, it tells the total number of pixels or areal size correctly predicted by the model to be flooded, in relation to the reference data, by considering both the overlap and the underestimation made by the model. Maximum POD score is 1 in models with perfect overlap with the reference data. According to Mason [15] and Hunter [9], the POD measure alone cannot be used as a performance estimator because the equation is affected by the size of the *hits* (A). Large hits (and low underestimation) can generate high performance score, even if the model has largely overestimated the flooding. Thus, the POD equation should be supplemented with information that considers errors in overestimation [9], through the *probability of false detection* (also known as the *false alarm rate*) and the *false alarm ratio*. $POFD$ accounts for the proportion of overprediction made by the model in relation to the *correct rejections* (X), while the FAR score considers the proportion of overestimation in relation to the *hits*. Maximum scores for both performance measures are 0, i.e., no overestimation made by the model. However, these two can also pose similar problems as the POD . As the $POFD$ is related only to *correct rejections*, how well the inundation is produced in terms of the overlap or how the underprediction is minimised are not considered in the equation. On the contrary, although FAR accounts for the effect of the size of overlap made by the model, the size underpredicted is not accounted in the equation.

A further measure that can be applied to spatial model verification is the $BIAS$. This measure is for quantifying the consistency between the model result and the observed flood event [9] but does not indicate the model skill or performance [15]. Therefore, the bias score is considered more of a descriptive statistics that specifies the ratio of the predicted data to the observation [15]. In flooding applications, this measure indicates if overall the model result underestimates ($BIAS < 1$) or overestimates ($BIAS > 1$) the flood. A value of 1 shows no bias. The farther away the score from 1, the larger the bias on either under- or overestimation.

3. Materials and Methods

Model performance measures are evaluated for model results based on different DEM resolutions in combination with different roughness values or single-handedly by the DEM resolution. To meet the aims, there were three study areas at different geographical locations in Sweden used (Figure 1): Voxna, Testebo, and Eskilstuna (two different parts) (Figure 1). Voxna and Testebo rivers were used to determine the influence of DEM together with Manning's n on the performance scores. In analysing the effect of the DEM resolution (including its errors), the Eskilstuna river was used as a case. Simulation results from earlier studies of Lim and Brandt [12] (Voxna and Testebo), Klang and Klang [19], and Brandt [20, 21] (Eskilstuna) were used in the current study. Specific data processing and modelling procedures are thereby described in the said articles in detail.

TABLE 2: Different flood verification measures implemented for raster and vector data (revised from Hunter [9]).

Verification measures	Binary classification (raster-based)	Areal size (vector-based)	Values
Feature agreement statistics:			
$F1$	$\frac{\sum P_{M_1 D_1}}{\sum P_{M_1 D_1} + \sum P_{M_1 D_0} + \sum P_{M_0 D_1}}$	$\frac{A}{A+B+C}$	0 to 1
$F2_O$	$\frac{\sum P_{M_1 D_1} - \sum P_{M_1 D_0}}{\sum P_{M_1 D_1} + \sum P_{M_1 D_0} + \sum P_{M_0 D_1}}$	$\frac{A-B}{A+B+C}$	-1 to 1
$F2_U$	$\frac{\sum P_{M_1 D_1} - \sum P_{M_0 D_1}}{\sum P_{M_1 D_1} + \sum P_{M_1 D_0} + \sum P_{M_0 D_1}}$	$\frac{A-C}{A+B+C}$	-1 to 1
$F3$	$\frac{\sum P_{M_1 D_1} - \sum P_{M_1 D_0} - \sum P_{M_0 D_1}}{\sum P_{M_1 D_1} + \sum P_{M_1 D_0} + \sum P_{M_0 D_1}}$	$\frac{A-B-C}{A+B+C}$	-1 to 1
Hit rate/probability of detection (POD)	$\frac{\sum P_{M_1 D_1}}{\sum P_{M_1 D_1} + \sum P_{M_0 D_1}}$	$\frac{A}{A+C}$	0 to 1
Probability of false detection (POFD)/false alarm rate	$\frac{\sum P_{M_1 D_0}}{\sum P_{M_1 D_0} + \sum P_{M_0 D_0}}$	$\frac{B}{B+X}$	0 to 1
False alarm ratio (FAR)	$\frac{\sum P_{M_1 D_0}}{\sum P_{M_1 D_1} + \sum P_{M_1 D_0}}$	$\frac{B}{A+B}$	0 to 1
BIAS	$\frac{\sum P_{M_1 D_1} + \sum P_{M_1 D_0}}{\sum P_{M_1 D_1} + \sum P_{M_0 D_1}}$	$\frac{A+B}{A+C}$	0 to ∞

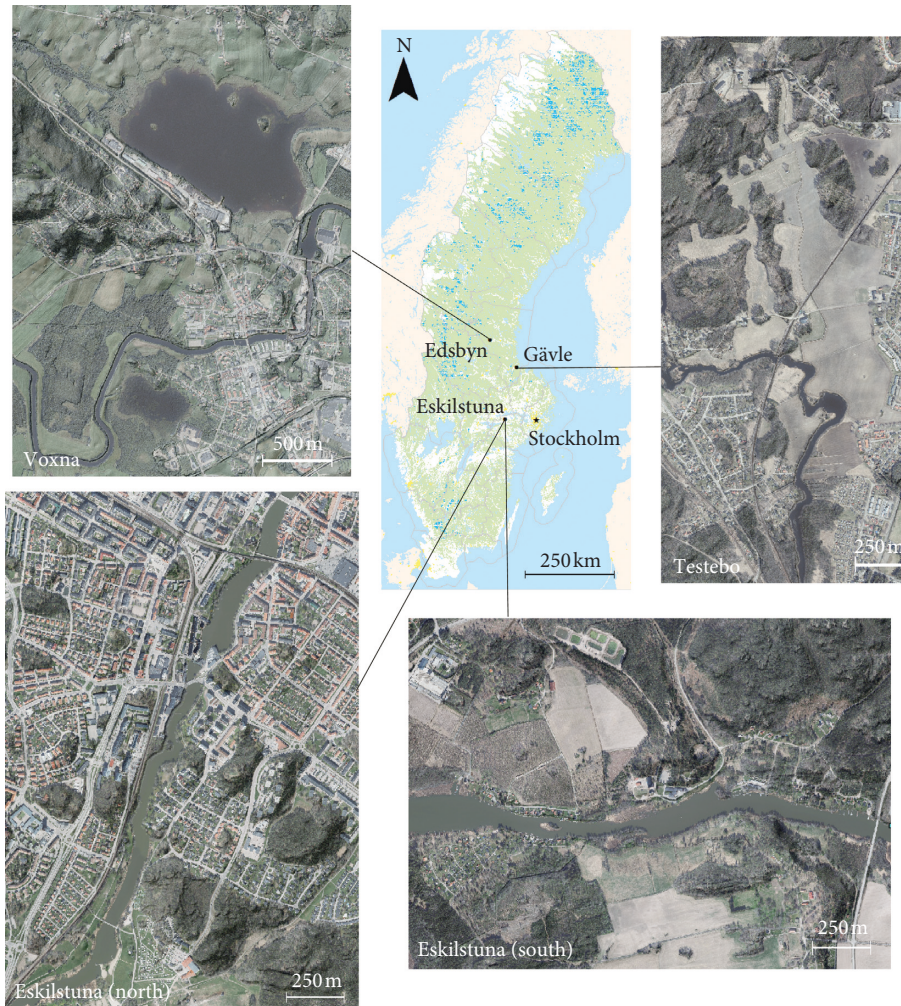


FIGURE 1: Locations of the study areas ©Lantmäteriet.

3.1. Study Areas, Data, and Hydraulic Modelling

3.1.1. Voxna River. The first site is the Voxna river, situated in Edsbyn. The total size of the study area is about 14.7 km². Its western part is flat, consisting mainly of agricultural lands and forests. At the east, the river flows through the town of Edsbyn, where mostly built-up areas are present. This part of the river is steeper. The Voxna river has a mean annual flow of 40 m³/s at the outlet.

Topographic data used for creating the digital elevation models for Voxna came from a combination of bathymetric and LiDAR data. The DEMs were produced from the topographic data through TIN generation and conversion to raster, which is the main input required by the hydraulic model used [12]. The different DEMs used for this river had resolutions of 3, 4, 5, 10, 15, 20, 25, and 50 m. The highest resolution DEMs were not possible to be used for the study area due to the technical limitations of the 2D hydraulic model in terms of the size of the site. For each DEM, 10 different Manning's roughnesses were used, ranging from 0.010 to 0.100, with 0.01 increments in accordance with Horritt and Bates [7]. This was mainly to see how these different roughness coefficients affect the model results from different DEM resolution models.

The simulated flow was 360 m³/s, which is equal to the big flood event in 1985. A corresponding reference flood inundation map was provided by Ovanåker municipality for this particular event. The flow was modelled as steady state 2D flow in CAESAR-LISFLOOD software (Coulthard et al. [22]). Eighty simulations from the different combinations of DEM and Manning's n were carried out for the river.

3.1.2. Testebo River. The second area is around the Testebo river at Forsby, north of Gävle. It has a mean annual flow of 12 m³/s. The surrounding areas of the river, particularly its central portion is mainly flat arable land, with some mixed forests. Most residential areas are situated at the edges of these lands. Steeper sections of the river are located at the eastern and southern parts of the study site.

DEMs produced for Testebo river were processed in the same way as for the Voxna river. Similar DEM resolutions (except for the 1 and 2 m resolution, which were also included) and range of roughness values as for the Voxna river were used for the modelling. Here, the simulated flow was 160 m³/s, which coincides with the 100-year flood. Gävle municipality provided a flood inundation map over the 1977 flood, which is equivalent to this flow. A steady state 2D flow using the CAESAR-LISFLOOD software was also implemented to the study area [12]. A total of 100 simulations were conducted for the combinations of resolution and roughness values.

3.1.3. Eskilstuna River. The third location consists of two parts of the Eskilstuna river (with a mean annual flow of 24 m³/s) in Eskilstuna. The northern part of the study area is located in the city centre where most residential, commercial, and industrial establishments are concentrated. This site is characterised by relatively steeper banks. The other

location is situated just south of the city, where the floodplain is flatter. Residences are visible in the western part of this study site, along the river. Some forests are also lining up the river. At the edges of these forested areas are arable lands.

DEM resolutions used for the modelling were 1.04, 2.09, 3.13, 10, 25, and 50 m. Note, however, that these particular DEMs have not been derived in the same way as those for Voxna and Testebo rivers, where linear interpolation of point cloud data was used to construct the DEMs of the desired resolution. Here, the original point cloud data, which had a density of 1.64 and 1.36 points/m², corresponding to cell sizes of 0.78 and 0.86 m for the flat and steep subareas, respectively, were used to produce the reference elevation model. This DEM was then resampled and degraded by introducing random errors to simulate the behaviour of the results from a Leica ALS50 LiDAR instrument for different flight heights. Details of the DEM degeneration can be found in Klang and Klang [19] and Brandt [20, 21].

A single roughness value (0.033) was used for all model runs. This Manning's n is the most commonly suggested friction coefficient for rivers in Sweden. As a single Manning's n was used, this means that the uncertainties of modelled flood extents can be isolated to only depend on the characteristics of the DEM and not on the DEM resolution in combination with roughness [20, 21]. Flow equivalent to the maximum probable flow of 198 m³/s was used for the simulations. A steady state 1D flow was simulated using the HEC-RAS software (Hydrologic Engineering Center [23]).

3.1.4. Model Performance Evaluation. Different feature agreement statistics, which are applied in flood extent validation studies, were used to assess the overall performance of the simulation results. Each model result was compared to the observed flood data (i.e., the historical flood maps for Voxna and Testebo rivers and the simulation result from the original point cloud data in case of Eskilstuna). Since the reference data were all in vector formats, equations accounting for areal size (cf. Table 2) were used. This was implemented by overlaying the reference and the given modelled flood map resulting from simulating a given DEM, or DEM and Manning's n combination. Then, the sizes of overlap and under- and overestimation were taken (Figure 2), prior to the application of the specific F -statistics equation.

Aside from using the F -statistics, each simulation and best model results from the different resolution DEMs were also evaluated using two other spatial performance measures that can help understand the performance scores provided by the F -statistics, in terms of the *probability of detection* and *false alarm ratio*. Both statistics were considered to be able to determine how well the model produces the inundation in relation to the hits, as well as underestimation it produces (*POD*) [9], and how it overpredicted the results (*FAR*). *Probability of false alarm* or the *false alarm rate* was not used in this study, due to its inclusion of *correct rejection* (X) in the equation, which is difficult to account in spatial model results such as in flood extents because of huge dry areas being modelled [10]. To further understand whether the

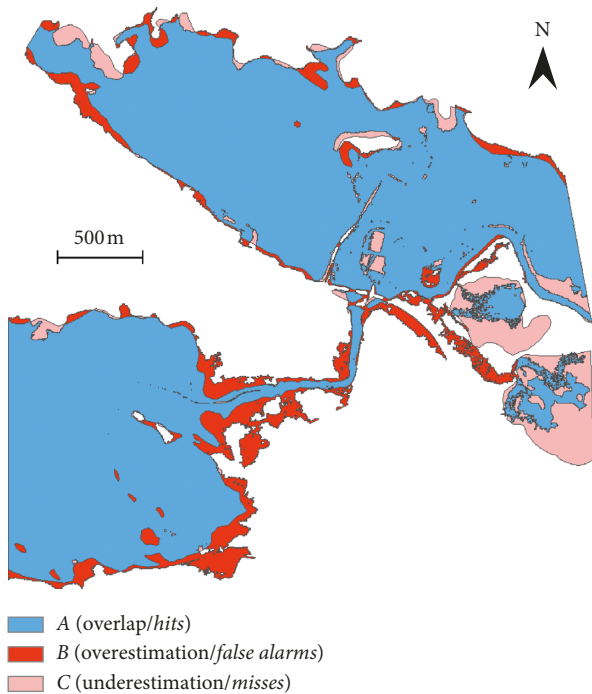


FIGURE 2: Derivation of areal sizes for each of the components of F -statistics for one of the simulation results.

model from a given performance, DEM, and DEM and Manning's n combination tends to over- or underestimate the flood predictions, $BIAS$ scores were also computed.

4. Results

The effects of performance in evaluating quality of flood models' results as influenced by both the DEM and Manning's n used (Testebo and Voxna), and by the DEM (Eskilstuna, North and South), were analysed through the following: (1) the overall performance scores of the simulation results, (2) the most optimal models' performance scores and their corresponding spatial extents and size of inundation areas, (3) changes in the sizes of overlap and over- and underestimation produced by the model for the given DEM and DEM and roughness combinations, and (4) the POD , FAR , and $BIAS$ scores of the models.

4.1. Combined Effects of DEM and Roughness Values (Testebo and Voxna Rivers)

4.1.1. Overall Performance Results. For both Testebo and Voxna rivers, various DEM resolution together with different roughness values were evaluated to find out how they affect the quantified performance scores using the different feature agreement statistics. From the 3D surface plots in Figure 3, it can be seen that the DEMs produced varying performance values in each measure, depending on the Manning's n paired with them. Moreover, from the two study sites, the Testebo river produced more variation in the performance score (for each goodness-of-fit measure) when using high-to-low-resolution DEMs, compared with the

Voxna river. Overall, the Voxna river resulted in higher performances from the different combinations of DEMs and roughnesses, with only 1 to 4 model results (out of 80) having $F < 0.50$ in the four F -statistics. It can also be observed that, regardless of the goodness-of-fit measure used for both study areas, higher performances were more concentrated in medium to lower resolution DEMs (from 10 to 50 m), paired with a wider range of Manning's n values, whereas better results from higher resolution DEMs (1–5 m) came from a smaller range of roughness values.

Among the different feature agreement statistics, $F2_O$ had fewer simulation results that gave higher performance. Lower roughness values also led to better results for this measure, especially when paired with coarser resolution DEMs. With $F2_U$, more simulation results produced higher performances. Nevertheless, it can also be seen that higher resolution DEMs performed poorly with lower Manning's values (particularly for the Testebo river, producing more negative performances), while coarser resolution DEMs performed well with most of Manning's n , especially for the Voxna river. The performance patterns for $F1$ and $F3$ were the same, but the latter produced lower and even negative values, especially for the higher resolution DEMs paired with lower roughness.

4.1.2. Most Optimal Performance Results. The four performance measures considered different pairs of DEM and Manning's n to be the most optimal from the ensemble of 80 (Voxna) and 100 (Testebo) simulations (Figure 4). In general, $F2_O$ produced the best results from each DEM with much lower roughness values, while $F2_U$ produced the best results with higher friction. $F1$ and $F3$, which had the same optimal model results, almost followed the roughness pattern of $F2_U$ for each resolution, but using a lower friction coefficient. It is also visible from the diagram that the best models from the three performance estimators ($F1$, $F2_U$, and $F3$) that used higher resolution DEMs (1–5 m) worked well with higher roughness, and that the most optimal Manning's n used decreased as the resolution became coarser.

When considering the maximum performance scores for the different DEMs, the lowest resolution DEMs (25 and 50 m) produced the most optimal performance in all four F -statistics for the Testebo river ($F1_{50\text{ m}|n0.030} = 0.730$, $F2_{O,25\text{ m}|n0.040} = 0.651$, $F2_{U,50\text{ m}|n0.010} = 0.646$, and $F3_{50\text{ m}|n0.030} = 0.460$). For the Voxna river, the 10 m DEM got the highest scores when using $F1_{n0.040}$ (0.850), $F2_{U,n0.080}$ (0.807), and $F3_{n0.040}$ (0.70), while the 5 m DEM received the highest with $F2_{O,n0.030}$ (0.763). Although the maximum performance range did not vary much within each F -statistics (Tables 3 and 4), the variations in extents using the different DEMs and Manning's roughness were more discernible when compared with each other visually (Figure 5). Flood extents having the highest $F2_O$ values produced big underestimations particularly for the highest resolution DEMs in both rivers. The 1 to 5 m DEMs underestimated the southern part of the Testebo river and the southeastern section of Voxna river. The 10 to 50 m DEMs underpredicted the flooding in the north of Testebo, while in Voxna, these resolutions overpredicted the

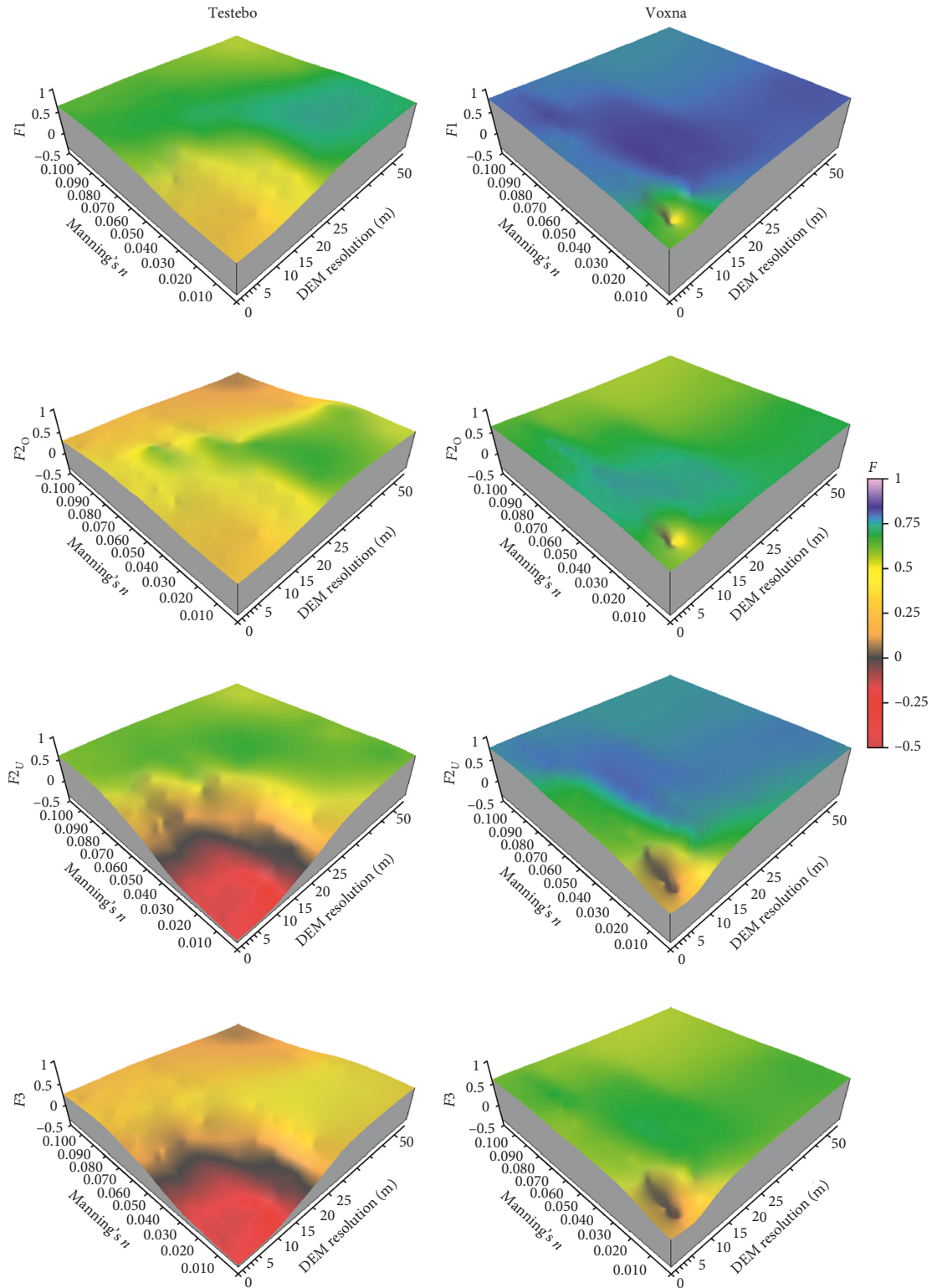


FIGURE 3: Different performance results for the Testebo and Voxna rivers using various combinations of DEM resolution and roughness parameter.

flooding. $F2_U$ produced larger extents in all DEM resolutions for Testebo (especially in the south and southeast) than $F1|F3$ (except for the 50 m DEM) because of the higher roughness values used. In Voxna, the difference in

extents between $F2_U$ and $F1|F3$ were less noticeable in the map, but if the size of the inundation area will be compared, the former had a larger flooded area as brought by using the higher roughness value (i.e., $n = 0.030$) (Table 4).

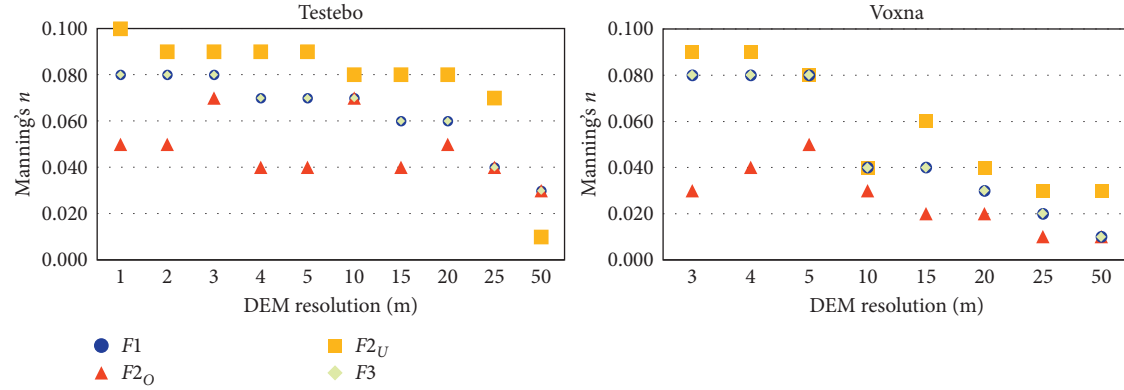


FIGURE 4: DEM and Manning's n combinations that produced the most optimal performances for the different feature agreement statistics.

TABLE 3: Performance scores of most optimal DEM resolutions (with associated roughness in small font) for the Testebo river, together with inundation areas and the percent differences in size from the reference data.

Res. (m)	F1 and F3				F2 _O			F2 _U		
	Max. score F1 F3	Flood area (km ²)	% diff.	Max. score	Flood area (km ²)	% diff.	Max. score	Flood area (km ²)	% diff.	
1	0.668 _{0,080} 0.337 _{0,080}	0.674	17.42	0.468 _{0,050}	0.419	-27.00	0.607 _{0,100}	0.789	37.46	
2	0.669 _{0,080} 0.339 _{0,080}	0.683	18.99	0.467 _{0,050}	0.428	-25.44	0.601 _{0,090}	0.743	29.44	
3	0.667 _{0,080} 0.333 _{0,080}	0.691	20.38	0.465 _{0,070}	0.624	8.71	0.604 _{0,090}	0.752	31.01	
4	0.670 _{0,070} 0.340 _{0,070}	0.635	10.63	0.494 _{0,040}	0.311	-45.82	0.608 _{0,090}	0.760	32.40	
5	0.674 _{0,070} 0.348 _{0,070}	0.639	11.32	0.472 _{0,040}	0.29	-49.48	0.605 _{0,090}	0.762	32.75	
10	0.694 _{0,070} 0.388 _{0,070}	0.512	-10.80	0.590 _{0,070}	0.512	-10.80	0.622 _{0,080}	0.733	27.70	
15	0.697 _{0,060} 0.395 _{0,060}	0.643	12.02	0.525 _{0,040}	0.367	-36.06	0.638 _{0,080}	0.782	36.24	
20	0.715 _{0,060} 0.430 _{0,060}	0.575	0.17	0.616 _{0,050}	0.476	-17.07	0.630 _{0,080}	0.742	29.27	
25	0.721 _{0,040} 0.442 _{0,040}	0.487	-15.16	0.651 _{0,040}	0.487	-15.16	0.645 _{0,070}	0.790	37.63	
50	0.730 _{0,030} 0.460 _{0,030}	0.573	-0.17	0.596 _{0,030}	0.573	-0.17	0.646 _{0,010}	0.574	0.00	

TABLE 4: Performance scores of most optimal DEM resolutions (with associated roughness in small font) for the Voxna river, together with inundation areas and the percent differences in size from the reference data.

Res. (m)	F1 and F3				F2 _O			F2 _U		
	Max. score F1 F3	Flood area (km ²)	% diff.	Max. score	Flood area (km ²)	% diff.	Max. score	Flood area (km ²)	% diff.	
3	0.823 _{0,080} 0.646 _{0,080}	5.410	8.80	0.739 _{0,030}	4.331	-12.91	0.787 _{0,090}	5.585	12.33	
4	0.823 _{0,080} 0.647 _{0,080}	5.457	9.75	0.734 _{0,040}	4.479	-9.92	0.787 _{0,090}	5.605	12.72	
5	0.843 _{0,080} 0.687 _{0,080}	5.303	6.65	0.763 _{0,050}	4.410	-11.31	0.802 _{0,080}	5.303	6.65	
10	0.850 _{0,040} 0.700 _{0,040}	5.241	5.40	0.75 _{0,030}	5.086	2.29	0.807 _{0,040}	5.241	5.40	
15	0.841 _{0,040} 0.682 _{0,040}	5.263	5.84	0.738 _{0,020}	5.051	1.59	0.805 _{0,060}	5.550	11.61	
20	0.843 _{0,030} 0.685 _{0,030}	5.176	4.10	0.744 _{0,020}	5.040	1.35	0.803 _{0,040}	5.339	7.37	
25	0.823 _{0,020} 0.655 _{0,020}	5.300	6.59	0.715 _{0,010}	5.154	3.65	0.790 _{0,030}	5.438	9.36	
50	0.828 _{0,010} 0.657 _{0,010}	5.407	8.73	0.697 _{0,010}	5.407	8.73	0.794 _{0,030}	5.556	11.73	

The size of flooded areas produced by the best models for each resolution and performance measure and the percent difference in areal size in relation to the reference data are further shown in Tables 3 and 4. A percentage equal to 0 means that the size of the inundation area from the simulation is the same as the reference data. Take note that this value does not signify an exact match in extents (overlap) between the model and the reference. A negative value (<0) means that the modelled flood area is smaller than the reference data, while if it is positive (>0), the modelled size is larger. The farther away the value is from 0 means the smaller or larger the under- or overestimation is. Here, the values clearly show that models computed with the highest

$F2_U$ scores have bigger modelled areal size than the reference data, in both study sites, and the other three performance measures (except for the 50 m DEM for the Testebo river). Inundation areas of best models derived from this performance measure for the Testebo river have size differences from the reference data ranging from 27 to 37%. For Voxna, the differences in sizes were smaller (5–12%). In the Testebo river, the 50 m DEM that was paired with $n = 0.010$ produced a size equal to the reference data (0% difference), but it can be seen in Figure 3 that they did not exactly match each other's extents. Results with the highest $F2_O$ have generally smaller inundation areas, especially for the Testebo river. But again, for this river, although the areal size of inundation

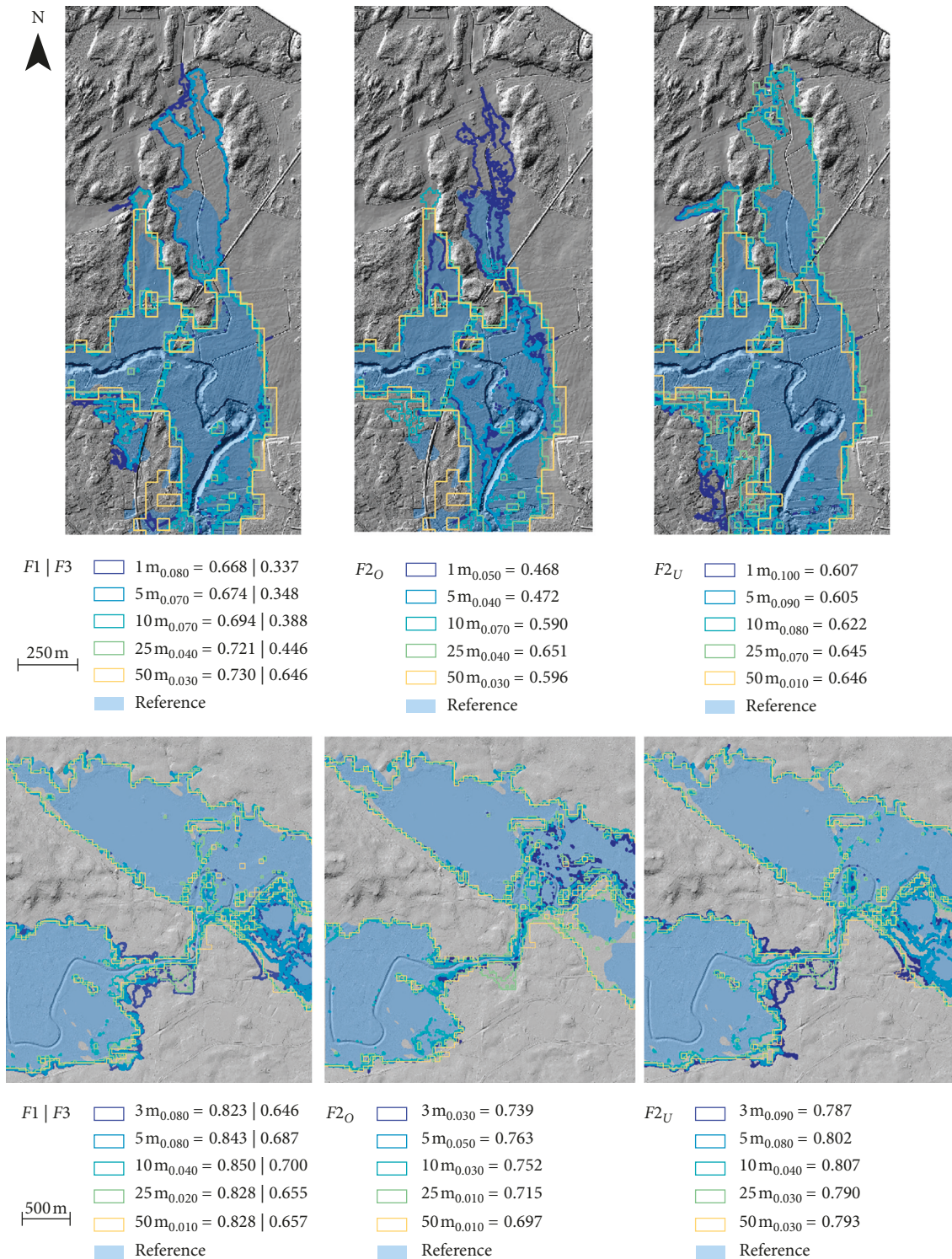


FIGURE 5: Extent comparison of most optimal results produced for each performance measure. $F1$ and $F3$ have the same results although the scores were lower for the latter.

produced from the 50 m DEM was smaller than the actual flood data, the percent difference was very small (-0.17%) compared with the other DEMs. In addition, the most optimal results based on the highest resolution DEMs for this performance measure have smaller inundated areas than

the reference (-25 to -49% difference for the 1, 2, 4, and 5 m for Testebo and -9 to -13% for Voxna). With $F1$ and $F3$, all optimal models produced larger flood extents than the reference data in Voxna, whereas in Testebo, the 10, 25, and 50 m DEMs produced smaller flood areas than the rest of the DEMs.

4.2. Resolution's Effect on Quantified Performance (Eskilstuna River). For the Eskilstuna river, a constant roughness ($n = 0.033$) was used for all DEMs to produce the results. Irrespective of the topographic characteristics of the study area, i.e., steep (north) or flat (south), the highest resolution data (1 m) received the highest performance in all four measures (Figure 6 and Table 5). A distinct trend is also shown that the performance decreased as the resolution became coarser. Among the goodness-of-fit measures, $F1$ showed a more gradual decrease in performance from finer to coarser resolution, while $F3$ manifested a more significant decrease. From the two study areas, it can be noticed that the shift in performance between the highest resolution and the 10 m DEM was more prominent for the northern part of the river (i.e., from 0.93–0.96 down to 0.74–0.87), particularly when $F2_U$ and $F3$ were used.

When looking at the inundation areas produced by the different resolution DEMs (Table 5), 50 m produced the largest flood areas in both sites although there was larger difference in the north (10.55%). Also noticeable is that 3 m data produced the next largest difference after 50 m. Lowest percent difference in areal size was made by 1 m DEM, both in the northern and southern parts of the river. The 25 m also generated smaller percent difference in flooded area than some of the higher resolution DEMs.

When the inundation extents are examined (Figure 7), there were higher degree of overlaps (with the reference) produced by the higher resolution (1–10 m) DEMs. But after these resolutions, the mismatches at the edges became more recognisable, especially when 50 m was used. Over- and underestimations in flooding in some parts of the study areas also became obvious with this resolution.

4.3. Changes in Sizes of Overlap and Over- and Underestimation for the Different Resolution DEMs. All performance measures' equations are based on accounting for the overlap, overestimation, and underestimation sizes produced by the simulation results. If these three will be looked at for each of the results from the different study cases (Figure 8), and for each DEM resolution, it can be seen that the general pattern for the Voxna and Testebo rivers were similar; i.e., there were more overlaps attained when using the lower resolution data and high roughness. Nonetheless, these resolutions also generated more overpredictions (but minimal underpredictions), especially when they were paired with higher roughness values. On the contrary, the sizes of overlaps produced by higher resolution DEMs were generally lower than the coarser resolution DEMs. Furthermore, higher friction coefficients paired with them generated better overlap size, as well as overestimations, while lower frictions produced underestimations. The big shifts in the size of overlap and over- and underestimation from the highest (1 m) to the lowest (50 m) DEMs were most obvious for the Testebo river.

In both the southern and northern parts of Eskilstuna river, the overlap sizes did not vary much among the results from the different digital elevation models, but 1 m got the highest inundation match with the reference data. In

addition, the overlap size decreased as resolution became coarser. The increase in size of overestimation from finest to coarsest DEM was similar to the Testebo and Voxna rivers. Nevertheless, the pattern that followed for the underestimation was opposite the two other study areas; i.e., the coarser resolution DEMs generated more underpredictions for the Eskilstuna river.

4.4. POD, FAR, and BIAS Assessment of All Simulations and Best Model Results. Both Testebo and Voxna rivers had the highest *hit rate* or *probability of detection (POD)* value of 0.98 attained for the 50 and 25 m DEMs, whereas the higher resolution DEMs received lower maximum values (Figure 9). It can also be seen in the graphs that there was more spread in the *POD* values of results that used finer resolution, compared with coarser resolution DEMs (due to the effect of roughness), especially for the Testebo river. Higher overall *POD* scores were computed for Voxna river. The models that used 10 to 50 m data for this study site received higher *POD* values ($POD \geq 0.886$). Eskilstuna showed an opposite trend in the *probability of detection* scores. Unlike the two other rivers, the maximum *POD* value (0.98) was attained in both sites by the 1 m resolution data. It is also shown in the figure that the *POD* decreased as the resolution became coarser.

If the *POD* scores of the most optimal results according to the different *F*-statistics (as marked in Figure 9) will be considered, it can be seen that they varied with the different goodness-of-fit measures. The most optimal results from $F2_O$ had lower *hit rate* compared with the results from $F2_U$ and $F1 | F3$. In the case of Testebo, best models quantified using $F2_U$ received the highest *POD* scores. For Voxna, the *hit rates* of most optimal results based on $F1 | F3$ and $F2_U$ were very close to each other.

False alarm ratio values have inverse performance relationship from *PODs*; the closer the *FAR* value is to 0 (maximum), the better. The pattern manifested in *false alarm ratio* most likely agreed in all three rivers; i.e., they decreased as the resolution became coarser. Simulations that came from the 50 m DEM also received the lowest *FAR* values, specifically for the Testebo river ($FAR = 0.45$). The highest *FAR* scores attained were as follows: Testebo = 0.0198 (10 m), Voxna = 0.037 (5 m), Eskilstuna_{North} = 0.014 (1 and 2 m), and Eskilstuna_{South} = 0.009 (1 m).

Models with the highest performance using $F2_O$ had *FAR* values closer to the maximum. *FAR* values of $F2_U$ results for Testebo river were farther from 0, especially for the 1 m data, while the *FAR* score for the 50 m DEM was closer to 0. In Voxna, *FAR* values of highest performing models quantified through $F2_U$ and $F1 | F3$ were the same. Like Testebo river, the highest resolution DEMs (3 m and 4 m) had lower *FAR* scores, while the rest had values closer to the maximum *FAR* score of 0.

Looking at the *BIAS* scores of the different simulations results, it can be seen how the lower resolution DEMs, mainly the 50 m data, produced results that overestimated the flooding. For Testebo and Voxna rivers, there were more variations in the *BIAS* values of the higher to medium

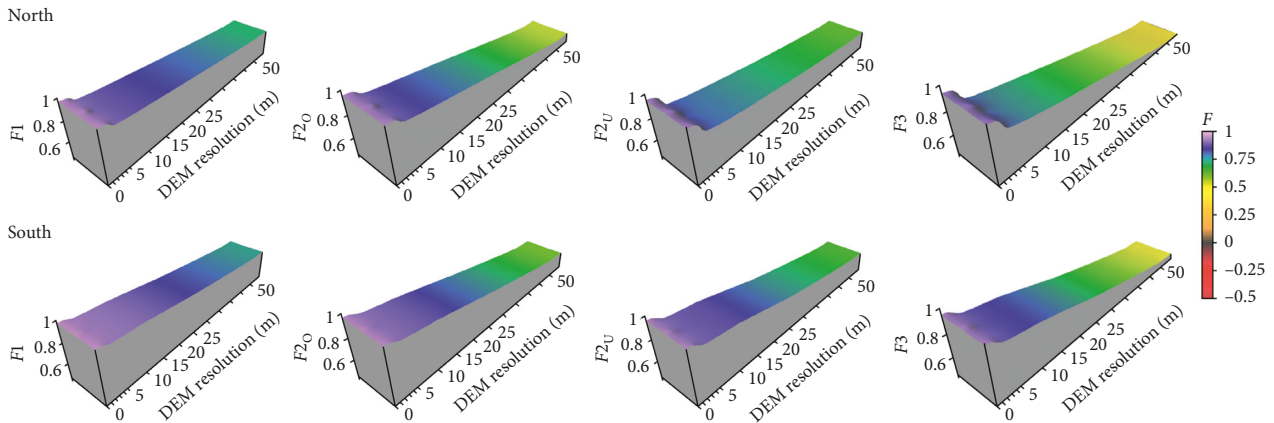


FIGURE 6: Model performances of simulation results using different DEM resolutions for the northern and southern parts of the Eskilstuna river.

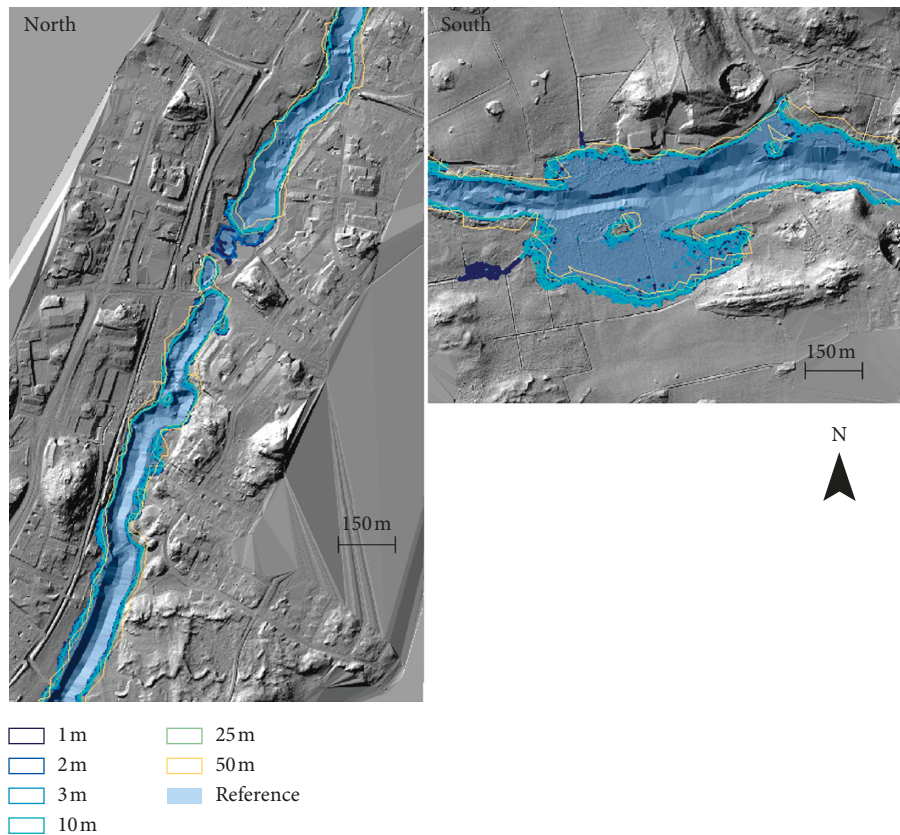


FIGURE 7: Flood extents for the Eskilstuna river using different resolution DEMs.

resolution DEMs. In the former, the results from 1 m to 10 m DEMs produced more results that underestimated the flooding ($BIAS < 1$), while the 25 and 50 m gave more overpredictions ($BIAS > 1$). For the latter, the 10 to 50 m DEM caused overestimations in the model.

The majority of the best model results derived using $F1 | F3$ and $F2_U$ for Testebo and Voxna rivers had $BIAS > 1$, especially for $F2_U$. For the Voxna river, the $BIAS$ scores of the best models from $F1 | F3$ and $F2_U$ for the lower resolution DEMs were closer to 1. With $F2_O$, optimal models

from almost all the resolutions for the Testebo river had $BIAS$ towards underprediction. With Voxna river, the high-resolution DEMs with maximum $F2_O$ values also underpredicted the inundation. From 10 to 50 m, despite the overprediction, the $BIAS$ scores were closer to 1. Computed $BIAS$ scores for the Eskilstuna river were all closer to 1, ranging from 0.946 to 1.106. All DEM resolutions, with the exception of the 50 m data, had values less than 1. The 1 m DEMs had the $BIAS$ score closest to 1 (i.e., 0.99), followed by the 25 m (0.989) DEM, in both sites.

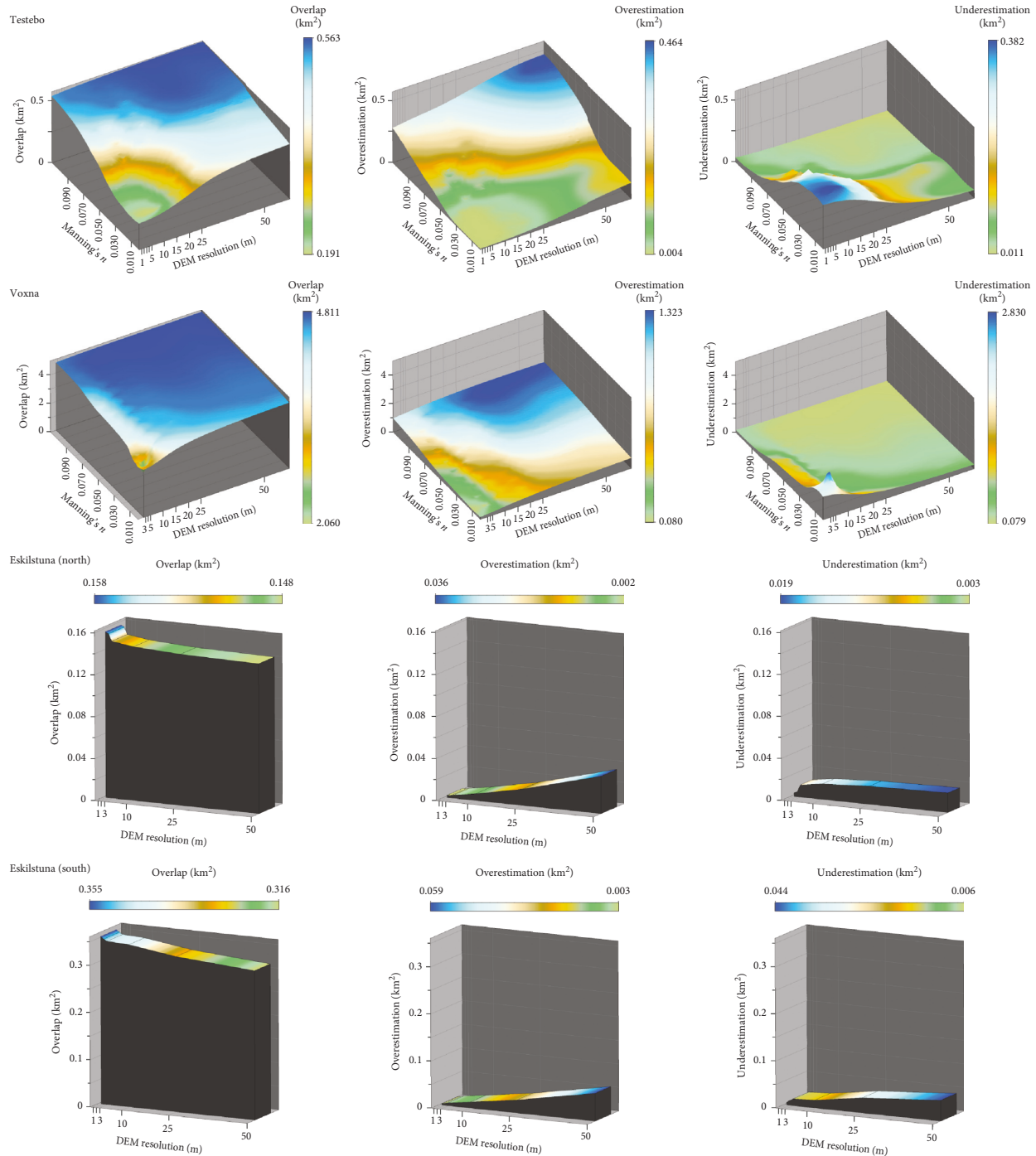


FIGURE 8: Changes in overlap and over- and underestimation sizes in the different study cases.

5. Discussion

If models are calibrated using a combination of DEM and roughness values, the best performing models varied among the feature agreement statistics used, as what was exemplified in the Testebo and Voxna cases. This was because the different equations try to handle the sizes of overlap, overestimation, and underestimation differently in the numerator. Also, as roughness values have impact on the size of the flooding produced (i.e., flood area increases with

increased Manning's n), the friction coefficient paired with a given DEM can affect the scores in a given performance measure, especially with $F2_O$ and $F2_U$. The most optimal models derived for different resolution DEMs using $F2_O$ were paired with lower roughness values (mostly from 0.01 to 0.05) (Figure 4), as they produced smaller inundations. Since the equation tries to penalise the overlap with the overprediction by the model, a lower size of overestimation will give higher performance scores. Contradictory to this was the result using $F2_U$, which tries to suppress the

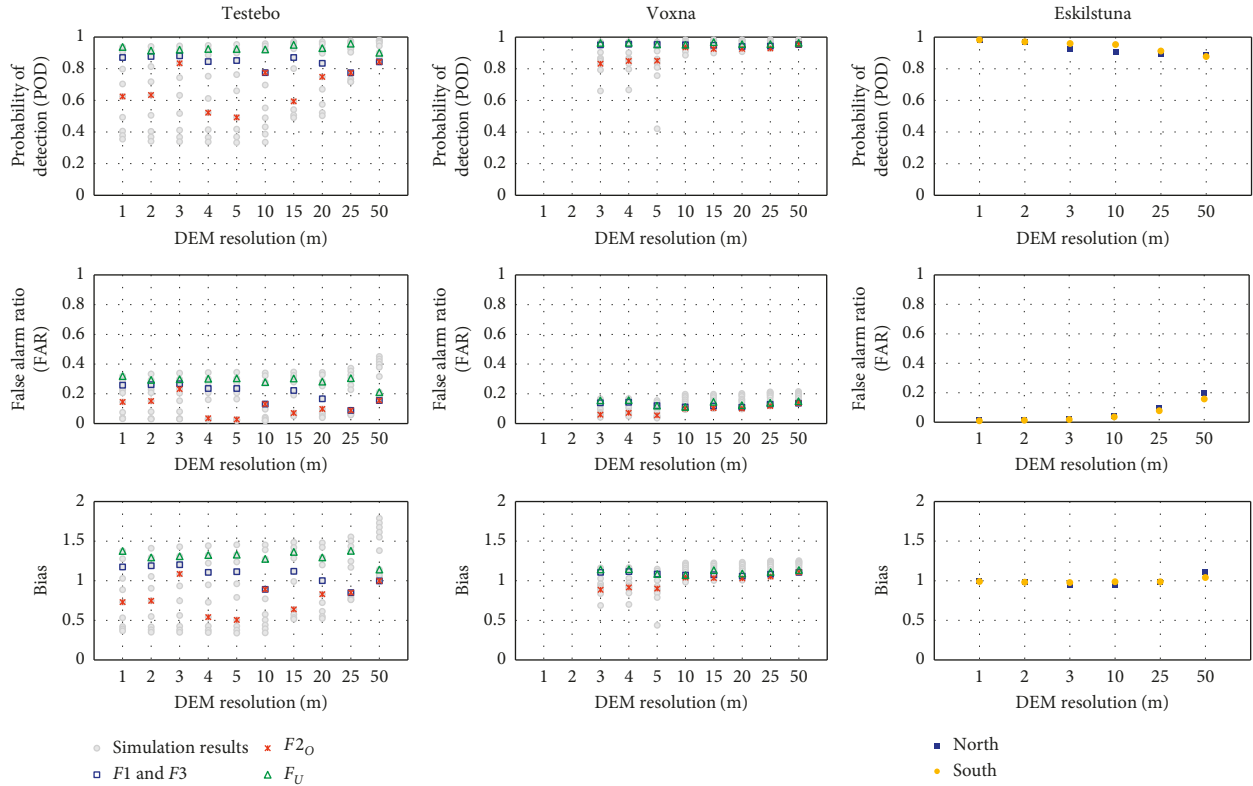


FIGURE 9: POD, FAR, and BIAS scores derived from the results of the three study cases.

underestimation produced in the model. Thus, models with lowest underestimations, i.e., those produced by higher roughness values, received maximum performance using this measure. $F3$, on the contrary, produced the lowest overall performance in all feature agreement statistics although the combinations of best performing models it considered were the same as $F1$. The equation tries to limit the effect of the overlap size to the quantified performance value, which is the problem with $F1$ that was mentioned by Hunter [9]. In the constraint that $F3$ applies in the numerator, it subtracts the overlap with both the sizes of over- and underestimation, balancing the effects of $F2_O$ and $F2_U$. This prevents the model from attaining higher scores, which can help identify better performing models. This also means that if the $F3$ value is high, the model can be considered to be very good. However, the use of $F2_O$ and $F2_U$ may be good to use if the modeller seeks to find minimum or maximum, respectively, probable flood inundation areas.

Furthermore, the roughness value used together with the DEM resolution was important to get higher performance in the case of Testebo and Voxna rivers. As generally seen in the results of the performance scores (Figure 3), higher roughness values worked better with higher resolution DEMs, while lower resolution DEMs performed better with lower Manning’s n . Also clear is that a particular DEM paired with the right Manning’s n can attain high performance values, which was especially true for the coarser resolution DEMs. As shown in Tables 3 and 4, the maximum performance scores received by the lowest resolution DEMs (25 and 50 m) in at least three goodness-of-fit measures ($F1$,

$F2_U$, and $F3$) were higher than the finest resolution DEMs. The overlap size with the reference data produced by them was also the highest (Figure 8). Even the POD scores (Figure 9) were high and yielded the least varied values compared with the other resolution data. But, despite the high quantified performance that they received, the extents generated by them were not better than the higher resolution DEMs in terms of details and their accuracy at the edges (Figures 5 and 7). These resolutions (specifically 50 m) also produced more overestimation of the flooding, lower FAR scores, and gave higher $BIAS$ in overestimation.

Peculiarly, the high performance scores manifested by the low-resolution DEMs for the Testebo and Voxna rivers were opposite to that of the Eskilstuna river, wherein the highest resolution DEMs received the highest performance scores. In addition, a more significant decrease in performance is noticeable for the Eskilstuna test sites as the resolution was decreased. Even when the performance scores for the Testebo and Voxna rivers using different DEMs paired with similar Manning’s n of 0.03, the 1–5 m DEMs received lower performances than the coarsest resolution DEMs. One of the possible explanations can be the reference data used to compare the results to derive the different performance values. For both Testebo and Voxna rivers, historical flood observations were used for extent validation, while for Eskilstuna, the reference data were derived from simulations using the original laser scanned point cloud data of 0.78 m (North) and 0.86 m (South) DEMs, due to the absence of a flood extent from historical flood event. The 1 m DEM gave the highest performance in all F -statistics (from $F = 0.93$ – 0.974 in Table 5)

TABLE 5: Performance scores of results from the Eskilstuna river, based on using different resolution DEMs.

	Resolution (m)	$F1$	$F2_O$	$F2_U$	$F3$	Inundation area (km ²)	% diff.
Eskilstuna north	1	0.965	0.951	0.944	0.930	0.1604	-0.67
	2	0.956	0.943	0.926	0.912	0.1588	-1.69
	3	0.911	0.892	0.839	0.821	0.1528	-5.41
	10	0.874	0.835	0.786	0.747	0.1532	-5.16
	25	0.814	0.726	0.716	0.629	0.1598	-1.09
	50	0.724	0.543	0.630	0.446	0.1786	10.55
Eskilstuna south	1	0.974	0.966	0.958	0.949	0.3578	-0.83
	2	0.959	0.946	0.930	0.917	0.3548	-1.68
	3	0.943	0.926	0.904	0.887	0.3526	-2.30
	10	0.920	0.886	0.875	0.841	0.3567	-1.15
	25	0.847	0.776	0.765	0.694	0.3567	-1.15
	50	0.754	0.613	0.648	0.507	0.3754	4.05

and better details and match in the borders generated (Figure 7) because it was most similar to these two resolutions. The 50 m, on the contrary, was the most dissimilar in extent and performance because of the resolution difference from the reference model. The tendency of getting higher performance for the finest DEM resolution when benchmarking with a better topographic data was similar to the results of Cook and Merwade [5] and Peña and Nardi [6]. As also seen in Table 5, the percent difference in the inundated area between the reference model and the modelled floods became larger (due to the modelled areas getting smaller) as DEM resolution changed from 1 to 3 m. Why the modelled areas became smaller for 3 m than 1 m resolution is unclear to us, but it may have to do with local conditions and where the elevation data points have been sampled. However, with further change in resolution, the percent difference first decreased between 10 and 25 m DEM, followed by an increase for 50 m resolution. The modelled inundated areas are now getting bigger and bigger. The effect is most profound for the Northern area, which has a narrower floodplain. The reason for this behaviour can be attributed to raised bed levels when the DEM cell size is getting closer to or even exceeding the width of the channel. Small depressions that used to be present in the high-resolution DEMs were removed and replaced by higher lying areas, with elevated water levels as a result. With very big cell sizes, the cells would then represent the surrounding terrain, rather than being representative of the river channel. This effect was shown in Lim and Brandt [12] for the Testebo and Voxna rivers. Cook and Merwade [5] and Saksena and Merwade [4] also show in their results that the size of inundation areas become larger when using coarser grid resolution. Hence, from a flood risk perspective, the use of coarse-resolution models may actually increase the chances of being on the “safe” side when the flood map is used for planning purposes.

Maximum scores in all performances (from the entire ensemble of models) for both Testebo and Voxna rivers were also lower than for the Eskilstuna river. This is not surprising as the deviations in result for the Eskilstuna river only depended on the quality of the DEMs. However, besides adding roughness as an influencing parameter, these low scores could also have been influenced by the historical data used for the validation. According to Lim and Brandt [12], the data can have accuracy issues in terms of how they were

generated (e.g., how precise the flood borders were digitised or produced), and their timeliness (i.e., the time difference between the event and generation of topographic data), which can affect getting better inundation matches. Thus, an accurate estimation of performance scores can also be subjective to the observation data, as what is stated in Merwade et al. [24]. Moreover, a perfect or very high match between the modelled and real flood extents can be difficult to achieve because of other factors, which can affect the actual flood extents, that are not taken into account by the model used or in the modelling performed.

The single roughness Manning’s n of 0.033 also worked well for Eskilstuna and Voxna rivers in the four performance estimators although this did not produce the most optimal results for the latter. This was regardless of the hydraulic models used (HEC-RAS 1D for Eskilstuna and 2D CAESAR-LisFlood for Voxna). However, for the Voxna river, performance scores among the different resolution DEMs using this friction had lower variability in the three feature agreement statistics (except for $F2_U$) than the Eskilstuna river. But even when considering the performance results from the ensemble, the quantified performances for the Voxna river were higher and less varied than the two other study areas. For the Testebo river, this roughness led to lower performance for higher resolution DEMs, especially when using $F2_U$ and $F3$. This was for the reason that higher roughness values worked well with these resolutions for Testebo river, while lower resolution DEMs were better with lower roughness values.

The result that the Eskilstuna river’s flat terrain area received better performance measures than the steeper area might at first seem surprising, as the modelled flood borders clearly are at further distance from the reference model in the flat area. Nonetheless, Cook and Merwade [5] also achieved similar results in their study over the flat Brazos river (better performance) and the steeper Strouds creek (lower performance). This can be attributed to the flatter sites’ relatively larger inundated areas in comparison to the fringe that will be either over- or underestimated. But, it is still important to notice that the disparity distances between the modelled and the reference flood edges are always bigger in the flatter areas. This makes it questionable to only rely on the feature statistics treated in this paper. Instead, the

distance disparities described in Brandt [21] and Lim and Brandt [12] should also be considered. These measures will provide better estimates on local flood extent uncertainties, especially where the terrain is flat.

Finally, it is clear from the results that when high-resolution DEMs are used, calibration of the roughness coefficient is of utmost significance. Important to note here that calibrated results from earlier models, as well as standard Manning's n values, are not advisable to be used. Calibration should be done according to the current DEM, study area, model, and model conditions. As what is shown in Figure 4, although the general trend for roughness values and DEM for each performance measure have similarities, the most optimal roughness still differed. These differences in the friction values reflect sampling variation, which is typical for any model parameter. In the case of Testebo and Voxna, the varying roughness values can be ascribed to the differences in their physical characteristics, which affect the flow characteristics in the river. As different study areas are spatially heterogeneous, the friction values will vary from one site to another. In addition, because the DEM provides the topography of the area for the model, its quality in terms of resolution will affect the flow characteristics, which in turn can impact the friction to be used and the flood extent produced. The usage of the 1D or 2D model can also have an effect on the optimal roughness values derived, due to their assumptions in solving the energy loss equation [25] (cf. Horritt and Bates [7]). For the 2D model results (Voxna and Testebo), if the basis of optimality will be $F1 | F3$ for the highest resolution DEMs (1–5 m), the most optimal Manning's n is 0.08 but varied as the resolution decreased. For the Eskilstuna river, the most optimal roughness will be difficult to know as only a single roughness was used. Likewise, the discharge used can also produce varying inundation extents and patterns, as well as lead to different optimal roughnesses [7]. Maximum discharges were used for the different study sites. Although they were roughly of the same magnitude, the flow differed a bit (360 m³/s for Voxna, 160 m³/s for Testebo, and 198 m³/s for Eskilstuna). This can be another reason for the varying friction values. All these factors can affect the modelling results, as what is also shown in earlier studies, and as a result of the equifinality problem [1]. However, since our study focused on the variability of performance measures as effect of the DEM resolution and roughness, our results are centred to the effects of topography in the flood extents and performance measures, rather than the model or the flow used.

From a feature statistics point-of-view, it may seem unnecessary to use high-resolution DEMs, when average resolution DEMs provide similar F -statistics scores, as in the case of Voxna and Testebo rivers. However, as the results from Eskilstuna river show (wherein only the effect of the DEM is considered), feature statistics clearly get better when resolution is increased. The positive effect of resolution in the flood model results when considering both the effects of DEM and roughness became more evident when the disparity distance measures were used, especially for Voxna river. In Lim and Brandt [12], the mean and median disparities for 3 to 5 m were 59.71–63.16 m and 10.75–15.18 m,

respectively. These were clearly better than for the 50 m DEM ($\bar{D}=117.7$ m and $\tilde{D} = 41.17$ m). Nonetheless, the results of the disparity measures are more unclear for the Testebo river.

6. Conclusions

This study has highlighted the implications of using feature statistics in assessing modelled flood inundation areas. Some of the most frequently used feature statistics have been tested on three different rivers, whereof one constituted two different topographies and flat and steep side slopes, respectively. From the results, it is clear how the performance values using the feature statistics varied when going from the most commonly used $F1$ that divides the overlap area of modelled and reference flood with the total combined area of modelled and reference flood, over the $F2_O$ and $F2_U$ that penalises over- and underpredicted areas, respectively, to $F3$ that penalises both over- and underpredicted areas. This suggests that a high $F3$ value, i.e., close to 1, more or less guarantees a high match between modelled and reference flood area. However, even when feature statistics show high values, caution should be taken especially for local or flat areas. Consequently, alternative performance measures, such as disparity distances, may be better substitutes.

The direct relationship between the roughness value and the size of flooding was also shown to affect quantified performance, especially from $F2_O$ and $F2_U$ equations. As the flooded area increases with higher Manning's n , the tendency to overestimate flood becomes higher. Because $F2_O$ penalises the model with overestimation produced, lower roughness values that generate smaller extents and minimal overprediction performed better with this measure. On the contrary, $F2_U$ worked well with higher friction because the equation tries to minimise the underestimation made by the model.

The results also showed that DEMs of poor resolution can receive relatively high performance scores over a wide range of roughnesses. But despite the high scores, there are more spatial inconsistencies in the flood extents produced from low-resolution data. Therefore, assumptions on the goodness of results based on poorer resolution DEMs must be carefully made. Usage of higher resolution DEMs remains advantageous for modelling as they represent the topography of the study area better. As the results from the Eskilstuna river showed, which is only dependent on the quality of the DEM, better resolution has the potential to always bring better results. However, high-resolution DEMs needs to be carefully calibrated through the roughness value, to be able to fully utilise their modelling advantage. If not calibrated properly, the feature agreement statistics will directly show decreased scores.

Performance scores also varied in the different study areas. Regardless of the measure used, Eskilstuna and Voxna rivers received higher overall performances than the Testebo river. These variations in the scores can be caused by several factors such as the modelling assumptions of the model utilised (1D vs. 2D) or the spatial heterogeneities of the study areas, which can both influence the flow being modelled, and

the inundation extents produced. Moreover, the reference data and its quality can also affect the quantified performance.

Data Availability

The data used to support the findings of this study have not been made available because they are the property of Lantmäteriet (the Swedish mapping, cadastral, and land registration authority) and the municipalities of the studied areas.

Disclosure

This research has been carried out as part of the employment at University of Gävle.

Conflicts of Interest

The authors declare that there are no conflicts of interest regarding the publication of this paper.

Acknowledgments

We would like to thank the reviewers for constructive feedback on a previous version of this paper.

References

- [1] K. Beven and J. Freer, "Equifinality, data assimilation, and uncertainty estimation in mechanistic modelling of complex environmental systems using the GLUE methodology," *Journal of Hydrology*, vol. 249, no. 1–4, pp. 11–29, 2001.
- [2] N. J. Lim, *Modelling, Mapping and Visualisation of Flood Inundation Uncertainties*, Ph.D. thesis, University of Gävle, Gävle, Sweden, 2018.
- [3] P. D. Bates and A. P. J. de Roo, "A simple raster-based model for flood inundation simulation," *Journal of Hydrology*, vol. 236, no. 1–2, pp. 54–77, 2000.
- [4] S. Saksena and V. Merwade, "Incorporating the effect of DEM resolution and accuracy for improved flood inundation mapping," *Journal of Hydrology*, vol. 530, pp. 180–194, 2015.
- [5] A. Cook and V. Merwade, "Effect of topographic data, geometric configuration and modeling approach on flood inundation mapping," *Journal of Hydrology*, vol. 377, no. 1–2, pp. 131–142, 2009.
- [6] F. Peña and F. Nardi, "Floodplain terrain analysis for coarse resolution 2D flood modeling," *Hydrology*, vol. 5, no. 4, p. 52, 2018.
- [7] M. S. Horritt and P. D. Bates, "Evaluation of 1D and 2D numerical models for predicting river flood inundation," *Journal of Hydrology*, vol. 268, no. 1–4, pp. 87–99, 2002.
- [8] M. S. Horritt and P. D. Bates, "Predicting floodplain inundation: raster-based modelling versus the finite-element approach," *Hydrological Processes*, vol. 15, no. 5, pp. 825–842, 2001.
- [9] N. Hunter, *Development and Assessment of Dynamic Storage Cell Codes for Flood Inundation Modelling*, Ph.D. thesis, University of Bristol, Bristol, UK, 2005.
- [10] G. Aronica, P. D. Bates, and M. S. Horritt, "Assessing the uncertainty in distributed model predictions using observed binary pattern information within GLUE," *Hydrological Processes*, vol. 16, no. 10, pp. 2001–2016, 2002.
- [11] V. Tayefi, S. N. Lane, R. J. Hardy, and D. Yu, "A comparison of one- and two-dimensional approaches to modelling flood inundation over complex upland floodplains," *Hydrological Processes*, vol. 21, no. 23, pp. 3190–3202, 2007.
- [12] N. J. Lim and S. A. Brandt, "Flood map boundary sensitivity due to combined effects of DEM resolution and roughness in relation to model performance," *Geomatics, Natural Hazards and Risk*, vol. 10, no. 1, pp. 1613–1647, 2019.
- [13] K. J. Beven, *Environmental Modelling: An Uncertain Future*, CRC Press, Boca Raton, FL, USA, 2009.
- [14] A. H. Murphy, "What is a good forecast? An essay on the nature of goodness in weather forecasting," *Weather and Forecasting*, vol. 8, no. 2, pp. 281–293, 1993.
- [15] I. B. Mason, "Binary events," in *Forecast Verification: A Practitioner's Guide In Atmospheric Science*, I. T. Jolliffe and D. B. Stephenson, Eds., pp. 37–76, John Wiley & Sons, West Sussex, UK, 2003.
- [16] J. Schaefer, "The critical success index as an indicator of warning skill," *Weather Forecast*, vol. 5, no. 4, pp. 570–575, 1990.
- [17] N. M. Hunter, P. D. Bates, M. S. Horritt, A. P. J. De Roo, and M. G. F. Werner, "Utility of different data types for calibrating flood inundation models within a GLUE framework," *Hydrology and Earth System Sciences*, vol. 9, no. 4, pp. 412–430, 2005.
- [18] D. C. Mason, P. D. Bates, and J. T. Dall' Amico, "Calibration of uncertain flood inundation models using remotely sensed water levels," *Journal of Hydrology*, vol. 368, no. 1–4, pp. 224–236, 2009.
- [19] D. Klang and K. Klang, "Analys Av Höjdm modeller för Översvämningsmodellering," Unpublished Report for Myn-digheten för samhällsskydd och beredskap and Lantmäteriet, October 2009, <https://docplayer.se/docview/57/39936952.pdf>.
- [20] S. A. Brandt, "Betydelse av höjdmodellers kvalitet vid endimensionell översvämningsmodellering," Högskolan i Gävle, Gävle, Sweden, FoU-Rapport Nr. 35, 2009.
- [21] S. A. Brandt, "Modeling and visualizing uncertainties of flood boundary delineation: algorithm for slope and DEM resolution dependencies of 1D hydraulic models," *Stochastic Environmental Research and Risk Assessment*, vol. 30, no. 6, pp. 1677–1690, 2016.
- [22] T. J. Coulthard, J. C. Neal, P. D. Bates, J. Ramirez, G. A. M. de Almeida, and G. R. Hanrock, "Integrating the LISFLOOD-FP 2D hydrodynamic model with the CAESAR model: implications for modelling landscape evolution," *Earth Surface Processes and Landforms*, vol. 38, no. 15, pp. 1897–1906, 2013.
- [23] US Army Corps of Engineers Hydrologic Engineering Center, *HEC-RAS: River Analysis System. User's Manual (v. 4.0)*, US Army Corps of Engineers Hydrologic Engineering Center, Davis, CA, USA, 2008.
- [24] V. Merwade, F. Olivera, M. Arabi, and S. Edleman, "Uncertainty in flood inundation mapping: current issues and future directions," *Journal of Hydrologic Engineering*, vol. 13, no. 7, pp. 608–620, 2008.
- [25] N. M. Hunter, P. D. Bates, M. S. Horritt, and M. D. Wilson, "Simple spatially-distributed models for predicting flood inundation: a review," *Geomorphology*, vol. 90, no. 3–4, pp. 208–225, 2007.

Research Article

A Meshless WCSPH Boundary Treatment for Open-Channel Flow over Small-Scale Rough Bed

Yang Shi ^{1,2,3}, Jiahua Wei ^{1,3}, Shaowu Li ², Peng Song ² and Bangwen Zhang ^{1,2}

¹State Key Laboratory of Hydro-Science and Engineering, Tsinghua University, Beijing 100084, China

²State Key Laboratory of Hydraulic Engineering Simulation and Safety, Tianjin University, Tianjin 300072, China

³State Key Laboratory of Plateau Ecology and Agriculture, Qinghai University, Xining 810016, China

Correspondence should be addressed to Jiahua Wei; weijiahua@tsinghua.edu.cn

Received 24 April 2019; Revised 17 July 2019; Accepted 25 July 2019; Published 21 August 2019

Academic Editor: Giorgio Besagni

Copyright © 2019 Yang Shi et al. This is an open access article distributed under the Creative Commons Attribution License, which permits unrestricted use, distribution, and reproduction in any medium, provided the original work is properly cited.

A weakly compressible smoothed particle hydrodynamics (WCSPH) method was developed to model open-channel flow over rough bed. An improved boundary treatment is proposed to quantitatively characterize bed roughness based on the ghost boundary particles (GBPs). In this model, the velocities of GBPs are explicitly calculated by using evolutionary polynomial regression with a multiobjective genetic algorithm. The simulation results show that the proposed boundary treatment can well reflect the influence of wall roughness on the vertical flow structure. A fully developed open channel is established, and its flume length, processing time, and turbulent model are discussed. The mixed-length-based subparticle scale (SPS) turbulence model is adopted to simulate uniform flow in open channel, and this model is compared with the Smagorinsky-based one. For the modified WCSPH model, the results show that the calculated vertical velocity and turbulent shear stress distribution are in good agreement with experimental data and fit better than the calculations obtained from the traditional Smagorinsky-based model.

1. Introduction

Computational fluid dynamics (CFD) is widely used in hydraulic engineering simulations with good computational efficiency and accuracy. As an important branch of CFD, meshless methods such as smoothed particle hydrodynamics (SPH) method, moving particle semi-implicit (MPS) method, and discrete element method (DEM) have received wide attention due to their ability to consider large deformations of free interface and multiple interfaces without mesh distortion. The SPH method is a widely used Lagrangian meshless method that was originally developed by Gingold and Monaghan [1] and Lucy [2] to solve astrophysics problems and later used in fluid dynamics applications such as fluid-structure interaction [3–5], underwater explosion [6, 7], local scour [8, 9], other transport phenomena [10], and related applications [11–13]. Despite advances in SPH methodology, the SPH method has not yet been widely adopted for the simulation of open-channel flows in natural rivers and artificial channels. Thus, the focus

of this study was to address the use of SPH for simulation of open-channel flows.

Boundary conditions can directly affect the calculation accuracy and efficiency for the accurate simulation of open-channel flows. However, it is quite challenging to achieve strict boundary conditions in the SPH framework due to the interpolation procedures. Previous studies of numerical simulations of free surface flows mainly focused on boundary treatments of inflow and outflow. A variety of nonreflecting boundary schemes such as open boundary condition [6, 14] and sponge layer [15–17] have been applied in the field of free surface flow to minimize undesirable boundary effects. However, the influence of bed surface roughness on the flow field has not been explicitly stated or well considered in the most open-channel flow simulation [18–22]. In some works, the bottom boundary is roughly treated as slip or no-slip wall [18–20]. López et al. [21] proposed that uneven distribution of Lennard-Jones repulsive force exerting on particles near the solid wall can be considered as numerical resistance caused by roughness,

which may suffer from spurious behavior [23]. Chern and Syamsuri [22] used corrugated solid walls to represent rough bed surface resistance, in which different bed boundaries such as triangle-type, trapezoid-type, and sinusoid-type are characterized by discrete particles. Although these simple approaches are reasonable approximations, the roughness of the bed surface can only be qualitatively expressed in these works, and thus, the effect of the bed roughness on the fluid structure cannot be accurately described.

An additional complication is that open-channel beds in nature have different forms and different scales of roughness, such as fine sand bed, pebble river bed, or vegetation river bed. The bed roughness can exert an important influence on the flow field characteristics, such as average flow rate, time-averaged pressure, Reynolds stress, and turbulent energy. The slip/no-slip treatment on the bottom boundary directly affects the overall accuracy of the simulation results for the open-channel flow. Therefore, the bottom boundary should be carefully described. To the best of our knowledge, there are two major types of approaches to accurately account for the effects of bed roughness on the open-channel flow. One approach is to express the effect of the rough bed on the fluid by adding a source term in the fluid-governing equation [24, 25]. For example, Khayyer and Gotoh [24] investigated the effect of bed friction on a dam-break flow by applying a frictional drag force between a near-bed fluid particle and its neighboring wall particle. However, the proposed drag force is a purely artificial drag force that lacks physical meaning such as bed roughness. Kazemi et al. [25] also proposed a drag-based formulation to account for the large-scale roughness bed surface in depth-limited turbulent open-channel flow. In that work, the thickness of the roughness zone ranged from 0.009 m to 0.011 m, which refers to gravel according to river sediment classification [26]. It is not clear whether this drag force model could be applied to a small-sized rough bed surface, such as silt and sand with particle size that is at least an order of magnitude lower than that of gravel. Another approach to account for the effects of bed roughness on the open-channel flow is to describe the shearing effect of the rough boundary on the ambient flow by indirectly modifying the velocity gradient of the bed particles and ambient fluid particles [27, 28]. Violeau and Issa [27] used the wall function model to reproduce the logarithmic velocity distribution near a solid wall, but the particle disorder can be clearly found near the bed surface (see Figure 9 in their paper). The velocity of ghost particles in the bottom boundary was revised by Fu and Jin [28] to force the vertical velocity distribution of water flow to logarithmic form. The ghost particle velocity is thought to be only related to water depth and roughness height but independent of the slope of the bed surface. Similar to the second approach [27, 28], Barreiro et al. [29] modified the artificial viscosity value for interactions between fluid and bottom to mimic the Manning roughness coefficient of vegetation [26]. However, there is still no universal roughness boundary of free surface flow in the current SPH framework for different flow patterns such as hydraulic smooth flow, hydraulic rough flow, or hydraulic

transition flow. Therefore, a focus of this work is the proposal of a more comprehensive rough bed boundary treatment method for the SPH framework.

In addition to boundary conditions, the turbulence model is equally important in simulating open-channel flows. The turbulence phenomena are quite complex, preventing full resolution through full-proof theory. Existing turbulence models are primarily based on semiempirical assumptions. For example, the Reynolds stress caused by momentum exchange can be related to the average flow field by the eddy viscosity assumption [30]. One of the earliest and commonly used turbulent models in mesh-free method is the subparticle scale (SPS) turbulence model, proposed by Gotoh et al. [31]. The main idea of the SPS turbulence model is to apply a certain filtering function to decompose the instantaneous motion of the turbulent flow into two parts: large-scale vortex and small-scale vortex. Large-scale vortex can be directly solved using the Navier–Stokes (N-S) equation, and small-scale vortex is set by SPS formulation. Subsequently, the SPS turbulence model was adopted to applications such as dam break [32], hydraulic jump [22], and sediment transport [33], although most cases are mainly based on a smooth bed surface. In addition to the spatial average-based SPS model, other turbulence models are based on the Reynolds average of the flow field physical quantities in the time domain, such as the k - ϵ model [23, 34] and the explicit algebraic Reynolds stress model (EARS) [27]. These two models can successfully predict complex free surface with strong distortion and rotation. However, these models [27, 34] do not consider the effect of bed roughness on fluid turbulence, and the near-wall particle distribution is chaotic. Recently, De Padova et al. [35] investigated undular hydraulic jumps over small-scale rough bed for bed roughness of $0.02H$, where H denotes the water depth. The SPH mixing-length turbulence model exhibits satisfactory performance for simulating hydraulic jump as long as strong turbulent rollers are not present and is applicable for open-channel flow simulation [25, 36]. Overall, there have been insufficient studies of the open-channel flow over rough bed using SPH methods. Therefore, the aim of this work was to further investigate rough-bed boundary treatment and the turbulent model and extend this model to simulate open-channel flows in natural rivers and artificial channels with wide hydraulic conditions.

The remainder of this paper is organized as follows: After the introduction, the methodology of the SPH model is presented in detail and an improved bottom boundary treatment is proposed for small-scale rough bed. Next, a numerical open channel is established with a revised turbulence model for open-channel flow in Section 3. In Section 4, turbulent open channel flows over a small-scale rough bed surface are simulated, and the error is analyzed. In Section 5, the conclusions are summarized.

2. Materials and Methods

2.1. SPH Approximation. SPH is a purely Lagrangian method, using a series of particles to discretize the continuum. For the fluid dynamics, the value of field functions

such as mass, density, velocity, and pressure at each discrete particle can be approximated based on the physical properties of surrounding particles:

$$f(r_a) \approx \sum_b f(r_b)W(r_a - r_b, h)\Delta V_b, \quad (1)$$

where the subscripts a and b denote the particles at locations of r_a and r_b , respectively; $f(r_a)$ and $f(r_b)$ denote the field function of the target particle a and its neighboring particle b , respectively; W denotes the kernel function; h denotes the influencing domain of the kernel function or smoothing length; and ΔV_b denotes the volume of particle b . $\Delta V_b = m_b/\rho_b$, where m_b and ρ_b denote the mass and density of particle b , respectively.

A commonly used smoothing kernel is a quintic function, as proposed by Wendland [37], and can be expressed as

$$W(r, h) = \begin{cases} \alpha_D \left(1 - \frac{q}{2}\right) (2q + 1), & 0 \leq q < 2, \\ 0, & q \geq 2, \end{cases} \quad (2)$$

where α_D is taken as $7/4\pi h^2$ for the 2D case and q denotes the dimensionless distance between particles.

2.2. Governing Equations. The Reynolds-averaged Navier-Stokes (RANS) equations can be expressed as

$$\begin{aligned} \frac{d\rho}{dt} &= -\rho \nabla \cdot \mathbf{u}, \\ \frac{d\mathbf{u}}{dt} &= -\frac{1}{\rho} \nabla p + \nu_0 \nabla^2 \mathbf{u} - \frac{1}{\rho} \nabla \cdot (\rho \vec{\tau}) + g, \end{aligned} \quad (3)$$

where ρ denotes the fluid density, \mathbf{u} denotes the velocity vector of fluid, p denotes the fluid pressure, ν_0 denotes the kinetic viscosity, $\vec{\tau}$ denotes the turbulence stress tensor, and g denotes the gravitational acceleration.

In the SPH notation, the governing equations can be rewritten as [38,39]

$$\frac{d\rho_a}{dt} = \sum_b m_b \mathbf{u}_{ab} \cdot \nabla_a W_{ab}, \quad (4)$$

$$\begin{aligned} \frac{d\mathbf{u}_a}{dt} &= -\sum_b m_b \left(\frac{p_b}{\rho_b^2} + \frac{p_a}{\rho_a^2} \right) \nabla_a W_{ab} \\ &+ \sum_b m_b \left(\frac{4\nu_0 r_{ab} \nabla_a W_{ab}}{(\rho_a + \rho_b) |r_{ab}|^2} \right) \nu_{ab} \\ &+ \sum_b m_b \left(\frac{\vec{\tau}_a}{\rho_a^2} + \frac{\vec{\tau}_b}{\rho_b^2} \right) \nabla_a W_{ab} + g_a, \end{aligned} \quad (5)$$

where the subscripts a and b denote the index of the target particle and its neighbor in the support domain, respectively. \mathbf{u}_a , p_a , $\vec{\tau}_a$, and g_a refer to the velocity, pressure, shear stress, and gravity acceleration of particle a , respectively. \mathbf{u}_{ab} and r_{ab} refer to the relative velocity and location between particles a and b and are expressed as $\mathbf{u}_{ab} = \mathbf{u}_a - \mathbf{u}_b$ and

$r_{ab} = r_a - r_b$. The $\nabla_a W_{ab}$ refers to the gradient of smoothing kernel $W(r_a - r_b, h)$ for particles a and b .

To close the governing equations (4) and (5), the sub-particle-scale (SPS) model is adopted to model the turbulence stress tensor with its elements as

$$\frac{\tau_{ij}}{\rho} = \nu_t \left(2S_{ij} - \frac{2}{3} k \delta_{ij} \right) - \frac{2}{3} C_I \Delta l^2 \delta_{ij} |S_{ij}|^2, \quad (6)$$

where subscripts i and j denote the index of spatial coordinates, respectively. ν_t denotes the eddy viscosity coefficient, S_{ij} denotes an element of the SPS strain tensor, $S_{ij} = 1/2 (\partial u_i / \partial x_j + \partial u_j / \partial x_i)$, k denotes the turbulence kinetic energy, $C_I = 0.0066$, Δl denotes particle spacing, and δ_{ij} denotes the Kronecker delta function.

In the original SPS turbulence model, the eddy viscosity coefficient is taken as $\nu_t = (C_s \Delta l)^2 |S|$, where C_s denotes the Smagorinsky constants with a range of 0.1~0.2 and $|S|$ denotes the local strain rate and can be calculated as $|S| = (2S_{ij} S_{ij})^{1/2}$. In this study, the eddy viscosity coefficient is modified with reference to mixed length theory [36] and can be expressed as follows:

$$\nu_t = l_m^2 |S|, \quad (7)$$

$$\frac{l_m}{H} = \kappa \sqrt{1 - \xi} \left[\frac{1}{\xi} + \pi \prod \sin(\pi \zeta) \right]^{-1}, \quad (8)$$

where l_m denotes the mixed length, $|S|$ denotes the local strain rate, κ denotes the von Karman constant, and ζ denotes the vertical relative position and is equal to y/H . \prod denotes the Coles parameter, and when it approaches 0, equation (8) degenerates to

$$l_m = \kappa y \sqrt{1 - \frac{y}{H}}. \quad (9)$$

Following Dalrymple and Rogers [38], the fluid in the SPH formalism is considered weakly compressible with fluid pressure determined via the Tait state equation as follows:

$$p = \frac{c_0^2 \rho_0}{\gamma} \left[\left(\frac{\rho}{\rho_0} \right)^\gamma - 1 \right], \quad (10)$$

where c_0 denotes the speed of sound at the reference density ρ_0 and γ denotes the isentropic expansion factor and is taken as 7 for the case of water. The sound speed should be at least ten times larger than the maximum fluid velocity to restrict density variation to less than 0.01. Fluid pressure is explicitly expressed by the state equation without solving the Poisson equation iteratively, so the problem of poor convergence and low computational efficiency of the linear system can be avoided.

To limit spurious high-frequency noise in the density field, the dissipative term proposed by Molteni and Colagrossi [40] should be included in the right side of equation (4) and can be written as

$$\Lambda = 2\delta h c_0 \sum_b (\rho_b - \rho_a) \frac{r_{ab} \cdot \nabla_a W_{ab}}{r_{ab}^2} \frac{m_b}{\rho_b}, \quad (11)$$

where δ denotes the delta-SPH coefficient and is taken as 0.1. Note that this is a numerical artifact that is used only in SPH notation.

2.3. Boundary Treatment

2.3.1. Inlet and Outlet Conditions. The computing domain is divided into three parts of inflow domain, internal fluid domain, and outflow domain (Figure 1). The inflow and outflow domains are considered part of the buffer layer to apply appropriate boundary conditions to the internal fluid. The width of inflow and outflow domains should be at least as wide as the smoothing radius to guarantee full function of kernel interpolation for fluid particles in the internal fluid region. In this study, the buffer length of the inlet/outlet is taken as two times the smoothing length (or three times the particle diameter), as used in Wang et al. [6] and Tafuni et al. [14]. The particles in the inflow, internal, and outflow domains are called inflow particles, internal fluid particles, and outflow particles, respectively. The inflow and outflow flow particles are treated as fluid particles, as are the internal fluid particles.

The properties of the internal fluid particles are determined by the governing equations, and the properties of the inflow and outflow particles are controlled by the specified boundary conditions. The velocities of particles in the inflow and outflow domains are controlled by a specified flow velocity, which is analogous to the physical pumping process. The density and pressure conditions for the inflow and outflow particles are both determined by the hydrostatic pressure of the free surface flow. Because the velocity and pressure of particles in the buffer layer are forcibly allocated, particle instability and diverging velocity field near the interface between the internal fluid and the buffer layer could arise. Therefore, the flume length should be long enough to avoid undesirable boundary effects and to reduce any overconstrained issues in inflow and outflow regions.

Similar to the periodic boundary condition proposed by Gomez-Gesteira et al. [41], the outflow particles that pass through the end of the outflow region will immediately flow into the computational domain from the front of the inflow region (Figure 1). Unlike most open boundary treatments like Verbrugge et al. [42], there are no particle additions and deletions within the calculation domain, so the total number of particles remains the same and mass conservation of fluid is implicitly satisfied. The particle positions are adjusted according to the periodic boundary, and the particle properties such as velocity, density, and pressure in the buffer layer of the inlet and outlet are artificially specified. Thus, it is not necessary to extend the support domain of outflow particles into the inlet domain.

2.3.2. Free Surface Condition. No special attention is paid to the particles at the free surface because the continuous density method (equation (4)) is adopted to solve particle density. The kinematic condition is intrinsically satisfied at the free surface by the Lagrangian solver. In the simulation of open-channel flows over a small-scale rough bed, when

the flow in the water flume tends to stabilize, the water elevation in the streamline direction is almost constant.

2.3.3. Bottom Boundary Condition. Open-channel water flow is always affected by fluid resistance and energy dissipation, especially for rough bed. The roughness of the bed surface significantly influences the formation and development of the water flow structure, i.e., the vertical flow velocity distribution. To quantitatively describe the bed surface roughness, equivalent roughness is generally introduced, also known as Nikuradse's equivalent roughness [43]. The flow state can be divided into hydraulic smooth flow, hydraulic rough flow, and hydraulic transition flow according to the bed surface roughness. For a hydraulic smooth flow ($R_e^* = u^*k_s/\nu_0 < 5$, where R_e^* denotes friction Reynolds number, u^* is the friction current velocity, k_s is the equivalent roughness, and ν_0 is the kinematic viscosity), the bed surface roughness height is smaller than the adhesive bottom layer thickness, the coarse elements are submerged in the viscous bottom layer, and the bulk flow does not perceive bed roughness. For this condition, the flow velocity distribution in the logarithmic zone and the outer zone is not affected by the bed surface roughness but is affected by the viscosity of the fluid. With regard to hydraulic rough flow ($R_e^* > 70$), the bed surface roughness height is much greater than the viscous bottom layer thickness. The flow velocity distribution in the logarithmic zone and the outer zone is affected by the roughness of the bed surface but is not affected by the viscosity of the fluid. For hydraulic transition flow, the roughness of the bed surface is equivalent to the thickness of the viscous bottom layer, and the flow velocity distribution can be affected by both surface roughness and fluid viscosity.

The treatment of bed surface roughness in the SPH method has always been a complex issue. If the governing equations of equations (1) and (2) are solved using a direct numerical simulation (DNS) method, the solid boundary and the nearby turbulence field can be directly resolved in the computational mesh. However, DNS methods are computationally intensive and thus are not usable for most engineering problems. Therefore, a generalized wall function model is proposed to simulate turbulent open-channel flow over the small-scale rough bed surface. The wall function in the particle method is similar to that in the grid method, but this function does not directly modify the velocity of the first layer of the near-wall mesh. In the present study, the velocity of the solid-wall boundary particle is modified to create a velocity gradient with the ambient fluid particles. Based on the equivalent roughness of the bed surface, the bottom shear stress of the near-wall fluid particle is corrected by adjusting the virtual velocity of the solid-walled particle, thereby modifying the flow velocity profile according to the following expression:

$$u^{**} = \frac{1}{\kappa} \ln\left(\frac{y^* + \Delta y^*}{\zeta^*}\right) + B, \quad (12)$$

where u^{**} denotes the dimensionless current velocity ($u^{**} = u/u^*$), y^* denotes the dimensionless vertical distance

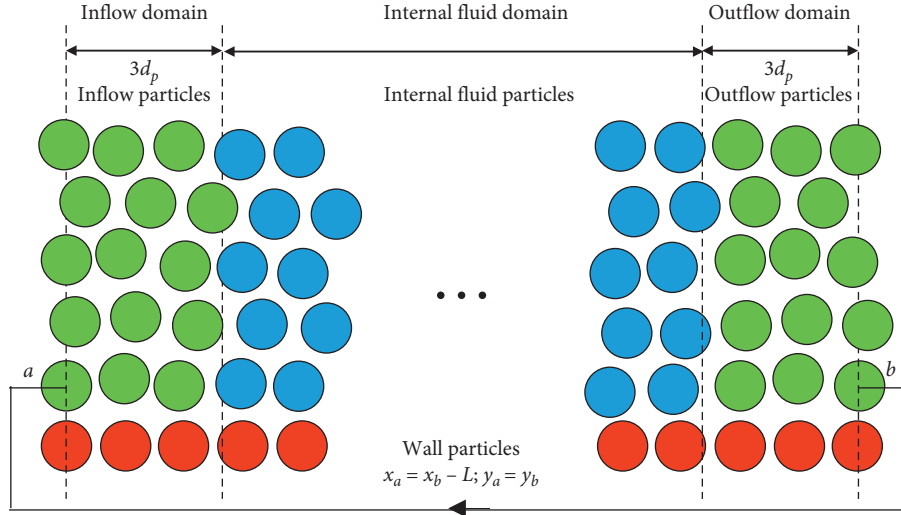


FIGURE 1: Schematic diagram of inlet and outlet conditions.

$(y^* = yu^*/v_0)$, and κ denotes the von Karman constant and is equal to 0.41. Δy^* denotes the dimensionless distance between the top of the rough element and the reference bed surface, where the logarithmic curve zero is located. ζ^* denotes the dimensionless vertical distance offset of velocity log profile (Figure 2). B denotes the logarithmic integration constant and can be written as

$$B = \begin{cases} 5.5 + 2.5 \ln R_e^*, & R_e^* < 5, \\ 8.5 + (2.5 \ln R_e^* - 3) \exp[-0.121 (\ln 2.42 R_e^*)], & 5 \leq R_e^* \leq 70, \\ 8.5, & R_e^* > 70, \end{cases} \quad (13)$$

where R_e^* denotes the friction Reynolds number.

For the hydraulic smooth flow and the hydraulic transition flow, the wall function method can be adopted. For the hydraulic rough flow, the rough scale should be evaluated, and the small-scale rough bed can be adopted. The scale of roughness in the SPH method is a relative concept, where small-scale rough is if $\Delta y^* < d_p$, and large-scale rough is if $\Delta y^* > d_p$, where Δy^* is equal to $0.25k_s$ [44]. The wall function method is only applicable to small-scale roughness because the horizontal current velocity in the Δy^* range does not meet the log-profile distribution. The shear stress can be correctly transferred to the fluid in the log rate region only if the distance between the inner water particles and the side wall is greater than the thickness of the bottom boundary layer (Figure 2).

The ghost particle velocity of the bottom boundary must be determined by trial calculation. When the numerical result of the cross-sectional velocity distribution is closest to the theoretical flow velocity distribution, the ghost particle velocity corresponds to the equivalent roughness.

2.4. Solution Algorithm. A two-stage predictor-corrector algorithm is used for the numerical integration scheme in this study [45], with the fluid properties of particle a , i.e., velocity (\mathbf{u}_a), position (r_a), and density (ρ_a) initially predicted at the half time step $n + 1/2$, and can be written as

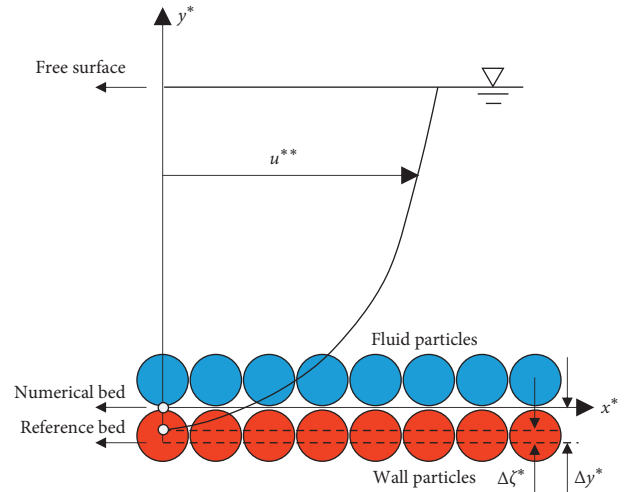


FIGURE 2: Schematic diagram of the bottom boundary condition.

$$\begin{aligned} \mathbf{u}_a^{n+1/2} &= \mathbf{u}_a^n + \frac{\Delta t}{2} \left(\frac{d\mathbf{u}_a^{n+(1/2)}}{dt} \right), \\ r_a^{n+1/2} &= r_a^n + \frac{\Delta t}{2} \left(\frac{dr_a^{n+(1/2)}}{dt} \right), \\ \rho_a^{n+1/2} &= \rho_a^n + \frac{\Delta t}{2} \left(\frac{d\rho_a^{n+(1/2)}}{dt} \right), \end{aligned} \quad (14)$$

and corrected at the time step $n + 1$ with the following expressions:

$$\begin{aligned} \mathbf{u}_a^{n+1} &= \mathbf{u}_a^n + \Delta t \left(\frac{d\mathbf{u}_a^{n+(1/2)}}{dt} \right), \\ r_a^{n+1} &= r_a^n + \Delta t \left(\frac{dr_a^{n+(1/2)}}{dt} \right), \\ \rho_a^{n+1} &= \rho_a^n + \Delta t \left(\frac{d\rho_a^{n+(1/2)}}{dt} \right). \end{aligned} \quad (15)$$

As suggested by Monaghan and Kos [46], the time step is then adjusted according to the Courant–Friedrichs–Lewy (CFL) condition, and the forcing terms and the viscous diffusion term can be written as

$$\Delta t = \text{CFL} \min \left(\min_a \left(\frac{h}{|f_a/m_a|} \right), \min_a \left(\sqrt{\frac{h}{c_a + \max_b |h \mathbf{u}_{ab} \cdot r_{ab}/r_{ab}^2|}} \right) \right), \quad (16)$$

where CFL denotes the Courant–Friedrichs–Lewy number and f_a/m_a denotes the fluid force per unit mass exerted on particle a .

3. Simulation of Open-Channel Flows

3.1. Model Setup and Verification. To validate the proposed model, a case with water depth $H=0.05$ m, bed slope $s=0.002$, and bed roughness $k_s=0.01$ m was tested. The bed roughness of the open channel was calculated in accordance with Section 2.3, with the velocity of ghost particles in bottom boundary being determined by trial calculation and taken as -0.025 m/s. The height of the model calculation domain is equal to the water depth, and the length is 100 times the water depth (Figure 3). The initial particle spacing values (d_p) were set as 0.002 m, 0.003 m, or 0.004 m. For the case with particle spacing of 0.002 m, the whole computational domain is modeled by using 3753 solid particles and 31275 water particles. A computer with an octa-core Intel® Core™ i7-6700 processor (clock speed of 3.40 GHz and 16.0 GB RAM) was used to carry out the simulation. The simulated time of 8 s costs nearly 8.8 h of CPU time.

In the test scenario, the numerical sensors were evenly arranged in the middle section to monitor the sectional water level process (Figure 3). The wave gauges WG1–4 were positioned in the streamline direction at $x=50H$, $x=60H$, $x=70H$, and $x=80H$, respectively. The water surface is considered stable as long as the error between the sensor value and the target water level is less than 2%. As described in Section 2.3, inflow and outflow particles in the buffer layer were assigned hydrostatic pressure and specific flow velocity. The specific flow velocity was obtained by trial calculation based on the following principle. When the water levels determined by the four sensors are consistent with the target water level (Figure 3), the flow velocity for the particles in the buffer layer is considered reasonable. The water surface can be stabilized when the specific current velocity in the buffer layer is equal to 0.312 m/s. The maximum error between the sensor value of water elevation and the target value is 0.08% (Table 1).

Figure 4 presents the simulated velocity and pressure fields for the model including the wall function. The instantaneous flow field is captured at the moment of 6 s. The results show that fully developed uniform flow is obtained at the middle of water flume without numerical noise.

3.2. Optimization of the Calculation Domain. The fluid boundary layer and open-channel turbulence can be fully developed under a sufficiently long computational domain in the streamline direction. However, it is necessary to minimize the length of the computing domain due to limited computing resources. The suitable flume length must be determined by trial calculation and is initially taken as up to 100 times the water depth. The length of the front, middle, and rear sections of the numerical water flume is taken as 50, 20, and 30 times the water depth, respectively (Figure 3). The development of the open-channel flow directly depends on the flow distance. Figure 5 presents the simulated results of current velocity versus the variation of flow distance for measuring points located at different water depths. Due to speed constraints in the inflow and outflow regions, the upstream uniform velocity fluid gradually stratifies until the velocity profile along the water depth becomes consistent with the logarithmic one. The downstream fluid is also affected by the outflow region, and the average flow velocity of this fluid will converge to 0.312 m/s. For a particle size of 0.002 m, the current velocity of the upper fluid with $y=H$ increases with increasing flow distance and tends to stabilize to 0.36 m/s at $x \approx 35H$. However, the fluids in the lower layer show different trends. For example, at $y=1/5H$, the current velocity gradually decreases to 0.25 m/s at $x \approx 25H$ as flow distance increases due to the friction from the bottom boundary. In Figure 5(b), it can be seen that the profile of the flow velocity along the water depth converges to a stable value until the flow distance reaches 40 times the water depth. The flow velocity constraint in the outflow region will nonphysically affect the flow field structure. At a distance of about $5H$ from the end of the water flume, the flow velocity of each monitoring section significantly changes to 0.312 m/s. The results show little effect of particle size on the influence range of the inflow and outflow boundaries (Figure 5(a)). The velocity development range of inflow particles and the influence range of the outlet boundary are about $40H$ and $10H$, respectively, for different particle sizes. This indicates that the fully developed flow field structure including the flow velocity profile can be achieved with a flume length of $50H$. Thus, to reduce computing resources, the computing domain is taken as 50 times the water depth in the following study.

3.3. Optimization of Time-Average Operation. The development of open-channel flow requires a certain amount of time, and the simulation time is directly related to the boundary and initial conditions. Therefore, for a specific model, it is crucial to determine the appropriate simulation time. Figure 6 presents the evolution process of the streamline component of current velocity at the position of $x=40H$. The flow velocities at different water depths are developed from an initial value of 0.312 m/s towards stable values so that the vertical velocity distribution is in accordance with logarithm law. In general, a large particle spacing corresponds to a shorter flow time or convergence time (Figure 6(a)). For fine particle spacing of 0.002 m, the current velocities at all depths become stable after a flow time of 6 s. The flow time required for the fluid near the free surface to reach a steady velocity is larger than that close to

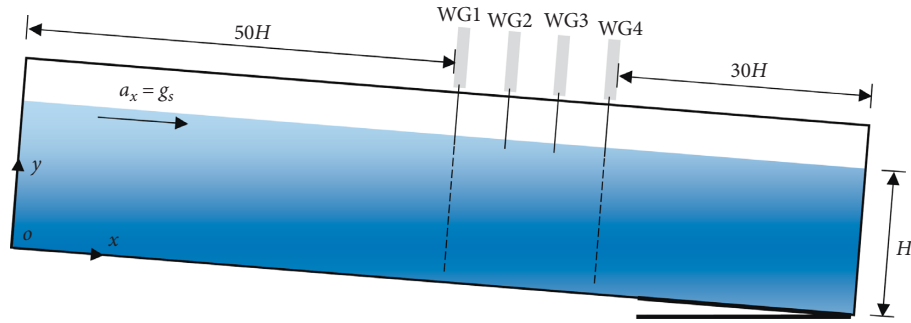


FIGURE 3: Schematic diagram of numerical water flume, where x and y denote coordinates in the streamline and vertical direction, respectively, with “o” as the origin. H denotes the water depth and s denotes the bed slope.

TABLE 1: Numerical water elevation for a specific current velocity of 0.312 m/s.

Gauge number, G_n (-)	WG1	WG2	WG3	WG4
Water elevation, H_{wg} (m)	0.05004	0.05002	0.04997	0.05003

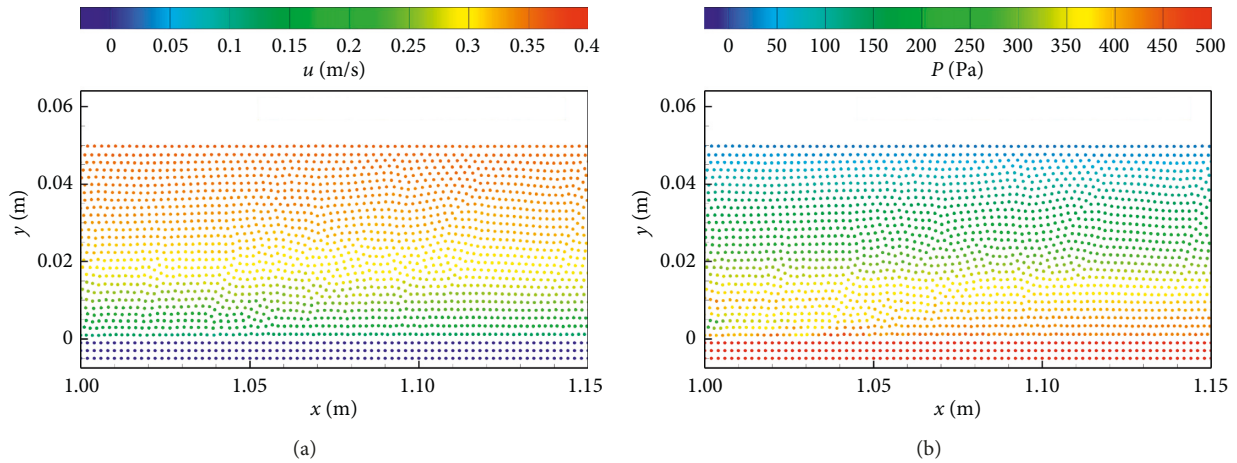


FIGURE 4: Instantaneous velocity (a) and pressure (b) fields for the model including the wall function.

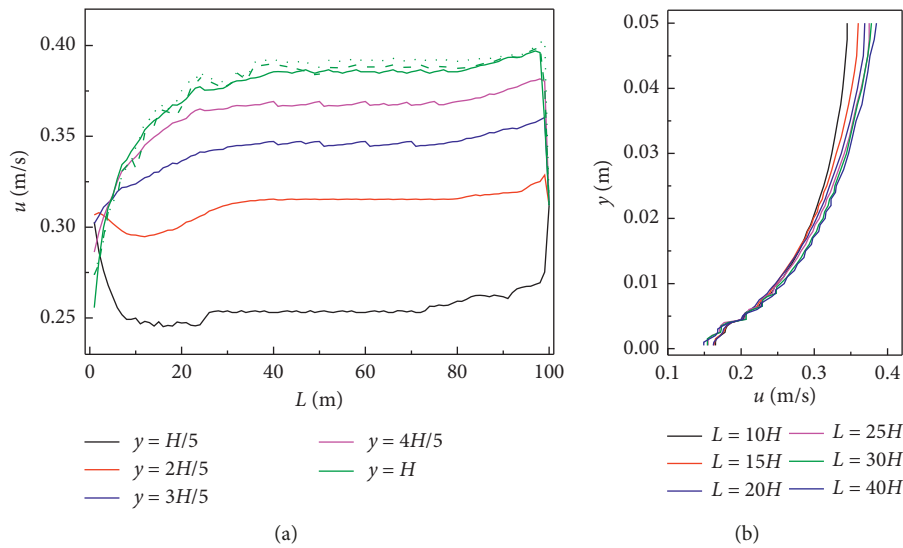


FIGURE 5: Simulated results of current velocity u versus the flow distance L in the streamline direction of water flume for measuring points at different water depths (a) and its evolution process (b). The solid line represents particle spacing of 0.002 m, the dashed line represents particle spacing of 0.003 m, and the dotted line represents particle spacing of 0.004 m.

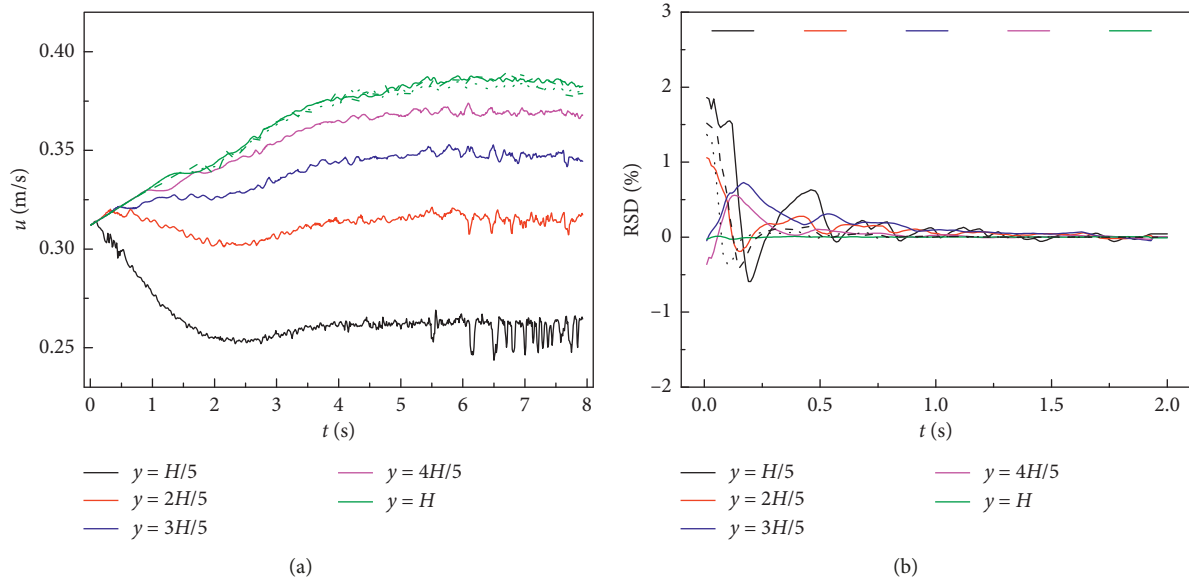


FIGURE 6: Numerical current velocity in the streamline direction u (a) and its relative standard deviation value RSD (b) versus flow time t for measuring points at different water depths. The solid line represents particle spacing of 0.002 m, the dashed line represents particle spacing of 0.003 m, and the dotted line represents particle spacing of 0.004 m.

the flume bottom, indicating that the boundary layer is developing upward from the flume bottom.

Since fluid turbulence can cause spatiotemporal fluctuation in fluid parameters such as current velocity and water pressure, especially for fluid near the flume bottom, time and space averaging are required to reduce the oscillation of flow parameters. The particle approximation process (equation (1)) in the SPH method is essentially spatial interpolation [6], where the physical quantities of a target particle are obtained from its neighbor particles in the supporting domain. A time-average operation is adopted to update the physical quantities of the boundary particles. To determine the time interval of the time-average operation, it is necessary to carry out time convergence analysis of the main flow rate at different depths. Figure 6(b) presents the relative standard deviation (RSD) values of the current velocities in the streamline direction for measuring points at different water depths. The RSD values of coarse particles ($d_p = 0.004$ m) are relatively smaller than those of finer ones, and the convergence time is relatively shorter for coarser particles. For cases with different particle spacings, the flow velocities at all depths can reach convergence within 1.75 s~2 s, with an RSD value in the range of $\pm 0.5\%$. Except for the current velocity near the bottom wall, current velocities at other water depths can be considered to converge by 1 s.

The average current velocities under four other flow conditions were analyzed in the same way, with case I ($H = 0.05$ m, $s = 0.001$, $k_s = 0.00005$ m), case II ($H = 0.08$ m, $s = 0.001$, $k_s = 0.01$ m), case III ($H = 0.08$ m, $s = 0.002$, $k_s = 0.002$ m), and case IV ($H = 0.1$ m, $s = 0.001$, $k_s = 0.01$ m), where H denotes water depth, s denotes bed slope, and k_s denotes equivalent roughness. The simulation results show that the average main flow velocities under the four flow conditions with different water depths, bed slopes, and particle spacings can be stabilized after 6 s (Figure 7(a)) and

that the time interval used for time averaging is less than 2 s (Figure 7(b)). Therefore, in this analysis, the processing time of 2 s was adopted to average fluid quantities.

3.4. Smagorinsky-Based and Mixed-Length-Based SPS Model. The original SPS model [31], known as the Smagorinsky-based SPS turbulence model, has been successfully applied to some coastal applications such as fluid-structure interaction [4, 47, 48]. However, the performance of this model to simulate open-channel flow is not satisfactory. Figure 8 shows the comparison of current velocity and turbulent shear stress with changing water depth for the Smagorinsky-based SPS turbulence model with different Smagorinsky constants (C_s). None of the simulated results were consistent with the theoretical result. This is likely because the tested C_s values are suitable for non-constant flow problems and should be revised for a case of constant uniform flow.

For cases with C_s value being of similar magnitude, the velocity profiles for different C_s values are almost the same (Figure 8(a)). The value of C_s affects the current velocity distribution of the open-channel flow if the C_s value has a different order of magnitude. In general, the larger the C_s value, the greater the numerical error, with overestimation of current velocity near the water surface and underestimation near the channel bottom (Figure 8(b)). The C_s value also has a significant influence on the fluid shear stress. A larger C_s value corresponds to larger fluid shear stress (Figure 8(c)), but even the largest shear stress obtained in the Smagorinsky-based model is less than the theoretical value (Figures 8(d)–8(f)).

The $C_s \Delta t$ value shows a certain degree of influence on the flow field distribution of the open-channel flow. Figure 9

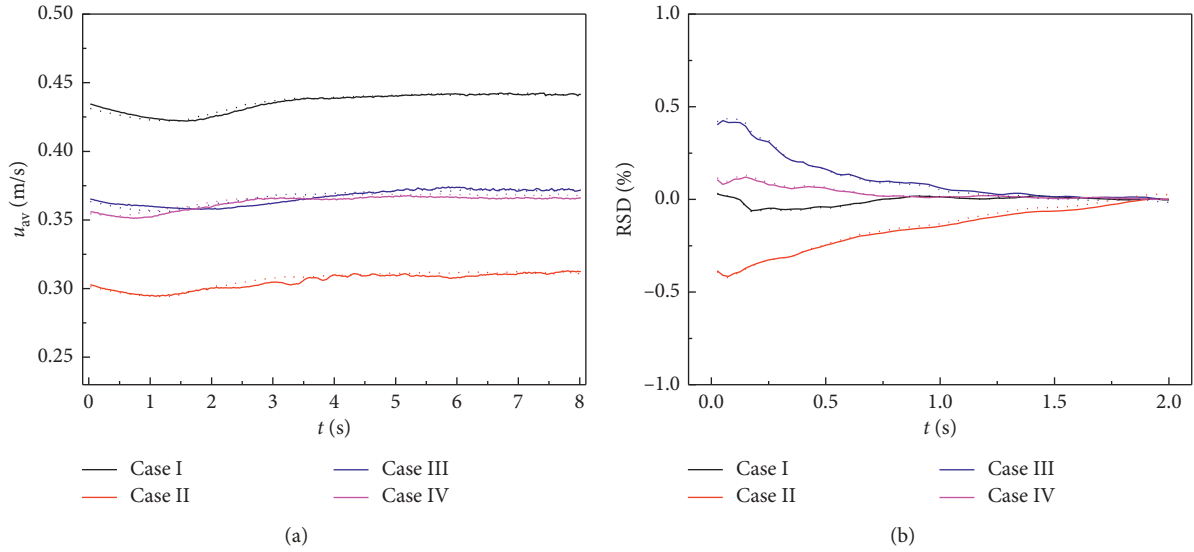


FIGURE 7: Averaged current velocity u_{av} (a) and its relative standard deviation value RSD (b) over time for different water flow conditions. The solid line represents particle spacing of 0.002 m, and the dotted line represents particle spacing of 0.004 m.

shows the effect of particle spacing on the current velocity and shear stress for the Smagorinsky-based SPS turbulence model. A more uniform velocity profile can be obtained by using a relatively larger $C_s\Delta l$ value (Figure 9(a)). The shear stress increases with increasing $C_s\Delta l$ (Figure 9(b)), while even the largest value is still lower than the theoretical shear stress. The low turbulent shear stress obtained by the Smagorinsky-based turbulence model is attributed to the loss of the turbulent stress by spatial filtering during the long-term development of the water flow. In this model, the particle spacing has almost no effect on the flow velocity at free surface due to the loss of the surface shear force.

Mayrhofer et al. [49] simulated open-channel flow using a Smagorinsky-based eddy viscosity model and found that the resolution of the particle-based method needed to be at least 16 times higher than that of the grid-based method in order to correctly redistribute the energy between the Reynolds stress components in the SPH-LES frame. This indicates that the open-channel flow cannot be well resolved if the resolution size is not sufficiently dense. For the Smagorinsky-based turbulence model, it is difficult to reconcile the simulated velocity profile with the theoretical value by adjusting particle resolution for this particle scale.

To obtain a reasonable shear force, some researchers have tried to modify the original SPS model based on other perspectives. For example, Gotoh et al. [48] modified the Smagorinsky-based model in the near-wall region. The original turbulence eddy viscosity $\nu_t = (C_s\Delta l)^2 S$ was modified to $\nu_t = [\min(C_s\Delta l, \kappa d_{wall})]^2 S$, where C_s denotes the Smagorinsky constant, Δl denotes the particle spacing, κ denotes the von Karman constant, d_{wall} denotes the minimum distance of particles from the wall, and S denotes the local strain rate. The treatment proposed by Gotoh et al. [48] is quite similar to the simplified mixed length formula proposed by Nezu et al. [50]. In this study, a mixed-length-based

SPS model (equation (7)) is adopted to simulate the open-channel flow. As shown in Figure 10, the turbulent shear stress is obviously improved by using the SPS model based on mixed length. The vertical distribution of the mixed length and Reynolds stress obtained by numerical simulation are quite similar to the theoretical values. Since this method allows determination of the correct turbulent shear stress, the vertical velocity profile can be well matched with the theoretical curve.

4. General Boundary Treatment for Rough Bed Surface

In Section 3, the improved wall function model and turbulence model in the WCSPH framework are successfully employed to represent the open-channel flow over a rough bed with a roughness height of 0.001. To apply the wall function model to various types of rough bed, a general boundary treatment for a rough bed surface is proposed in this section.

4.1. Investigation of Bed Surface with Wide Roughness. To investigate open-channel flow with wide bed roughness, a series of numerical cases were designed with reference to the actual size of river sediment particles [26] (Table 2). The values of equivalent roughness were selected as 0.00005 m, 0.001 m, 0.002 m, and 0.01 m; the values of the water depth are 0.05 m, 0.08 m, and 0.1 m; the values of bed slope are 0.001, 0.002, and 0.004; and the values of particle spacing are 0.002 m, 0.003 m, and 0.004 m. As described in Section 2.3, bed surface roughness is achieved by exerting proper wall shear stress on the bottom boundary. The shear stress can be correctly transferred to the fluid only if the first layer of fluid particles near the lower wall is in the log rate region of open-channel flow. This means that the particle spacing should be

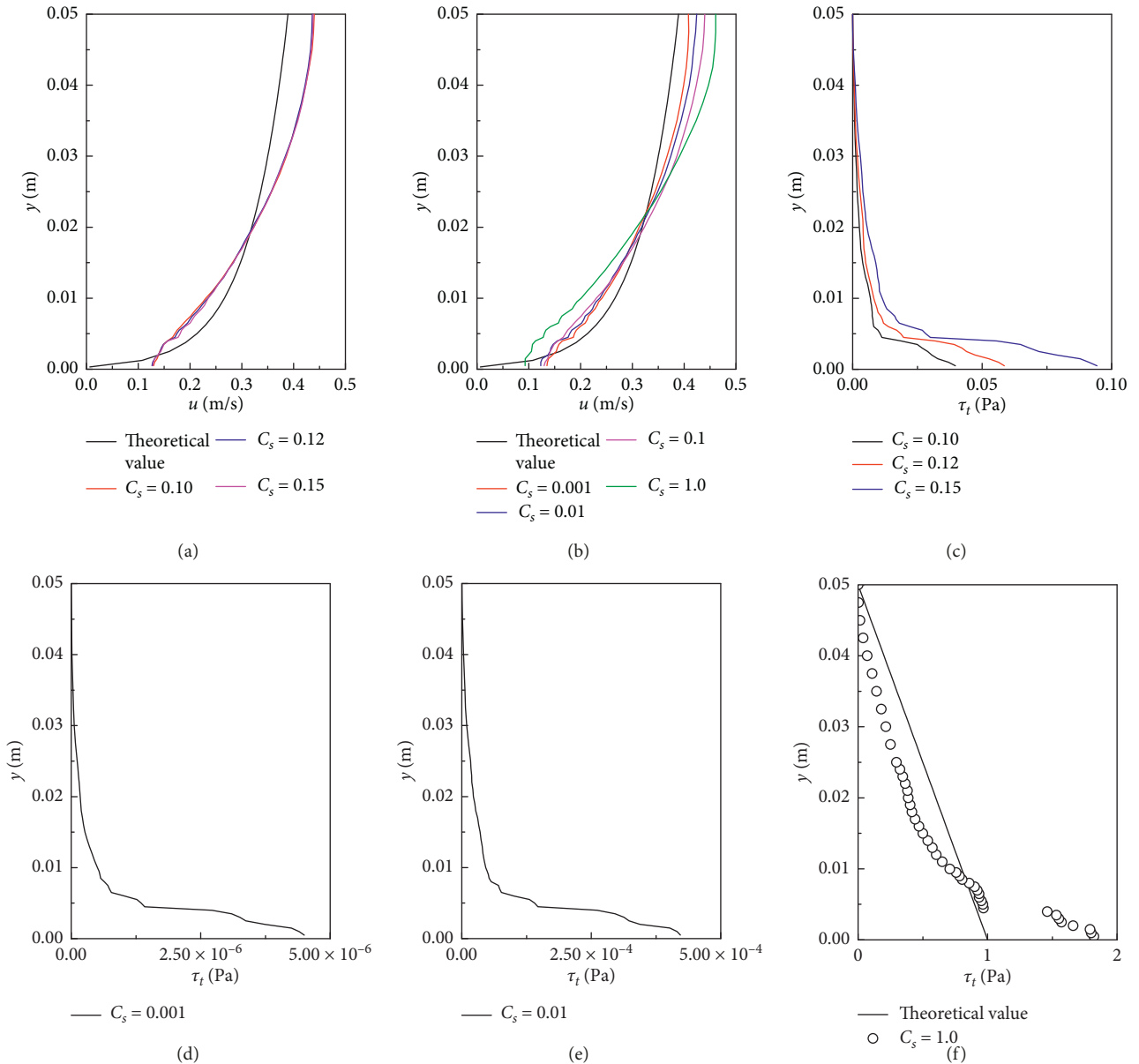


FIGURE 8: Comparison of current velocity and turbulent shear stress with water depth under different Smagorinsky constants. (a) Velocity profile for different C_s in the same order, (b) velocity profile for different C_s not in the same order, (c) turbulent shear stress profile for different C_s in the same order, (d) turbulent shear stress profile for $C_s = 0.001$, (e) turbulent shear stress profile for $C_s = 0.01$, and (f) turbulent shear stress profile for $C_s = 1.0$.

larger than the dimensionless distance between the top of the rough element and the reference bed surface, or $\Delta y^* > d_p$, where Δy^* equal to $0.25k_s$.

The numerical cases were divided into hydraulic smooth flow, hydraulic rough flow, and hydraulic transition flow based on calculation of the friction Reynolds number. Here, a total of 159 sets of cases were performed. Among them, 51 sets made up the hydraulic smooth flow experimental group, 39 sets made up the hydraulic transition flow experimental group, and 69 sets made up the hydraulic rough flow experimental group (see Supplemental data (available here)). The test case is named according to the water depth, slope, equivalent roughness, and particle spacing. For example, for

the case mentioned in Section 3.1 ($H = 0.05$ m, $s = 0.002$, $k_s = 0.01$ m, $d_p = 0.002$ m), the test case name is H50s2ks10(2).

The distribution of current velocity in the entire vertical section should be consistent with that of the theoretical curve by specifying the appropriate ghost particle velocity, so the ghost particle velocity can be matched with flow condition and bed surface roughness. Figure 11 presents the simulated results of the dimensionless velocity distribution for the model with wall function. Satisfactory results were obtained regardless of the flow regime. However, there was a significant deviation at the free surface and near the bottom surface, especially for the near-bottom area. The deviation at the free surface is mainly due to the absence of Coles' wake

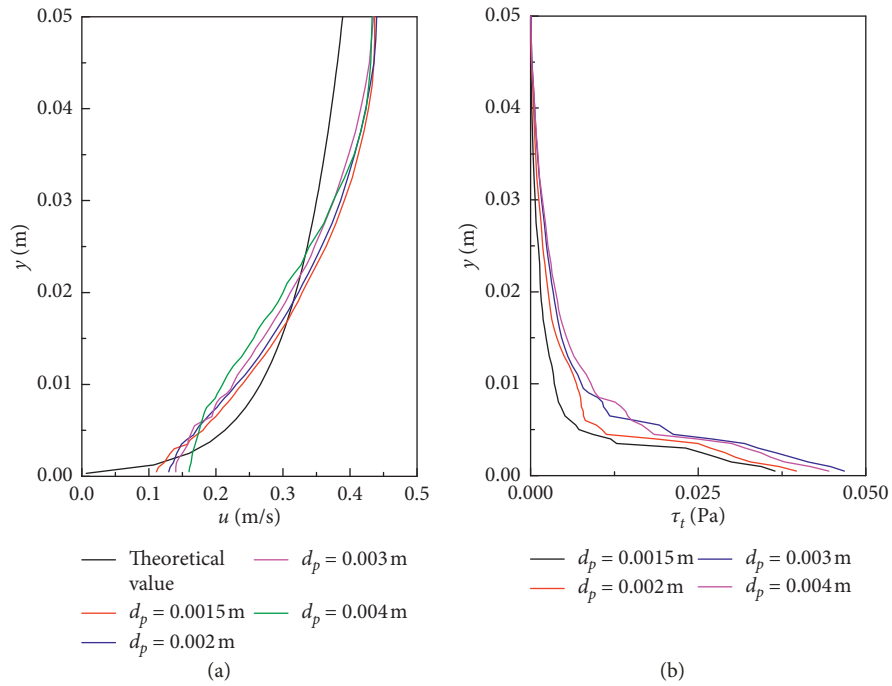


FIGURE 9: Effect of particle spacing on current velocity (a) and shear stress (b) for the Smagorinsky-based SPS turbulence model.

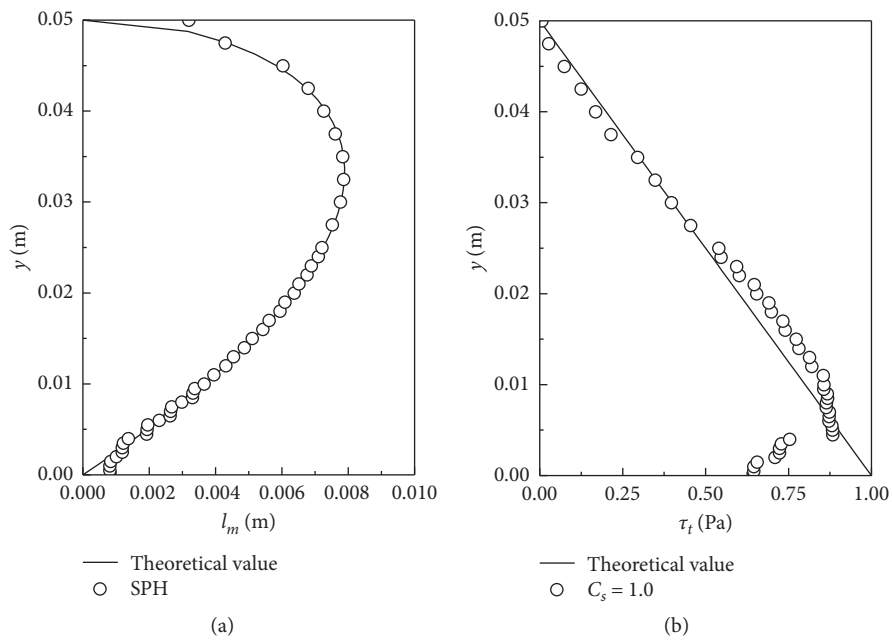


FIGURE 10: Continued.

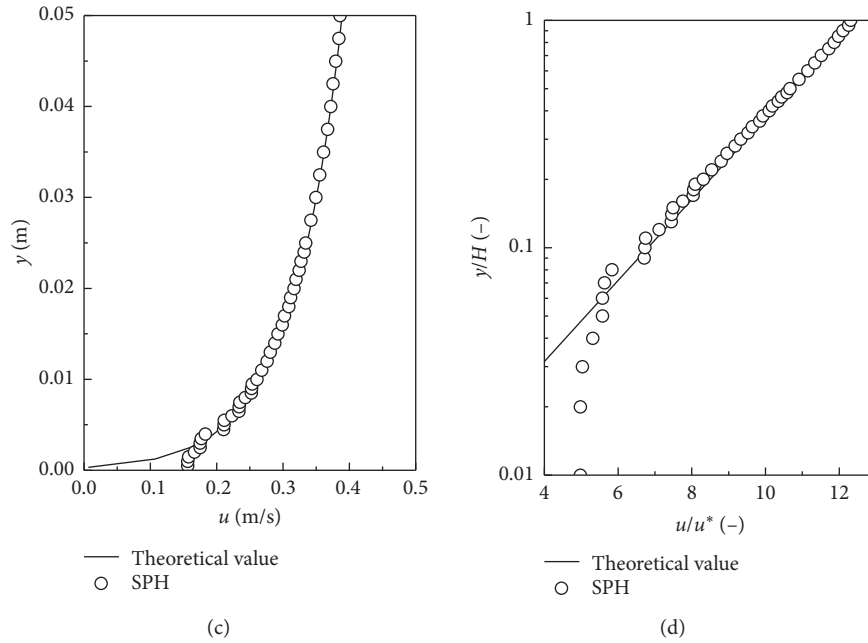


FIGURE 10: Simulated results of mixed length (a), shear stress (b), current velocity (c), and dimensionless current velocity (d) for the mixed-length-based SPH turbulence model.

TABLE 2: River sediment classification (cosmid and boulder sizes were not considered in this simulation).

Type	Cosmid	Silt	Sand	Gravel	Cobble	Boulder
Size ($\times 10^{-3}$ m)	<0.004	0.004~0.062	0.062~2.0	2.0~16.0	16.0~250.0	>250.0

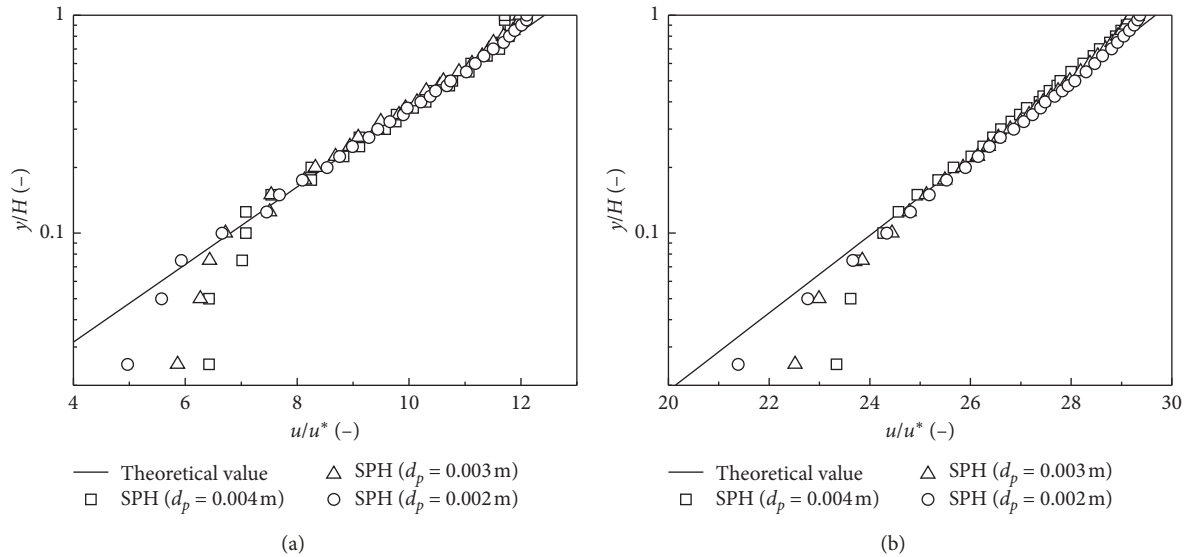


FIGURE 11: Simulated results of the dimensionless velocity distribution for the model with the wall function method. (a) H50s001ks1 and (b) H100s004ks005.

function [51]. However, the apparent deviation near the bottom is the inevitable result of using a meshless method with the wall function model. The wall function itself cannot resolve particle velocity inside the transition zone and the

viscous bottom layer, only improving the flow velocity distribution in and/or outside the logarithmic region. In addition, since the computational domain is composed of particles, the shear stress of the fluid must be transmitted

through interactions between particles. It is necessary to exert reasonable force on the internal fluid particles through the ghost particles. However, strictly speaking, the shear force is exerted at the positions of the upper fluid particles yet not directly on the upper fluid particle itself, making the external force subject to the particle size.

Figure 12 shows the effect of particle spacing on the wall function method. The particle spacings shown in Figure 12 are d_{p1} , d_{p2} , and d_{p3} , respectively, where $d_{p1} < d_{p2} < d_{p3}$. The shear stress required by the bottom fluid particles for each case is equal to the theoretical shear stress corresponding to the height of the fluid particle. That is, the smaller the particle size, the larger the required shear stress of the fluid and the smaller the required ghost particle velocity.

We next performed an error analysis of the velocity distribution of all the test cases (Figure 13). The average relative error (MRE) describes the error of the WCSPH model coupled with the wall function method. In the vertical direction, the fluid region can be roughly divided into three layers, the inner zone ($y/h < 0.2$), the main zone ($0.2 \leq y/h \leq 0.8$), and the near-surface zone ($y/h > 0.8$). There is only a small relative average error in the mainstream and near-surface regions, roughly below 2%, while the relative average error in the inner region varies widely, mainly due to the influence of particle size. As shown in Figure 13, common laws can be obtained from the error distribution of typical cases with different water flow conditions: (i) the error in the mainstream area is generally smaller than that in the inner area; (ii) the error in the mainstream area and the near-surface area is hardly affected by the test conditions but significantly affected by the test conditions in the inner area; (iii) for the case with the same particle size, the deeper the water depth, the smaller the data error in the inner zone; (iv) the error is positively correlated with bed roughness, especially for hydraulic rough flow; and (v) the bed slope has almost no effect on the error of the inner zone for hydraulic smooth flow, but the error in the inner zone increases with the increase of the channel slope for hydraulic rough flow.

According to the above findings, the bed slope and the equivalent roughness are positively correlated determinants of the numerical error. Obviously, for the same hydraulic condition, the result will be more accurate for smaller particle spacing, but more computing resources will be needed.

4.2. Explicit Rough Wall Treatment. From the analysis presented above, a reasonable current velocity distribution can be obtained by adjusting the velocity of the ghost particles on the bed surface. However, this method would be cumbersome if it was necessary to determine the ghost particle velocity every time by trial and error. Therefore, it is necessary to establish relationships between ghost particle velocity and case condition such as bed slope, bed surface roughness, water depth, and particle resolution.

As a powerful data-mining method, the evolutionary polynomial regression with multiobjective genetic algorithm

(MOGA-EPR) technique is widely used to construct non-linear polynomial expression [52, 53]. It is interesting that the variable relationship and structure parameters of polynomial expression do not need to be identified in prior, making this approach especially suitable to solve multi-objective value optimization problems with unclear relationship structure.

Based on the simulation results presented in Section 4.1, a total of 159 sets of training data including hydraulic smooth flow, hydraulic rough flow, and hydraulic transition flow were used to determine the ghost particle velocity, essential to exert reasonable turbulence shear stress in open-channel flow. In this study, six potential dimensionless candidate variables were selected in terms of relative water depth ($h_{dp} = H/d_p$), relative bed surface roughness ($k_{sdp} = k_s/d_p$), channel bed slope (s), roughness scale ($h_{ks} = H/k_s$), dimensionless water depth ($h^* = Hu^*/v_0$), dimensionless particle resolution ($d_p^* = d_p u^*/v_0$), and dimensionless bed surface roughness ($k_s^* = k_s u^*/v_0$). The nonnegative least-squares method was adopted for global regression, with logarithmic function as the interfunction of the Pareto front [54]. The maximum number of terms of the Pareto sets was taken as 4. Three empirical formulae were derived from the EPR-MOGA in terms of hydraulic smooth flow, hydraulic rough flow, and hydraulic transition flow and were written as

$$u_g^* = 92609500.83 \frac{s^2}{h_{dp} h_{ks}^{0.5}} \ln \left(\frac{k_s^{*0.5}}{h_{dp}^{0.5}} \right) + 1.53 \ln \left(\frac{d_p^{*1.5} k_s^{*1.5}}{h_{dp}^{0.5}} \right) + 0.00056s^2 h^{*2} k_s^{*2} \ln(k_s^{*0.5}) + 3.37, \quad R_e^* < 5, \quad (17)$$

$$u_g^* = 0.033 \frac{d_p^*}{h_{ks}^{0.5}} \ln \left(\frac{1}{k_{sdp}^2} \right) + 0.014s^{0.5} h^* d_p^* + 2.76, \quad 5 \leq R_e^* \leq 70, \quad (18)$$

$$u_g^* = 1.5 \ln \left(\frac{d_p^{*2}}{k_{sdp}^{0.5}} \right) + 7.9s^{1.5} k_s^{*2} + 1779.5s^2 k_s^{*1.5} \cdot \ln(s^{0.5} k_s^{*0.5}), \quad R_e^* > 70, \quad (19)$$

where u_g^* , h_{dp} , k_{sdp} , h_{ks} , d_p^* , and k_s^* denote the dimensionless ghost particle velocity ($u_g^* = u_g/u^*$), the relative water depth, relative bed surface roughness, dimensionless water depth, dimensionless particle resolution, and dimensionless bed surface roughness, respectively.

From Table 3, it can be seen that (i) numerical boundary condition is indeed related to particle resolution as described in Section 4.1; (ii) returned equations have satisfactory accuracy and also conform to physical insights. For example, the velocity of the ghost particle on the bed surface is positively correlated with bed slope and dimensionless particle resolution (see Figure 12 for detail); and (iii) some potential information can be inferred from the empirical formula. For example, the ghost particle velocity is almost irrelevant to the relative water depth.

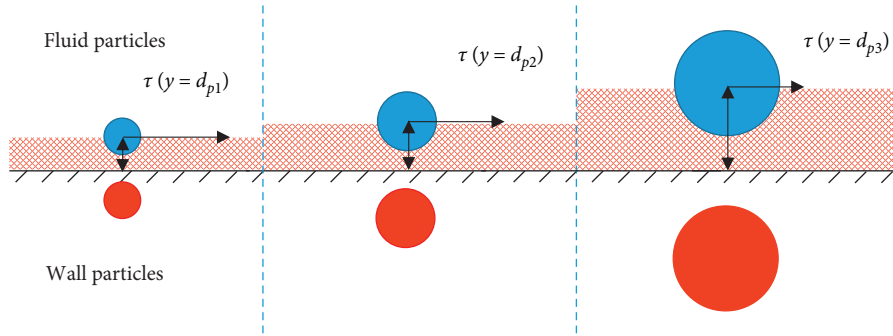


FIGURE 12: Effect of particle spacing on the wall function method.

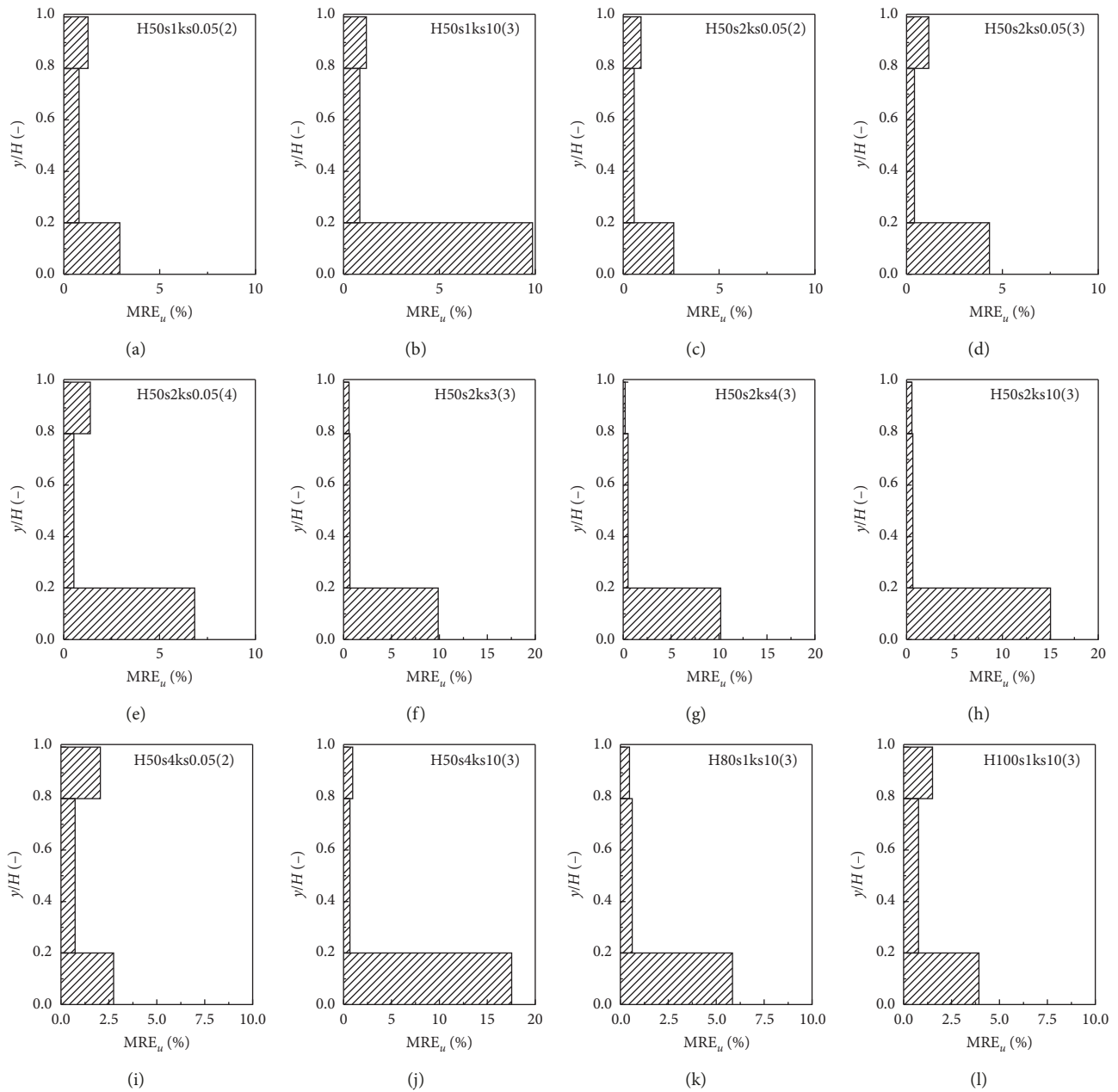


FIGURE 13: Error analysis of the wall function model for hydraulic smooth flows a, c, d, e, and i and hydraulic rough flows b, f, g, h, j, k, and l.

TABLE 3: Statistical value of empirical formulae from EPR-MOGA.

Formulae	Candidate variables							Complexity		Accuracy	
	h_{dp}	$k_{s,dp}$	s	h_{ks}	h^*	d_p^*	k_s^*	X_i	A_j	SSE	CoD
Equation (17)	—	—	+	—	+	+	+	6	4	0.34	0.88
Equation (18)	—	—	+	—	+	+	—	6	2	1.03	0.77
Equation (19)	—	—	+	—	—	+	+	4	3	0.28	0.86

X_i and A_j denote the number of independent variables and term number, respectively. SSE and CoD denote the sum of squared errors and determining coefficient, respectively. The symbols +, —, and / denote positive correlation, negative correlation, and no-correlation between the dependent variable and the independent variables, respectively.

5. Conclusions

In this study, an in-depth study on the simulation of the open-channel flow over roughness bed based on WCSPH was performed. Through the numerical test, the influence of bed surface roughness on the flow structure was clarified. Numerical tests showed that the Smagorinsky-based SPS turbulence model performs poorly near the rough bed surface in the open-channel flow, showing deviation of the vertical velocity and turbulent shear stress distribution from the theoretical values, but the improved mixed-length-based SPS turbulence model achieved satisfactory fluid structure.

Based on the principle of the wall function model in the grid method, an improved meshless wall function was developed for small-scale rough boundary and the sensitivity of this method was determined and error analysis was performed. There was relatively small numerical error in the mainstream and near-surface regions, but the error varied widely for the inner region. This error is positively correlated with the channel bed slope and the equivalent roughness. In addition, for the convenience of model application, empirical formulae are proposed to calculate the ghost particle velocity under different hydraulic conditions using data mining. The proposed rough bed model is expected to be useful for open-channel turbulence simulation.

Data Availability

The training data of the multiobjective genetic algorithm used to support the findings of this study are included within the supplementary information file.

Conflicts of Interest

The authors declare that there are no conflicts of interest regarding the publication of this paper.

Acknowledgments

The improved WCSPH code used in this paper was developed from the open source SPHysics code developed by Prof. M. Gomez-Gesteira at University of Vigo, Prof. R.A. Dalrymple at Johns Hopkins University, and others. This research was supported by the National Key Research and Development Project (grant nos. 2017YFC0403600 and 2016YFE0201900), the State Key Laboratory of Hydro-Science and Engineering, Tsinghua University, Beijing, China (grant no. 2017-ky-04); and the China Postdoctoral Science Foundation (grant no. 2018M641372).

Supplementary Materials

Supplemental test results including average currently in inflow and outflow regions, friction velocity, Reynolds number, Froude number, friction Reynolds number, and the velocity of ghost particle in the wall function model can be accessed from the online version of the paper. Totally, 159 sets of training data in terms of hydraulic smooth flow, hydraulic rough flow, and hydraulic transition flow are open-sourced for a potential researcher. (*Supplementary Materials*)

References

- [1] R. A. Gingold and J. J. Monaghan, "Smoothed particle hydrodynamics: theory and application to non-spherical stars," *Monthly Notices of the Royal Astronomical Society*, vol. 181, no. 3, pp. 375–389, 1977.
- [2] L. B. Lucy, "A numerical approach to the testing of the fission hypothesis," *The Astronomical Journal*, vol. 82, pp. 1013–1024, 1977.
- [3] B. Ren, M. He, Y. Li, and P. Dong, "Application of smoothed particle hydrodynamics for modeling the wave-moored floating breakwater interaction," *Applied Ocean Research*, vol. 67, pp. 277–290, 2017.
- [4] B. Ren, H. Wen, P. Dong, and Y. Wang, "Numerical simulation of wave interaction with porous structures using an improved smoothed particle hydrodynamic method," *Coastal Engineering*, vol. 88, no. 2, pp. 88–100, 2014.
- [5] A.-M. Zhang, P.-N. Sun, F.-R. Ming, and A. Colagrossi, "Smoothed particle hydrodynamics and its applications in fluid-structure interactions," *Journal of Hydrodynamics*, vol. 29, no. 2, pp. 187–216, 2017.
- [6] P. Wang, A.-M. Zhang, F. Ming, P. Sun, and H. Cheng, "A novel non-reflecting boundary condition for fluid dynamics solved by smoothed particle hydrodynamics," *Journal of Fluid Mechanics*, vol. 860, pp. 81–114, 2018.
- [7] F. R. Ming, A. M. Zhang, Y. Z. Xue, and S. P. Wang, "Damage characteristics of ship structures subjected to shockwaves of underwater contact explosions," *Ocean Engineering*, vol. 117, pp. 359–382, 2016.
- [8] D. Wang, S. Li, T. Arikawa, and H. Gen, "ISPH simulation of scour behind seawall due to continuous tsunami overflow," *Coastal Engineering Journal*, vol. 58, no. 3, Article ID 1650014, 2016.
- [9] D. Wang, S. Shao, S. Li, Y. Shi, T. Arikawa, and H. Zhang, "3D ISPH erosion model for flow passing a vertical cylinder," *Journal of Fluids and Structures*, vol. 78, pp. 374–399, 2018.
- [10] Y. Shi, S. Li, H. Chen, M. He, and S. Shao, "Improved SPH simulation of spilled oil contained by flexible floating boom

- under wave-current coupling condition,” *Journal of Fluids and Structures*, vol. 76, pp. 272–300, 2018.
- [11] H. Gotoh and A. Khayyer, “On the state-of-the-art of particle methods for coastal and ocean engineering,” *Coastal Engineering Journal*, vol. 60, no. 1, pp. 79–103, 2018.
- [12] D. Violeau and B. D. Rogers, “Smoothed particle hydrodynamics (SPH) for free-surface flows: past, present and future,” *Journal of Hydraulic Research*, vol. 54, no. 1, pp. 1–26, 2016.
- [13] M. S. Shadloo, G. Oger, and D. Le Touzé, “Smoothed particle hydrodynamics method for fluid flows, towards industrial applications: motivations, current state, and challenges,” *Computers & Fluids*, vol. 136, pp. 11–34, 2016.
- [14] A. Tafuni, J. M. Domínguez, R. Vacondio, and A. J. C. Crespo, “A versatile algorithm for the treatment of open boundary conditions in smoothed particle hydrodynamics GPU models,” *Computer Methods in Applied Mechanics and Engineering*, vol. 342, pp. 604–624, 2018.
- [15] C. Altomare, J. M. Domínguez, A. J. C. Crespo et al., “Long-crested wave generation and absorption for SPH-based DualSPHysics model,” *Coastal Engineering*, vol. 127, pp. 37–54, 2017.
- [16] S. J. Lind, R. Xu, P. K. Stansby, and B. D. Rogers, “Incompressible smoothed particle hydrodynamics for free-surface flows: a generalised diffusion-based algorithm for stability and validations for impulsive flows and propagating waves,” *Journal of Computational Physics*, vol. 231, no. 4, pp. 1499–1523, 2012.
- [17] K. Gong, H. Liu, and B.-L. Wang, “Water entry of a wedge based on SPH model with an improved boundary treatment,” *Journal of Hydrodynamics*, vol. 21, no. 6, pp. 750–757, 2009.
- [18] A. J. Sahebari, Y.-C. Jin, and A. Shakibaeinia, “Flow over sills by the MPS mesh-free particle method,” *Journal of Hydraulic Research*, vol. 49, no. 5, pp. 649–656, 2011.
- [19] A. Shakibaeinia and Y.-C. Jin, “MPS-based mesh-free particle method for modeling open-channel flows,” *Journal of Hydraulic Engineering*, vol. 137, no. 11, pp. 1375–1384, 2011.
- [20] I. Federico, S. Marrone, A. Colagrossi, F. Aristodemo, and M. Antuono, “Simulating 2D open-channel flows through an SPH model,” *European Journal of Mechanics—B/Fluids*, vol. 34, pp. 35–46, 2012.
- [21] D. López, R. Marivela, and L. Garrote, “Smoothed particle hydrodynamics model applied to hydraulic structures: a hydraulic jump test case,” *Journal of Hydraulic Research*, vol. 48, no. S1, pp. 142–158, 2010.
- [22] M.-J. Chern and S. Syamsuri, “Effect of corrugated bed on hydraulic jump characteristic using SPH method,” *Journal of Hydraulic Engineering*, vol. 139, no. 2, pp. 221–232, 2013.
- [23] M. Ferrand, D. R. Laurence, B. D. Rogers, D. Violeau, and C. Kassiotis, “Unified semi-analytical wall boundary conditions for inviscid, laminar or turbulent flows in the meshless SPH method,” *International Journal for Numerical Methods in Fluids*, vol. 71, no. 4, pp. 446–472, 2013.
- [24] A. Khayyer and H. Gotoh, “On particle-based simulation of a dam break over a wet bed,” *Journal of Hydraulic Research*, vol. 48, no. 2, pp. 238–249, 2010.
- [25] E. Kazemi, A. Nichols, S. Tait, and S. Shao, “SPH modelling of depth-limited turbulent open channel flows over rough boundaries,” *International Journal for Numerical Methods in Fluids*, vol. 83, no. 1, pp. 3–27, 2017.
- [26] S. Dey, *Fluvial Hydrodynamics: Hydrodynamic and Sediment Transport Phenomena*, Springer, Berlin, Germany, 2014.
- [27] D. Violeau and R. Issa, “Numerical modelling of complex turbulent free-surface flows with the SPH method: an overview,” *International Journal for Numerical Methods in Fluids*, vol. 53, no. 2, pp. 277–304, 2007.
- [28] L. Fu and Y.-C. Jin, “A mesh-free method boundary condition technique in open channel flow simulation,” *Journal of Hydraulic Research*, vol. 51, no. 2, pp. 174–185, 2013.
- [29] A. Barreiro, J. M. Domínguez, A. J. C. Crespo, H. Gonzalez-Jorge, D. Roca, and M. Gomez-Gesteira, “Integration of UAV photogrammetry and SPH modelling of fluids to study runoff on real terrains,” *PLoS One*, vol. 9, no. 11, pp. 1–11, 2014.
- [30] J. Boussinesq, *Theorie Analytique de la Chaleur*, Gauthier-Villars, Paris, France, 1903.
- [31] H. Gotoh, T. Shibahara, and T. Sakai, “Sub-particle-scale turbulence model for the MPS method Lagrangian flow model for hydraulic engineering,” *Advanced Methods for Computational Fluid Dynamics*, vol. 9, pp. 339–347, 2001.
- [32] R. Issa, D. Violeau, and D. Laurence, “A first attempt to adapt 3D large eddy simulation to the smoothed particle hydrodynamics gridless method,” in *Proceedings of the International Conference on Computational & Experimental Engineering Sciences, 1st Symposium on Meshless Methods*, Stara-Lesna, Slovakia, June 2005.
- [33] G. Pahar and A. Dhar, “On force consideration in coupled ISPH framework for sediment transport in presence of free-surface flow,” *Environmental Fluid Mechanics*, vol. 18, no. 3, pp. 555–579, 2018.
- [34] D. Violeau, “One and two-equations turbulent closures for smoothed particle hydrodynamics,” *Hydroinformatics*, vol. 2, pp. 87–94, 2004.
- [35] D. De Padova, M. Mossa, and S. Sibilla, “SPH modelling of hydraulic jump oscillations at an abrupt drop,” *Water*, vol. 9, no. 10, p. 790, 2017.
- [36] E. Gabreil, S. J. Tait, S. Shao, and A. Nichols, “SPHysics simulation of laboratory shallow free surface turbulent flows over a rough bed,” *Journal of Hydraulic Research*, vol. 56, no. 5, pp. 727–747, 2018.
- [37] H. Wendland, “Piecewise polynomial, positive definite and compactly supported radial functions of minimal degree,” *Advances in Computational Mathematics*, vol. 4, no. 1, pp. 389–396, 1995.
- [38] R. A. Dalrymple and B. D. Rogers, “Numerical modeling of water waves with the SPH method,” *Coastal Engineering*, vol. 53, no. 2-3, pp. 141–147, 2006.
- [39] E. Y. Lo and S. Shao, “Simulation of near-shore solitary wave mechanics by an incompressible SPH method,” *Applied Ocean Research*, vol. 24, no. 5, pp. 275–286, 2002.
- [40] D. Molteni and A. Colagrossi, “A simple procedure to improve the pressure evaluation in hydrodynamic context using the SPH,” *Computer Physics Communications*, vol. 180, no. 6, pp. 861–872, 2009.
- [41] M. Gomez-Gesteira, B. D. Rogers, A. J. C. Crespo, R. A. Dalrymple, M. Narayanaswamy, and J. M. Domínguez, “SPHysics—development of a free-surface fluid solver—Part 1: theory and formulations,” *Computers & Geosciences*, vol. 48, pp. 289–299, 2012.
- [42] T. Verbrugge, J. M. Domínguez, C. Altomare et al., “Non-linear wave generation and absorption using open boundaries within DualSPHysics,” *Computer Physics Communications*, vol. 240, pp. 46–59, 2019.
- [43] H. Schlichting and K. Gersten, *Boundary-Layer Theory*, Springer, New York, NY, USA, 2016.
- [44] L. C. Van Rijn, *Principles of Sediment Transport in Rivers, Estuaries and Coastal Seas*, Aqua Publications, Netherlands, Amsterdam, 1993.

- [45] J. J. Monaghan, "On the problem of penetration in particle methods," *Journal of Computational Physics*, vol. 82, no. 1, pp. 1–15, 1989.
- [46] J. J. Monaghan and A. Kos, "Solitary waves on a Cretan beach," *Journal of Waterway, Port, Coastal, and Ocean Engineering*, vol. 125, no. 3, pp. 145–155, 1999.
- [47] S. Shao and H. Gotoh, "Simulating coupled motion of progressive wave and floating curtain wall by SPH-LES model," *Coastal Engineering Journal*, vol. 46, no. 2, pp. 171–202, 2004.
- [48] H. Gotoh, S. Shao, and T. Memita, "SPH-LES model for numerical investigation of wave interaction with partially immersed breakwater," *Coastal Engineering Journal*, vol. 46, no. 1, pp. 39–63, 2004.
- [49] A. Mayrhofer, D. Laurence, B. D. Rogers, and D. Violeau, "DNS and LES of 3-D wall-bounded turbulence using smoothed particle hydrodynamics," *Computers & Fluids*, vol. 115, pp. 86–97, 2015.
- [50] I. Nezu, H. Nakagawa, and G. H. Jirka, "Turbulence in open-channel flows," *Journal of Hydraulic Engineering*, vol. 120, no. 10, pp. 1235–1237, 1994.
- [51] D. Coles, "The law of the wake in the turbulent boundary layer," *Journal of Fluid Mechanics*, vol. 1, no. 2, pp. 191–226, 1956.
- [52] O. Giustolisi and D. A. Savic, "Advances in data-driven analyses and modelling using EPR-MOGA," *Journal of Hydroinformatics*, vol. 11, no. 3-4, pp. 225–236, 2009.
- [53] O. Giustolisi and D. A. Savic, "A symbolic data-driven technique based on evolutionary polynomial regression," *Journal of Hydroinformatics*, vol. 8, no. 3, pp. 207–222, 2006.
- [54] V. Pareto, *Cours d'économie Politique*, Librairie Droz, Rouge, Lausanne, 1964.

Research Article

Investigation of Interaction Solutions for Modified Korteweg-de Vries Equation by Consistent Riccati Expansion Method

Jin-Fu Liang ¹ and Xun Wang ²

¹School of Physics and Electronic Science, Guizhou Normal University, Guiyang 550025, China

²Key Laboratory of Speech Acoustics and Content Understanding, Institute of Acoustics, Chinese Academy of Sciences, Beijing 100190, China

Correspondence should be addressed to Jin-Fu Liang; liang.shi2007@163.com

Received 29 March 2019; Accepted 2 July 2019; Published 18 July 2019

Guest Editor: Shaowu Li

Copyright © 2019 Jin-Fu Liang and Xun Wang. This is an open access article distributed under the Creative Commons Attribution License, which permits unrestricted use, distribution, and reproduction in any medium, provided the original work is properly cited.

A consistent Riccati expansion (CRE) method is proposed for obtaining interaction solutions to the modified Korteweg-de Vries (mKdV) equation. Using the CRE method, it is shown that interaction solutions such as the soliton-tangent (or soliton-cotangent) wave cannot be constructed for the mKdV equation. More importantly, exact soliton-cnoidal periodic wave interaction solutions are presented. While soliton-cnoidal interaction solutions were found to degenerate to special resonant soliton solutions for the values of modulus (n) closer to one (upper bound of modulus) in the Jacobi elliptic function, a normal kink-shaped soliton was observed for values of n closer to zero (lower bound).

1. Introduction

The direct study of exact solutions to nonlinear evolution equations (NLEEs) has received much attention from many mathematicians and physicists due to the fact that new strides in nonlinear science, which were made possible by a substantial increase in computational platforms such as Mathematica, Maple, and MATLAB, have enabled improvements in the performance of complicated and tedious numerical computational methods. Indeed, several powerful methods such as the Tanh-function method [1–3], F-expansion method [4], Jacobian elliptic function method [5], and variational approach [6, 7] have been proposed for constructing exact solutions to NLEEs. Despite the successful implementation of such methods, it is still challenging to obtain solutions for interactions among different types of nonlinear excitations such as the soliton-soliton interaction.

Recently, some new soliton structure solutions were obtained for nonlinear systems. Chen *et al.* studied the vortex solitons in Bose-Einstein condensates with spin-orbit coupling and Gaussian optical lattices, based on the analytical and numerical method [8]. Milan *et al.* found exact fundamental soliton solutions in the spiraling guiding structures

by the modified Petviashvili iteration method [9]. Cheng *et al.* investigated the formation and propagation of a multipole soliton in a cold atomic gas with a parity-time symmetric potential using the modified square operator method [10]. Liu *et al.* obtained the three-soliton solutions for high-order nonlinear Schrödinger equation by Hirota's bilinear method [11].

Specially, Lou [12] proposed a consistent Riccati expansion (CRE) method, which is a more generalized yet simpler method to find interaction solutions for various NLEEs [13–17]. The core concept of CRE is the construction of interaction solutions based on the usual Riccati equation method and the consistent equation or the w -equation [12]. The CRE method is critical to finding more new solutions to the w -equation.

In this study, the CRE method is used to construct several types of interaction solutions for the focusing real modified Korteweg-de Vries (mKdV) equation [18] shown in

$$u_t + \alpha u^2 u_x + \beta u_{xxx} = 0, \quad (1)$$

where α and β are arbitrary constants. The mKdV equation plays an important role in describing some physical phenomena, such as optical cycles [19, 20], soliton propagation in

plasma [21] and lattices [22], the Schottky barrier transmission lines [23], and fluid mechanics [24].

To provide better insights into these physical phenomena, finding and analyzing exact solutions to the mKdV equation is important. Previously, many powerful methods have been proposed for constructing exact solutions to the mKdV equation. For instance, in 1972, Hirota obtained an exact solution to the mKdV equation for the case of multiple collisions of solitons with different amplitudes [25]. Subsequently, he also derived the exact envelope soliton solution to the mKdV equation [26]. In 1973, Ablowitz *et al.* obtained exact solutions to the mKdV equation by using the inverse scattering technique [27]. In 1988, Akhmediev *et al.* used the Darboux transformation scheme to obtain second-order periodic solutions to the mKdV equation [28]. In 2004, Kevrekidis *et al.* derived some classes of periodic solutions to the mKdV equation by using direct methods [29]. In 2015, Jiao and Lou constructed a new soliton-cnoidal periodic wave interaction solution by using the CRE method [30]. However, they did not investigate how the soliton-cnoidal interaction solutions may be used to derive soliton-soliton or soliton-periodic wave interaction solutions among other types of solutions. Moreover, new interaction solutions to the mKdV equation involving different types of nonlinear waves must be investigated in depth.

The present article is structured as follows. Section 2 introduces the CRE solvability of the mKdV equation. Section 3 describes new explicit interaction solutions such as soliton-soliton, multiple resonant soliton, soliton-cosine wave, and soliton-cnoidal wave solutions to the mKdV equation obtained using the CRE method. Furthermore, it is demonstrated that interaction solutions such as the soliton-tangent wave solution cannot be constructed for the mKdV equation. The last section presents a summary and discussion.

2. CRE Solvability of the mKdV Equation

Consider the following NLEE, shown in (2), with independent variables $X \equiv (t, x_1, x_2, \dots, x_m)$ and a dependent variable $u \equiv u(X)$

$$P(u, u_t, u_{x_i}, u_{x_i x_i}) = 0, \quad (2)$$

where P is a polynomial function of some arguments with the subscripts denoting partial derivatives. We assume that the solution to (2) is the following possible truncated expansion form

$$u = \sum_{j=0}^n u_j R^j(w), \quad (3)$$

where n is determined from the leading order analysis of (2). All the expansion coefficient functions (u_j) are determined by substituting (3) into (2) and then vanishing all the coefficients for a given power of $R(w)$. Further, u_j and w are functions of (x, y, t) and $R(w)$ satisfies the following simple Riccati equation shown below:

$$R_w = \sigma + R^2, \quad (4)$$

$$R \equiv R(w),$$

which includes the following five special solutions [31]. For $\sigma < 0$,

$$R = -\sqrt{-\sigma} \tanh(\sqrt{-\sigma} w), \quad (5a)$$

$$R = -\sqrt{-\sigma} \coth(\sqrt{-\sigma} w). \quad (5b)$$

For $\sigma > 0$,

$$R = \sqrt{\sigma} \tan(\sqrt{\sigma} w), \quad (6a)$$

$$R = -\sqrt{\sigma} \cot(\sqrt{\sigma} w). \quad (6b)$$

For $\sigma = 0$,

$$R = -\frac{1}{w}. \quad (7)$$

Definition. If the equation for u_j ($j = 0, 1, \dots, n$) and w , obtained by vanishing all the coefficients of each power in $R(w)$ after the substitution of (3) into (2), is either consistent or not overdetermined, then the expansion in (3) is considered a CRE and the nonlinear system in (2) is said to be CRE solvable [8].

According to the CRE method defined above, one can obtain the following form based on the leading order analysis of the mKdV equation in (1)

$$u = u_0 + u_1 R(w), \quad (8)$$

where u_0, u_1 , and w are functions of (x, y, t) and $R(w)$ satisfies the Riccati equation (see (4) above).

Substituting (8) and (4) into (1) and vanishing all the coefficients of different powers of $R(w)$, one obtains

$$u_1 = -\frac{\sqrt{6\beta} w_x}{\sqrt{-\alpha}}, \quad (9)$$

$$\text{or } u_1 = \frac{\sqrt{6\beta} w_x}{\sqrt{-\alpha}},$$

$$u_0 = -\frac{\sqrt{3\beta} w_{xx}}{\sqrt{-2\alpha w_x}}, \quad (10)$$

$$\text{or } u_0 = \frac{\sqrt{3\beta} w_{xx}}{\sqrt{-2\alpha w_x}}$$

$$w_t = 2\sigma\beta w_x^3 - \frac{3\beta w_{xx}^2}{2w_x} + \beta w_{xxx}. \quad (11)$$

Based on the definition above, (11) is the consistent equation of the mKdV equation (or the mKdV w -equation). If w is a solution to the MDWW w -equation in (11), the mKdV equation in (1) is CRE solvable. In this study, we set $\alpha = -6$ and $\beta = 1$. Thus, the solutions to the mKdV equation are expressed as follows.

$$u = -\frac{w_{xx}}{2w_x} - w_x R(w), \quad (12a)$$

$$u = \frac{w_{xx}}{2w_x} + w_x R(w). \quad (12b)$$

3. Interaction Solutions to the mKdV Equation

Upon the determination of solutions to (11) by using (12), the corresponding solutions to the mKdV equation in (1) can be obtained. In this section, we construct interaction solutions to the mKdV equation by using different types of trivial solutions to (11).

3.1. Soliton-Soliton Interaction Solutions to the mKdV Equation. To obtain soliton-soliton interaction solutions to the mKdV equation, we consider the following form in (13) as the trial solution to (11):

$$\begin{aligned} w &= k_1 x + w_1 t + R(\phi), \\ \phi &= k_2 x + w_2 t, \end{aligned} \tag{13}$$

where $R(\phi)$ satisfies the following Riccati equation in

$$R_\phi = r + R(\phi)^2, \tag{14}$$

where r is an arbitrary constant. This equation has special solutions similar to those in (5a), (5b), (6a), (6b), and (7). By vanishing all the coefficients for each power of R_ϕ after the substitution of (13) and (14) into the mKdV w -equation in (11), one can obtain

$$\begin{aligned} \sigma &= -\frac{1}{4}, \\ r &= -1, \\ k_2 &= -\sqrt[3]{\frac{w_2}{2r}}, \\ k_1 &= \frac{k_2 w_1}{w_2}, \\ w_1 &= -w_2. \end{aligned} \tag{15}$$

From (15), it can be seen that both σ and r are less than 0 when $w_1 \neq 0$. Based on (5a), (5b), (6a), and (6b), Eqs. (4) and (14) have only solitary solutions (*viz.*, (5a) and (5b)) but not tangent or cotangent solutions such as the ones described in (6a) and (6b). This shows that interaction solutions such as soliton-tangent (or soliton-cotangent) wave cannot be constructed for the mKdV equation.

Under condition (15), from (5a), (5b), (12a), and (13), the soliton-soliton interaction solutions of the mKdV equation are expressed as

$$\begin{aligned} u &= \frac{2k_2^2 \tanh \phi}{k_1 + 2k_2 + k_1 \cosh(2\phi)} + \frac{1}{2} (k_1 + k_2 \operatorname{sech}^2 \phi) \\ &\cdot \tanh \left(\frac{1}{2} (-k_1 x - w_1 t) - \tanh \phi \right), \end{aligned} \tag{16a}$$

$$u = \frac{k_2^2 \operatorname{csch}^2 \phi \coth \phi}{-k_1 + k_2 \operatorname{csch}^2(\phi)} + \frac{1}{2} (k_1 - k_2 \operatorname{csch}^2 \phi) \tag{16b}$$

$$\cdot \tanh \left(\frac{1}{2} (-k_1 x - w_1 t) - \coth \phi \right),$$

$$u = \frac{k_2^2 \operatorname{sech}^2 \phi \tanh \phi}{k_1 + k_2 \operatorname{sech}^2(\phi)} + \frac{1}{2} (k_1 + k_2 \operatorname{sech}^2 \phi) \tag{16c}$$

$$\cdot \coth \left(\frac{1}{2} (-k_1 x - w_1 t) - \tanh \phi \right),$$

$$u = \frac{-k_2^2 \coth \phi \operatorname{csch}^2 \phi}{k_1 - k_2 \operatorname{csch}^2(\phi)} + \frac{1}{2} (k_1 - k_2 \operatorname{csch}^2 \phi) \tag{16d}$$

$$\cdot \coth \left(\frac{1}{2} (-k_1 x - w_1 t) - \coth \phi \right).$$

3.2. Interaction Solution between and Trigonometric Periodic Wave for the mKdV Equation. To investigate the interaction between a soliton and a periodic wave in the interaction solution to the mKdV equation, we consider a solution of the following form (11):

$$\begin{aligned} w &= k_1 x + w_1 t \\ &+ c_0 \ln(\cos(k_2 x + w_2 t) \exp(k_2 x + w_2 t)), \end{aligned} \tag{17}$$

where c_0 is determined constant. Substituting (17) into (11) and then vanishing all coefficients of powers $\tan(k_2 x + w_2 t)$, we can obtain

$$\begin{aligned} \sigma &= -\frac{1}{4}, \\ k_1 &= -\frac{k_2}{\sqrt{-2\sigma}}, \\ c_0 &= \frac{2(2\sigma k_1^3 k_2 - k_1 k_2^3)}{k_2^4 - 8\sigma k_1^2 k_2^2 + 4\sigma^2 k_1^4}, \\ w_1 &= \frac{2(2c_0 k_1 k_2^3 + 3c_0^2 k_2^4 - \sigma k_1^4)}{k_1}, \\ w_2 &= 4(k_2^3 - 3\sigma k_1^2 k_2 - 6\sigma c_0 k_1 k_2^2). \end{aligned} \tag{18}$$

Then, based on (5a), (17), and (12a), one can obtain a soliton-trigonometric periodic wave interaction solution as

$$\begin{aligned} u &= k_2 \frac{(6 \sec^2(M) - \sqrt{2}(1 + 2 \tan^2(M)))}{6 + 12 \tan(M)} \\ &+ \frac{\tanh \left((3k_2(x + k_2^2 t) - 2 \ln(M \cos(M))) / 3\sqrt{2} \right)}{6 + 12 \tan(M)}, \end{aligned} \tag{19}$$

where $M = k_2 x + 2k_2^3 t$.

3.3. Interaction Solutions between Soliton and Cnoidal Wave for the mKdV Equation. In [26], Jiao and Lou constructed a solution of the following form for (11)

$$w = k_1 x + w_1 t + AE_\pi [\operatorname{sn}(k_2 x + w_2 t, \mu_1), \nu, \kappa], \tag{20}$$

where $\text{sn}(\zeta, \mu)$ is the usual Jacobi elliptic sine function and $E_\pi(\xi, \nu, \kappa)$ is the third type of incomplete elliptic integral. Jiao and Lou used the following parameters in (21) to obtain a special soliton-cnoidal wave interaction solution to the mKdV equation:

$$\{\mu_1, k_1, k_2\} = \{1.5, 2, 1\}. \quad (21)$$

As seen from (21), Jiao and Lou chose the modulus (μ_1) of Jacobi elliptic function to be 1.5, which is outside the allowed range ($0 < \mu_1 < 1$) [13].

In this study, we will further investigate how soliton-cnoidal interaction solutions can be used to derive soliton-soliton and soliton-periodic wave interaction solutions among other types of solutions. To this end, we performed all the substitutions and evaluations by using the Mathematica software.

Consider a trial solution of the following form for solving (11)

$$w = k_1x + w_1t + W(k_2x + w_2t), \quad (22)$$

where

$$W(k_2x + w_2t) = W(\xi) = W, \quad (23)$$

satisfies the following elliptic equation:

$$\begin{aligned} W_{1\xi}^2 &= C_0 + C_1W_1 + C_2W_1^2 + C_3W_1^3 + C_4W_1^4, \\ W_1 &\equiv W_\xi. \end{aligned} \quad (24)$$

Substituting (22) and (24) into (11), one obtains

$$\begin{aligned} C_0 &= C_0, \\ C_1 &= \frac{3C_0k_2^4 - 2k_1w_1 - 4\sigma k_1^4}{k_1k_2^3}, \\ C_2 &= \frac{C_1k_2^4 - k_2w_1 - k_1w_2 - 8\sigma k_2k_1^3}{k_1k_2^3}, \\ C_3 &= \frac{C_2k_2^3 - 2w_2 - 24\sigma k_2k_1^2}{3k_1k_2^2}, \\ C_4 &= -4\sigma. \end{aligned} \quad (25)$$

From the analysis of (24), we assume the solution of (24) in the following form

$$W_1 = A_0 + A_1 \text{sn}(m(k_2x + w_2t), n). \quad (26)$$

Substituting (26) into (24) and setting the coefficient of $\{\text{sn}(m(k_2x + w_2t), n), \text{cn}(m(k_2x + w_2t), n), \text{dn}(m(k_2x + w_2t), n)\}$ equal to zero, one obtains

$$\begin{aligned} A_0 &= A_0, \\ A_1 &= A_0, \\ C_0 &= \frac{-m^2 A_0^2 A_1^2 + m^2 A_1^4 + m^2 n^2 A_0^4 - m^2 n^2 A_0^2 A_1^2}{A_1^2}, \\ C_1 &= \frac{2(2C_0 + m^2 A_0^2 - 2m^2 A_1^2 + m^2 n^2 A_0^2)}{A_0}, \\ C_2 &= \frac{-3C_1 + 4m^2 A_0 + 4m^2 n^2 A_0}{2A_0}, \\ C_3 &= \frac{2(C_2 + m^2 + m^2 n^2)}{3A_0}, \\ C_4 &= \frac{C_3}{4A_0}. \end{aligned} \quad (27)$$

Based on (25) and (27), one can find a group solution

$$\begin{aligned} k_2 &= \sqrt[3]{-\frac{2w_2}{m^2(5-n^2)}}, \\ k_1 &= \frac{600\sigma w_1 w_2 - \sqrt{360000\sigma^2 w_1^2 w_2^2 - 4(N_1)(N_2)}}{2(N_2)}, \\ A_0 &= \frac{-4m^2 k_1 k_2^3 - 4m^2 n^2 k_1 k_2^3 + 3w_1 k_2 + w_2 k_1}{4k_2(m^2 k_2^3 + m^2 n^2 k_2^3 - w_2)}, \\ A_1 &= -\sqrt{\frac{6(m^2 n^2 k_2 k_1^2 + 2m^2 n^2 k_1 k_2^2 A_0 + m^2 n^2 k_2^2 A_0^2)}{m^2 k_2^3 + m^2 n^2 k_2^3 + 2w_2}}, \end{aligned} \quad (28)$$

where $N_1 = -160m^6 k_2^7 + 992m^6 n^2 k_2^7 - 236m^4 w_2 k_2^4 - 616m^4 n^2 w_2 k_2^4 + 20m^4 n^4 w_2 k_2^4 + 168m^2 w_2^2 k_2 + 40m^2 n^2 w_2^2 k_2 + 300\sigma w_1^2 k_2$, and $N_2 = 375\sigma m^4 k_2^5 - 1950\sigma m^4 n^4 k_2^5 + 375\sigma m^4 n^4 k_2^5 + 600\sigma m^2 w_2 k_2^2 + 600\sigma m^2 n^2 w_2 k_2^2$. Under the substitution of (26), (22), and (5a) into (12a), under the conditions imposed by (28), one obtains

$$\begin{aligned} u &= \frac{-mA_1 k_2^2 CD}{2(k_1 + k_2 A_0 + k_2 A_1 S)} \\ &+ \frac{2(k_1 + k_2 A_0 + k_2 A_1 S)^2 \sqrt{-\sigma} \tanh(\sqrt{-\sigma} T)}{2(k_1 + k_2 A_0 + k_2 A_1 S)}, \end{aligned} \quad (29)$$

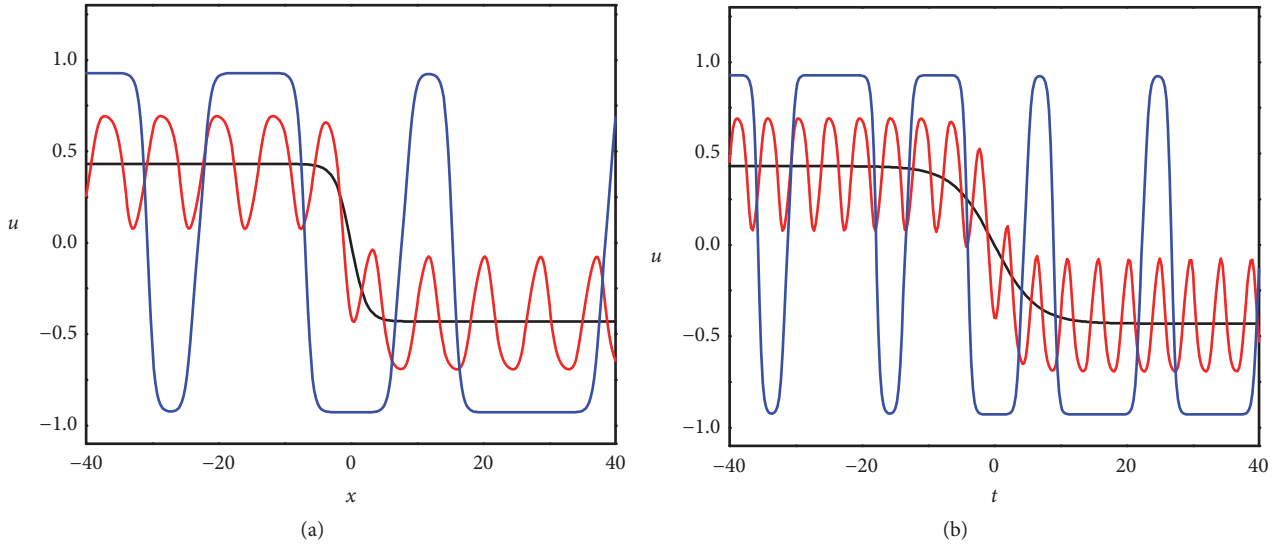


FIGURE 1: (Color online) The evolution of the soliton-cnoidal wave interaction solution shown in (29) obtained by using the parameters listed in (31). The profiles at $t = 0$ and $x = 0$ are shown in (a) and (b), respectively. Different color traces represent different values for the modulus $n = 0.00001$ (black), $n = 0.5$ (red), and $n = 0.99999$ (blue).

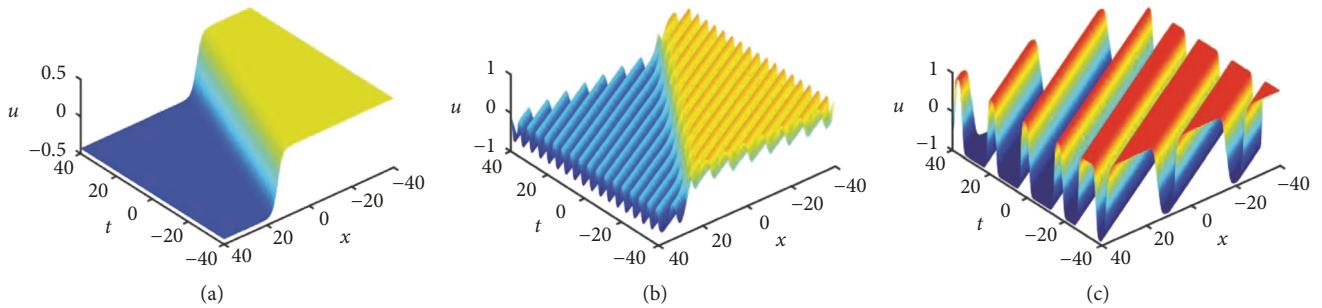


FIGURE 2: (Color online) The evolution of the soliton-cnoidal wave interaction solution shown in (29) obtained by using the parameters listed in (31) with different modulus values as a function of both x and t . The modulus values for different panels are (a) $n = 0.00001$, (b) $n = 0.5$, and (c) $n = 0.99999$.

where

$$\begin{aligned}
 S &= \operatorname{sn}(m(k_2x + w_2t), n), \\
 C &= \operatorname{cn}(m(k_2x + w_2t), n), \\
 D &= \operatorname{dn}(m(k_2x + w_2t), n), \\
 T &= (k_1 + k_2A_0)x + (w_1 + w_2A_0)t \\
 &\quad + \frac{A_1 \ln(D - \sqrt{n}C)}{m\sqrt{n}}.
 \end{aligned}
 \tag{30}$$

To investigate how the soliton-cnoidal interaction solutions could be used to derive soliton-soliton interaction or other types of solutions, we illustrate the following two cases corresponding to the soliton-cnoidal wave interaction solution described in (29) by selecting different sets of parameters. For the first case, the parameters are chosen as

$$\begin{aligned}
 \sigma &= -1, \\
 w_1 &= 0.5, \\
 w_2 &= 0.8, \\
 m &= 2.
 \end{aligned}
 \tag{31}$$

While Figure 1 shows two-dimensional views for interaction solution at $t = 0$ and $x = 0$. Figure 2 displays three-dimensional plots for the evolution of soliton-cnoidal wave interaction solution with different values for the modulus in the Jacobian elliptic function, *viz.*, $n = 0.000001$, 0.5 , and 0.99999 . While $n = 0.5$ exhibited a particular periodic-kink soliton wave interaction, the extreme values of $n = 0.00001$ (a value close to the lower modulus limit or 0) showed a normal kink-shaped soliton and $n = 0.99999$ (a value close to the upper modulus limit or 1) displayed an interaction between a periodic wave and another periodic wave.

For the second case, the parameters were altered as shown in (32) by changing the angular frequency w_2

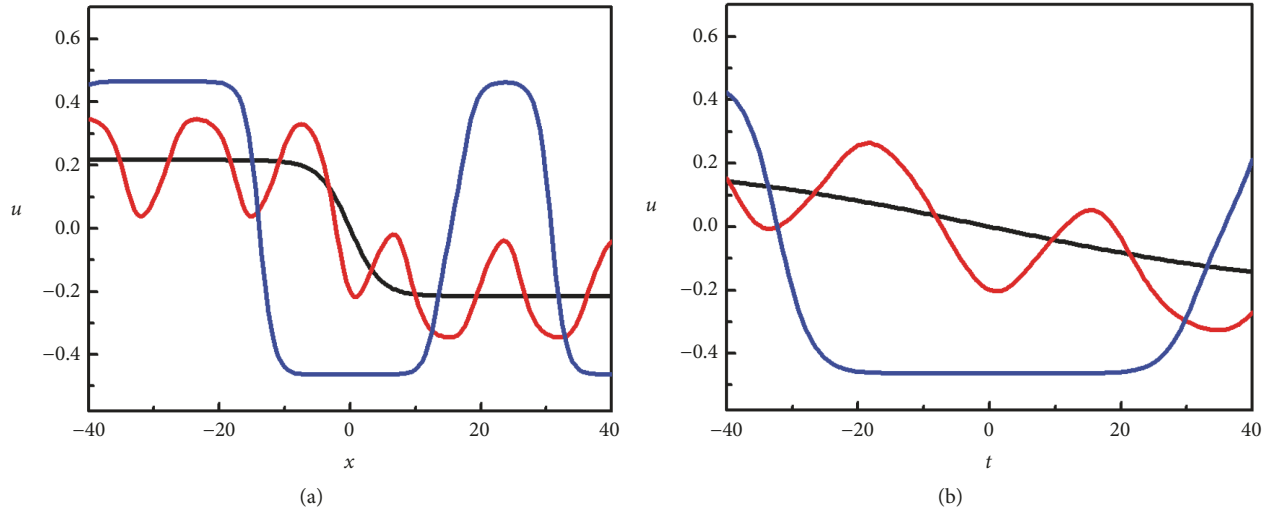


FIGURE 3: (Color online) The evolution of the soliton-cnoidal wave interaction solution shown in (29) obtained by using the parameters in (32). The profiles at $t = 0$ and $x = 0$ are shown in (a) and (b), respectively. Different color traces represent different values for the modulus $n = 0.00001$ (black), $n = 0.5$ (red), and $n = 0.99999$ (blue).

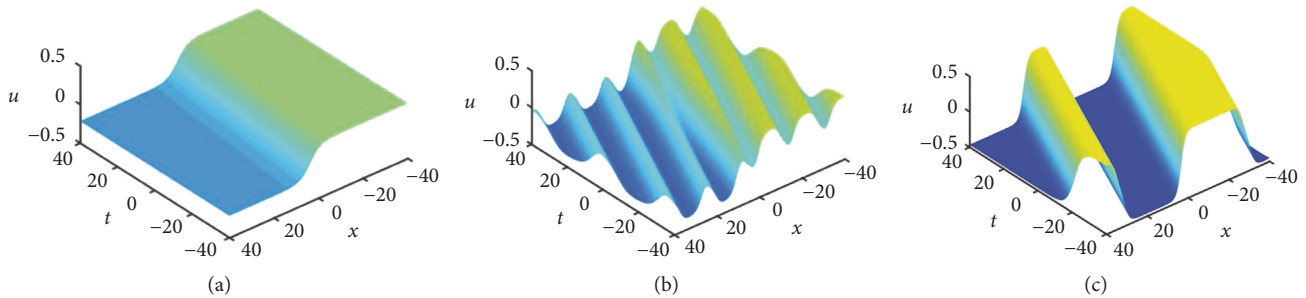


FIGURE 4: (Color online) The evolution of the soliton-cnoidal wave interaction solution shown in (29) obtained by using the parameters listed in (32) with different modulus values as a function of both x and t . The modulus values for different panels are (a) $n = 0.00001$, (b) $n = 0.5$, and (c) $n = 0.99999$.

$$\begin{aligned}
 \sigma &= -1, \\
 \omega_1 &= 0.5, \\
 \omega_2 &= 0.1, \\
 m &= 2.
 \end{aligned}
 \tag{32}$$

Similar to the first case, we illustrate the structures of the soliton-cnoidal wave interaction solution for different values of $n = 0.00001$, 0.5 , and 0.99999 . Clearly, as shown in Figures 3 and 4, wavenumbers and the amplitudes in the range of $x(-40,40)$ and $t(-40,40)$ are less than that of the first case (cf. Figures 1 and 2). While there is still a normal kink soliton in the $x-u$ plot for $n = 0.00001$, an incomplete kink soliton is observed in the $t-u$ plot in contrast to the first case shown in Figure 1(b). Building on the above two cases, soliton and soliton-soliton wave interaction solutions are derived from the soliton-cnoidal wave interaction solution by making the limit of the modulus approach either 0 or 1.

4. Summary and Discussion

In this study, we investigated the focusing mKdV equation by using the CRE method. This nonlinear equation was shown to be CRE solvable and interaction solutions; namely, soliton-soliton, soliton-trigonometric periodic waves, and soliton-cnoidal periodic wave for the mKdV w -equation shown in (11). In addition, analytical solutions for interactions between soliton and cnoidal wave were provided and their properties were discussed graphically. According to the presented analysis, soliton and soliton-soliton wave interaction solutions can be derived from the soliton-cnoidal wave interaction solution by making the limit of the modulus approach either 0 or 1 (i.e., lower or upper bounds for the modulus in the Jacobi elliptical function).

Data Availability

No data were used to support this study.

Conflicts of Interest

The authors declare that there are no conflicts of interest regarding the publication of this paper.

Acknowledgments

This work was supported by the National Natural Science Foundation of China (Grant No. 11864007 and No. 11564006), the Doctor Foundation of Guizhou Normal University (2015), and the Science and Technology Planning Project of Guizhou Province (Grant No. [2018]5769).

References

- [1] H. A. Abdusalam, "On an improved complex tanh-function method," *International Journal of Nonlinear Sciences and Numerical Simulation*, vol. 6, no. 2, pp. 99–106, 2005.
- [2] M. A. Abdou and A. A. Soliman, "Modified extended tanh-function method and its application on nonlinear physical equations," *Physics Letters A*, vol. 353, no. 6, pp. 487–492, 2006.
- [3] D. L. Sekulic, M. V. Sataric, and M. B. Zivanov, "Symbolic computation of some new nonlinear partial differential equations of nanobiosciences using modified extended tanh-function method," *Applied Mathematics and Computation*, vol. 218, no. 7, pp. 3499–3506, 2011.
- [4] W. W. Li, Y. Tian, and Z. Zhang, "F method and its application for finding new exact solutions to the sine-Gordon and sinh-Gordon equations," *Applied Mathematics and Computation*, vol. 219, no. 3, pp. 1135–1143, 2012.
- [5] A. H. Bhrawy, M. A. Abdelkawy, and A. Biswas, "Cnoidal and snoidal wave solutions to coupled nonlinear wave equations by the extended Jacobi's elliptic function method," *Communications in Nonlinear Science and Numerical Simulation*, vol. 18, no. 4, pp. 915–925, 2013.
- [6] H. Liu, "Variational approach to nonlinear electrochemical system," *International Journal of Nonlinear Sciences and Numerical Simulation*, vol. 5, no. 1, pp. 95–96, 2004.
- [7] J. F. Liang and L. X. Gong, "Complex wave solutions for (2+1)-dimensional modified dispersive water wave system," *Communications in Theoretical Physics*, vol. 52, no. 1, pp. 17–22, 2009.
- [8] S. F. Chen, Q. Guo, S.-L. Xu et al., "Vortex solitons in bose-einstein condensates with spin-orbit coupling and gaussian optical lattices," *Applied Mathematics Letters*, vol. 92, pp. 15–21, 2019.
- [9] S. P. Milan, S. Aleksandra, A. Branislav, and R. Milivoj, "Rotating solitons supported by a spiral waveguide," *Physical Review A: Atomic, Molecular and Optical Physics*, vol. 98, no. 5, Article ID 063822, 2017.
- [10] J. Cheng, S. Xu, M. R. Belic et al., "Multipole solitons in a cold atomic gas with a parity-time symmetric potential," *Nonlinear Dynamics*, vol. 95, no. 3, pp. 2325–2332, 2019.
- [11] X. Liu, H. Triki, Q. Zhou et al., "Generation and control of multiple solitons under the influence of parameters," *Nonlinear Dynamics*, vol. 95, no. 1, pp. 143–150, 2019.
- [12] S. Y. Lou, "Consistent Riccati expansion for integrable systems," *Studies in Applied Mathematics*, vol. 134, no. 3, pp. 372–402, 2015.
- [13] X. Liu, J. Yu, and Z. Lou, "New interaction solutions from residual symmetry reduction and consistent Riccati expansion of the (2+1)-dimensional Boussinesq equation," *Nonlinear Dynamics*, vol. 92, no. 4, pp. 1469–1479, 2018.
- [14] L. Huang, Z. Qiao, and Y. Chen, "Soliton-cnoidal interactional wave solutions for the reduced Maxwell-Bloch equations," *Chinese Physics B*, vol. 27, no. 2, Article ID 020201, 2018.
- [15] J. Chen, H. Wu, and Q. Zhu, "Bäcklund transformation and soliton-cnoidal wave interaction solution for the coupled Klein-Gordon equations," *Nonlinear Dynamics*, vol. 91, no. 3, pp. 1949–1961, 2018.
- [16] Y. Li and H. Hu, "Nonlocal symmetries and interaction solutions of the Benjamin-Ono equation," *Applied Mathematics Letters*, vol. 75, pp. 18–23, 2018.
- [17] J. Liang and X. Wang, "Consistent Riccati expansion for finding interaction solutions of (2+1)-dimensional modified dispersive water-wave system," *Mathematical Methods in the Applied Sciences*, 2019.
- [18] S. Liu and S. Liu, *Nonlinear Equation in Physics*, Peking University Press, Beijing, China, 2000.
- [19] H. Leblond and D. Mihalache, "Few-optical-cycle solitons: modified korteweg-de vries sine-gordon equation versus other non-slowly-varying-envelope-approximation models," *Physical Review A: Atomic, Molecular and Optical Physics*, vol. 79, no. 6, Article ID 063835, 2009.
- [20] H. Leblond and D. Mihalache, "Few-optical-cycle dissipative solitons," *Journal of Physics A: Mathematical and Theoretical*, vol. 43, no. 37, Article ID 375205, 2010.
- [21] N. J. Zabusky and M. D. Kruskal, "Interaction of solitons in collisionless plasma and the recurrence of initial states," *Physical Review Letters*, vol. 15, no. 6, pp. 240–243, 1965.
- [22] H. Ono, "Soliton fission in anharmonic lattices with reflectionless inhomogeneity," *Journal of the Physical Society of Japan*, vol. 61, no. 12, pp. 4336–4343, 1992.
- [23] V. Ziegler, J. Dinkel, C. Setzer, and K. E. Lonngren, "On the propagation of nonlinear solitary waves in a distributed Schottky barrier diode transmission line," *Chaos Solitons and Fractals*, vol. 12, no. 9, pp. 1719–1728, 2001.
- [24] M. A. Helal, "Soliton solution of some nonlinear partial differential equations and its applications in fluid mechanics," *Chaos Solitons and Fractals*, vol. 13, no. 9, pp. 1917–1929, 2002.
- [25] R. Hirota, "Exact solution of the korteweg—de vries equation for multiple collisions of solitons," *Physical Review Letters*, vol. 27, no. 18, pp. 1192–1194, 1971.
- [26] R. Hirota, "Exact envelope-soliton solutions of a nonlinear wave equation," *Journal of Mathematical Physics*, vol. 14, pp. 805–809, 1973.
- [27] M. J. Ablowitz, D. J. Kaup, A. C. Newell, and H. Segur, "Nonlinear-evolution equations of physical significance," *Physical Review Letters*, vol. 31, no. 2, pp. 125–127, 1973.
- [28] N. Akhmediev, V. I. Korneeve, and N. V. Mitskevich, "N-modulation signals in a single-mode optical fiber with allowance for nonlinearity," *Journal of Experimental and Theoretical Physics*, vol. 94, pp. 159–170, 1988.
- [29] P. G. Kevrekidis, A. Khare, A. Saxena, and G. Herring, "On some classes of mKdV periodic solutions," *Journal of Physics A: Mathematical and General*, vol. 37, no. 45, pp. 10959–10965, 2004.
- [30] X. Jiao and S. Lou, "CRE method for solving mKdV equation and new interactions between solitons and cnoidal periodic waves," *Communications in Theoretical Physics*, vol. 63, no. 1, pp. 7–9, 2015.

- [31] S. H. Ma, J. Y. Fang, and C. L. Zheng, "New exact solutions for the (3+1)-dimensional Jimbo-Miwa system," *Chaos Solitons and Fractals*, vol. 40, no. 3, pp. 1352–1355, 2009.

Review Article

Remote Sensing: An Advanced Technique for Crop Condition Assessment

Karim Ennouri ^{1,2} and **Abdelaziz Kallel**¹

¹Digital Research Centre of Sfax, Technopark of Sfax, Sfax, Tunisia

²Laboratory of Amelioration and Protection of Olive Genetic Resources, Olive Tree Institute, University of Sfax, Sfax, Tunisia

Correspondence should be addressed to Karim Ennouri; lkarimennouri@gmail.com

Received 9 May 2019; Accepted 7 July 2019; Published 17 July 2019

Guest Editor: Raffaele Albano

Copyright © 2019 Karim Ennouri and Abdelaziz Kallel. This is an open access article distributed under the Creative Commons Attribution License, which permits unrestricted use, distribution, and reproduction in any medium, provided the original work is properly cited.

Actually, cultivators are increasingly arranging innovative high technical and scientific estimations in the aim to enhance agricultural sustainability, effectiveness, and/or plant health. Innovative farming technologies incorporate biology with smart agriculture: computers and devices exchange with one another autonomously in a structured farm management system. Throughout this structure, smart agriculture can be accomplished; cultivators decrease plantation inputs (pesticides and fertilizers) and increase yields via integrated pest management and/or biological control. The emerging concept of remote sensing may provide a framework to systematically consider these issues of smart farming technology and to embed high-tech agriculture better. The impact(s) may be beneficial depending on how tools, such as data mining, and imagery technologies, such as picture treatment and analysis, are applied. Remote sensing technology is discussed in this review and demonstrates its possibility to create novel opportunities for scientists (and agronomists) to explore aspects of biological phenomena that cannot be accessed through usual mechanisms or processes.

1. Introduction

It is evident that agriculture can be considered as the “vertebral column” of the humanity life and has considerable control on economy. This highlights the process requirement for usual monitoring of the crop state. There are an assortment of features to supervise crop state starting from soil humidity accessibility, plant vigour situation, and stress provided by abiotic causes (for example, humidity, rainfall, and temperature) and also biotic causes (for example, pest and illness). Any delay from the ordinary development parameter influences crop growth in addition to ultimately diminishing the production and productivity, and for this reason it is especially imperative to examine crop state for complete cycle of development.

Appropriate and suitable crop evaluation at better level requires observing wide regions by a powerful system. Remote sensing skill offers this through nondestructive synoptic screening capacities. It is well known that spectral answer of the soil attribute is different for various areas of electromagnetic spectrum. These sensed measures assist

distantly in the detection and recognition of the globe surface trait.

The fundamental aim of appliance of remote sensing in cultivation is to conclude vegetation characteristics by examining the data included in the dispersed/returned signal [1]. The initial most important operational implement in the farming uses of remote sensing was that of Large Area Crop Inventory Experiment (LACIE) [2], where an effort was produced to approximate country-wise wheat land and yield via LANDSAT digital information. Landsat is an operation of Earth surveillance satellites expanded under a combined program of the National Aeronautics and Space Administration (NASA) and United States Geological Survey (USGS). Evaluations of the consequence of edaphic and meteorological answer aspects to crop have stayed a principal subject; there are a huge number of features as edaphic, climatic, biotic, hydrologic, and agronomic, which control a crop development and production. Furthermore, weather has a considerable position over the development and productivity reaction of crops. Remote sensing method by means of the potential of multispectral, multitemporal,

and synoptic exposure has revealed an excellent potential in giving broad rank of crop situation and production potential at local stage. With remote sensing method, the form of crops developed in an area, crop state, and yield can be considered. Recording crop state by remote sensing can get the crop status in addition to the condition and progress of their development. Obtaining the crop situation data at early steps of crop development is still more significant than acquiring the fixed production after harvest period.

2. Indices of Remote Sensing and Signification

Crop state estimation necessitates an information input, for example, environmental conditions such as air temperature, relative humidity, and rainfalls and surface condition like soil moisture and soil temperature. Remote sensing indices like Normalized Difference Vegetation Index (NDVI), Land Surface Water Index (LSWI), Temperature-Vegetation Dryness Index (TVDI), Soil Adjusted Vegetation Index (SAVI), Water Deficit Index (WDI), etc. obtained from satellite imagery are helpful to derive crop development state and/or soil humidity state. The Normalized Difference Vegetation Index (NDVI) calculates vegetation density through evaluating the variation between near-infrared (which vegetation powerfully returns) and red luminosity (which vegetation attracts). Moreover, the Land Surface Water Index (LSWI) employs the Shortwave Infrared (SWIR) and the Near-Infrared (NIR) zones of the electromagnetic range [3]. There is powerful luminosity assimilation by liquid water in the SWIR, and the LSWI is well recognized to be susceptible to the entire quantity of liquid water in vegetation and its soil [4]. In addition, the Temperature-Vegetation Dryness Index (TVDI) is acquired from spatial Land Surface Temperature-NDVI and can be employed as a marker of soil humidity and therefore the vegetation water pressure [5]. The SAVI (Soil Adjusted Vegetation Index) takes in consideration the visual soil characteristics on the plant cover reflectance [6]. The WDI represents the relative rate of hidden heat change, so it illustrates a rate of “zero” for totally wet surface and a value of “one” concerning dry surfaces where there is no hidden heat change [7]. Remote sensing method aids to create a temporal development profile of plants over its development phase. With the recovery of environmental factors in addition to remote sensing indices, it is simple to recognize the development model of crop and also their connection among each other and consequence of concerned variables on crop development. On the basis of preceding information and test, remote sensing method is especially helpful in estimating the crop development at land level in addition to large level. Assimilation of ecological, surface, and crop state acquired through remote sensing method in addition to soil station aids in improvement of model to calculate the crop state [8].

3. Role of Remote Sensing in Crop State Evaluation

Remote sensing gives immense occasion to obtain a general synoptic vision of the globe organization [9]. Numerous

classes of selective information on available resources such as soil humidity, soil use and cover, crop natures and state, and soil type data can be mined since the satellite information [10].

Remote sensing as a device will provide information frequently and at an inexpensive value to permit, in the appropriate time, interference for recovery of crop state. Satellite structures offer spatially and temporally permanent records cover of the globe [11]. Satellite records of visual sensors similar to SPOT (in French: Satellite Pour l'Observation de la Terre), Moderate Resolution Imaging Spectroradiometer (MODIS), Atmospheric Infrared Sounder (AIRS), and LANDSAT, are employed for diverse domains. The Landsat task offers the greatest permanent space-based record of Earth's soil, beginning from 1972 and the Landsat 1 satellite.

Starting through Landsat 4, each of the satellites represented the Earth's surface at a 30-meter resolution about once each five to ten days by means of thermal and multispectral devices. SPOT is an elevated-quality visual imaging globe inspection satellite structure controlling from space. It has been made to develop the understanding and managing of the globe via discovering the globe's reserves, perceiving and predicting phenomena engaging oceanography and also climatology, and supervising human movements as well as innate phenomena. The SPOT structure comprises a chain of satellites and land control reserves for satellite management and training and picture creation and delivery (Table 1) [12].

The Moderate Resolution Imaging Spectroradiometer (MODIS) is known as an imaging device launched into globe orbit by means of NASA [13]. The devices capture records in 36 spectral bands varying in wavelength starting from 0.4×10^{-6} m to 14.4×10^{-6} m and at varying spatial motions. The Atmospheric Infrared Sounder, AIRS, is a service tool whose objective is to help climate study and develop weather prediction.

On the other hand, the Sentinel-2 operation, funded by the European Space Agency (ESA), includes two polar-orbiting satellites: Sentinel-2A and Sentinel-2B. It offers systematic overall treatment of land coverage and surfaces among latitudes 83° North and 56° South [14]. Various functions such as land cover change, agriculture, and mapping of biological parameters (leaf area indicator, leaf chlorophyll amount, and leaf water amount) can be estimated [14].

Sentinel-2A (launched in 2015) furnishes general reporting of the Earth's land every ten days and, when it is connected with Sentinel-2B (launched in 2017), the treatment duration has reduced to five days. The two satellites are similar and transmit a single mixture of general coverage: methodical and organized acquisition of high-resolution pictures, elevated revisit rate of five days, extensive vision field of approximately 290 km, elevated resolution of ten meters and, due to a high-tech Multispectral Imager, thirteen spectral bands [14, 15], of which three are comprised into the ‘red edge’ fraction of the spectral field.

Because of developed attributes evaluated to preceding operations, Sentinel-2 is able to identify early modifications in plant healthiness, to differentiate between diverse crop

TABLE 1: Common thermal bands of different sensors and their specifications.

Platform	Sensor	Spatial resolution (m)	Band(s)	Wavelength range (μm)
MTI	MWIR	20	J	3.50-4.10
			K	4.87-5.07
	LWIR		L	8.00-8.40
			M	8.40-8.85
			N	10.2-10.7
Landsat	TM	120	6	10.40-12.50
	ETM+	30	6	10.40-12.50
	OLI	TIRS 1	10.60-11.19	
TIRS 2		11.50-12.51		
ASTER	TIR	90	11	8.125-8.475
			12	8.475-8.825
			13	8.925-9.275
			14	10.250-10.950
			15	10.950-11.650
MODIS	TIR	1000	20	3.660-3.840
			21	3.929-3.989
			22	3.292-3.989
			23	4.020-4.080
			24	4.433-4.498
AVHRR	TIR	1090	25	4.482-4.549
			1	0.58-0.68
			2	0.725-1.00
			3A	1.58-1.64
			3B	3.55-3.93
	4	10.30-11.30		
	5	11.50-12.50		

varieties, and distribute appropriate data on diverse biophysical factors. These constituents can facilitate tasks of users and specialists to identify precursors of food deficiencies in countries [16].

Moreover, predictions of crop productions, modelling yield, and crop stress recognition have been determined via remote sensing records. Detection and recognition of plant illness and preparation for efficient manage estimations are important to sustain crop production. One of the possible appliances of remote sensing in farming is the estimation of crop acreage and recognition of crop situation because of either water stress or pest. Vigorous plants provide an elevated reflectance in the near-infrared area and an inferior in the observable area. Illness influenced plants demonstrate an elevated reflectance in the perceptible band and a minor in infrared area. This theory can be employed in discerning vigorous and infected crop.

Once plants are infected with malady, assimilation of incident solar ray transformations in the perceptible and Near-Infrared range [17], this is possibly caused by reduced chlorophyll quantity and modifications in internal organization. The variation of assimilation accordingly affects the reflectance of infected plants. As a result, in evaluating the

range difference of infected and vigorous plants, scientists are able to recognize the stress potency of green foliage (Table 2) [12].

While the chlorophyll quantity tends to diminish under illness emphasis, assimilation of incident solar rays by green vegetation declines in the perceptible area. Subsequently, spectral reflectance is important in the red region and declines in the Near-Infrared range depending on the contamination potency. The powerful spectral reflectance of green trees in the Near-Infrared array is principally provoked by its foliar internal constitution. Besides, plants with malady stress show different degrees of morphological internal transformations, which conduct to a decline of spectral reflectance in the Near-Infrared array. These spectral attributes of foliage are the foundation for remote sensing of malady-stressed vegetation [13].

4. Imagery Treatment and Prediction in Mapping

Remotely sensed information has been employed for evaluation of land cover ever since remote sensing initiated.

TABLE 2: Main spectral vegetation indices used in agriculture.

Index	Equation	Usefulness
NG	$G / (NIR+R+G)$	Carotenoids, anthocyanins, xanthophylls
NR	$R / (NIR+R+G)$	Chlorophyll
DVI	NIR-R	Soil reflectance
GDVI	NIR-G	Chlorophyll, N status
NDVI	$(NIR-R) / (NIR+R)$	Vegetation cover
GNDVI	$(NIR-G) / (NIR+G)$	Chlorophyll and photosynthesis, N status

Abbreviation: A=adapted, D=difference, G=green, N=normalized, NIR=near-infrared, R=red, RVI=Ratio Vegetation Index, VI= Vegetation Index.

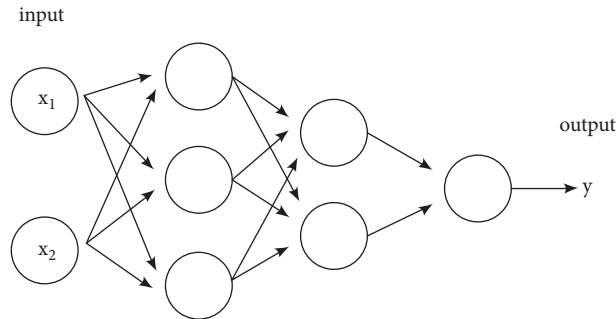


FIGURE 1: A neural network architecture.

Land cover estimation via employing remotely sensed records can no longer be identified as entire in the sense of their spatial and spectral determinations, except that land cover categorization of satellite images can be built by image operating and model detection methods [18]. Enhancement of land cover categorization and classification of satellite data can possibly be prepared by means of using techniques like k-nearest neighbor [19, 20], artificial neural nets [21, 22], decision tree analytical technique [23], and finally clustering division and segmentation methods for categorization [24, 25]. Artificial Neural Network designs the function or composition of biological neural networks. The principal objective is to achieve prototype matching for classification and regression problems. Nevertheless, the method imitates the approach employed by biological organisms rather than rigorously relying on an accurate math-based approach. Here are many examples of Artificial Neural Network architecture algorithms: Radial Basis Function Network (RBFN), Perceptron, Hopfield Network, Feed-forward Neural Network, and finally Self-Organizing Map (SOM) [26]. This algorithm is very helpful in finding samples that are in addition difficult for being physically mined and taught to identify to the calculation instrument. In the perspective of this composition, samples are initiated to the Artificial Neural Network via the input layer that has only one neuron for every element present in the input records and is corresponded to one or more hidden layers existing in the system [27]. In fact, the processing happens in the hidden layers through an arrangement of relationships distinguished via weights and biases. The input is collected and the neuron estimates a weighted amount accumulating as well the bias and in accordance with the outcome and a preset activation function, it makes a decision whether it should be discarded or

otherwise stimulated. Subsequently, the neuron spreads the record downstream to other joined neurons [28]. At the last part of the process, the final hidden layer is connected to the output layer which has one neuron for each potential wanted output (Figure 1).

Decision tree builds a model of decisions on the basis of real values found in records. The resulting tree configuration permits making comparisons among novel and existing data rapidly. This type of algorithm habitually sees application for regression and categorization problems [29]. Decision trees are machine learning algorithms that gradually separate data sets into less important data sets on the basis of an explanatory attribute, until they achieve sets that are little as much as necessary to be explained via a number of label (Figure 2). They necessitate that data is marked; hence they attempt to validate novel data based on this understanding. Decision tree algorithms are ideal to resolve regression and classification problems.

Regression trees are employed while the dependent value is considered as quantitative or continuous and classification trees are employed while the dependent value is considered as qualitative or categorical. We discern some frequent decision tree algorithms: Chi-squared Automatic Interaction Detection (CHAID), C4.5 and C5.0, Classification and Regression Tree (CART), and Iterative Dichotomiser 3 (ID3) [30].

Clustering method expresses a model for managing data through class or other norms. In general, information points that are in the identical set should have analogous characteristics or else descriptions (Figure 3), although information points in dissimilar sets should have very divergent characteristics or descriptions [31]. The results are frequently hierarchical or else centroid. We obtain data relationships in a way that assists making sense of the data, that is, how

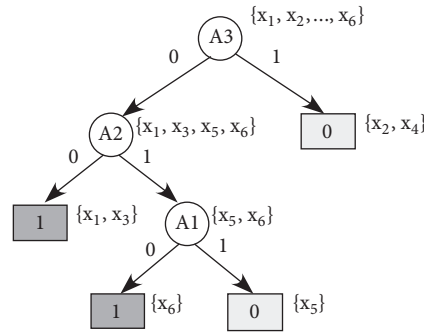


FIGURE 2: Example of decision tree.

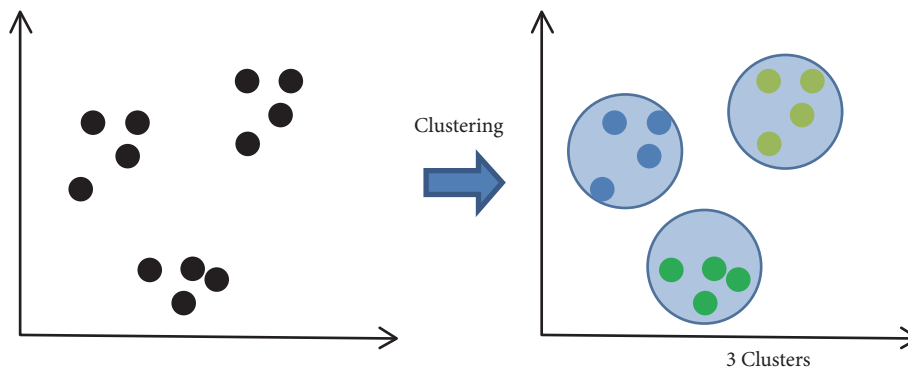


FIGURE 3: Example of clustering.

the values influence each other. There are many examples of clustering construction algorithms: Hierarchical Clustering, K-medians, Expectation Maximisation (EM), and K-means [32].

The imagery arrangement of remote sensing records either can be prepared in the direction of achieving different spectral groups on the basis of spectral brightness rate or can, besides, be further planned to instinctively concerned soil use categories in regard to the soil-truth plan. The soil-truth plan is made by means of assistance of user interface via imagery treatment method and understanding of categories on the land. Generally, the spectral model existing inside the information for every pixel is utilized as the numeric source for classification. Spectral model identification makes reference to the set of categorization processes that employs the pixel-per-pixel spectral data like the foundation for computerized land cover categorization [33]. Spatial form recognition holds the categorization of illustration pixels on the basis of the spatial connection among pixels neighboring them [34]. These sorts of groups try to repeat the type of spatial fusion done by means of special analysts through ocular analysis operations found on picture quality and texture, pixel nearness, attribute dimension, contour, and duplication, in addition to environment. The objective consists of determining spectral prototypes via spatial liaisons in given remote sensing records instead of exploring by a temporal methodology in which case one would investigate transformations in examples over the specific period of time by means of numerous years of records [35].

Spectral picture categorization is generally separated into two main categorization methods of supervised and unsupervised classifications. The basic distinction among these methods is that supervised classification entails a training stage succeeded by a categorization stage. In the unsupervised theory, the picture data are primarily categorized through combining them into the natural spectral assemblages, otherwise groups, contained in the recorded data. These spectral clusters are in that case categorized by evaluating them to soil reference record. Imagery experts can in addition decide how well a categorization has classified an illustrated subgroup of pixels employed in the training procedure by means of a precision estimate. Model-based clustering has expressed excellent results in imagery examination [36]. One of the most common indications of describing categorization precision is the construction of a classification error table. Obtained findings from the organization and arrangement of remotely sensed records are generally recapitulated as contingency table or else confusion matrix. Error matrices evaluate, on a categorical basis, the possible connection among reference records (symbolizing the soil reality) in addition to the related results of a computerized organization. These particular matrices are called square, through the sum of columns and rows equivalent to the sum of categories whose classification precision is being considered [37]. Picture categorization has frequently been achieved via employing usual numerical and machine learning methods in the earlier periods. Numerical methods such as Bayesian networks are excellent while the data is considered as normalized or noise-free [38], whereas

implicit designs, also known as machine learning algorithms, like Artificial Neural Networks (ANN), are further than a “black box” system, depending on repetitive training in the aim of regulating and adjusting factors by transferring functions to enhance their projecting aptitude concerning training results for which the outputs are acknowledged [39, 40]. The numerical theory achieves more once *a priori* instruction regarding categories is accessible; nevertheless they have restrictions in the case of purpose categorization and when the dispersion of recorded points are not identified, like the case with remote sensing spatial records. Data mining skills have become progressively more important methods to treat information from a large pool of records [41].

The word “data mining” has existed for a few decades, while the majority of the machine learning processes and statistics, for example, Artificial Neural Networks (ANN) and Decision Tree (DT), nowadays attached with data mining were progressed [42].

Nowadays, numerous image classification techniques have been ameliorated and employed to extract significant information from remote sensing descriptions [43]. Assortment of appropriate classification techniques is especially imperative to effectively extract useful results from imagery [43]. Analytical classifiers such as Artificial Neural Networks [44] and Decision Tree [45] do not employ statistical factors to recognize classes. They are better adapted for investigating noisy, multimodal, and/or missing records [18]. In fact, Szuster et al. [46] studied the land cover and land use classification via Artificial Neural Networks. Lakshmi and Vijaya [47] used machine learning methods such as decision tree and Artificial Neural Networks for categorization and classification on the samples. The samples were able to attain good precision, which was elevated for decision trees when evaluating with others. On the other hand, Zanaty [48] applied an evaluation study by using Artificial Neural Networks and Support Vector Machines for data classification and categorization.

Data mining for spatial form recognition is the method of determining interesting information, for instance, configurations, relationships, modifications, irregularities, and major organisations, from big volumes of data stocked in data servers or other data sources [49]. Because of the disposal of colossal quantities of records, data mining has attracted important consideration in the information management business. Generally, data mining assignments can be categorized into two classes: predictive and descriptive data mining [50]. The latter refers to the information set in a brief way and highlights common data characteristics; the first achieves interpretation on the obtainable data set and efforts to forecast the novel data compartment.

A data mining structure could realize at least one of the data mining assignments: (1) arrangement, (2) connection, (3) forecast, and (4) clustering [51]. Between diverse data mining methods and techniques, the Artificial Neural Network (ANN) technique is one of the most extensively employed methodologies in engineering, particularly when data or information is accessible from several sources, in addition to *a priori* understanding of explanatory arrangements or developments which is accessible because of

capacity of ANN to study complex configurations rapidly [52]. This method was successfully employed in many fields as biology [53–56], physics [57, 58], chemistry [59, 60], etc. Besides, the decision tree systems of data mining approaches are more directly adapted for classification, from the time when data symbolising a specified individual are classed through the decision tree construction to be classified directly into a preprogrammed group [61, 62]. They not only signify an effective organization technique, but also have the supplementary benefit of simplicity of elucidation of the factors employed to classify data sets to their suitable groups, although concurrently carrying to highlight the relative significance of diverse variables in the concerned system [63, 64]. It is particularly laborious to retrieve clarifications for occurrences when ANN methods are employed because of the “black-box” methodology in ANN [65].

The designs are learnt by ANN via iterative learning successions of illustrative data, hence generating forecasts of spectral ranges by detecting unidentified pixels [66, 67]. Decision trees, conversely, employ dichotomization to route available data to the precise group, as is observed in vegetal basics. Even if the distinction conditions at each stage of the decision tree arrangement are produced by the software, it is probable to examine the conditions in an effort to comprehend what origin distinction has been completed [68, 69].

5. Conclusion

Remote sensing as a device will provide information frequently and at an inexpensive value to permit, in the appropriate time, interference for recovery of crop state. Satellite structures offer spatially and temporally permanent records cover of the globe. Along through the expansion of remote sensing functions, satellite information has become the principal data foundation to supervise high-dimension crop situation. With the aid of satellite and digital imaging methods, it is simple and also price efficient in planning and observing the crop situation.

Conflicts of Interest

The authors declare that there are no conflicts of interest regarding the publication of this paper.

References

- [1] P. Li and W. Ge, “A soft shadow detection method based on MRF for remote sensing images,” *Mathematical Problems in Engineering*, 2015.
- [2] J. M. Salmon, M. A. Friedl, S. Frolking, D. Wisser, and E. M. Douglas, “Global rain-fed, irrigated, and paddy croplands: A new high resolution map derived from remote sensing, crop inventories and climate data,” *International Journal of Applied Earth Observation and Geoinformation*, vol. 38, pp. 321–334, 2015.
- [3] M. Wang, S. Son, and W. Shi, “Evaluation of MODIS SWIR and NIR-SWIR atmospheric correction algorithms using SeaBASS

- data,” *Remote Sensing of Environment*, vol. 113, no. 3, pp. 635–644, 2009.
- [4] Z. Dong, Z. Wang, D. Liu et al., “Mapping wetland areas using landsat-derived ndvi and lswi: a case study of west songnen plain, northeast china,” *Journal of the Indian Society of Remote Sensing*, vol. 42, no. 3, pp. 569–576, 2014.
 - [5] P. Rahimzadeh-Bajgiran, K. Omasa, and Y. Shimizu, “Comparative evaluation of the Vegetation Dryness Index (VDI), the Temperature Vegetation Dryness Index (TVDI) and the improved TVDI (iTVDI) for water stress detection in semi-arid regions of Iran,” *ISPRS Journal of Photogrammetry and Remote Sensing*, vol. 68, pp. 1–12, 2012.
 - [6] A. A. Gitelson, Y. J. Kaufman, R. Stark, and D. Rundquist, “Novel algorithms for remote estimation of vegetation fraction,” *Remote Sensing of Environment*, vol. 80, no. 1, pp. 76–87, 2002.
 - [7] J. L. Hatfield, A. A. Gitelson, J. S. Schepers, and C. L. Walthall, “Application of spectral remote sensing for agronomic decisions,” *Agronomy Journal*, vol. 100, no. Supplement_3, p. S-117, 2008.
 - [8] M. Borengasser, W. S. Hungate, and R. Watkins, *Hyperspectral Remote Sensing: Principles and Applications*, CRC press, 2007.
 - [9] D. Huang, D. Zhao, L. Wei, Z. Wang, and Y. Du, “Modeling and analysis in marine big data: advances and challenges,” *Mathematical Problems in Engineering*, 2015.
 - [10] T. Blaschke, S. Lang, and G. Hay, *Object-Based Image Analysis: Spatial Concepts for Knowledge-Driven Remote Sensing Applications*, Springer Science & Business Media, 2008.
 - [11] B. Bhatta, *Remote Sensing and GIS*, Oxford University Press, 2008.
 - [12] C. Pohl and J. V. Genderen, *Remote Sensing Image Fusion: A Practical Guide*, CRC Press, 2016.
 - [13] X. Zhang, M. A. Friedl, C. B. Schaaf et al., “Monitoring vegetation phenology using MODIS,” *Remote Sensing of Environment*, vol. 84, no. 3, pp. 471–475, 2003.
 - [14] ESA, *Sentinel-2 User Handbook*, 2015.
 - [15] F. Gascon, “Sentinel-2 products and algorithms,” in *Workshop Preparations for Sentinel 2 in Europe*, Oslo, Norway, 2014.
 - [16] ESA, *S2 MPC – Data Quality Report*, vol. 16, European Space Agency, 2017.
 - [17] G. A. Carter and A. K. Knapp, “Leaf optical properties in higher plants: linking spectral characteristics to stress and chlorophyll concentration,” *American Journal of Botany*, vol. 88, no. 4, pp. 677–684, 2001.
 - [18] J. Rogan and D. Chen, “Remote sensing technology for mapping and monitoring land-cover and land-use change,” *Progress in Planning*, vol. 61, no. 4, pp. 301–325, 2004.
 - [19] Q. Meng, C. J. Cieszewski, M. Madden, and B. E. Borders, “K nearest neighbor method for forest inventory using remote sensing data,” *GIScience & Remote Sensing*, vol. 44, no. 2, pp. 149–165, 2007.
 - [20] E. Blanzieri and F. Melgani, “Nearest Neighbor Classification of Remote Sensing Images With the Maximal Margin Principle,” *IEEE Transactions on Geoscience and Remote Sensing*, vol. 46, no. 6, pp. 1804–1811, 2008.
 - [21] J. Wang, T. Zheng, P. Lei, and X. Bai, “A hierarchical convolution neural network (cnn)-based ship target detection method in spaceborne sar imagery,” *Remote Sensing*, vol. 11, no. 6, p. 620, 2019.
 - [22] L. Wang, Y. Jia, Y. Yao, and D. Xu, “Accuracy assessment of land use classification using support vector machine and neural network for coal mining area of hegang city,” *Nature Environment and Pollution Technology*, vol. 18, no. 1, pp. 335–341, 2019.
 - [23] Z. Xie, M. Wang, Y. Han, and D. Yang, “Hierarchical decision tree for change detection using high resolution remote sensing images,” in *Proceedings of the International Conference on Geoinformatics in Sustainable Ecosystem and Society*, pp. 176–184, Springer, Singapore, 2018.
 - [24] Y. Zhong and L. Zhang, “A new fuzzy clustering algorithm based on clonal selection for land cover classification,” *Mathematical Problems in Engineering*, 2011.
 - [25] F. Ye, W. Luo, M. Dong, H. He, and W. Min, “SAR image retrieval based on unsupervised domain adaptation and clustering,” *IEEE Geosci. Remote S*, 2019.
 - [26] K. Gurney, *An Introduction to Neural Networks*, CRC press, 2014.
 - [27] J. Cao and Z. Lin, “Extreme learning machines on high dimensional and large data applications: a survey,” *Mathematical Problems in Engineering*, 2015.
 - [28] Yu-Jun Zheng, Sheng-Yong Chen, Yao Lin, and Wan-Liang Wang, “Bio-inspired optimization of sustainable energy systems: a review,” *Mathematical Problems in Engineering*, vol. 2013, Article ID 354523, 12 pages, 2013.
 - [29] L. Breiman, *Classification and Regression Trees*, Routledge, 2017.
 - [30] C. C. Aggarwal, *Data Classification: Algorithms and Applications*, CRC Press, 2014.
 - [31] A. A. A. Esmin, R. A. Coelho, and S. Matwin, “A review on particle swarm optimization algorithm and its variants to clustering high-dimensional data,” *Artificial Intelligence Review*, 2013.
 - [32] B. Mirkin, *Mathematical Classification and Clustering*, vol. 11, Springer Science & Business Media, 2013.
 - [33] R. Sharma, S. S. Kamble, and A. Gunasekaran, “Big GIS analytics framework for agriculture supply chains: A literature review identifying the current trends and future perspectives,” *Computers and Electronics in Agriculture*, vol. 155, pp. 103–120, 2018.
 - [34] H. Zhang and D. Li, “Applications of computer vision techniques to cotton foreign matter inspection: a review,” *Computers and Electronics in Agriculture*, vol. 109, pp. 59–70, 2014.
 - [35] S. Sankaran, A. Mishra, R. Ehsani, and C. Davis, “A review of advanced techniques for detecting plant diseases,” *Comput. Electron Agr*, vol. 72, no. 1, pp. 1–13, 2010.
 - [36] R. Wehrens, L. M. Buydens, C. Fraley, and A. E. Raftery, “Model-based clustering for image segmentation and large datasets via sampling,” *Journal of Classification*, vol. 21, no. 2, pp. 231–253, 2004.
 - [37] R. G. Congalton and K. Green, *Assessing the Accuracy of Remotely Sensed Data: Principles and Practices*, CRC press, 2008.
 - [38] A. Kamilaris, A. Kartakoullis, and F. X. Prenafeta-Boldú, “A review on the practice of big data analysis in agriculture,” *Computers and Electronics in Agriculture*, vol. 143, pp. 23–37, 2017.
 - [39] B. Yegnanarayana, *Artificial Neural Networks*, PHI Learning Pvt. Ltd, 2009.
 - [40] G. Daniel, *Principles of Artificial Neural Networks*, vol. 7, World Scientific, 2013.
 - [41] M. Kantardzic, *Data Mining: Concepts, Models, Methods, And Algorithms*, John Wiley & Sons, 2011.

- [42] H. F. Jelinek, J. H. Abawajy, A. V. Kelarev, M. U. Chowdhury, and A. Stranieri, "Decision trees and multi-level ensemble classifiers for neurological diagnostics," *AIMS Medical Science*, vol. 1, no. 1, pp. 1–12, 2014.
- [43] D. Lu and Q. Weng, "A survey of image classification methods and techniques for improving classification performance," *International Journal of Remote Sensing*, vol. 28, no. 5, pp. 823–870, 2007.
- [44] T. Kavzoglu and P. M. Mather, "The use of backpropagating artificial neural networks in land cover classification," *International Journal of Remote Sensing*, vol. 24, no. 23, pp. 4907–4938, 2003.
- [45] M. C. Hansen, R. S. Defries, J. R. G. Townshend, and R. Sohlberg, "Global land cover classification at 1 km spatial resolution using a classification tree approach," *International Journal of Remote Sensing*, vol. 21, no. 6-7, pp. 1331–1364, 2000.
- [46] B. W. Szuster, Q. Chen, and M. Borger, "A comparison of classification techniques to support land cover and land use analysis in tropical coastal zones," *Applied Geography*, vol. 31, no. 2, pp. 525–532, 2011.
- [47] S. V. Lakshmi and M. S. Vijaya, "Efficient prediction of phishing websites using supervised learning algorithms," *Procedia Engineering*, vol. 30, pp. 798–805, 2012.
- [48] E. A. Zanaty, "Support vector machines (svms) versus multi-layer perceptron (mlp) in data classification," *Egyptian Informatics Journal*, vol. 13, no. 3, pp. 177–183, 2012.
- [49] H. Li, Z. Zhang, and Z. Z. Zhao, "Data-Mining for processes in chemistry, materials, and engineering," *Processes*, vol. 7, no. 3, p. 151, 2019.
- [50] S. García, J. Luengo, F. Herrera, and S. García, *Data Preprocessing in Data Mining*, Springer, New York, NY, USA, 2015.
- [51] R. J. Roiger, *Data Mining: a Tutorial-Based Primer*, Chapman and Hall/CRC, 2017.
- [52] O. I. Abiodun, A. Jantan, A. E. Omolara, K. V. Dada, N. A. Mohamed, and H. Arshad, "State-of-the-art in artificial neural network applications: A survey," *Heliyon*, vol. 4, no. 11, Article ID e00938, 2018.
- [53] K. Ennouri, R. B. Ayed, M. A. Triki et al., "Multiple linear regression and artificial neural networks for delta-endotoxin and protease yields modelling of *Bacillus thuringiensis*," *3 Biotech*, vol. 7, no. 3, p. 187, 2017.
- [54] K. Ennouri, H. B. Hlima, R. B. Ayed et al., "Assessment of Tunisian virgin olive oils via synchronized analysis of sterols, phenolic acids, and fatty acids in combination with multivariate chemometrics," *European Food Research and Technology*, pp. 1–14, 2019.
- [55] A. Kamilaris and F. X. Prenafeta-Boldú, "Deep learning in agriculture: a survey," *Computers and Electronics in Agriculture*, vol. 147, pp. 70–90, 2018.
- [56] S. Smaoui, K. Ennouri, A. Chakchouk-Mtibaa et al., "Modeling-based optimization approaches for the development of Anti-*Agrobacterium tumefaciens* activity using *Streptomyces* sp TN71," *Microbial Pathogenesis*, vol. 119, pp. 19–27, 2018.
- [57] M. R. Hush, "Machine learning for quantum physics," *Science*, vol. 355, no. 6325, pp. 580–580, 2017.
- [58] J. A. Hertz, *Introduction to the Theory of Neural Computation*, CRC Press, 2018.
- [59] G. B. Goh, N. O. Hodas, and A. Vishnu, "Deep learning for computational chemistry," *Journal of Computational Chemistry*, vol. 38, no. 16, pp. 1291–1307, 2017.
- [60] H. Li, Z. Zhang, and Z. Liu, "Application of artificial neural networks for catalysis: a review," *Journal of Catalysis*, vol. 7, no. 10, p. 306, 2017.
- [61] M. Benza, J. R. Weeks, D. A. Stow, D. López-Carr, and K. C. Clarke, "A pattern-based definition of urban context using remote sensing and GIS," *Remote Sensing of Environment*, vol. 183, pp. 250–264, 2016.
- [62] W. Chen, X. Xie, J. Peng, J. Wang, Z. Duan, and H. Hong, "GIS-based landslide susceptibility modelling: a comparative assessment of kernel logistic regression, Naïve-Bayes tree, and alternating decision tree models," *Geomatics, Natural Hazards and Risk*, vol. 8, no. 2, pp. 950–973, 2016.
- [63] J. Im, Z. Lu, J. Rhee, and L. J. Quackenbush, "Impervious surface quantification using a synthesis of artificial immune networks and decision/regression trees from multi-sensor data," *Remote Sensing of Environment*, vol. 117, pp. 102–113, 2012.
- [64] K. Ennouri, R. B. Ayed, S. Ercisli, S. Smaoui, M. Gouiaa, and M. A. Triki, "Variability assessment in Phoenix dactylifera L. accessions based on morphological parameters and analytical methods," *Acta Physiologiae Plantarum*, vol. 40, no. 1, p. 5, 2018.
- [65] S. J. Russell and P. Norvig, *Artificial Intelligence: A Modern Approach*, Pearson Education Limited, Malaysia, 2016.
- [66] F. Hu, G.-S. Xia, J. Hu, and L. Zhang, "Transferring deep convolutional neural networks for the scene classification of high-resolution remote sensing imagery," *Remote Sensing*, vol. 7, no. 11, pp. 14680–14707, 2015.
- [67] B. Yang, C. Cao, Y. Xing, and X. Li, "Automatic classification of remote sensing images using multiple classifier systems," *Mathematical Problems in Engineering*, 2015.
- [68] M. Xu, P. Watanachaturaporn, P. K. Varshney, and M. K. Arora, "Decision tree regression for soft classification of remote sensing data," *Remote Sensing of Environment*, vol. 97, no. 3, pp. 322–336, 2005.
- [69] H. Duan, Z. Deng, F. Deng, and D. Wang, "Assessment of groundwater potential based on multicriteria decision making model and decision tree algorithms," *Mathematical Problems in Engineering*, 2016.

Research Article

Mechanism of Fracturing in Shaft Lining Caused by High-Pressure Pore Water in Stable Rock Strata

Jihuan Han ¹, Jiuqun Zou,¹ Weihao Yang ^{1,2} and Chenchen Hu ¹

¹State Key Laboratory for Geomechanics and Deep Underground Engineering, China University of Mining and Technology, Xuzhou 221116, Jiangsu Province, China

²School of Mechanics and Civil Engineering, China University of Mining and Technology, Xuzhou 221116, Jiangsu Province, China

Correspondence should be addressed to Weihao Yang; whyang@cumt.edu.cn

Received 8 March 2019; Revised 3 June 2019; Accepted 11 June 2019; Published 26 June 2019

Guest Editor: Raffaele Albano

Copyright © 2019 Jihuan Han et al. This is an open access article distributed under the Creative Commons Attribution License, which permits unrestricted use, distribution, and reproduction in any medium, provided the original work is properly cited.

With the increase in shaft depth, the problem of cracks and leakage in single-layer concrete lining in porous water-rich stable rock strata has become increasingly clear, in which case the mechanism of fracturing in shaft lining remains unclear. Considering that the increase in pore water pressure can cause rock mass expansion, this paper presents the concept of hydraulic expansion coefficient. First, a cubic model containing spherical pores is established for studying hydraulic expansion, and the ANSYS numerical simulation, a finite element numerical method, was used for calculating the volume change of the model under the pore water pressure. By means of the multivariate nonlinear regression method, the regression equation of the hydraulic expansion coefficient is obtained. Second, based on the hydraulic expansion effect on the rock mass, an interaction model of pore water pressure-porous rock-shaft lining is established and further solved. Consequently, the mechanism of fracturing in shaft lining caused by high-pressure pore water is revealed. The results show that the hydraulic expansion effect on the surrounding rock increases with its porosity and decreases with its elastic modulus and Poisson's ratio; the surrounding rock expansion caused by the change in pore water pressure can result in the outer edge of the lining peeling off from the surrounding rock and tensile fracturing at the inner edge. Therefore, the results have a considerable guiding significance for designing shaft lining through porous water-rich rock strata.

1. Introduction

In recent years, with the implementation of China's western development strategy, the abundant coal resources in some water-rich bedrock areas (Shaanxi, Ningxia, Gansu, Inner Mongolia, etc.) have been mined on a large scale [1]. Since the shaft is the passageway of mine production, the shaft lining should be designed with sufficient strength, rigidity, and waterproof performance to meet the requirements of safety, sealing, and durability. However, with the increase in coal mining depth, the non-mining-related deformation and fracture of the shaft lining under the action of high water pressure is still very serious. At present, scholars at home and abroad have carried out a lot of considerable research on shaft fracture caused by groundwater activities. Regarding the study topic on groundwater seepage, Farmer [2] studied the hydrostatic stresses acting on shaft lining based on the

theory of surrounding rock permeability. Bear [3] carried out a microscopic study on the seepage mechanism, indicating that the change in pore shape is a sensitive factor that causes permeability coefficient changes. Bruno [4] studied the effect of pore pressure on the tensile fracture of rock on the basis of Biot theory and noted the importance of fluid-solid coupling in hydraulic fracturing. Zimmerman [5] briefly deduced the linear porous-elasticity and thermoelastic equation by using the three-dimensional fluid-solid coupling seepage model. Jiang [6] used a high-pressure permeability test to simulate the deformation law of rock mass fracturing under the action of pore water pressure. Regarding the study topic on hydrophobic settlement, Lou [7] derived a general formula for calculating the additional stress in the shaft lining based on the drainage consolidation theory. According to the principle of superposition and strain compatibility, Yang [8] derived the theoretical solution of vertical additional stress

on the shaft lining by using a numerical method. Wang [9] obtained the additional stress value at complex alluvium strata by the negative friction coefficient between the shaft lining and surrounding rock. Zhang [10] studied the fluid-solid coupling numerical simulation of sharp severely aquifer drainage in underground mining and analyzed the influence of drainage location and drainage rate on the stability of shaft lining. Regarding the study on unstable rock strata, Sun [11] simulated and analyzed the deformation and stress characteristics of surrounding rock and shaft lining under the interactive geological conditions of soft and hard rock strata, and the conclusion that the shear failure occurred in shaft lining under the inhomogeneous pressure of surrounding rock was obtained. In addition, Yang [12] deduced the elastic approximate stress and displacement solution of irregular inclined shaft lining subjected to water pressure and proposed the optimal design for inclined shaft lining. Meng [13] classified and studied the constructing techniques for the inclined shaft penetrating the drift sand stratum, and the problems such as the stability of inclined shaft structure and the sealing of water and sand were solved. It is well known that shaft lining in porous water-rich rock strata is constructed by the temporary drainage method or the frozen water method. When the drainage or freezing is stopped, the pore water pressure of the surrounding rock will rise, and at this time, cracking and leakage of lining often occurs. However, no leakage occurs before the shaft lining fractures, inhibiting seepage in the surrounding rock. Additionally, the theory of vertical additional stress caused by mining hydrophobic settlement is applicable to mainly alluvium. Clearly, although some existing theories have matured, the fracture mechanism of shaft lining in high-pressure water-rich stable rock strata has not been clarified.

Based on the compressive and expansive deformation properties of the porous media under the action of stress, in analogy with the coefficient of thermal expansion, this paper defines the linear expansion coefficient of the rock caused by unit pore water pressure as the hydrostatic expansion coefficient, which is expressed as α . With the advantage of solving complex problems that cannot be solved by theoretical and experimental research and having the characteristics suitable for any problem geometry and boundary conditions [14], the finite element numerical method has become one of the most effective methods to solve scientific and engineering problems. Therefore, the ANSYS numerical simulation is adopted to obtain the volume change of the cubic model under the pore water pressure. Based on the calculation results, the approximate analytical solution of the hydraulic expansion coefficient is derived by means of the multivariate nonlinear regression method. By comprehensively analyzing the influence of various factors on the shaft lining stress, the mechanism of fracturing in shaft lining due to high-pressure pore water is clarified, providing an effective and scientific basis for lining safety.

2. Hydraulic Expansion Coefficient Solution

2.1. Basic Assumptions. (1) The rock mass is composed of an infinite number of identical cubic microunits containing

spherical pores of equal diameter, and the rock is a homogeneous and isotropic linear elastic medium.

(2) The effect of pore water pressure on a microunit can be regarded as free expansion, and the effect on the rock is the superposition of the expansive effect of each microunit [15].

The elastic modulus, Poisson's ratio, and porosity of the cubic model containing spherical pores are expressed by E_0 , μ_0 , and n_0 , respectively. Since the elastic modulus reflects the degree of rock elastic deformation, E_0 is clearly inversely proportional to α . According to the basic assumptions, the hydraulic expansion coefficient of the entire porous water-rich rock is equal to that of any single cubic microunit containing spherical pores under conditions of a free boundary. Assuming α_v is the volumetric hydraulic expansion coefficient of the rock, $\alpha_v = 3\alpha$ when the infinitesimal of higher order is ignored. Considering that n_0 and μ_0 are both dimensionless parameters, then αE_0 can be studied as dimensionless. When the compressive stress is specified as positive, the following equations can be derived from the theory of elastic mechanics.

$$\tilde{\alpha} = \frac{\Delta\tilde{V}}{(3\Delta\tilde{p}_w)}, \quad (1)$$

$$n_0 = \frac{\pi\tilde{r}_0^3}{6}, \quad (2)$$

$$\tilde{\alpha} = \alpha E_0,$$

$$\Delta\tilde{p}_w = \frac{\Delta p_w}{E_0}, \quad (3)$$

$$\Delta\tilde{V} = \frac{\Delta V}{V},$$

$$\tilde{r}_0 = \frac{r_0}{a} < 1,$$

where V is the total volume of the cubic model, p_w is the pore water pressure, r_0 is the pore radius, and a is the half length of the microunit.

2.2. Solution Result. According to the characteristics of the solution model, a 1/8 cubic model containing spherical pore is established by ANSYS numerical simulation, and the volume change in the model with different values of n_0 and μ_0 under the action of pore water pressure is calculated. When $\Delta\tilde{p}_w = 0.1$, taking $n_0=0.1$, $\mu_0=0.2$ as an example, the model after mesh generation is shown in Figure 1, and the equivalent displacement cloud of the model after solution is shown in Figure 2.

By means of the same method, $\Delta\tilde{V}$ can be calculated with different parameters of cubic model, as shown in Figure 3.

Based on the changing laws of the data in Figure 3, the multivariate nonlinear regression method is adopted to obtain the expression of $\Delta\tilde{V}$ for n_0 and μ_0 , which satisfies that when $n_0 \approx 0$, $\Delta\tilde{V} \approx 0$. Toward this goal, the objective function can be expressed as

$$\Delta\tilde{V} = \frac{\Delta\tilde{p}_w n_0 (\lambda_1 n_0^2 + \lambda_2 n_0 + \lambda_3) (\lambda_4 - \mu_0)}{(\lambda_5 - n_0)}, \quad (4)$$

TABLE 1: Regression coefficients values.

λ_1	λ_2	λ_3	λ_4	λ_5	R^2
-3.509	-0.261	1.952	1.087	0.505	0.9995

Note: R^2 is the goodness of fit.

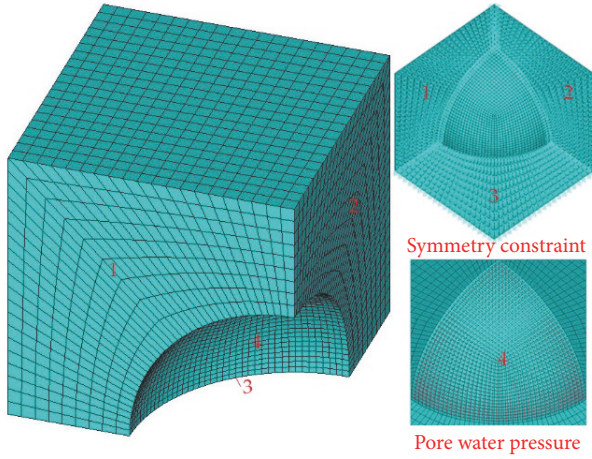


FIGURE 1: Mesh generation.

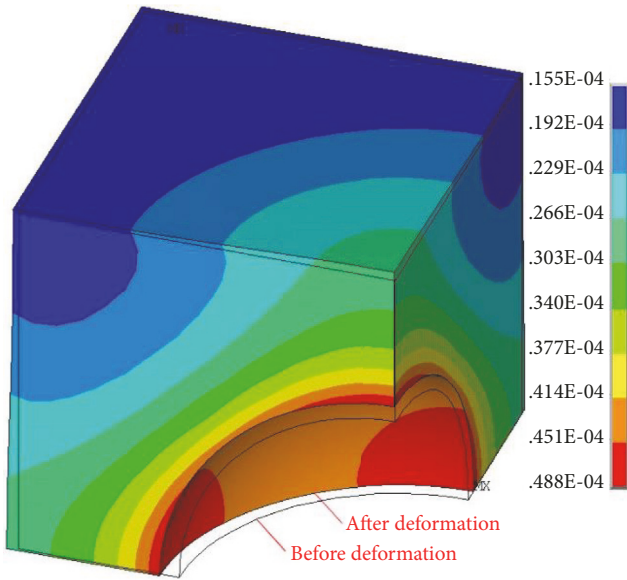
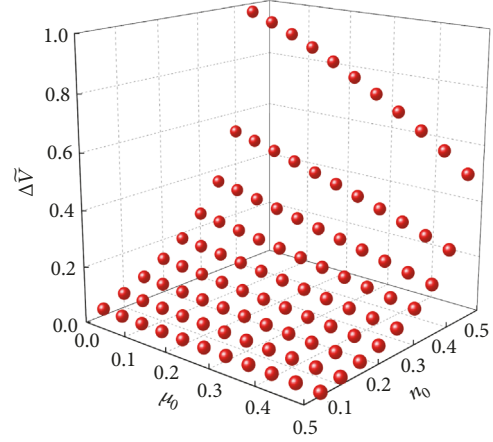


FIGURE 2: Equivalent displacement cloud (deformation scale factor: 1000).

where n_0 satisfies the general rock porosity value; i.e., $n_0 < 0.5$, $\lambda_1, \lambda_2, \lambda_3, \lambda_4$, and λ_5 are the regression coefficients, the values of which are shown in Table 1.

Substitute (4) into (1). Then,

$$\bar{\alpha} = \frac{n_0 (0.651 - 0.087n_0 - 1.17n_0^2)}{0.505 - n_0} (1.087 - \mu_0). \quad (5)$$


 FIGURE 3: Values of $\Delta\bar{V}$ with different parameters.

3. The Variation Law of the Coefficient of Hydraulic Expansion

3.1. Regular Analysis. Analysis of the relationship between the hydraulic expansion coefficient and the various parameters is helpful to better understand the influence law of hydraulic expansion on underground structures in different water-rich rock strata and has an important guiding significance for mitigation of the shaft lining fracture problem. Therefore, the partial derivatives of n_0 and μ_0 for (5) are solved, and (6) and (7) are always satisfied.

$$\frac{\partial \bar{\alpha}}{\partial n_0} > 0, \quad (6)$$

$$\frac{\partial \bar{\alpha}}{\partial \mu_0} < 0, \quad (7)$$

$$\frac{\partial^2 \bar{\alpha}}{\partial \mu_0^2} = 0.$$

The results show that the hydraulic expansion coefficient increases with n_0 and linearly decreases with μ_0 .

3.2. Influence of Pore Shape on Hydraulic Expansion Effect. Rock is a typical porous medium, in which the internal pores are not a sphere but an irregular space with various forms and a fractal dimension [16]. Therefore, an equal-porosity cubic model with a regular N -polyhedron is adopted to analyze the influence of pore shape on the hydrostatic expansion effect, where $N=4, 6, 8, 12, 20$, and ∞ (sphere). If the hydraulic expansion coefficient of the model with a regular N -polyhedron pore is expressed as α_N , then $\bar{\alpha}_N =$

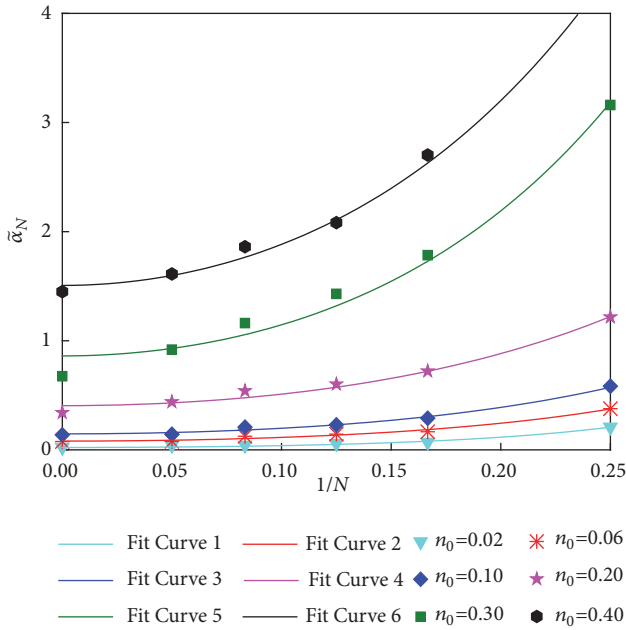
TABLE 2: Fitting coefficient values.

Curve Num.	n_0	η_1	η_2	R^2	Adj. R^2
1	0.02	0.651	10.920	0.9837	0.9796
2	0.06	0.669	8.877	0.9831	0.9789
3	0.10	0.719	8.304	0.9910	0.9887
4	0.20	1.031	7.003	0.9818	0.9772
5	0.30	1.432	7.896	0.9847	0.9808
6	0.40	1.878	7.124	0.9856	0.9809

Note: Adj. R^2 is the goodness of fit after correction.

TABLE 3: The range value of $f(n_0, N)$.

N	4	6	8	12	20
$f(n_0, N)$	3.0~7.8	1.8~3.0	1.5~2.0	1.2~1.6	1.0~1.4

FIGURE 4: The relationship between $\tilde{\alpha}_N$ and $1/N$.

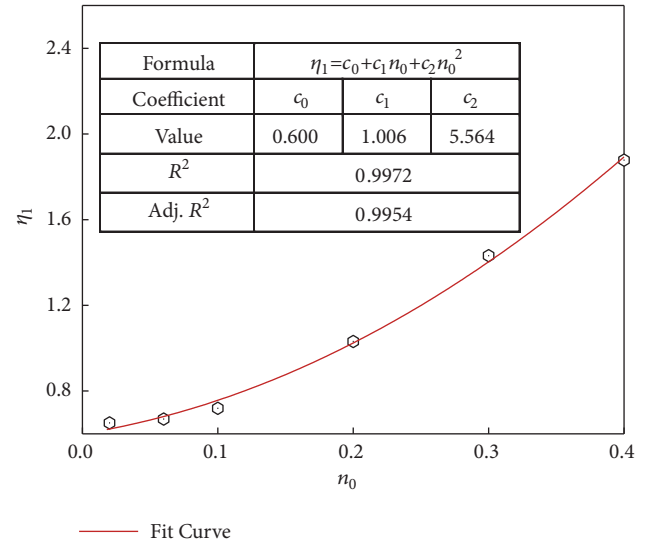
$\alpha_N E_0$. Taking $\mu_0=0.2$ as an example, the relationship between $\tilde{\alpha}_N$ and $1/N$ at different n_0 values can be obtained by the ANSYS numerical simulation (see Figure 4). The expressions of the fitting function in Figure 4 can be expressed in the form of (8), and the corresponding fitting coefficient values are shown in Table 2.

As shown in Figure 4, $\tilde{\alpha}_N$ increases with n_0 and decreases with N . The hydraulic expansion coefficient of the model containing the tetrahedral pore is the largest, while that of the model containing the spherical pore is the smallest.

$$\tilde{\alpha}_N = n_0 \eta_1 \left[\exp\left(\frac{\eta_2}{N}\right) + \exp\left(\frac{-\eta_2}{N}\right) \right], \quad (8)$$

where η_1 and η_2 are both functions in terms of n_0 .

Based on the data in Table 2, the polynomial regression formulae of η_1 and η_2 can be calculated, as shown in Figures 5 and 6, respectively.

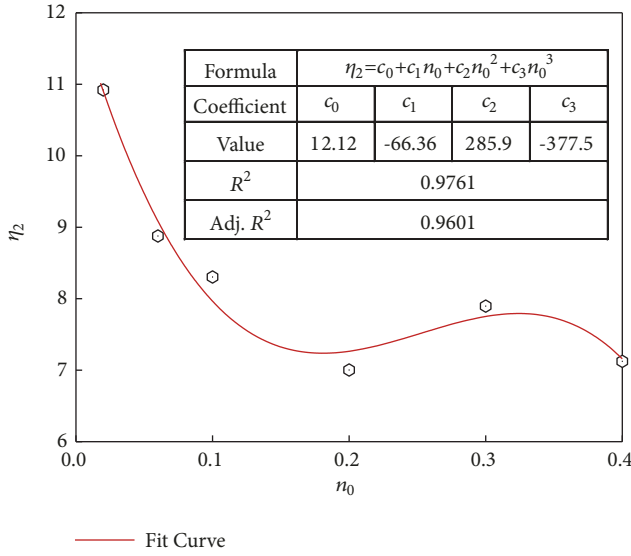
FIGURE 5: The expression of η_1 .

Since both $\tilde{\alpha}_N$ and $\tilde{\alpha}$ are functions of regarding n_0 and N , the function $f(n_0, N)$ can be used to represent the value of $\tilde{\alpha}_N/\tilde{\alpha}$. When $\mu_0=0.2$, the expression of $f(n_0, N)$ can be derived from (5) and (8) as follows:

$$f(n_0, N) = \frac{(0.505 - n_0) \eta_1 [\exp(\eta_2/N) + \exp(-\eta_2/N)]}{0.577 - 0.077n_0 - 1.038n_0^2} \quad (9)$$

The value of $f(n_0, N)$ for different rock porosities can be solved by (9). Therefore, when μ_0 is between 0.1 and 0.3 and n_0 is between 0.02 and 0.4, the range of $f(n_0, N)$ can be obtained, as seen in Table 3.

As seen in Table 3, the hydraulic expansion coefficient of the model containing regular polyhedral pores is approximately (1.0~7.8) α and decreases with the number of pore faces.


 FIGURE 6: The expression of η_2 .

4. Mechanism of Shaft Lining Fracture Analysis

4.1. Stress and Displacement Solution

4.1.1. Basic Assumptions. In the absence of water, the elastic moduli of the surrounding rock and the shaft lining are E_1 and E_2 , the corresponding Poisson's ratios are μ_1 and μ_2 , the corresponding porosities are n_1 and n_2 , respectively, and the porosity of the contact surface between the surrounding rock and the shaft lining is n_3 .

According to the nature of the problem, the following assumptions are made.

(1) The elastic modulus and Poisson's ratio of the surrounding rock mass and the rock matrix approximately satisfy the linear relations as follows:

$$E_1 = E_0 (1 - k_1 n_1), \quad (10)$$

$$\mu_1 = \mu_0 (1 - k_2 n_1), \quad (11)$$

where k_1 and k_2 are constants related to pore shape, for spherical pores [17]: $k_1=2.08$, and $k_2=0.345$.

(2) The porosity of contact surface n_3 can be calculated according to the probability statistical method, namely, $n_3 = n_1 + n_2 - n_1 n_2$.

(3) The shaft lining is a homogeneous, continuous, and isotropic linear elastic medium.

(4) The expansion effect of the pore water pressure on the surrounding rock can be equivalent to the volume expansion of elastomer, which is similar to the thermal expansion.

(5) The inner and outer radii of the shaft lining are r_1 and r_2 , respectively, and the inner and outer radii of the surrounding rock are r_2 and r_3 , respectively. The outer boundary of the surrounding rock is fixed, as shown in Figure 7.

Assume that the interaction force between the surrounding rock and the shaft lining under the action of

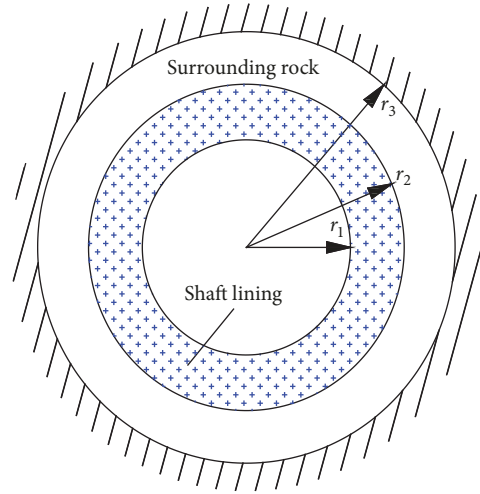


FIGURE 7: Stress analysis model of shaft lining.

pore water pressure is a compressive stress, and the stress direction is defined as positive. The radial displacement is expressed by u_r , and the radial stress and circumferential stress are expressed by σ_r and σ_θ , respectively, and the radial strain and circumferential strain are expressed by ϵ_r and ϵ_θ , respectively. The total stress at the interface is p_0 , and the effective stress is p_1 . The bonding strength is f_1 , the uniaxial compressive design strength and the uniaxial tensile design strength of the concrete are f_c and f_t , respectively, and the compressive design strength and the tensile design strength of the reinforcement are f'_y and f_y , respectively. To facilitate the analysis, the relevant parameters are dimensionless as follows:

$$d\bar{\sigma}_r = \frac{d\sigma_r}{\Delta p_w},$$

$$d\bar{u}_r = \frac{du_r}{dr},$$

$$d\bar{r} = \frac{dr}{r},$$

$$\bar{u}_r = \frac{u_r}{r},$$

$$\bar{\sigma}_r = \frac{\sigma_r}{\Delta p_w},$$

$$\bar{\sigma}_\theta = \frac{\sigma_\theta}{\Delta p_w},$$

$$\bar{r}_{12} = \frac{r_1}{r_2},$$

$$\bar{r}_{23} = \frac{r_2}{r_3},$$

$$\bar{E}_{12} = \frac{E_1}{E_2},$$

$$\bar{\alpha}_1 = \alpha E_1,$$

$$\begin{aligned}
\tilde{p}_0 &= \frac{P_0}{\Delta P_w}, \\
\tilde{p}_1 &= \frac{P_1}{\Delta P_w}, \\
\tilde{f}_1 &= \frac{f_1}{\Delta P_w}, \\
\tilde{f}_c &= \frac{f_c}{\Delta P_w}, \\
\tilde{f}_t &= \frac{f_t}{\Delta P_w}, \\
\tilde{f}'_y &= \frac{f'_y}{\Delta P_w}, \\
\tilde{f}_y &= \frac{f_y}{\Delta P_w}, \\
\Delta \tilde{p}_{w1} &= \frac{\Delta P_w}{E_1}, \\
\Delta \tilde{p}_{w2} &= \frac{\Delta P_w}{E_2}.
\end{aligned} \tag{12}$$

4.1.2. *Stress and Displacement Solution in the Surrounding Rock Zone.* The equations of equilibrium in the surrounding rock zone can be expressed as [18]

$$\frac{d\tilde{\sigma}_r}{d\tilde{r}} + \tilde{\sigma}_r - \tilde{\sigma}_\theta = 0. \tag{13}$$

The equations of geometry for the axisymmetric plane strain problem can be written as

$$\begin{aligned}
\varepsilon_r &= d\tilde{u}_r, \\
\varepsilon_\theta &= \tilde{u}_r.
\end{aligned} \tag{14}$$

The equations of constitution in the surrounding rock zone under the action of water pressure expansion can be expressed as

$$\varepsilon_r = \Delta \tilde{p}_{w1} (1 + \mu_1) [(1 - \mu_1) \tilde{\sigma}_r - \mu_1 \tilde{\sigma}_\theta + \tilde{\alpha}_1], \tag{15}$$

$$\varepsilon_\theta = \Delta \tilde{p}_{w1} (1 + \mu_1) [(1 - \mu_1) \tilde{\sigma}_\theta - \mu_1 \tilde{\sigma}_r + \tilde{\alpha}_1]. \tag{16}$$

The boundary conditions of the surrounding rock can be expressed as

$$\tilde{\sigma}_r|_{r=r_2} = \tilde{p}_0, \tag{17}$$

$$\tilde{u}_r|_{r=r_3} = 0. \tag{18}$$

According to (13)~(18), the analytical solutions of the stress and displacement in the surrounding rock zone can be obtained as

$$\tilde{\sigma}_r = \frac{(1 - 2\mu_1) \tilde{p}_0 + \tilde{\alpha}_1}{1 + (1 - 2\mu_1) / \tilde{r}_{23}^2} \left(\frac{1}{1 - 2\mu_1} + \frac{r_3^2}{r^2} \right) - \frac{\tilde{\alpha}_1}{1 - 2\mu_1}, \tag{19}$$

$$\tilde{\sigma}_\theta = \frac{(1 - 2\mu_1) \tilde{p}_0 + \tilde{\alpha}_1}{1 + (1 - 2\mu_1) / \tilde{r}_{23}^2} \left(\frac{1}{1 - 2\mu_1} - \frac{r_3^2}{r^2} \right) - \frac{\tilde{\alpha}_1}{1 - 2\mu_1}, \tag{20}$$

$$\tilde{u}_r = \Delta \tilde{p}_{w1} (1 + \mu_1) \frac{(1 - 2\mu_1) \tilde{p}_0 + \tilde{\alpha}_1}{1 + (1 - 2\mu_1) / \tilde{r}_{23}^2} \left(1 - \frac{r_3^2}{r^2} \right). \tag{21}$$

4.1.3. *Stress and Displacement Solution in the Shaft Lining Zone.* The equations of equilibrium and geometry in the shaft lining zone are the same as those in the surrounding rock zone, and the equations of constitution can be expressed as

$$\varepsilon_r = \Delta \tilde{p}_{w2} [(1 - \mu_2) \tilde{\sigma}_r - \mu_2 (1 + \mu_2) \tilde{\sigma}_\theta], \tag{22}$$

$$\varepsilon_\theta = \Delta \tilde{p}_{w2} [(1 - \mu_2) \tilde{\sigma}_\theta - \mu_2 (1 + \mu_2) \tilde{\sigma}_r]. \tag{23}$$

The boundary conditions of the shaft lining can be expressed as

$$\tilde{\sigma}_r|_{r=r_1} = 0, \tag{24}$$

$$\tilde{\sigma}_r|_{r=r_2} = \tilde{p}_0. \tag{25}$$

The analytical solutions of the stress and displacement in the shaft lining zone can be derived as

$$\tilde{\sigma}_r = \frac{1 - r_1^2/r^2}{1 - \tilde{r}_{12}^2} \tilde{p}_0, \tag{26}$$

$$\tilde{\sigma}_\theta = \frac{1 + r_1^2/r^2}{1 - \tilde{r}_{12}^2} \tilde{p}_0, \tag{27}$$

$$\tilde{u}_r = \Delta \tilde{p}_{w2} \tilde{p}_0 (1 + \mu_2) \frac{1 - 2\mu_2 + r_1^2/r^2}{1 - \tilde{r}_{12}^2}. \tag{28}$$

4.2. Stress Analysis at the Interface between the Surrounding Rock and Shaft Lining

4.2.1. *Total Stress Analysis.* Considering the conditions of single-valued displacement at the interface between the surrounding rock and the shaft lining, \tilde{p}_0 can be solved by (21) and (28) as follows:

$$\tilde{p}_0 = \frac{\tilde{\alpha}_1}{\left[1 - 2\mu_1 + ((1 + \mu_2) / (1 + \mu_1)) ((1 - 2\mu_2 + \tilde{r}_{12}^2) (1 - 2\mu_1 + \tilde{r}_{23}^2) / (1 - \tilde{r}_{12}^2) (1 - \tilde{r}_{23}^2)) \right] \tilde{E}_{12}}. \tag{29}$$

The partial derivative of \tilde{r}_{23} for \tilde{p}_0 is

$$\frac{\partial \tilde{p}_0}{\partial \tilde{r}_{23}} < 0. \quad (30)$$

According to (30), the smaller the value of \tilde{r}_{23} is, the larger the value of \tilde{p}_0 is. Therefore, when the outer boundary of

$$\tilde{p}_0 = \frac{\tilde{\alpha}_1}{\left\{ (1 - 2\mu_1) \left[1 + \left(\frac{1 + \mu_2}{1 + \mu_1} \right) \left(\frac{1 - 2\mu_2 + \tilde{r}_{12}^2}{1 - \tilde{r}_{12}^2} \right) \tilde{E}_{12} \right] \right\}}. \quad (31)$$

By analyzing (31), it can be found that

- (1) when $\tilde{E}_{12} \approx \infty$, $\tilde{p}_0 \approx 0$;
- (2) when $\tilde{E}_{12} \approx 0$, $\tilde{p}_0 = \tilde{\alpha}_1 / (1 - 2\mu_1)$;
- (3) when $\tilde{r}_{12} \approx 1$, $\tilde{p}_0 \approx 0$.

The results show that when the elastic modulus of the surrounding rock is too large compared with the shaft lining, p_0 is close to 0; otherwise, p_0 is constant. Additionally, when the lining thickness is very small, p_0 approaches 0; when the pore water pressure increases ($\Delta p_w > 0$), p_0 is a compressive stress, and a compressive fracture forms at the inner edge of the shaft lining. Finally, when the pore water pressure decreases ($\Delta p_w < 0$), p_0 is a tensile stress, and a tensile fracture forms at the inner edge of the shaft lining.

4.2.2. Effective Stress Analysis. According to the composition of the stress at the contact surface between the surrounding rock and the shaft lining, the effective stress (or skeleton stress) at the contact surface can be expressed as

$$\tilde{p}_1 = \tilde{p}_0 - n_3. \quad (32)$$

By analyzing (32), it can be found that

- (1) when $\tilde{p}_0 = n_3$, then $\tilde{p}_1 = 0$; that is, the contact skeleton stress is equal to 0;
- (2) when the pore water pressure increases, if $\tilde{p}_0 < n_3$, then $\tilde{p}_1 < 0$, and the skeleton stress at contact surface is tensile stress; if $\tilde{p}_0 > n_3$, then $\tilde{p}_1 > 0$, and the skeleton stress at contact surface is compressive stress;
- (3) when the pore water pressure decreases, if $\tilde{p}_0 < n_3$, then $\tilde{p}_1 < 0$, and the skeleton stress at contact surface is compressive stress; if $\tilde{p}_0 > n_3$, then $\tilde{p}_1 > 0$, and the skeleton stress at contact surface is tensile stress.

The results show that when the skeleton stress at the contact surface is subjected to tensile stress, the shaft lining has a risk of peeling off the surrounding rock.

4.3. Shaft Lining Fracture Condition Analysis

4.3.1. Fracture Condition at Inner Edge of Shaft Lining. When p_0 is the compressive stress, the inner edge of the shaft lining is in compression. According to the Code [19], the compressive failure condition at the inner edge of the shaft lining is

$$\tilde{\sigma}_\theta|_{r=r_1} > \eta \tilde{f}_c + \nu \tilde{f}_y', \quad (33)$$

the surrounding rock is farther from the interface between the lining and the surrounding rock, the interaction force at the interface is greater under the unit pore water pressure. When $\tilde{r}_{23} \approx 0$, the interaction force is a constant value equal to

where η is the improvement coefficient of the concrete strength under multiaxial stress, η is related to σ_θ and σ_r (in general, $\eta = 1.2$), and ν is the minimum steel content.

When p_0 is a tensile stress, the inner edge of the shaft lining is in tension. According to the Code [20], the tensile failure condition at the inner edge of the shaft lining is

$$\tilde{\sigma}_\theta|_{r=r_1} > |\eta \tilde{f}_t + \nu \tilde{f}_y|. \quad (34)$$

4.3.2. Stripping Condition at Outer Edge of Shaft Lining. To avoid the hydrostatic action of groundwater on the entire outside surface of the shaft lining, there must be a certain bonding strength between the shaft lining and surrounding rock to ensure that the two are not separated. Therefore, when the contact surface skeleton is subjected to tension, the condition for peeling of the outer edge of the shaft lining away from the surrounding rock is

$$|\tilde{p}_1| > |\tilde{f}_1|. \quad (35)$$

The Code [20] stipulates that the bonding strength of shotcrete should be no less than 0.8 MPa with Class I and Class II surrounding rock and should be no less than 0.5 MPa with Class III surrounding rock, respectively. However, the bonding strength between the pouring concrete and the surrounding rock is less than these values. In fact, the maximum bonding strength between the shaft lining and the surrounding rock in engineering is less than 1 MPa.

5. Engineering Example

A shaft passes through water-rich bedrock strata with Class III surrounding rock. The radius of the shaft is $r_1 = 3$ m, and the shaft lining is made of C60 concrete and HRB335 steel, that is, $f_c = 27.5$ MPa, $f_t = 2.04$ MPa, $f_y = 300$ MPa, and $f_y' = 300$ MPa. The other parameters are as follows: $E_0 = 15$ GPa, $E_2 = 36$ GPa, $\mu_0 = 0.16$, $\mu_2 = 0.2$, $n_1 = 0.15$, $n_2 = 0.12$, $\nu = 0.2\%$, $f_1 = 0.8$ MPa. For a change in groundwater level in the water-rich bedrock strata of 500 m, the fracturing in the lining with different thicknesses is shown in Figures 8 and 9.

The calculation results show that $\tilde{p}_1 < 0$. Figures 8 and 9 show that when the water level rises, there is no compressive failure at the inner edge of the shaft lining, while stripping failure occurs at the outer edge of the shaft lining when $\tilde{r}_{12} > 0.918$; when the water level drops, only the inner edge of the shaft lining undergoes tensile fracturing.

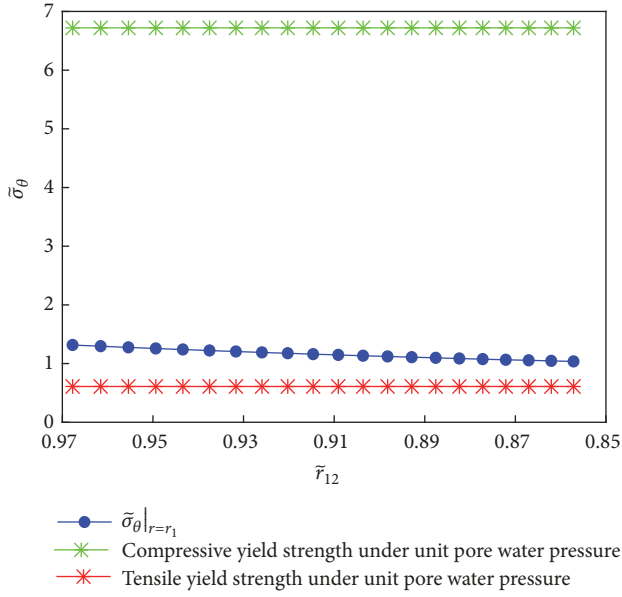


FIGURE 8: Fracture condition at inner edge of shaft lining.

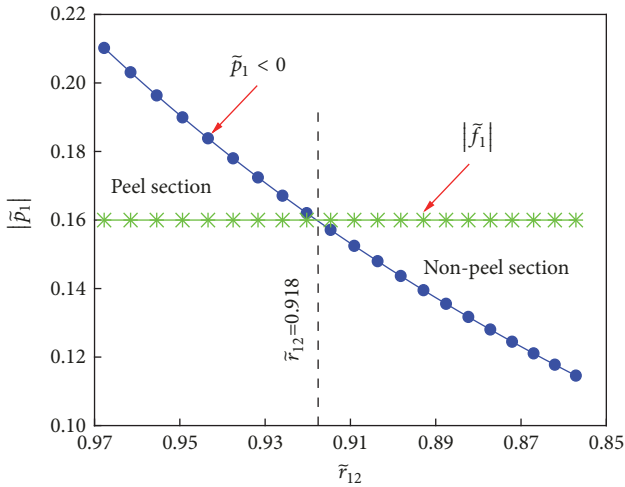


FIGURE 9: Stripping condition at outer edge of shaft lining.

To further study the relationship between the stress and the deformation at the outer edge of the shaft lining, the lateral stiffness coefficient K_c of the lining can be calculated from (28) and (32), which can be derived as

$$K_c = \frac{p_0}{u_r|_{r=r_2}} = \frac{(1 - \bar{r}_{12}^2)}{(1 + \mu_2)(1 - 2\mu_2 + \bar{r}_{12}^2)} \frac{E_2}{r_2}. \quad (36)$$

According to (36), the values of K_c with different thicknesses are shown in Figure 10.

As shown in Figure 10, K_c decreases approximately linearly with \bar{r}_{12} , indicating that the increase in shaft lining thickness can effectively improve the lateral stiffness coefficient.

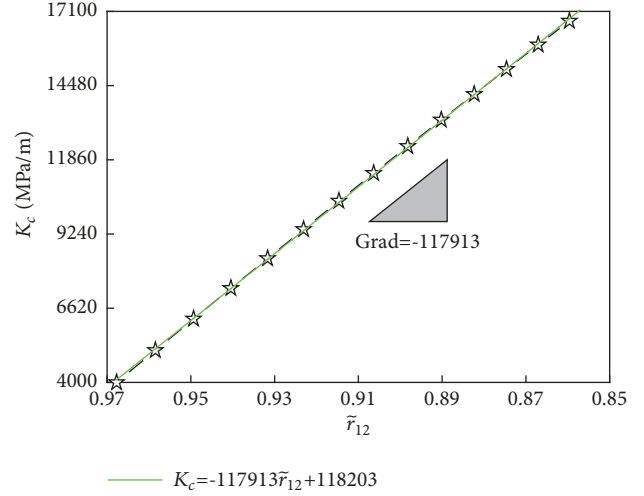


FIGURE 10: Values of K_c with different \bar{r}_{12} .

6. Conclusions

Based on the cubic model of hydraulic expansion containing a spherical pore, its volume change is calculated by the ANSYS numerical simulation, and the approximate analytical solution of the hydraulic expansion coefficient is obtained by the multivariate nonlinear regression method. Finally, the mechanism of fracturing in single-layer concrete lining caused by high-pressure pore water in stable rock strata is revealed by analyzing the interaction between the pore water pressure and the porous rock and shaft lining, and the following conclusions are obtained.

(1) The hydraulic expansion effect increases with the porosity of the surrounding rock and decreases with the elastic modulus and Poisson's ratio of the surrounding rock. Therefore, by reducing the porosity and improving the strength of the surrounding rock, the expansion effect of the surrounding rock on shaft lining can be weakened.

(2) The mechanism of fracturing in shaft lining in water-rich bedrock strata is as follows: the hydraulic expansion effect on the surrounding rock may lead to stripping failure at the outer edge or tensile failure at the inner edge of the shaft lining.

(3) When designing the shaft lining of water-rich bedrock section through the stable rock strata, the influence of pore water pressure change should be fully considered, which is to ensure that the shaft lining not only can take full advantage of deformation and compression effect but also has high bearing capacity.

Data Availability

The data used to support the findings of this study are available from the corresponding author upon request.

Conflicts of Interest

The authors declare that there are no conflicts of interest regarding the publication of this paper.

Acknowledgments

This research was supported by the National Key Research and Development Program of China (2016YFC0600904). The authors would like to thank the editor and reviewers for their contributions on the paper.

References

- [1] Z. S. Yao, H. Cheng, and C. X. Rong, "Shaft structural design and optimization of deep freezing," *Journal of China Coal Society*, vol. 35, no. 5, pp. 760–764, 2010.
- [2] I. W. Farmer and D. H. Jennings, "Effect of strata permeability on the radial hydrostatic pressures on mine linings," *International Journal of Mine Water*, vol. 2, no. 3, pp. 17–24, 1983.
- [3] J. Bear, "Dynamics of fluids in porous media," *Engineering Geology*, vol. 7, no. 2, pp. 174–175, 1972.
- [4] M. S. Bruno and F. M. Nakagawa, "Pore pressure influence on tensile fracture propagation in sedimentary rock," *International Journal of Mining Science and Technology*, vol. 28, no. 4, pp. 261–273, 1991.
- [5] R. W. Zimmerman, "Coupling in poroelasticity and thermoelasticity," *International Journal of Rock Mechanics and Mining Sciences*, vol. 37, no. 1-2, pp. 79–87, 2000.
- [6] Z. Jiang, S. Feng, and S. Fu, "Coupled hydro-mechanical effect of a fractured rock mass under high water pressure," *Journal of Rock Mechanics and Geotechnical Engineering*, vol. 4, no. 1, pp. 88–96, 2012.
- [7] G. D. Lou and L. F. Su, "Analysis of loading on shaft lining subjected to alluvium settlement due to water drainage," *Journal of China Coal Society*, vol. 16, no. 4, pp. 54–62, 1991.
- [8] W. H. Yang and H. L. Fu, "Theoretical investigation on the vertical additional force of shaft lining in special stratum," *Journal of China University of Mining and Technology*, vol. 9, no. 2, pp. 130–136, 1999.
- [9] Y. Wang, C. Zhang, L. Xue, and X. Huang, "Prediction and safety analysis of additional vertical stress within a shaft wall in an extra-thick alluvium," *Mining Science and Technology*, vol. 20, no. 3, pp. 350–356, 2010.
- [10] Z. Zhang, X. Tang, and Q. Yu, "Impact of aquifer drainage on shaft lining in underground mining of Eastern China," *Electronic Journal of Geotechnical Engineering*, vol. 21, no. 13, pp. 4721–4729, 2016.
- [11] X. Sun, G. Li, C. Zhao, Y. Liu, and C. Miao, "Investigation of deep mine shaft stability in alternating hard and soft rock strata using three-dimensional numerical modeling," *Processes*, vol. 7, no. 1, p. 17, 2019.
- [12] R. S. Yang, Q. X. Wang, and S. Z. Chen, "Elastic analysis of irregular inclined shaft lining subjected to water pressure," *Journal of China University of Mining and Technology*, vol. 46, no. 1, pp. 48–57, 2017.
- [13] Q. B. Meng, L. J. Han, R. J. Shi et al., "Study and application of construction technology for inclined shafts penetrating drift sand strata in coal mine," *Chinese Journal of Geotechnical Engineering*, vol. 37, no. 5, pp. 900–910, 2015.
- [14] O. C. Zienkiewicz, R. L. Taylor, and J. Z. Zhu, *The Finite Element Method: Its Basis and Fundamentals*, Elsevier/Butterworth Heinemann, Amsterdam, Netherlands, 7th edition, 2013.
- [15] J. Rutqvist, L. Börgesson, M. Chijimatsu et al., "Thermohydro-mechanics of partially saturated geological media: governing equations and formulation of four finite element models," *International Journal of Rock Mechanics and Mining Sciences*, vol. 38, no. 1, pp. 105–127, 2001.
- [16] C. H. Zhang, F. Jin, Y. L. Hou et al., *Discrete-Contact-Fracture Analysis of Rock and Concrete*, Tsinghua University Press, Beijing, China, 2008.
- [17] D. L. Bo, *Hydraulic Load of Underground Structure in Pore Water Bearing Rock*, China University of Mining and Technology, 2015.
- [18] S. P. Timoshenko and J. N. Goodier, *Theory of Elasticity*, McGraw-Hill, New York, NY, USA, 1970.
- [19] M. O. H. U.-R. D. P. R. China, *Code for Design of Concrete Structures (GB 50010-2010)*, China Architecture & Building Press, Beijing, China, 2015.
- [20] C. M. C. A., "Technical Code for Engineering of Ground Anchorages and Shotcrete Support (GB 50086)," Tech. Rep., China Planning Press, Beijing, China, 2015.

Research Article

Numerical Simulation on Thermodynamics Performance in the Fireproof Sealing by Finite Element Analysis

Shuai Gao,^{1,2,3} Guoqing Zhu ,^{1,2,3} Yunji Gao,^{1,2,3} Guoqiang Chai,^{1,2,3} and Jinju Zhou^{1,2,3}

¹Key Laboratory of Fire Protection of Urban Underground Space in Jiangsu Province, China University of Mining and Technology, Xuzhou 221116, Jiangsu, China

²School of Safety Engineering, China University of Mining and Technology, Xuzhou 221116, Jiangsu, China

³Fire Research Institute, China University of Mining and Technology, Xuzhou 221116, Jiangsu, China

Correspondence should be addressed to Guoqing Zhu; zgq119xz@cumt.edu.cn

Received 30 March 2019; Accepted 28 May 2019; Published 19 June 2019

Guest Editor: Dong Wang

Copyright © 2019 Shuai Gao et al. This is an open access article distributed under the Creative Commons Attribution License, which permits unrestricted use, distribution, and reproduction in any medium, provided the original work is properly cited.

In this paper, the finite element analysis was firstly employed to investigate the thermal analysis on two fireproof sealing models with ANSYS software under HC standard temperature-time condition. The main thermal parameters were analyzed and obtained, including temperature field, thermal flux, and thermal gradient. After comparing the two fireproof sealing models, the major conclusions are summarized as follows: In terms of temperature field, the temperature on the left side of the first model ranges from 60 to 524°C in. In contrast, the highest temperature on the left side of the second model eventually reaches below 151°C. Moreover, the vectors of thermal gradient in the first model are compared with the second model, and the temperature gradient disturbance is more obvious in the second fireproof sealing model, which is better to slow down temperature spreading. The accelerated speed of E_1 and G_1 is 0.0096°C/s and 0.0619°C/s partly, which are far more than C_2 and F_2 with values of 0.0028°C/s and 0.0078°C/s, respectively. In a word, the performance of the first fireproof sealing model is inferior to the second fireproof sealing model. The conclusions of the study are meaningful to improve the thermodynamic performance of the fireproof sealing in the converter station.

1. Introduction

Converter station is an important element in High Voltage Direct Current (HVDC) transmission system, which converts alternating current into direct current or converts direct current into alternating current, and electricity is the blood of industry and daily life. If a fire occurs at a converter station, the converter station will fail in the fire, which will result in loss of business and service and endanger people's lives. Therefore, the fireproof performance of the fireproof sealing isolated from the converter transformer side and the valve hall side of the converter station is studied.

Over the years, a large number of scholars have done a deal of investigations on fire protection with numerical simulation. Raduca et al. [1] used finite element method to present the modeling and simulation of the thermal transfer in the transformers from the high electric voltage stations, and the simulation of an optimal solution was obtained

regarding the correct usage of the transformers. Piloto et al. [2] investigated the thermal behavior of the unexposed surface and the nodal internal layers in light steel frame with numerical simulations. Jeyakumar et al. [3] carried out numerical simulations on Ag_2SO_4/ZnO (ASZ) nanocomposite coating with steady-state thermal analysis using ANSYS to validate the output in the numerical approach, and the results obtained showed that ASZ nanocomposite coating acted as an efficient thermal barrier coating for the exhaust manifold, thus increasing its reliability. Liu et al. [4] carried out some simulations and experiments about welding processes of martensitic steel (RAFM steel) in three-dimensional finite element models by ANSYS software, and the temperature fields and stress fields from simulations were contrasted with that from experiments, respectively. Mittal and Greiner [5] constructed two-dimensional and three-dimensional thermal models of a Nuclear Assurance Corporation Legal Weight Truck (NAC-LWT) cask using the

PATRAN commercial finite element package under normal and fire accident conditions. Liu et al. [6] analyzed firstly potential fire scenarios relevant to a cable-stayed bridge crossing the Yangtze River, then the temperature distribution in key elements and the global structural behavior of the bridge under tanker truck fires were calculated by using general purpose finite element analysis software ANSYS. Moreover, numerical simulation results demonstrated that cable-stayed bridge might collapse under some specific fire scenarios. Zhang [7] conducted a comprehensive modal analysis of Z-shaped beam electrothermal microactuators for the first time, and both longitudinal and lateral vibrations were taken into account to obtain the vibration equations of the unique geometric feature: a Z-shaped beam with a shuttle in the middle. Zivkovic et al. [8] investigated the influence of the boiler scale on the thermal stresses and strains of the structure of hot water boilers with the finite elements method by ANSYS software, and maximum thermal stresses appeared in the zone of the pipe-carrying wall of the first reversing chamber. Tomecek [9] studied thermal response of steel columns with lost protection material and varying amounts of missing protection when exposed to the ASTM-E-119 furnace environment by a finite element analysis of heat transfer. Moreover, some scholars studied the thermodynamic problem and design of fireproof sealing and plugging in building under the fire conditions. In addition, Chung et al. [10] conducted a simulation on the development of a finite element model capable of representing a blast-resistant flexible window (flex-window) system developed by the Air Force Research Laboratory, Airbase Technologies Division (AFRL/RXQ). Hatiegan and Raduca [11] conducted the thermal analysis on the hydrogenerator stator winding and found that the insulation aging is influenced first by the environmental conditions and second by the speed increase of the high temperature chemical reaction in materials. Moreover, Cindea and Hatiegan [12] investigated the influence of the thermal field on X60 carbon steel components during welding in CO_2 environment given that the heat source (electric arc) moves.

Sun and Zhou [13] studied the thermal properties on new fireproof sealing sheet with the principle of fireproof sealing and plugging in building and proposed the composite applications of fireproof sealing technical measures on the basis of combining the engineering application. Ro [14] investigated the designing of appropriate height of firewalls for toluene and methanol outdoor storage tank's pool fire accidents with considering input variables, such as thermal radiation, orifice diameter, and elevation, and the result of effect distances was obtained.

Fireproof sealing is widely employed to limit the scale of fire in multistory building, commercial building, industrial building, medical building, and other types of public buildings. However, the experiment on fireproof sealing is difficult to conduct to obtain the parameter of thermal and fire resistance. In this paper, the two fireproof sealing models are established by ANSYS, which is the first time to apply finite element analysis to the research of fireproof sealing and improve the effectiveness of the later experiment. Thus, the numerical simulation of finite element analysis is

introduced to study the fire protection of firewall sealing wall in this paper. Regarding finite element analysis, mathematical approximation is applied to simulate a real physical system (geometric and load conditions). With simple and interacting elements, a finite number of unknowns can be used to approximate an infinitely unknown real system. In this paper, the finite element analysis was employed to investigate the thermal parameters, such as temperature field, thermal flux, and thermal gradient. When optimum effective combination with different materials was assumed for the model, a good approach was achieved by the simple calculation model, and the fireproof sealing model was made of different material which would enhance fire protection performance.

2. Simulation Setup

2.1. Geometry Model and Material Parameters. The typical fireproof materials are selected for fireproof sealing models which are widely applied in the market and have the good fireproof performance. Moreover, the combination of various fireproof materials can greatly improve the mechanical and fireproof performance of a high-quality fireproof material. In addition, two typical models are selected for simulation study in combination experiment to explore whether the fire protection performance of various composite materials can be improved using specific research methods. Thus, the main fireproof materials are rock wool, aluminum silicate needle blanket, square steel, fire retardant coating, fire retardant module, ALC board, cement, and fire suppression module. When designing the fireproof sealing, not only fire resistance but also stress and explosion hazard are required, and the thermodynamics should be considered firstly due to the importance of thermal performance. In this paper, two different types of combination of fire sealing were simulated with finite element analysis by ANSYS, and the parameters of thermal were achieved as the evaluation criteria to obtain the optimum effective combination. The finite element analysis can be divided into three procedures. Firstly, the designated model should be built and the materials properties are applied in the models; secondly, the parameters of boundary conditions are given and the forces with different conditions are loaded; lastly, the data are obtained and analyzed to check the desired result after completing the simulation.

The fireproof sealing comprising rock wool, aluminum silicate needle blanket, square steel, and ALC board with fire suppression module was selected as the simulative materials of two models. And then thermal parameters, such as density, specific heat capacity, and heat conductivity, were set, respectively, in ANSYS software which could influence the thermal field and the velocity of temperature conduction, and the specific parameters of four materials are shown in Table 1 [15]. The apparatus of four material modules were shown separately in Figures 1(a) and 1(b), and the fire surfaces were on the right side of two models. On account of the thermal characteristic changing with fire spread, the type of analysis was selected as transient and three significant thermal parameters were chosen as different characteristics in various temperature fields.

TABLE 1: Different kinds of material properties.

Material category	Temperature (°C)	Thermal Conductivity (W/(m·K))	Specific Heat (J/(kg·K))	Density (kg/m ³)
Rock wool	0~300	0.039	150	750
	301~500	0.057		
	501~800	0.134		
	801~1200	0.197		
Aluminum silicate needle-punched blanket	0~400	0.043	96	900
	401~800	0.093		
	801~1200	0.147		
Square steel	0~1200	50	460	7850
ALC board	0~1200	0.2	1782.1	500
Fire suppression module	0~1200	0.3	1600	103

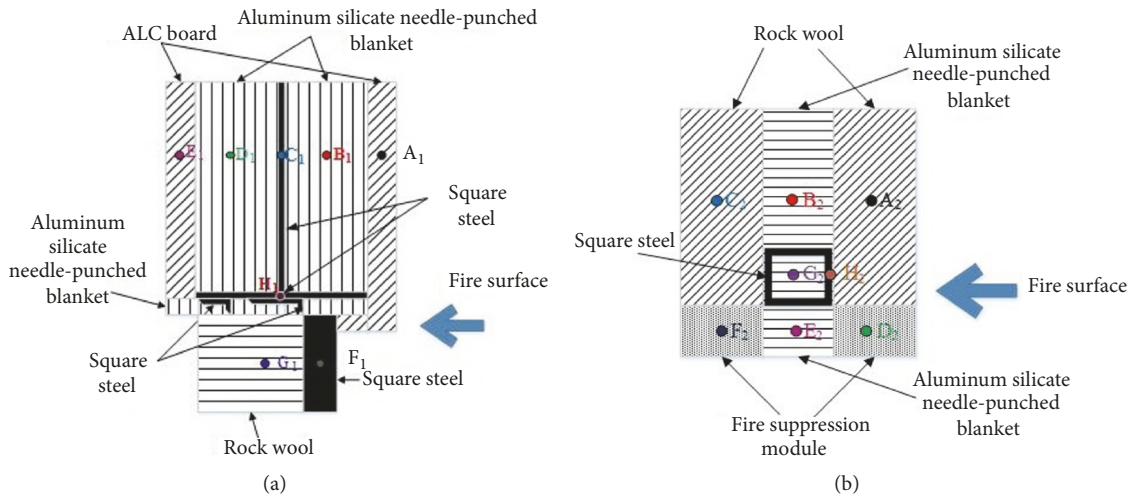


FIGURE 1: The designing model of fireproof sealing.

The differences of two fireproof sealing models were the model shape and the initial fire surface. Moreover, the fireproof performance of different materials was exhibited during the simulation in this paper. One fireproof sealing model was shown in Figure 1(a) which was made of four kinds of plates with 410 × 500 × 200 mm, and the T-shape was the shape of model in the front side. In contrast to Figure 1(a), the other fireproof sealing model was shown in Figure 1(b) which also consisted of four kinds of plates with 290 × 350 × 200 mm; however, the shape of model was rectangle to ensure protective sealing. A three-dimensional finite element model was built by ANSYS software, and then mesh was compared into 18 and 11 areas, respectively. Furthermore, 10 mm mesh was employed at every different kind and the total number of meshes were 46179 and 26360 partly to meet the accuracy of calculation results, which were exhibited in Figure 3.

2.2. Boundary and Temperature Conditions for Thermal Analysis. The fire surface of the first model is on the ALC board and square steel in the right of first model, and the fire surface of the second model is on the rock wool and fire suppression in the right of first model. The fire surface of the fireproof

sealing is one side and the two fireproof sealing models have the same initial loads. Thus, when evaluating the fire resistance of building components under liquid hydrocarbon fire conditions, a hydrocarbon (HC) heating curve can be used for fire resistance testing and is suited with the case. For the HC fires, the temperature-time relationship in the fire test furnace is expressed by

$$T = 108 \left(1 - 0.325e^{-0.167t} - 0.675e^{-2.5t} + T_0 \right) \quad (1)$$

where t denotes the time of simulation experiment whose unit is minutes (min) and T is the average temperature at the time t , which is measured in degrees Celsius (°C). Moreover, T_0 is the initial average temperature before the start of the test, which is required to be 5°C to 40°C, and the value of T_0 is 20°C in this simulation. The standard temperature-time curve of the hydrocarbon (HC) fire is shown in Figure 2. The possible application scenario of the fire temperature rise curve is the oil and gas fire at the converter station.

2.3. Thermal Analysis Model. In the thermal simulation, solid 8-node 70 elements were applied as element types as shown in

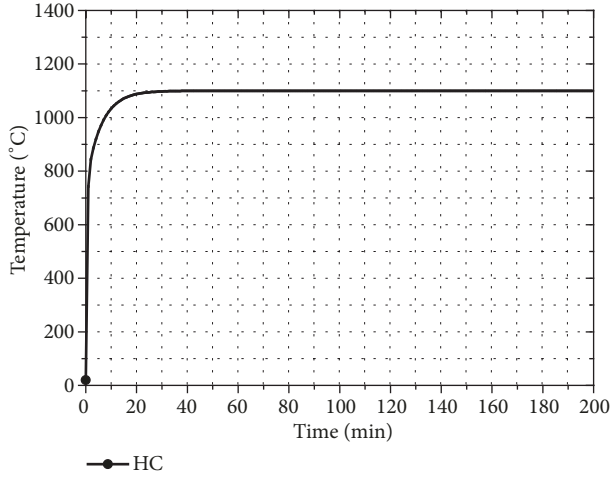


FIGURE 2: The curve of hydrocarbon (HC) temperature heating.

Figure 3. To realize the accuracy of simulation, the initial temperature was set to 20°C as simulation ambient temperature. On account of the temperature of models parameters ranging from 0 to 1200°C, thermodynamic propagations can work after the thermodynamic properties of materials are 20°C. The type of model contact is surface to surface in different materials, and the contact value between the contact surface and the target surface is 1000, which is coordinated with simulation requirement.

3. Results and Discussion

3.1. Temperature Field in Fireproof of Different Materials. According to heat transfer, if there is a temperature gradient inside the model, the energy will transfer from the high temperature zone to the low temperature zone, which is transferred in the form of heat conduction.

Heat conduction is subject to Fourier law; that is, the heat flow density of a place formed by heat conduction is proportional to the temperature gradient of the same place at the same time in the nonuniform temperature field, and its mathematical expression in the one-dimensional model temperature field is exhibited in [16]

$$q_x'' = -k \frac{dT}{dx} \quad (2)$$

where q_x'' is thermal flux, dT/dx is the temperature gradient in the x direction, and k is thermal conductivity.

When there is no internal heat source, the unsteady thermal conductivity differential equation of the three-dimensional model temperature field is as follows [17].

$$\frac{\partial T}{\partial t} = \alpha \left(\frac{\partial^2 T}{\partial x^2} + \frac{\partial^2 T}{\partial y^2} + \frac{\partial^2 T}{\partial z^2} \right) \quad (3)$$

It is demonstrated from Figure 4 that the distribution of temperature has diverse spread trend in the two fireproof sealing models with different materials. In Figures 4(a) and 4(b), since the right sides of the models are the fire surface, the

two models have highest temperature point in common and finally reach to 1100°C. Simultaneously, Figure 4(a) indicates that the temperature conduction to the left is a gradient of heat growth, but the temperature trend irregularly transfers to low energy, which is due to the law of the conservation of energy and the function of two fire surfaces [18]. Ultimately, the temperature on the left side of the first model ranges from 60 to 524°C, and the temperature of rock wool is above 524°C. However, the thermal performance of superstructure is superior to substructures, which demonstrates that the model widths can affect the thermal performance of fireproof sealing. In contrast, Figure 4(b) shows that the regularity of heat conduction is more obvious, and the speed of conduction is apparently slow which could meet the required application requirements. Moreover, the highest temperature on the left side of the second model eventually reaches below 151°C, and the temperature in different material could be fundamentally stabilized in the controlled range.

By comparing Figure 4(a) with Figure 4(b), the first model is inferior to the second model in the temperature field, and the second model is also an optimized choice in terms of heat conduction. In addition, the heat conduction equation employed for the calculation of temperature at various sections of the model is in accord with the law of thermodynamics.

3.2. Heat Flux in the Fireproof Sealing. The heat is mainly transmitted by heat conduction for fireproof sealing in a fire scenario, and the heat flux is explained by Fourier's law. In the one-dimensional model, the relation between heat flux $T(x)$ and the thermal conductivity k is as follows [19].

$$\phi_q = -k \frac{dT(x)}{dx} \quad (4)$$

The minus sign indicates that the heat flux moves from the higher temperature region to the lower temperature region.

In the three-dimensional model, the heat flux vectors are decomposed into several components.

$$\phi_q = -k \left(\vec{i} \frac{\partial T}{\partial x} + \vec{j} \frac{\partial T}{\partial y} + \vec{k} \frac{\partial T}{\partial z} \right) \quad (5)$$

Since the thermal field analysis in fireproof sealing is not constant, the analysis of heat flow is critical and thermal flux in the fireproof sealing is shown in Figure 5. It is noted from Figure 5 that the minimum value of the heat flux is far less than the maximum value in the fireproof sealing, and the maximum value of heat flux substantially exists in the square steel, which is due to high thermal conductivity in the square steel.

Thermal flux is a vector parameter, which illustrates the trend of heat flow. To show the best heat flow, the vectors of the thermal flux in the two fireproof sealing models are demonstrated in Figure 6. In Figure 6(a), on account of the combination of up and down heat, the vectors of thermal flux accumulate in the connection between square steel and aluminum silicate needle-punched blanket by the fire side, which demonstrates that the heat of bottom right aluminum silicate needle-punched blanket is dominated by the heat flux

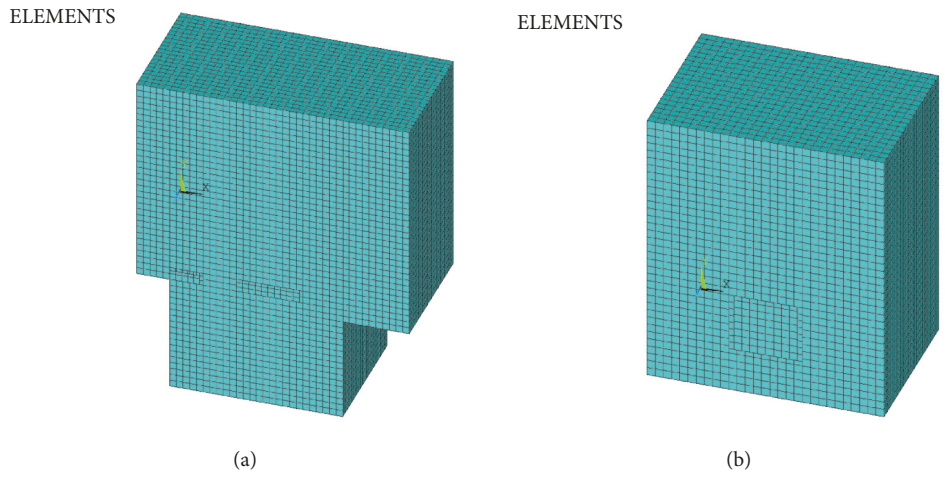


FIGURE 3: The grid with finite elements of geometrical model.

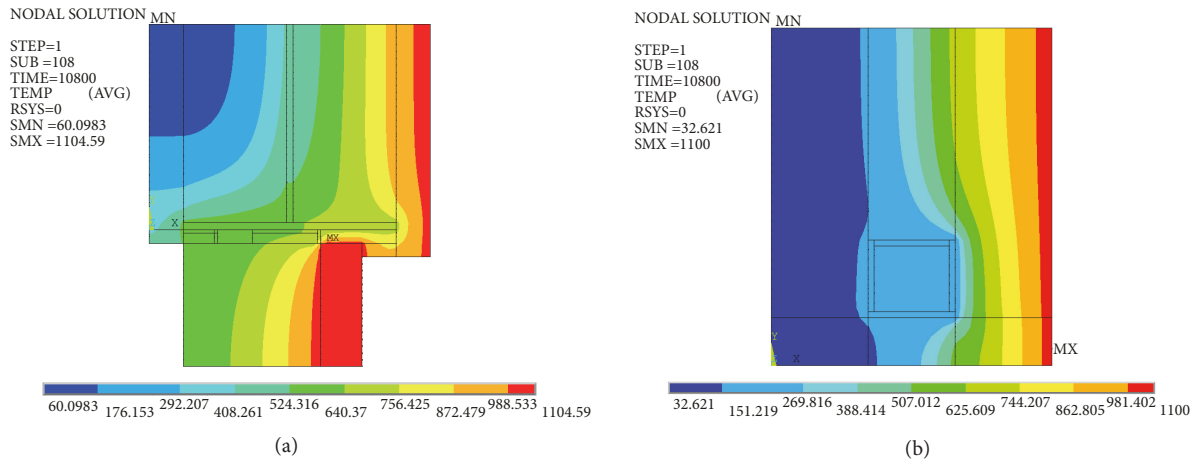


FIGURE 4: The distribution of the temperature in the fireproof sealing.

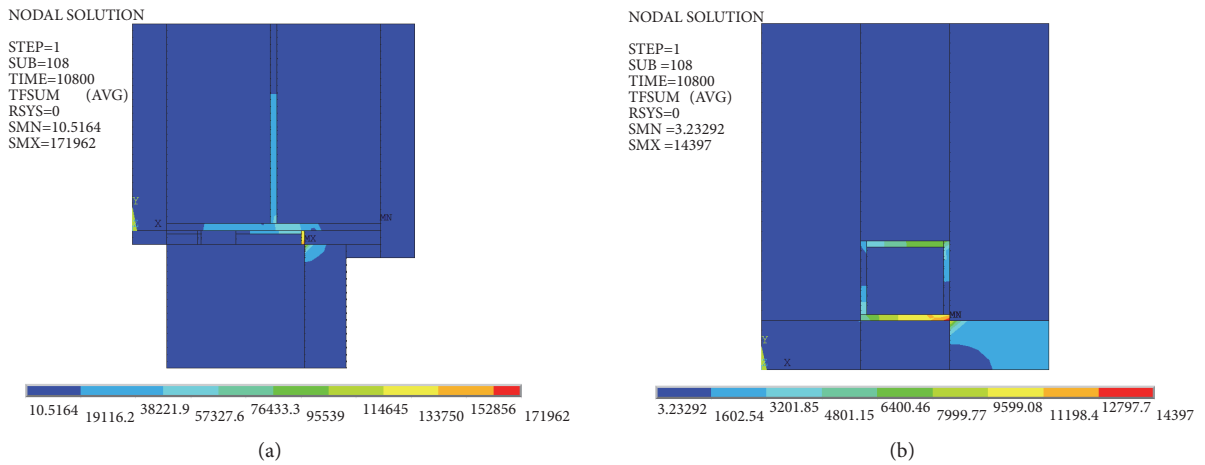


FIGURE 5: Thermal flux in the fireproof sealing.

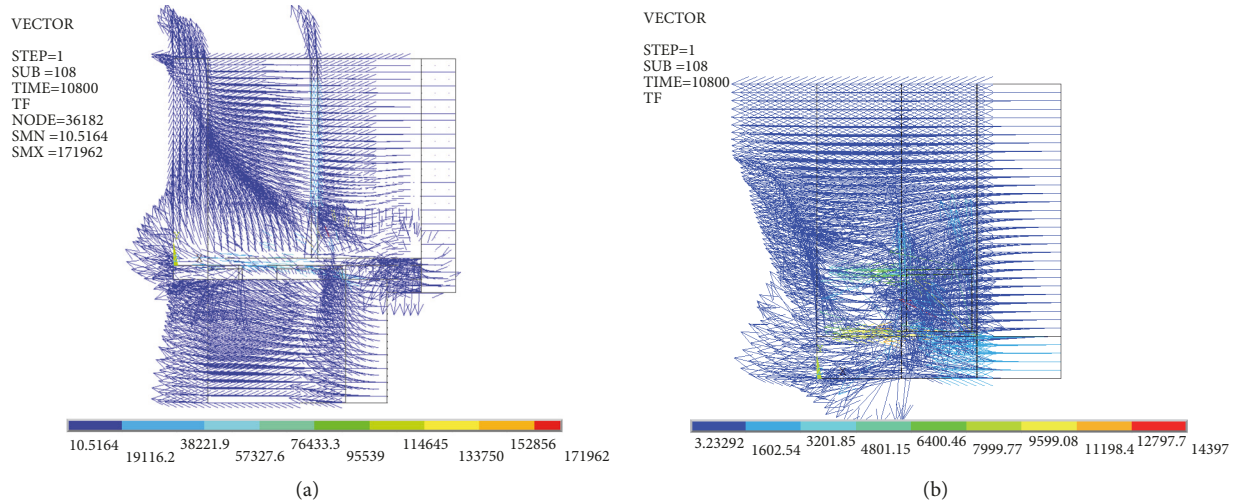


FIGURE 6: Vectors of the thermal flux in the fireproof sealing.

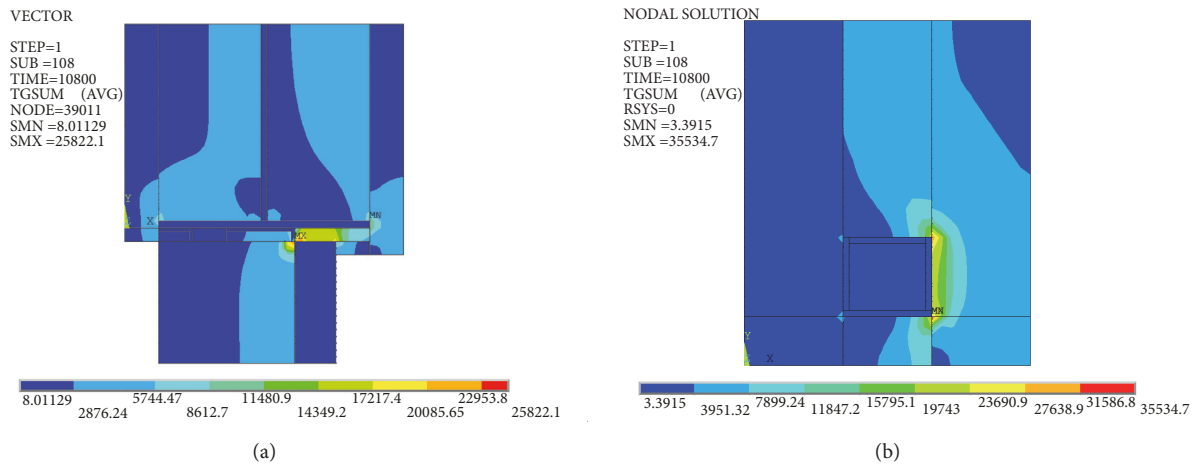


FIGURE 7: Distribution of the thermal gradient in the fireproof sealing.

of the two models. Moreover, the maximum of heat flux vector gathers on square steel commonly in Figures 6(a) and 6(b), which is far more than the other materials. With the heat flowing, the phenomenon of the energy concentration is gradually evident; the values of thermal flux are bigger and bigger with fast speed in the two fireproof sealing models, of which the vector direction is from the high temperature region to the low temperature region.

3.3. Thermal Gradient in Fireproof Sealing. The thermal gradient is a significant thermal parameter in the two fireproof sealing models, which can analyze where and what rate the temperature changes most rapidly under environmental conditions [20].

$$\text{Grad}T = \lim_{\Delta n \rightarrow 0} \left(\frac{\Delta T}{\Delta n} \right) = \left(\frac{\partial T}{\partial n} \right) \quad (6)$$

Here, n is the unit vector in the normal direction, and ∂ is the derivative of temperature in the n direction.

The thermal gradients are transient in the two fireproof sealing models, and the variation of distribution is demonstrated in Figure 7. It is noted from Figure 7(a) that the trend of thermal gradient is not uniform and is changed by the different thermal material properties, and the variation increases rapidly at the junction of square steel and rock wool, which is due to the thermal conductivity with great gap between square and rock wool. In contrast, the minimum value of thermal gradient is on the left of Figure 7 tending toward zero, which keeps away from the fire surface. It is demonstrated from Figure 7(a) that the highest value of thermal gradient is in the aluminum silicate needle blanket and the highest factor intensity of thermal gradient is also in the aluminum silicate needle blanket. However, the highest value of thermal gradient exists in the connection of rock wool and square steel, and the thermal gradient of the second

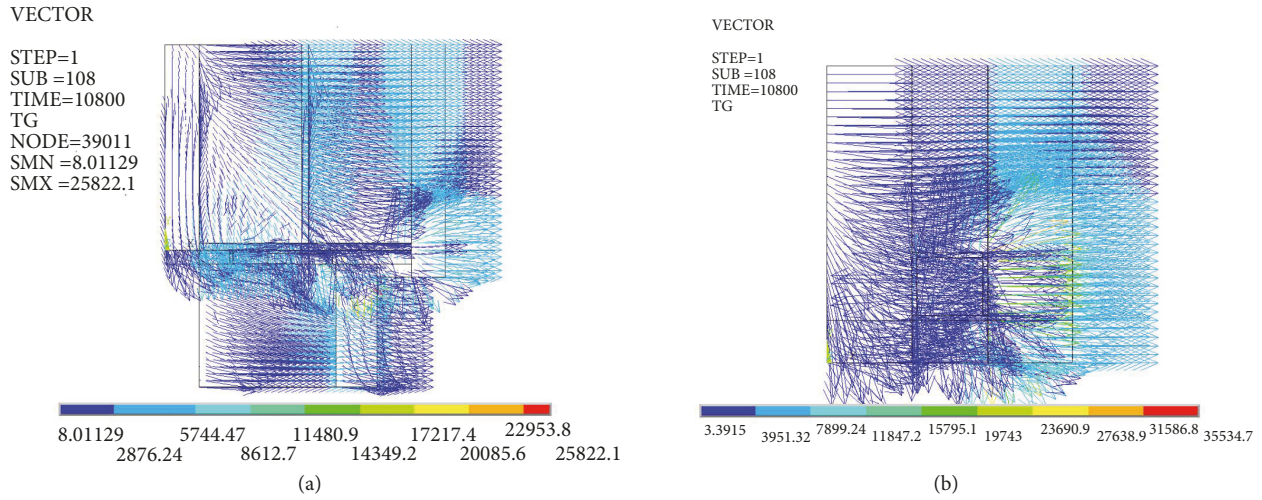


FIGURE 8: Vectors of the thermal gradient in the fireproof sealing.

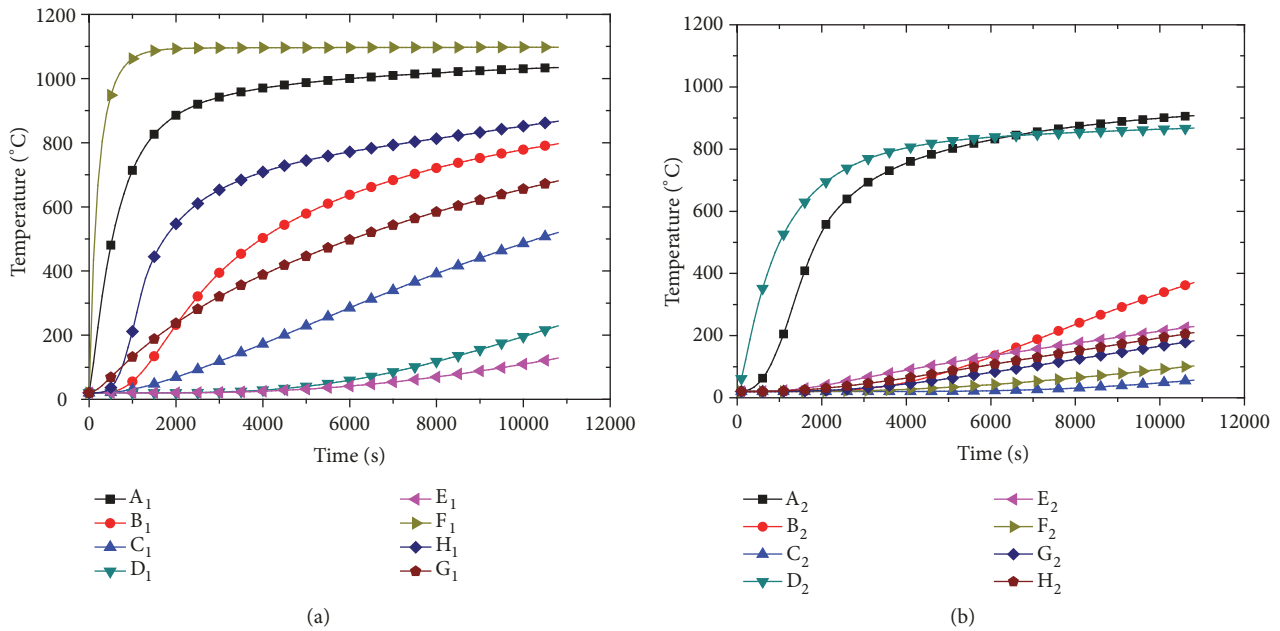


FIGURE 9: Temperature distribution of different material element in different nodes, (a) the first “T” shape model, (b) the second rectangle model.

fireproof sealing model is more regular; the increase of temperature gradient shows obvious gradient distribution, as shown in Figure 7(b).

The vectors of thermal gradient in two fireproof sealing models are exhibited in Figure 8. Contrary to thermal flux, the vector direction is from the low temperature region to the high temperature region. Nevertheless, the thermal gradient in different materials has the phenomenon of the regular flow, and the vector direction is in accord with the calculation of the thermal gradient with heat flow. However, the intersection of two heat flows results in the crossing of temperature gradient vectors, which affects the fire prevention effect of the

fireproof sealing. Moreover, the vectors of thermal gradient in Figure 8(a) are compared with the vectors of thermal gradient in Figure 8(b), and the temperature gradient disturbance is more obvious in the second fireproof sealing model, which is better to prevent the heat from spreading and slow down the propagation.

3.4. Temperature Field of Various Materials in Different Nodes. It is noted from Figure 1 that the different element points are selected to analyze the temperature field of various materials. Thereby, temperature trend on selected points of various materials is shown in Figure 9. It is noted from Figure 9(a)

that the temperature of the other nodes finally reached above 400°C except for the two points D_1 and E_1 , and the F1 point quickly rose to 1100°C at 100s, which is in fire surface to supply the high thermal energy. The temperatures of the A_1 , G_1 , B_1 , and H_1 point gradually increase and asymptotically attain the constant values after the rapid rise. However, the temperature at point C_1 tends to increase linearly, which demonstrates the stable heat transfer in steel plate. On the contrary, the temperatures at the points of D_1 and E rise slowly which are lower than 200°C, due to the protection of the thick protective layer at the two points of D_1 and E_1 . It is demonstrated from Figure 9(a) that the thermal insulation performance in different materials are diverse. The ALC board and aluminum silicate needle-punched blanket are better than square steel in the thermal insulation performance.

As shown in Figure 9(b), the temperature of different nodes in the second model increases slowly. Nevertheless, A_2 and D_2 increase at a high rate of speed with a power function growth trend. After rapid growth, the temperatures gradually tend to a fixed value, with the highest temperature reaching 1050°C. In contrast, the temperatures of B_2 , C_2 , E_2 , F_2 , G_2 , and H_2 grow slowly with a linear growth trend. Comparing the temperature trends of A_2 , D_2 , and other points, the difference of temperature between them is to 450°C, which indicates that the fire resistance of aluminum silicate needle blanket is better, while the temperatures of C_2 and F_2 near the left side of the model keep below 100°C all the time.

In terms of node temperature, the first model has a maximum temperature of 1050°C and a minimum temperature of 128°C; the second model has a maximum temperature of 908°C and a minimum temperature of 56°C. In contrast, the speed of heat in the first fireproof sealing model is significantly faster than the second model. By comparing the temperature of different nodes of two fireproof sealing models, the overall growth trend of the first model is faster than second model, and the final temperature of the first model is higher than the second model, which shows that the second model has better fire protection performance. Compared with E_1/G_1 and C_2/F_2 , the temperature of the second model is lower than that of the first model, and the advantage of the second model is obvious. Moreover, the accelerated speed of E_1 is 0.0096°C/s and the accelerated speed of G_1 is 0.0619°C/s, which is far more than the accelerated speed of C_2 and F_2 whose values are 0.0028°C/s and 0.0078°C/s, respectively. By comparing the temperatures of different nodes, the second fireproof sealing model is superior to the first fireproof sealing model.

The temperatures in various nodes have different trends because of the different energy transfer of the material. The energy formula and energy conversion formula are as follows.

Energy conversation formula [21]:

$$Q = c\rho v\Delta t \quad (7)$$

where c is the specific heat capacity; ρ is density; v is volume; Δt is temperature change; and Q is the change in energy.

4. Conclusion

In this paper, the finite element analysis was employed to investigate the thermal analysis on two fireproof sealing models with ANSYS software under HC standard temperature-time condition. The main thermal parameters, such as temperature field, thermal flux, and thermal gradient, were analyzed and obtained. After comparing two fireproof sealing models, the main conclusions of this paper are summarized as follows:

In terms of temperature field, the temperature conduction to the left is a gradient of heat growth, but the temperature trend irregularly transfers from high energy to low energy, which is due to the law of the conservation of energy and the function of two fire surfaces. Moreover, in the first model, the temperature on the left side ranges from 60 to 524°C and the temperature of rock wool is above 524°C. In contrast, the highest temperature on the left side of the second model eventually reaches below 151°C. In a word, the first model is inferior to the second model in the temperature field, and the second model is also an optimized choice in terms of heat conduction.

The minimum value of the heat flux is far less than the maximum value in the fireproof sealing. Moreover, with the heat flowing, the vector direction is from the high temperature region to the low temperature region, and the phenomenon of energy concentration is gradually evident. Nevertheless, the vectors of thermal gradient in the first model are compared with the vectors of thermal gradient in the second model, and the temperature gradient disturbance is more obvious in the second fireproof sealing model, which is better to prevent the heat from spreading and slow down the propagation.

By comparing the temperature of different nodes of two fireproof sealing models, the overall growth trend of the first model is faster than the second model, which shows that the second model has better fire protection performance. Compared with E_1/G_1 and C_2/F_2 , the accelerated speed of E_1 is 0.0096°C/s and the accelerated speed of G_1 is 0.0619°C/s, which is far more than the accelerated speed of C_2 and F_2 whose values are 0.0028°C/s and 0.0078°C/s, respectively. The temperature of the second model is lower than that of the first model, and the advantage of the second model is obvious.

In summary, the finite element analysis is firstly applied in the fireproof sealing as a reference for experiments, and this study is helpful to improve the thermodynamic performance of the fireproof sealing in the converter station. In the next research, it is still necessary to investigate the factors of stress, and the trend of stress and the different combination in different superior materials will be further studied.

Data Availability

The data used to support the findings of this study are included within the article.

Conflicts of Interest

The authors declare that they have no conflicts of interest.

Acknowledgments

This work was supported by National Key Research and Development Plan (Project No. 2016YFC0802900), the Fundamental Research Funds for the Central Universities (No. 2018BSCXC02), Postgraduate Research & Practice Innovation Program of Jiangsu Province (No. KYCX18_1914), and Fire Fighting and Rescue Technology Key Laboratory of MPS Open Project (No. KF201802).

References

- [1] M. Răduca, C. Hațiegan, N. Pop, E. Răduca, and G. Gillich, "Finite element analysis of heat transfer in transformers from high voltage stations," *Journal of Thermal Analysis and Calorimetry*, vol. 118, no. 2, pp. 1355–1360, 2014.
- [2] P. Piloto, M. Khetata, and A. Ramos, *Fire Performance of Non-Loadbearing Light Steel Framing Wall-Numerical and Simple Calculation Methods*, 2017.
- [3] N. Jeyakumar, A. C. A. Kayambu, R. Ramasubbu, and B. Narayanasamy, "Thermal analysis of nanostructured alumina stabilized zirconia coating on exhaust manifold," *Energy Sources Part A Recovery Utilization and Environmental Effects*, vol. 41, no. 7, pp. 1–12, 2018.
- [4] S. Liu, J. Sun, F. Wei, and M. Lu, "Numerical simulation and experimental research on temperature and stress fields in TIG welding for plate of RAFM steel," *Fusion Engineering and Design*, vol. 136, pp. 690–693, 2018.
- [5] K. Mittal and M. Greiner, "Thermal analysis of a NAC-LWT cask under normal and fire accident conditions," in *Proceedings of the ASME 2012 Pressure Vessels and Piping Conference, PVP 2012*, vol. 7, pp. 305–312, July 2012.
- [6] Y. J. Liu, B. Ning, and Y. Wang, "Study on thermal and structural behavior of a cable-stayed bridge under potential tanker truck fires," *Applied Mechanics and Materials*, vol. 238, pp. 684–688, 2012.
- [7] Z. Zhang, Y. Yu, and X. Zhang, "Theoretical modal analysis and parameter study of Z-shaped electrothermal microactuators," *Microsystem Technologies*, vol. 24, no. 7, pp. 3149–3160, 2018.
- [8] D. Zivkovic, D. Milic, M. Banic, and P. Milosavljevic, "Thermo-mechanical finite element analysis of hot water boiler structure," *Thermal Science*, vol. 16, no. Supplement 2, pp. S387–S398, 2012.
- [9] D. V. Tomecek and J. A. Milke, "A study of the effect of partial loss of protection on the fire resistance of steel columns," *Fire Technology*, vol. 29, no. 1, pp. 3–21, 1993.
- [10] J. H. Chung, G. R. Consolazio, R. J. Dinan, and S. A. Rinehart, "Finite-element analysis of fluid-structure interaction in a blast-resistant window system," *Journal of Structural Engineering*, vol. 136, no. 3, pp. 297–306, 2010.
- [11] C. Hatiegan, M. Răduca, D. Frunzăverde, E. Răduca, and N. Pop, "The modeling and simulation of the thermal analysis on the hydrogenerator stator winding insulation," *Journal of Thermal Analysis Calorimetry*, vol. 113, no. 3, pp. 1217–1221, 2013.
- [12] L. Cindea, C. Hațiegan, N. Pop et al., "The influence of thermal field in the electric arc welding of X60 carbon steel components in the CO₂ environment," *Applied Thermal Engineering*, vol. 103, pp. 1164–1175, 2016.
- [13] Z. Sun and Y. Zhou, "Discussion on fire-proof sealing technology and product," *Procedia Engineering*, vol. 135, pp. 644–648, 2016.
- [14] S. M. Ro, Y. W. Chon, I. M. Lee et al., "Firewall design for toluene & methanol outdoor storage tank in case of pool fire accidents," *Korean Journal of Hazardous Materials*, vol. 5, pp. 1–9, 2017.
- [15] T. T. Lie and R. J. Irwin, "Method to calculate the fire resistance of reinforced concrete columns with rectangular cross section," *ACI Structural Journal*, vol. 90, no. 1, pp. 52–60, 1993.
- [16] I.-S. Liu, "On Fourier's law of heat conduction," *Continuum Mechanics and Thermodynamics*, vol. 2, no. 4, pp. 301–305, 1990.
- [17] H. D. Baehr and K. Stephan, *Heat Conduction and Mass Diffusion*, 1998.
- [18] V. L. Morgunov, "Calorimeter energy calibration using the energy conservation law," *Pramana—Journal of Physics*, vol. 69, no. 6, pp. 1097–1100, 2007.
- [19] Z.-yW. Chunzhen Qiao and X Xiang, "Exothermal transfer law and calculation of one-dimensional steady state heat conduction process," *Journal of North China Electric Power University*, vol. 30, pp. 50–53, 2003.
- [20] M. J. Tholey, M. V. Swain, and N. Thiel, "Thermal gradients and residual stresses in veneered Y-TZP frameworks," *Dental Materials*, vol. 27, no. 11, pp. 1102–1110, 2011.
- [21] S. Kasap and T. Dan, "Thermal properties and thermal analysis," *Surveys in High Energy Physics*, pp. 336–338:385, 2006.

Research Article

Fatigue Strength Assessment of Trimaran Cross-Deck Structure Based on Spectral and Simplified Fatigue Method

Chunbo Zhen ¹, Tianlin Wang ¹, Pengyao Yu,¹ and Liang Feng ²

¹College of Naval Architecture and Ocean Engineering, Dalian Maritime University, Dalian 116026, China

²College of Engineering, Ocean University of China, Qingdao 266100, China

Correspondence should be addressed to Tianlin Wang; wangtianlin@dlnu.edu.cn

Received 28 February 2019; Revised 23 April 2019; Accepted 5 May 2019; Published 26 May 2019

Guest Editor: Raffaele Albano

Copyright © 2019 Chunbo Zhen et al. This is an open access article distributed under the Creative Commons Attribution License, which permits unrestricted use, distribution, and reproduction in any medium, provided the original work is properly cited.

In order to investigate the fatigue behaviour of trimaran cross-deck structural details, the spectral and simplified fatigue analysis approaches are proposed. In spectral fatigue approach, three-dimensional (3D) linear potential flow theory and global FE analysis are used for wave loads and stress transfer functions calculation; the stochastic spectral fatigue analysis is carried out considering the weighted wave headings factors. In simplified fatigue approach, based on the direct calculation procedure of LR rules, the evaluation of simplified fatigue loads and loading conditions are presented, and the stress ranges are obtained by global finite element (FE) analysis. Then the fatigue lives of a few hot spots are computed to demonstrate the application of the proposed method. The result shows that the method given in this paper has a good applicability. This study offers methodology for the fatigue analysis of trimaran cross-deck structure, which may be regarded as helpful references for structural design of these types of ships.

1. Introduction

Trimarans, being high-performance ships, have attracted more and more people's attention in recent years. Because of the unique configuration, trimarans have a lower resistance and a better transverse stability compared with conventional monohull ships. Further, they have large open decks for diverse design, transport capacity, and arrangement convenience, due to the suitable arrangement of the side hulls. Consequently, trimarans have become a high-performance vehicle type, which have been considered as alternative to monohulls in high speed transportation and in naval applications [1].

Because of the trimaran having so many advantages, many investigations have been performed on trimaran in the past years. Related researches are still going on worldwide. Most of the researches focused on hydrodynamics including the resistance and seakeeping performance. With regard to resistance, reducing the wave-making resistance and the optimization of placement of side hulls are widely investigated [2–4]. In terms of seakeeping performance study of a trimaran, several researches have been conducted to examine the seakeeping performance of the trimaran using

numerical and experimental methods [5–7]. For the trimaran wave loads study, Bingham et al. investigated the trimaran's wave induced motion and loads in regular head waves using three-dimensional pulsating source method [8]. In addition, Fang et al. used 3D translating-pulsating source distribution model to study the global loads of a trimaran in oblique waves, and the wave loads based spectral analysis for the optimal selection of trimaran side hulls arrangement are proposed [9, 10].

Fatigue is one of the most significant failure modes for marine structures [11]. Ships are prone to fatigue due to high cyclic loads predominantly caused by waves and varying loading conditions. Due to the unique structure, the stress concentration of trimaran's cross-deck structure is serious and the fatigue problem of cross-deck structure appears particularly serious [12]. Hence, evaluation of fatigue strength is vital for trimaran design.

The fatigue strength assessment of marine structure usually includes the $S - N$ curve approach and fracture mechanics approach [13]. The fracture mechanics approach is based on the existence of an initial crack and subsequent growth under cyclic loading. The $S - N$ curve approach is based on experimental fatigue test data along with Miner

linear cumulative damage criteria, which has been widely used for marine structure fatigue assessment. It can be further subdivided into the “simplified fatigue method” and “spectral fatigue method”. This approach is adopted by most of the world major classification societies such as ABS, BV, DNV GL, LR, and CCS. The fatigue analysis procedures of the conventional ship structures have been established by the major classification societies, in order to meet the fatigue strength requirement at the design stage. Lots of investigators have adopted $S - N$ curve approach for the study of marine structure’s fatigue strength, using both the “simplified fatigue method” and the “spectral fatigue method” [14–17]. Previous studies show that an extensive and in depth research in recent years on fatigue strength assessment of ship structures mainly focused on conventional vessels like bulk carriers, oil tankers, and container ships. However, few researchers have investigated the trimaran fatigue strength and relatively very little reference material is available in literature. Peng et al. made some important contributions to trimaran fatigue strength assessment [18]. They performed coarse meshed global finite element analysis of trimaran to identify the hot spots and computed fatigue damage by spectral fatigue analysis in conjunction with hot spot stress approach. Zhen et al. calculated the fatigue damage of a trimaran by using spectral analysis and discussed the effect of different sea area and heading angles’ time factors [19].

Furthermore, for the novel trimaran, there is only conceptual guideline providing for fatigue analysis, and no clear fatigue assessment procedure is available. At present, the only available rule for trimaran is the Lloyd’s Register Rules for Classification of Trimaran (LR Rules) [20]. But in LR Rules, only formulation of design loads and strength analysis are illustrated and the fatigue strength assessment is suggested to refer to the fatigue guidelines of conventional vessels. When the fatigue strength assessment is done according to conventional vessels’ fatigue guidelines, especially using the “simplified fatigue method”, there are some difficulties for the unique cross-deck structure. Firstly, we cannot use the conventional ship beam-theory to calculate the stress of the cross-deck structure. Secondly, the shape parameter h of the Weibull distribution is usually obtained by empirical formula about ship length for conventional vessel; it is obviously not appropriate for the unique cross-deck structure. Presently, because of the above problems, the literature regarding fatigue strength assessment of trimaran, which uses the “simplified fatigue method”, is very rare.

Therefore, there is a great significance of an in depth research on fatigue strength assessment of trimaran especially fatigue problems related to the cross-deck structure. In the present study, in order to investigate the fatigue behaviour of cross-deck structural details, a suitable simplified fatigue approach for trimaran is explored, which refers to the existing fatigue guidelines of conventional ships and the direct calculation procedure of LR rules for trimaran. At the same time, the stochastic spectral fatigue analysis is carried out with considering the weighted wave headings factors. Finally, the fatigue lives of a few hot spots are computed to demonstrate the application of the proposed method. Eventually the fatigue characteristic of trimaran cross-deck

structure is summarized, which includes the most dangerous fatigue position and the fatigue damage proportion of various wave heading directions.

2. Basic Theory of Ship Fatigue Analysis

2.1. S-N Curve and Palmgren-Miner Linear Cumulative Damage Theory. The fatigue strength of structural components is described by using the $S - N$ curve, which is obtained from fatigue tests. For ship structural details, the $S - N$ curve is usually represented by the following formula:

$$S^m \cdot N = A \quad (1)$$

where S is the stress range; N is the number of cycles to failure; m and A are constants, which are obtained from the fatigue test data.

Fatigue damage is defined as the ratio between the number of cycles in the design lifetime and the number of cycles to fatigue failure. Based on Palmgren-Miner linear cumulative damage theory, the total fatigue damage can then be calculated as

$$D = \sum_{i=1}^K D_i = \sum_{i=1}^K \frac{n_i}{N_i} = \frac{1}{A} \sum_{i=1}^K n_i S_i^m = \frac{N_L}{A} \overline{S^m} \quad (2)$$

where D_i is the fatigue damage in the stress amplitude S_i ; n_i is the number of cycles under the stress range S_i ; N_i is the number of cycles corresponding to fatigue failure at the same stress range S_i , based on the $S - N$ curve; N_L represents the total number of cycles in the duration; and $\overline{S^m}$ is the mathematical expectation of S^m .

When the stress range is a continuum function and its probability density function is $f_S(S)$, the total fatigue damage can be denoted as follows:

$$D = \frac{N_L}{A} \int_0^{+\infty} S^m f_S(S) dS \quad (3)$$

2.2. Short-Term and Long-Term Stress Range Distribution. Under the assumption of a stationary zero mean Gaussian wave elevation process within each short-term period, the stress response for the linear system is also a stationary zero mean Gaussian process, and the peak values of the stress follow Rayleigh probability density function:

$$f_Y(y) = \frac{y}{\sigma_X^2} \exp\left(-\frac{y^2}{2\sigma_X^2}\right) \quad 0 \leq y < +\infty \quad (4)$$

where y is the peak stress and σ_X is the standard deviation of the stress process.

The standard deviation of the stress process σ_X in terms of spectral moment can be described as

$$\sigma_X = \sqrt{\int_0^{+\infty} G_{XX}(\omega) d\omega} = \sqrt{m_0} \quad (5)$$

where ω is the frequency of the stress process; $G_{XX}(\omega)$ is the stress response spectrum; m_0 is the zero order spectral moment.

On the other hand, for a narrow band process, the following relationship applies to stress range and peak stress.

$$S = 2y \quad (6)$$

Then the stress range probability density function and distribution function can be expressed as

$$f_S(S) = \frac{S}{4m_0} \exp\left(-\frac{S^2}{8m_0}\right) \quad 0 \leq S < +\infty \quad (7a)$$

$$F_S(S) = 1 - \exp\left(-\frac{S^2}{8m_0}\right) \quad 0 \leq S < +\infty \quad (7b)$$

The stress range distribution over the entire structure life is referred as the long-term distribution of the stress range. The commonly used theoretical distribution to adequately approximate the long term distribution of wave induced stress range is two-parameter Weibull distribution [21]. The probability density function and distribution function of two-parameter Weibull distribution are expressed as

$$f_S(S) = \frac{h}{q} \left(\frac{S}{q}\right)^{h-1} \exp\left[-\left(\frac{S}{q}\right)^h\right] \quad 0 \leq S < +\infty \quad (8a)$$

$$F_S(S) = 1 - \exp\left[-\left(\frac{S}{q}\right)^h\right] \quad 0 \leq S < +\infty \quad (8b)$$

where h and q are Weibull shape and scale parameters, respectively.

The distribution function of two-parameter Weibull distribution $F_S(S)$ is usually obtained from weighted combination of short-term distribution functions of stress range:

$$F_S(S) = \frac{\sum_{i=1}^{n_S} \sum_{j=1}^{n_H} \nu_{ij} \cdot p_i \cdot p_j \cdot F_{S\theta ij}(S)}{\sum_{i=1}^{n_S} \sum_{j=1}^{n_H} \nu_{ij} \cdot p_i \cdot p_j} \quad (9)$$

$$= \sum_{i=1}^{n_S} \sum_{j=1}^{n_H} r_{ij} \cdot p_i \cdot p_j \cdot F_{S\theta ij}(S)$$

where n_S is the number of sea states; n_H is the number of wave headings; p_i is the probability of occurrence of the individual sea state; p_j is the probability of occurrence of the wave heading; ν_{ij} is the average zero crossing rate of stress alternating response in the sea state i and wave heading j ; r_{ij} is the ratio of average zero-crossing rate to total average response zero-crossing rate in the sea state i and wave heading j .

The shape parameter h of the Weibull distribution depends on the parameters of the ship, locations of the structure details, structure types, response characteristics, and the sailing routes during the design life. The values of shape parameter generally vary from 0.7 to 1.3. In this paper, the least square method is used to fit the shape parameter. In order to fit Weibull shape parameters by least square method, (8b) is rewritten in linear form as follows:

$$1 - F(s) = \exp\left[-\left(\frac{s}{q}\right)^h\right] \quad (10)$$

Taking natural logarithms on (10) and setting a function $Q(s)$ about s , (10) can be rewritten as

$$Q(s) = \ln\{-\ln[1 - F(s)]\} = h \cdot \ln s - h \cdot \ln q \quad (11)$$

From (11) we can find that $Q(s)$ is linear with $\ln s$, and the shape parameter h of the Weibull distribution is the slope of the line.

In practical application, $Q(s)$ and $\ln s$ can be obtained from a series values of stress range S by using the above method; then a set of sample values are obtained. The least square method is used to fit the sample data linearly, and the shape parameter is obtained.

The scale parameter q is described from the shape parameter and a reference stress response S_0 . The reference stress response S_0 is exceeded once out of the corresponding reference number of the stress cycles N_0 . The scale parameter q can be determined as

$$q = \frac{S_0}{(\ln N_0)^{1/h}} \quad (12)$$

2.3. Spectral Fatigue Damage Calculation. The ‘‘spectral fatigue method’’ usually involves direct wave load analysis in frequency domain and the stress response analysis to establish complex stress transfer functions [21, 22]. On the assumption of narrow band, the Rayleigh probability density function, which is used to describe the short-term stress range distribution, can be obtained by using the various orders of spectral moments of the stress response. The total fatigue damage of a structural element is calculated by adding up the short-term damages over all the applicable sea states in a specific wave scatter diagram. It is considered as the most reliable method for fatigue life estimation of ship structure due to its ability to take into account different sea states as well as their probabilities of occurrence.

The environmental wave spectrum for the different sea states can be defined as the Pierson-Moskowitz wave spectrum and expressed as

$$G_{\eta\eta}(\omega | H_s, T_z)$$

$$= \frac{H_s^2}{4\pi} \left(\frac{2\pi}{T_z}\right)^4 \omega^{-5} \exp\left(-\frac{1}{\pi} \left(\frac{2\pi}{T_z}\right)^4 \omega^{-4}\right) \quad (13)$$

where H_s is significant wave height; T_z is zero crossing period and ω is wave frequency.

For vessel with forward speed U and heading angle θ , the relation between wave frequency ω and the encounter frequency ω_e is given by

$$\omega_e = \omega \left(1 + \frac{2\omega U}{g} \cos \theta\right) \quad (14)$$

According to conservation of energy, using the value of ω_e from (14) and after some mathematical manipulation, wave spectrum $G_{\eta\eta}(\omega_e | H_s, T_z, \theta)$ for a given heading angle is given by the relation

$$G_{\eta\eta}(\omega_e | H_s, T_z, \theta) = \frac{G_{\eta\eta}(\omega | H_s, T_z)}{1 + (2\omega U/g) \cos \theta} \quad (15)$$

Assuming that ship structure is a linear system, the stress energy spectrum $G_{XX}(\omega_e | H_s, T_z, \theta)$ can be obtained from

$$G_{XX}(\omega_e | H_s, T_z, \theta) = |H_\sigma(\omega_e | \theta)|^2 \cdot G_{\eta\eta}(\omega_e | H_s, T_z, \theta) \quad (16)$$

where $H_\sigma(\omega_e | \theta)$ is the stress transfer function.

Then the n th order spectral moment of the response process for a given heading may be described as

$$m_n = \int_0^{+\infty} \omega_e^n \cdot G_{XX}(\omega_e | H_s, T_z, \theta) d\omega_e \quad (17)$$

According to (3) and (7a) and (7b) and after some mathematical manipulations, the short-term fatigue damage D_{ij} during the time of sailing T_{ij} in the specific sea state i and wave heading j can be written as

$$D_{ij} = \frac{T_{ij} f_{0ij}}{A} \left(2\sqrt{2m_{0ij}} \right)^m \Gamma \left(1 + \frac{m}{2} \right) \quad (18)$$

where f_{0ij} is zero-up crossing frequency of the stress response.

The cumulative fatigue damage D for the structural detail in the design life is calculated as

$$D = \sum_{i=1}^{n_s} \sum_{j=1}^{n_H} D_{ij} \quad (19)$$

$$= \frac{T}{A} \Gamma \left(1 + \frac{m}{2} \right) \sum_{i=1}^{n_s} \sum_{j=1}^{n_H} P_i P_j f_{0ij} \left(2\sqrt{2m_{0ij}} \right)^m$$

where T denotes the design life of a ship in seconds.

2.4. Simplified Fatigue Damage Calculation. The ‘‘simplified fatigue method’’ is based on the long-term stress range distribution, which follows the two parameter Weibull probability distribution [21]. The shape and scale parameters are obtained from the previous section. Then choosing basic design $S - N$ curves and according to the linear cumulative damage theory, the fatigue damage can be obtained.

Substituting the value of Weibull scale factor q from (12) into (8a) and then putting the value of long term stress range probability density function $f_S(S)$ from (8a) into (3), after mathematical manipulation, we get the fatigue damage:

$$D = \frac{N_L}{A} \int_0^{+\infty} S^m \frac{h}{q} \left(\frac{S}{q} \right)^{h-1} \exp \left[- \left(\frac{S}{q} \right)^h \right] dS \quad (20)$$

$$= \frac{N_L}{A} \frac{S_0^m}{(\ln N_0)^{m/h}} \Gamma \left(1 + \frac{m}{h} \right)$$

where Γ denotes gamma function.

When predicting the long-term response for trimaran per LR rules, the design life is generally to be taken as 20 years, which corresponds to a long-term probability level of 10^{-8} [20]. So the value of N_0 is 10^8 cycles, and the value of N_L is 0.6×10^8 cycles. Substituting these values and $S - N$ curve

TABLE 1: Wave load calculation parameters.

Parameter	Range	Increment	
Frequency	ω (rad/s)	0.1~2.9	0.1
Heading angle	θ ($^\circ$)	0~330	30

parameter $m = 3$, incorporating variables α (proportion of ship’s life in different loading condition) and μ (coefficient taking into account the change in slope of $S - N$ curve) in (20), we get

$$D = \alpha \frac{0.6}{A} \frac{S_0^3}{18.42^{3/h}} \mu \Gamma \left(\frac{3}{h} + 1 \right) \times 10^8 \quad (21)$$

From (21), we can find that only the reference stress response S_0 is the important parameter to be calculated. It can be obtained by complex empirical formulas global FE analysis.

3. FE Model and Location to Be Checked

Because of the complexity of trimaran’s hullform and structure, the local fine meshes at hot spot location in the whole FE model are used for the calculation of hot spot stress. This whole FE model extends over the full length, breadth, and depth of trimaran. All primary structures, such as deck plating, bottom and side shell plating, longitudinal and transverse bulkhead plating, transverse floors, and internal structural walls, are represented by plate elements. Secondary stiffening members are modeled using line elements having axial and bending stiffness (beams and bars). And the net thickness is used for the fatigue analysis. The whole FE model is shown in Figure 1(a). Structure analysis of trimaran based on direct calculation procedure of Lloyd’s Register Rules for the classification of trimarans is performed to identify locations of hot spots [19, 20]. Then the connection of the main hull and cross-deck at the front (Figure 1(b)) and two transverse sections of the main hull at the center of the cross-deck are selected to perform fatigue analysis.

4. Spectral Fatigue Analysis for Trimaran

4.1. Calculation of Wave Load. The calculation of wave load and stress transfer function is the key step in spectral method. The responses of trimaran motion and wave load are calculated using 3D linear potential flow theory. Parameters used in wave load calculation are summarized in Table 1.

After these parameters are determined, the responses of trimaran motion and hydrodynamic pressure on trimaran’s surface in unit wave amplitude regular waves are calculated. Under the condition of head sea and the wave frequency $\omega = 0.7$ rad/s, the hydrodynamic pressure on trimaran’s surface is shown in Figure 2.

4.2. Calculation of Stress Transfer Function. A global FE analysis of trimaran structure is performed for 4176 load cases by applying inertial load of trimaran motion and spectral fatigue pressure loads generated during previous step to generate stress transfer functions at hot spots. Stress transfer functions of selected hot spots are shown in Figure 3.

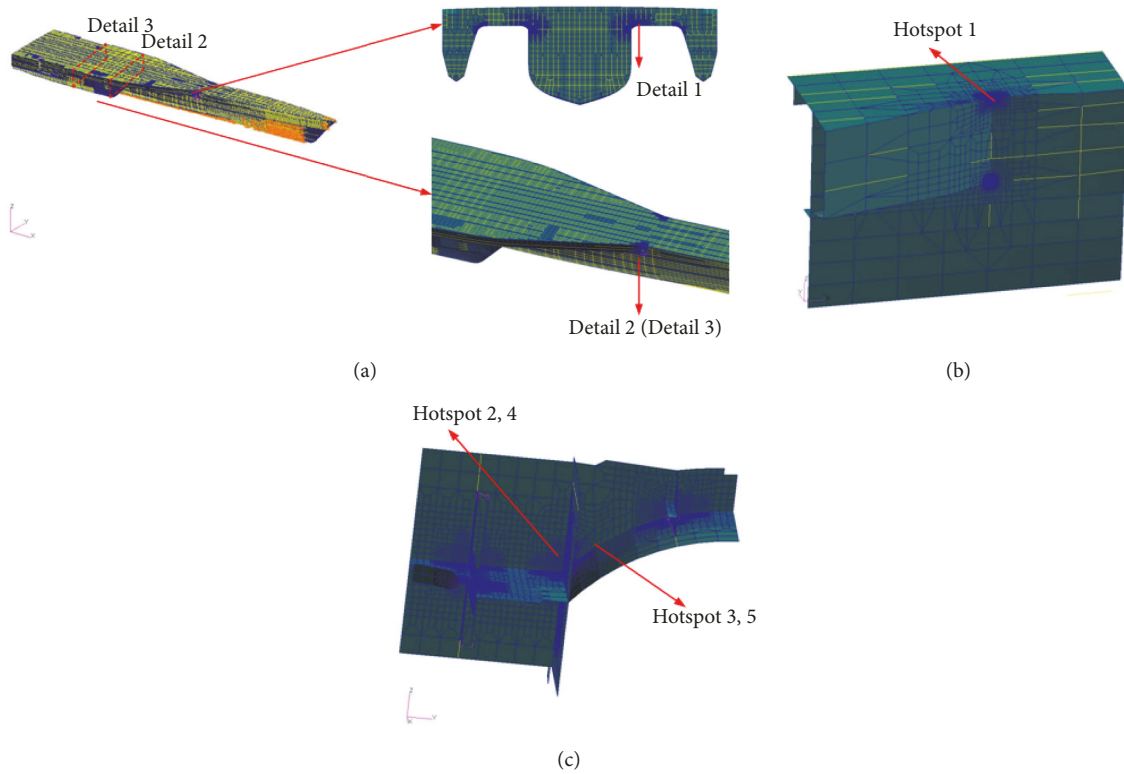


FIGURE 1: The whole FE model and fine mesh models. (a) The whole FE model and details. (b) Detail 1. (c) Detail 2 (Detail 3).

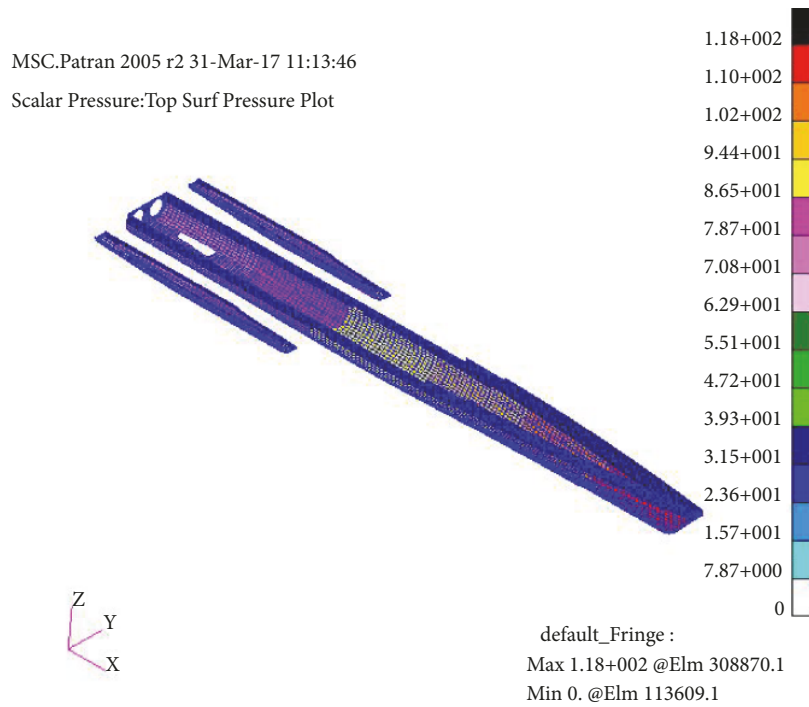


FIGURE 2: The hydrodynamic pressure on ship's surface.

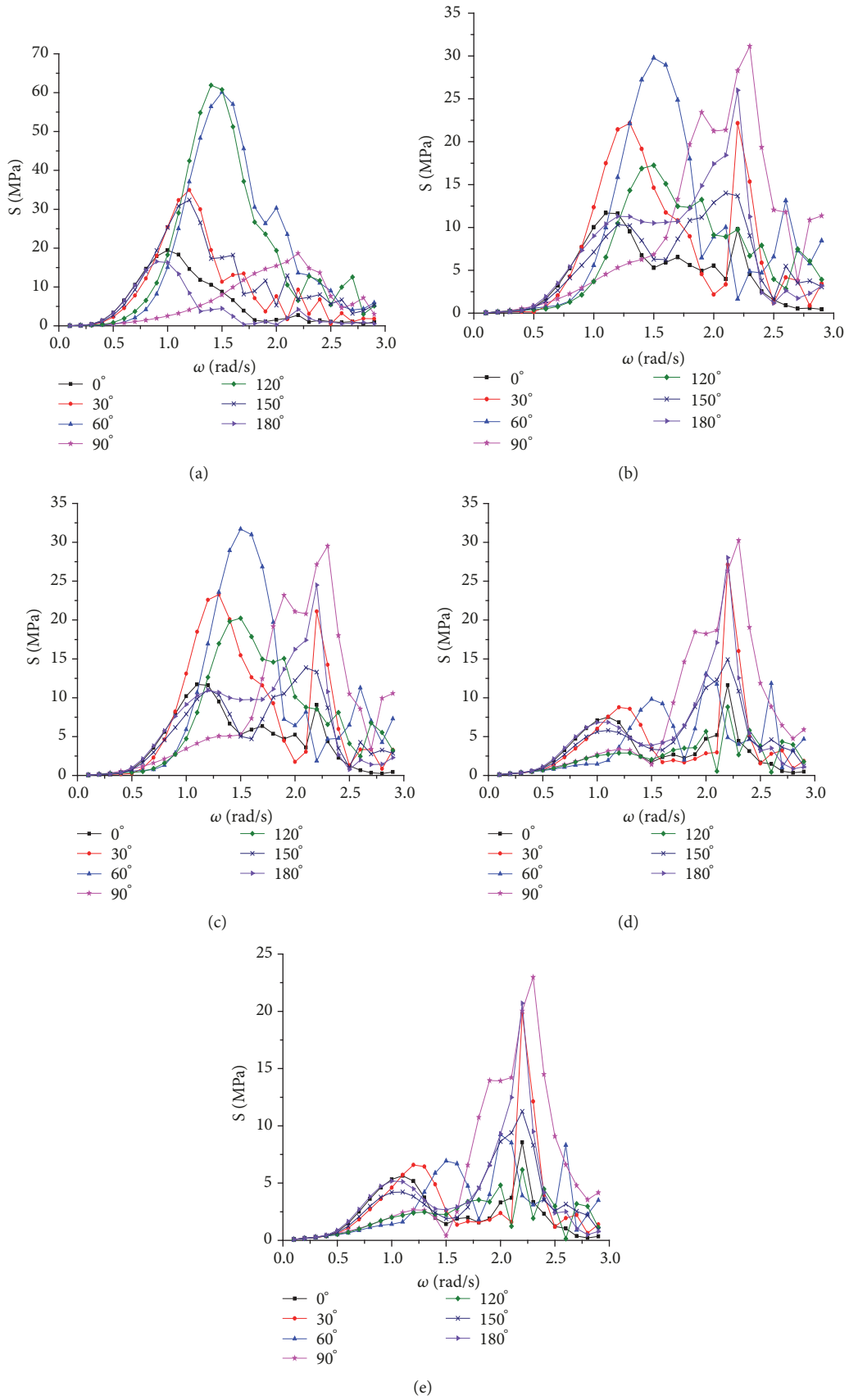


FIGURE 3: Stress transfer function. (a) Hot spot 1. (b) Hot spot 2. (c) Hot spot 3. (d) Hot spot 4. (e) Hot spot 5.

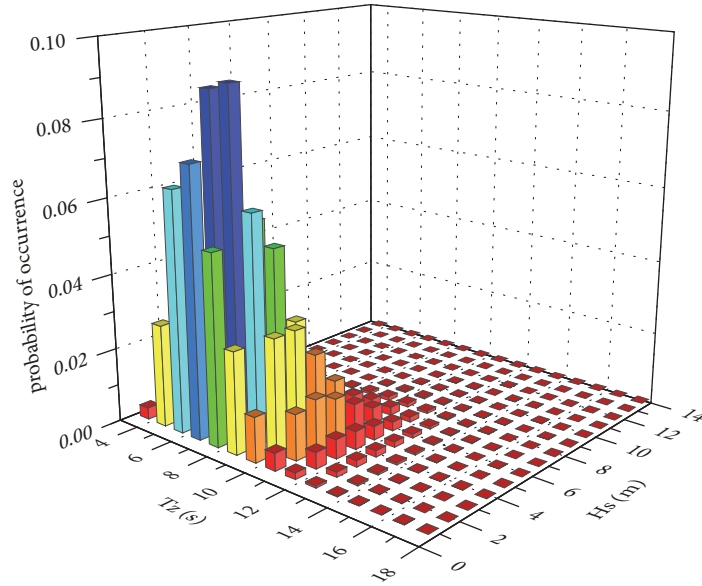


FIGURE 4: World Wide Trade wave scatter diagrams.

Figure 3 shows that the stress transfer function values of hot spot 1 are larger in the wave heading 60° and 120° . It can be inferred that the longitudinal torsional moment is the main load for structure detail 1. The stress transfer function values of hot spots 2, 3, 4, and 5 in the wave heading 60° and 90° are almost equivalent; the values in the wave heading 180° are also larger. It means that structural response in oblique sea is almost as large as that caused in beam sea, so the splitting moment and transverse torsional moment are the main load components for structure details 2 and 3. At the same time, following sea can also cause larger structural response.

4.3. Spectral Fatigue Analysis Results and Discussion. In this paper, fatigue damage is calculated by using wave scatter data of World Wide Trade (shown in Figure 4). And the Pierson-Moskowitz spectrum is chosen as wave energy spectrum.

Meanwhile, it is usually assumed that the ship has equal probability of encountering waves from all directions in spectral fatigue analysis. Corresponding to simplified fatigue method, the time allocation ratios of 50% head sea and following sea, 25% beam sea and 25% oblique sea are used for calculating the fatigue damage. In this paper, 0° is defined as head sea, 180° is defined following sea, 90° and 270° are defined as beam sea, and others are defined as oblique sea. Fatigue damage calculation results of hot spots in all wave headings are shown as Figure 5. The proportion of spectral fatigue damage in head sea, beam sea, and oblique sea is summarized in Figure 6.

From Figure 5, we can clearly find that the fatigue cumulative damage values of hot spot 1 are larger in all wave headings than that of other hot spots. It indicates that the fatigue problem of the connection of the main hull and cross-deck at the front is serious. Meanwhile, the fatigue cumulative damage values of hot spots 2, 3, 4, and 5 in the oblique wave headings are larger than other wave headings, so the oblique sea contributes the majority of fatigue damage. Figure 6

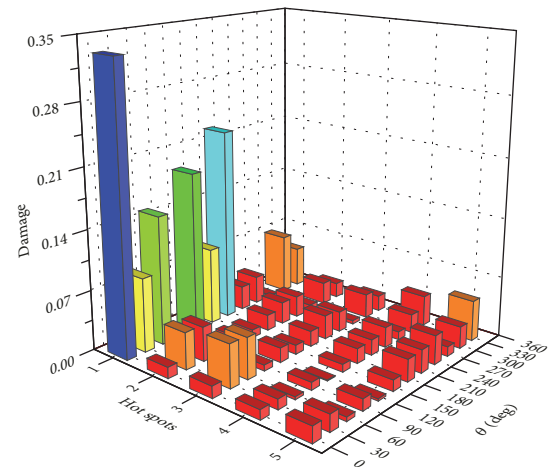


FIGURE 5: The spectral fatigue damage results.

shows that the fatigue damage caused in oblique seas are larger than beam sea and head sea for hot spots 2, 3, 4, and 5. Meanwhile, the fatigue damage is caused in oblique sea nearly as large as that caused in head sea for hot spot 1. Figure 6 also shows that the fatigue damage caused in beam sea is smaller than other sea conditions, especially for hot spot 1.

5. Simplified Fatigue Analysis for Trimaran

The simplified fatigue method is generally the first level procedure of the classification societies for fatigue assessment of ship structures. The analysis procedures have been established for conventional ships by the major classification societies. However, because the positions with severe fatigue problems are mainly located at trimaran cross-deck structure, application of this method for trimaran is complex since guidelines for fatigue loads, load cases, loading conditions,

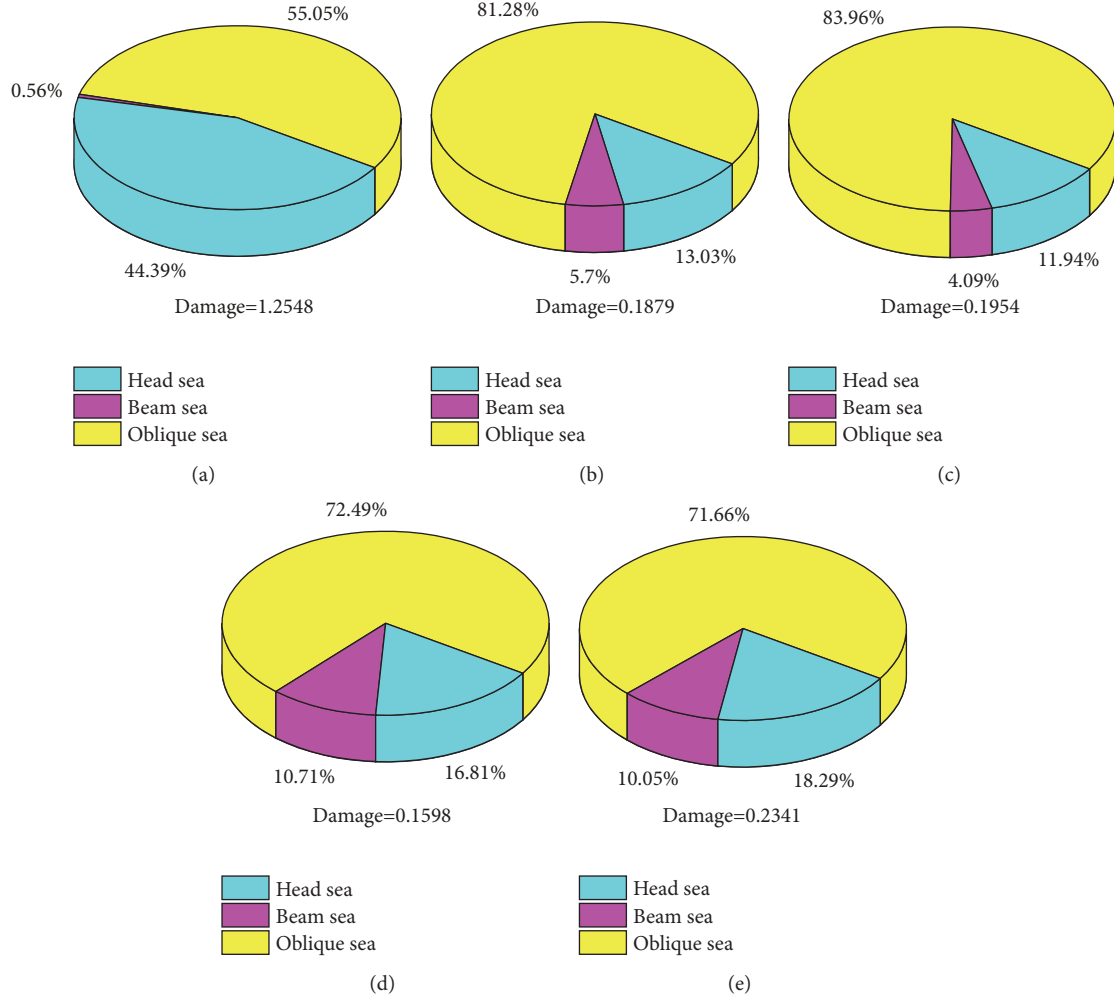


FIGURE 6: The proportion of spectral fatigue damage. (a) Hot spot 1. (b) Hot spot 2. (c) Hot spot 3. (d) Hot spot 4. (e) Hot spot 5.

and stress range evaluation are not available. The simplified fatigue method for trimaran in this study, the fatigue loads, and loading conditions are based on the manipulation of load combinations of the direct calculation procedure of LR Rules [20]. Stress ranges are computed by global FE analysis.

5.1. Calculation of Wave Load. The vertical wave bending moment M_w , at any position along the length of trimaran, is given by the following:

$$M_w = F_f \cdot D_f \cdot M_0 \quad (22)$$

where F_f is the correction factor of the hogging or sagging; D_f is the vertical bending moment distribution factor; M_0 is given by the following:

$$M_0 = 0.1L_f f_{serv} L_R^2 B_{WL} (C_b + 0.7) \quad (23)$$

where L_f is the factor varying with length of trimaran; f_{serv} is the service group factor; L_R is the Rule length; B_{WL} is the breadth of water line; C_b is the block coefficient.

The horizontal bending moment M_h is calculated as follows:

$$M_h = D_f L_f f_{serv} L_R^2 D (C_b + 0.7) \quad (24)$$

where D is the depth of main hull.

The splitting moments, for hog, M_{sph} , and for sag, M_{sps} , are given by the following:

$$\begin{aligned} M_{sph-I} &= 9.81 f_{serv} W_{sh} (1 + \alpha_z) \left(y_{sh} - \frac{B_{mh}}{2} \right) \\ M_{sph-O} &= 9.81 f_{serv} W_{sh} (1 + \alpha_z) (y_{sh} - y_O) \\ M_{sps-I} &= 9.81 f_{serv} \frac{(\Delta - 2\Delta_{sh})}{2} \alpha_z \left(y_{sh} - \frac{B_{mh}}{2} \right) \\ M_{sps-O} &= 9.81 f_{serv} \frac{(\Delta - 2\Delta_{sh})}{2} \alpha_z (y_{sh} - y_O) \end{aligned} \quad (25)$$

where W_{sh} is the total weight of one side hull; α_z is the vertical acceleration; B_{mh} is the main hull breadth; Δ is the total displacement of the side hulls and the main hull; Δ_{sh}

TABLE 2: Load combinations.

Wave direction	Load cases	Load components						
		M_{wh}	M_{ws}	M_h	M_{sph}	M_{sps}	M_{lt}	M_{tt}
Head seas	1	1.0	—	—	0.3	—	—	0.2
	2	—	1.0	—	—	0.3	—	0.2
Beam seas	3	0.1	—	—	1.0	—	0.2	—
	4	—	0.1	—	—	1.0	0.2	—
Oblique seas	5	—	—	0.3	0.4	—	1.0	0.3
	6	—	—	1.0	0.4	—	—	0.2
	7	—	0.2	0.2	0.6	—	—	1.0

is the total displacement of one side hull. Points I and O are referred to as LR Rules [21].

The longitudinal torsional moment M_{lt} is calculated as follows:

$$M_{lt} = 7.5 \left(T_f f_{serv} \rho V_{sh} + V_{cd} + \frac{V_{msh}}{2} y_{cs} a_{heave} \right) \quad (26)$$

where T_f is the distribution coefficient along trimaran length; ρ is the sea water density; V_{sh} is the volume of one side hull; V_{cd} is the volume of the cross-deck structure; V_{msh} is the volume of the main hull; y_{cs} is the transverse distance from centerline to the centre of area of a cross-section taken at mid length of the side hull; a_{heave} is the heave acceleration.

The transverse torsional moment M_{tt} , is uniform along the breadth of the cross-deck structure and is given by the following:

$$M_{tt} = 3.75 f_{serv} \rho (V_{sh} + V_{cd}) L_{sh} a_{heave} \quad (27)$$

where L_{sh} is the length of side hull.

5.2. Load Case. Fatigue analyses are carried out for the representative loading conditions according to the intended operation of trimaran. Fatigue loading conditions corresponding to LR Rules are summarized in Table 2 and categorized as three wave heading directions including head sea, beam sea, and oblique sea.

5.3. Evaluation of Stress Range. In simplified fatigue analysis of conventional ship, the stress range S_{ri} required for the calculation of accumulated damage is usually calculated based on simple beam theory assumptions. This method is obviously not appropriate for trimaran cross-deck structure due to its unique configuration. Alternatively, for trimaran, the global FE analysis is employed to directly calculate stress values, and the stress range evaluation is based on the results of that. According to various deflection pattern of trimaran for different loading conditions, load cases 1 and 2 of head seas cause the longitudinal hogging and sagging, whereas load cases 3 and 4 of beam seas result in transverse hogging and sagging. Therefore the stress ranges for head seas condition and beam seas condition can be expressed as

$$S_{head} = \sigma_{LC1} - \sigma_{LC2} \quad (28a)$$

$$S_{beam} = \sigma_{LC3} - \sigma_{LC4} \quad (28b)$$

For oblique seas condition, the relationship $S = 2\sigma$ is assumed between stress range S and stress amplitude σ . Thus, the stress range for oblique seas condition can be calculated as follows:

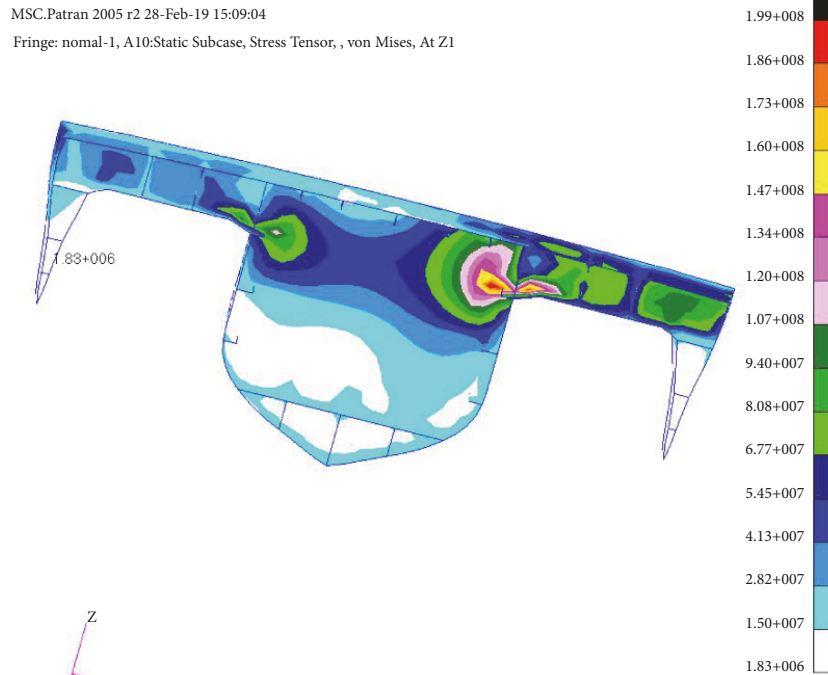
$$\begin{aligned} S_{oblique} &= \frac{1}{3} (S_{oblique-1} + S_{oblique-2} + S_{oblique-3}) \\ &= \frac{1}{3} (2\sigma_{LC5} + 2\sigma_{LC6} + 2\sigma_{LC7}) \end{aligned} \quad (29)$$

5.4. Simplified Fatigue Analysis Results and Discussion. A global FE analysis of trimaran in the seven load cases above is done. To limit the length of the paper, only the results of structural details 2 and 3 in load case 4 are given in Figure 7. The shape parameter h of the Weibull distribution is calculated by using the method given in Section 2.2. The short-term distribution functions of stress range are obtained by using the spectral method. And the parameters used in wave load calculation are the same as those for spectral fatigue analysis, which has given in Section 4.1. In this paper, 45 sample data (3-25MPa with 0.5MPa increments) are selected for fitting. The fitting results are shown in Figure 8.

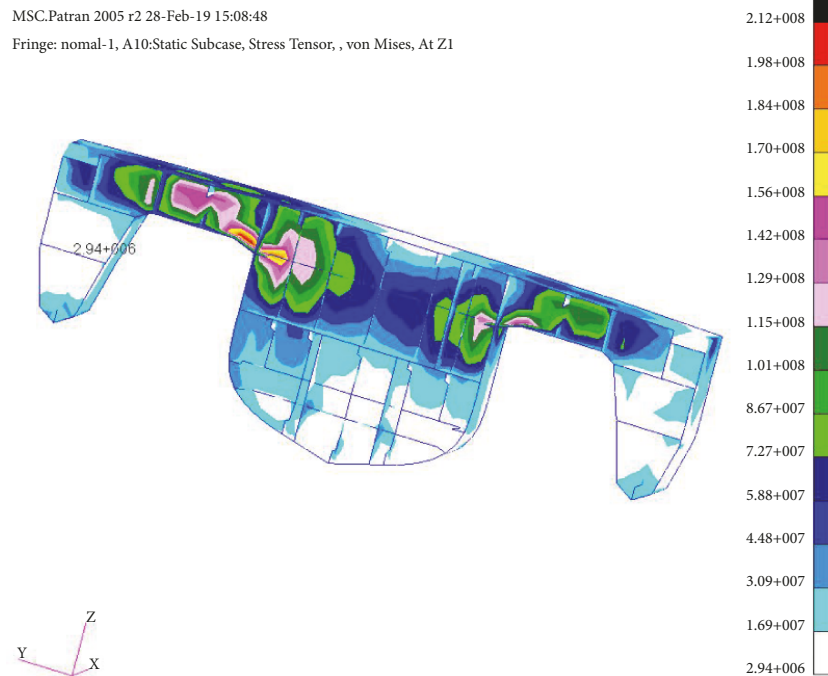
Figure 7 shows that the connections of the main hull and wet-deck in the cross-deck structure have serious stress concentration. From Figure 8, it can be seen that the data points are distributed near the fitting lines for all the five hot spots. The correlation coefficients are all close to 1; there is a strong linear correlation. The values of the Weibull distribution's shape parameter h are all near to 1 for these hot spots. But for hot spots 2 and 4, the values are larger.

The fatigue strength of trimaran cross-deck structure's hot spots, which are illustrated at Section 3, is evaluated by simplified fatigue method to demonstrate its application. The fatigue damage calculation results of hot spots in all wave headings are shown as Figure 9. The proportion of fatigue damage in head seas, beam seas, and oblique seas is summarized in Figure 10.

From Figures 9 and 10, we can see that the fatigue damage value of hot spot 1 is larger than other hot spots, which indicates that the connection of the main hull and cross-deck at the front has serious fatigue problem. The same conclusion can be obtained from spectral fatigue analysis result. Figure 9 shows that the fatigue damage values of hot spot 1 in the head seas and load case 6 of oblique seas are larger than other sea conditions. It can be inferred that the vertical and horizontal wave bending moment are the main loads for hot



(a)



(b)

FIGURE 7: The max principal stress contour in load case 4. (a) Detail2. (b) Detail3.

spot 1, which cause the majority of the fatigue damage. From Figure 10, we can also find that beam seas nearly do not cause fatigue damage; head seas cause the majority of fatigue damage for hot spot 1. But, for hot spots 2, 3, 4, and 5, the fatigue damage caused in oblique seas is larger than head seas and beam seas. Meanwhile, the fatigue damage values caused

in beam seas are also larger, which is mainly caused by the splitting moments.

5.5. *Further Discussion.* From the spectral and simplified analysis calculation results, it is found that the connection of the main hull and cross-deck at the front suffers maximum

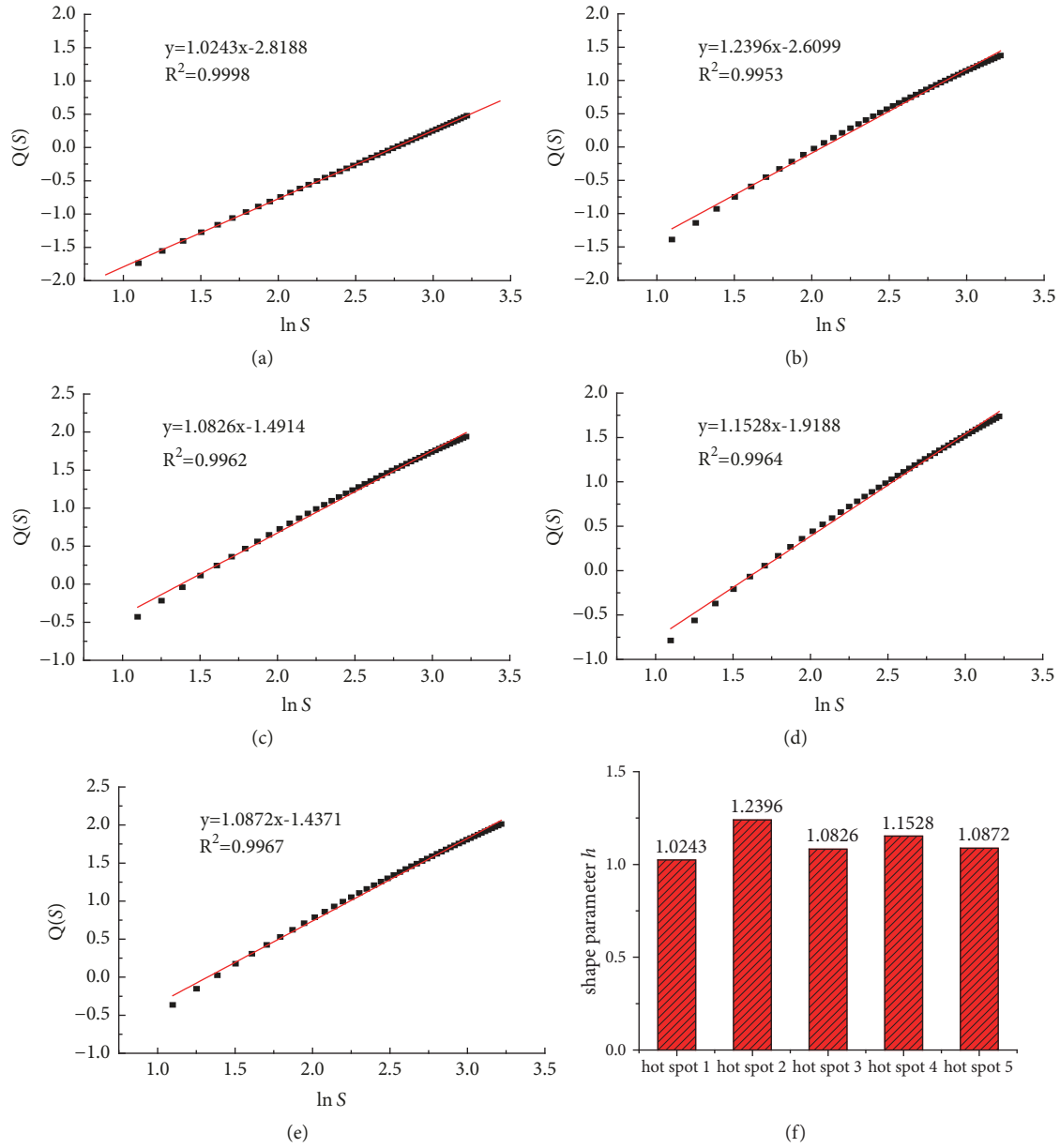


FIGURE 8: The fitting results of shape parameter. (a) Hot spot 1. (b) Hot spot 2. (c) Hot spot 3. (d) Hot spot 4. (e) Hot spot 5. (f) Values of hot spots' shape parameter.

fatigue damage for trimaran. The fatigue damage results in three wave headings obtained from both spectral and simplified fatigue method show that the cumulative damage from the beam sea can be neglected for hot spot 1. The cumulative damage values from the oblique sea are so large in all hot spots. It can be inferred that severe loads from head sea and oblique sea are the major factor of trimaran cross-deck structure's fatigue. Moreover, the predicted fatigue damage value of hot spot 1 exceeded the allowance, which indicates the requirement of structure strengthening and optimization at this location.

6. Conclusion

In this paper, the methodology of spectral and simplified fatigue analysis is adopted to investigate the fatigue characteristic of trimaran cross-deck structure. The following conclusions can be drawn based on the above study.

A methodology to perform simplified fatigue analysis of trimaran cross-deck structure is presented. In this simplified fatigue method, the total stress ranges are obtained by combining the stress ranges under different sea conditions. Due to the unique structure, they are achieved by global FE analysis based on direct calculation procedure.

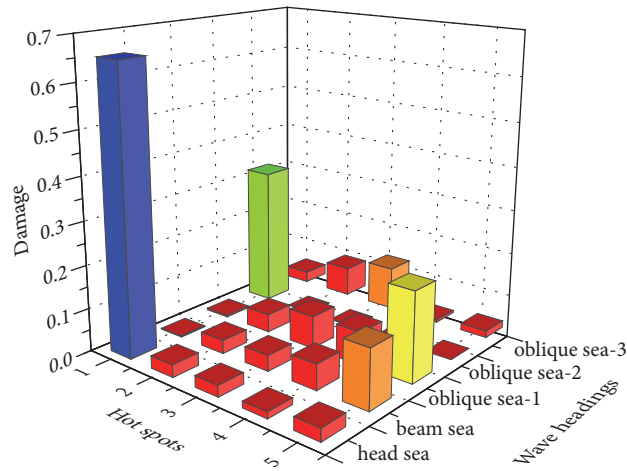


FIGURE 9: The simplified fatigue damage results.

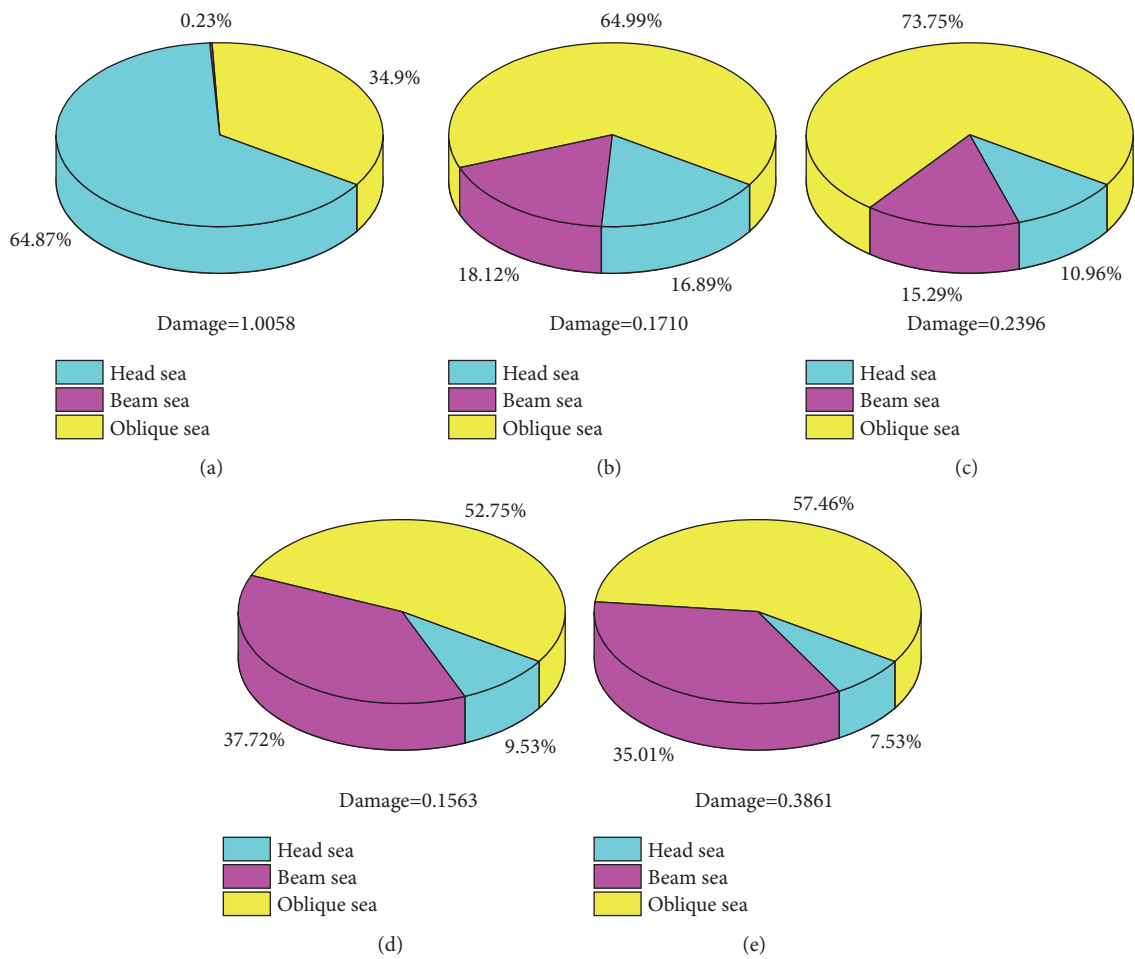


FIGURE 10: The proportion of simplified fatigue damage. (a) Hot spot 1. (b) Hot spot 2. (c) Hot spot 3. (d) Hot spot 4. (e) Hot spot 5.

The spectral and simplified fatigue analysis results give the basically same fatigue characteristics of trimaran cross-deck structure details. The fatigue analysis methodology of trimaran cross-deck structure presented in this paper is validated. Furthermore, the connection of the main hull and cross-deck at the front is the most dangerous fatigue position; it must attract sufficient attention. Meanwhile, the cross-deck structure's fatigue damage is mainly caused from head sea and oblique sea.

Data Availability

The data used to support the findings of this study are available from the corresponding author upon request.

Conflicts of Interest

The authors declare that they have no conflicts of interest.

Acknowledgments

This work is supported by the National Key Research and Development Program of China (no. 2016YFC0301500), the Fundamental Research Funds for the Central Universities (3132018206), the Open Fund of Key Laboratory of High Performance Ship Technology (Wuhan University of Technology), and Ministry of Education (gxnc18041403).

References

- [1] T. Armstrong, "On the performance of a large high-speed trimaran," *Australian Journal of Mechanical Engineering*, vol. 3, no. 2, pp. 123–131, 2006.
- [2] A. Aubault and R. W. Yeung, "Interference resistance of multi-hull vessels in finite-depth waters," in *Proceedings of the ASME 31th International Conference on Ocean, Offshore and Arctic Engineering*, Rio de Janeiro, Brazil, 2012.
- [3] S. Brizzolara, M. Capasso, and A. Francescutto, "Effect of hull form variations on the hydrodynamic performances for fast transportation," in *Proceedings of the 8th international conference on fast sea transportation, FAST*, Saint-Petersburg, Russia, 2005.
- [4] C. Yang, O. Soto, R. L., and R. Löhner, "Hydrodynamic optimization of a trimaran," *Ship Technology Research*, vol. 49, pp. 70–92, 2002.
- [5] S. M. Wang, S. Ma, and W. Y. Duan, "Seakeeping optimization of trimaran outrigger layout based on NSGA-II," *Applied Ocean Research*, vol. 78, pp. 110–122, 2018.
- [6] W. P. Zhang, Z. Zhong, and S. L. Ni, "Model testing of seakeeping performance of trimaran," *Journal of Hydrodynamics(Ser.A)*, vol. 22, no. 5, pp. 619–624, 2007.
- [7] C. Bertorello, D. Bruzzone, P. Cassella et al., "Trimaran model test results and comparison with different high speed craft," *Practical Design of Ships and Other Floating Structures*, vol. 1, pp. 143–149, 2001.
- [8] A. E. Bingham, J. K. Hampshire, and S. H. Miao, "Motions and loads for a trimaran travelling in regular waves," in *Proceedings of the 6th International Conference on Fast Sea Transportation*, Royal Institution of Naval Architects, pp. 167–176, 2001.
- [9] C. C. Fang, Y. H. Lee, H. S. Chan, and H. T. Wu, "Numerical investigation on wave load characteristics of a high speed trimaran in oblique waves," *Journal of Taiwan Society of Naval Architects and Marine Engineers*, vol. 27, no. 2, pp. 71–79, 2008.
- [10] M.-C. Fang and T.-Y. Chen, "A parametric study of wave loads on trimaran ships traveling in waves," *Ocean Engineering*, vol. 35, no. 8-9, pp. 749–762, 2008.
- [11] W. Cui, "A state-of-the-art review on fatigue life prediction methods for metal structures," *Journal of Marine Science and Technology*, vol. 7, no. 1, pp. 43–56, 2002.
- [12] H. Ren, C. Zhen, C. Li, and G. Feng, "Study on structural form design of trimaran cross-deck," in *Proceedings of the ASME 31th International Conference on Ocean, Offshore and Arctic Engineering*, Rio de Janeiro, Brazil, 2012.
- [13] I. Lotsberg, *Fatigue Design of Marine Structures*, Cambridge University Press, Cambridge, 2016.
- [14] W. Fricke, W. Cui, H. Kierkegaard et al., "Comparative fatigue strength assessment of a structural detail in a containership using various approaches of classification societies," *Marine Structures*, vol. 15, no. 1, pp. 1–13, 2002.
- [15] I. Lotsberg and E. Landet, "Fatigue capacity of side longitudinals in floating structures," *Marine Structures*, vol. 18, no. 1, pp. 25–42, 2005.
- [16] I. Lotsberg, "Assessment of fatigue capacity in the new bulk carrier and tanker rules," *Marine Structures*, vol. 19, no. 1, pp. 83–96, 2006.
- [17] Y. Wang, "Spectral fatigue analysis of a ship structural detail - A practical case study," *International Journal of Fatigue*, vol. 32, no. 2, pp. 310–317, 2010.
- [18] Y. H. Peng, J. H. Liu, and F. H. Wang, "Fatigue assessment and analysis of trimaran structure," *Shipbuilding of China*, vol. 52, no. 3, pp. 25–35, 2011.
- [19] C. B. Zhen, T. L. Wang, and P. Y. Yu, "The influencing factors analysis for direct calculation of trimaran structure's fatigue strength," *Chinese Journal of Ship Research*, vol. 12, no. 3, pp. 86–90, 2017.
- [20] Lloyd's Register, *Rules for the Classification of Trimarans*, Lloyd's Register, UK, 2006.
- [21] Det Norske Veritas, *Fatigue assessment of ship structures*, Det Norske Veritas, Oslo, Norway, 2010.
- [22] Y. R. Hu and B. Z. Chen, *Fatigue reliability analysis of the ship and ocean engineering structures*, Harbin Engineering University Press, Harbin, China, 2010.